CFD Analysis of an Axial Piston Pump

Thesis project submitted to obtain the degree of Doctor Engineer, PhD with European recognition

By

Sushil Kumar

Under the guidance of

Dr. Josep M Bergada

Fluid Mechanics Department
Universidad Politecnica de Catalunya.
May 2010.

Acknowledgement

The author would like to thanks Dr Josep M Bergada, who put a huge effort in doing the experimentations in the Fluid Power laboratory of Cardiff University, United Kingdom which have been used to test the developed computational models. He has been working from the past ten years with Prof John Watton, who is in charge of Fluid Power laboratory at Cardiff University. During this time period, he has done a lot of experiments and also has been an important member of the development team of these test rigs. As a result he is able to provide the author a proper guidance for better understanding of the different simulation results.

Author would also like to thank Prof. Ramon Codina, for the two courses which have been taken during the study of doctorate courses. It helped author in improving the level of his computational techniques and also for his advice in some valuable personal discussions which helped author in choosing and developing the proper computational technique and specifically choosing some proper boundary conditions for the slipper-swash plate model.

Author would like to point out that, the part of the work done in the present thesis has been published in following Articles

Published Journal Papers -

1. **Kumar S**., Bergada JM, Watton J. Axial piston pump grooved slipper analysis by CFD simulation of three dimensional NVS equation in cylindrical coordinates. Computer & Fluids (2009) Vol 38 N3 pp 648-663.
2. Bergada JM, Watton J, **Kumar S**. Pressure, flow, force and torque between the barrel and port plate in an axial piston pump. Journal of dynamic systems, measurement and control, Jan 2008, Vol 130. N 1. pp 011011-1/16

Published Conference Papers –

1. JM.Bergada, **S.Kumar**, J.watton. Towards an Analytical solution for Axial Piston Pump leakage and outflow Ripple. 15 juny Flucome 2007. Tallahassee, Florida – USA.
2. JM Bergadà; D.L Davies; Y Xue; **S. Kumar**.Experimental Investigation in axial piston pumps barrel dynamics 17-21August 2009. Flucome 2009. Moscow. Article No 160.

Submitted Journal Papers –

1. **S. Kumar**, Bergada JM. The effect of the grooves on the piston performance in an axial piston pump via CFD of Reynolds equation. Submitted to Computer & Fluids, May 2010.
2. J.M. Bergada[1]; D. Ll. Davies[2]; **S. Kumar[1]**; Y. Xue[2]; J. Watton[2]. The barrel dynamic behavior of axial piston pumps. Submitted to ASME, August 2009.

Paper under development –

1. **S. Kumar**, Bergada JM. Analysis of an Axial Piston Pump grooved slipper under tilted conditions by CFD simulation of 3-D NVS equation in cylindrical coordinates.
2. JM. Bergada[1] **S. Kumar[1]**,. D. Ll. Davies[2], J. Watton[2]. A complete analysis of Axial Piston Pump leakage and output flow ripples.

Abstract

In the field of Fluid Power, piston pumps possess the most sophisticated designs, in fact, pistons pumps are the only ones capable of working at high pressures, besides possessing the best performance (efficiency) of the entire group of existing pumps. However, it is noted that all the designs of piston pumps, are mostly based on the experience of the designers, thus there exist no mathematical tools for optimizing the design of the different parts of the pumps. On the other hand, there are now companies like Oilgear Towler, who inserted slots (grooves) in the slippers and in the pistons, (two major parts of these pumps) but there is no scientific study to analyze its advantages or disadvantages. There is therefore a need to understand mathematically to study the advantages and disadvantages due to the presence of the groove on the surface of different pump parts. There are four sliding surfaces in the piston pump, Slipper-swash plate gap, Barrel-valve plate gap, Piston-barrel chamber gap and Spherical bearing, where lubrication exists and leakages through these channels occur.

In this project, our aim is to analyze each of these different sliding surfaces separately to understand its design constrains and the effect of the design parameters on the pump behavior. After having a better understanding of all the different parts of the piston pump, all Studies conducted in the previous stage are going to be linked using the continuity equation applied to the piston chamber, also fluid compressibility will be taken into account. The aim is to model the dynamic behavior of pressure and flow at the outlet of the pump.

Slipper plate gap - There has been allot of research work done in literature on slippers without grooves or vented grooves by different researchers such as Hook, Iboshi, Yamaguchi, Ivantysynova etc. But no evidence has been found of any research focused on finding the leakage, pressure distribution, force and torque created by a slipper with a non vented groove and considering spin and tangential velocity. In order to full fill this objective, a three dimensional Navier Stokes equations in cylindrical coordinates have been applied to the slipper/plate gap, including the groove. The results presented in this thesis include, pressure distribution, leakage, force and torque variations when groove dimensions and position are being modified, the effect of slipper tangential velocity and tilt are also considered. Fluid momentum interchange inside the groove is studied, since vorticity inside the groove is analyzed under several working conditions. The CFD results were compared with experimental one, finding a good agreement for all of the cases studied. Design instructions to optimize slipper/groove performance are also given.

Barrel-valve plate gap - Despite the amount of research work published, evidence has not been found regarding a full investigation of pressure distribution, leakage, force and torque distribution in barrel port plate and then adding barrel dynamics. Present thesis, analyses the pressure distribution, leakage, force and torque between the barrel and the port plate of an axial piston pump by simulating Reynolds equations of lubrication by FDM (finite difference method). The overall mean force and torques over the barrel are evaluated from simulated pressure and it shows that the torque over the XX axis is much smaller than the torque over the YY axis. A detailed dynamic analysis is then studied.

Piston-barrel chamber gap - An interesting amount of work has been undertaken in literature, considering the geometric shape of the groves, friction parameters and its effect on the operating conditions in order to improve the piston performance, but despite all the work undertaken by previous researchers, there has never been studied, the effect of the number of grooves cut on the piston surface and specially the effect of modifying their position, including as well the piston tilt and its relative movement versus the cylinder. In this thesis, it is being investigated the piston performance by modifying the number of grooves and their position, pressure distribution in the clearance piston-cylinder, leakage force and torque acting over the piston will be discussed, also the locations where cavitation is likely to appear will be presented, discussing how to prevent cavitation from appearing via using grooves. A finite volume based Reynolds equation model has been formulated for the piston-cylinder clearance which considers the piston eccentricity and the relative tangential movement between piston and barrel. Different configurations of the grooves have been evaluated in search of finding minimum leakage, minimum appearance of cavitation and maximum restoring torque. Design instructions to optimize the piston behavior are also given.

Spherical bearing - The literature of the spherical bearing is much matured and the window for the further research is quite narrow. Therefore a very simple model of spherical bearing has been considered. Ball and bearing are considered as constrict. Such model already exists in literature.

Full pump Model - There exist several full pump models in the literature which studied the outflow pump ripple, but among these models which are based on fully numerical data produce very slow results, such model developed by Ivantysynova. Others define leakages using very simple equations, this is why in the present paper, an extensive set of explicit equations for every pump gap will be presented, all of the equations will be checked via performing a numerical analysis of the specified pump clearance, and the equations will then be combined to study dynamically pressure ripple and leakages. The effect on the flow ripple when modifying the pump design will also be presented.

Therefore in present thesis, a simulation model based on analytical equations has been developed which produce very fast results and clarify very precisely the effect of different leakages happened through the pump clearances.

Content

1

Introduction

In this chapter first we are going to establish the mechanical configuration of the piston pump and a little description of its different parts and working mechanism. Next, it is to be found a brief description of the work which has been done in this project.

1.1 Mechanical description of the pump.

A pump is a device used to transport fluids. Pumps fall into two major categories: positive displacement pumps and rotodynamic pumps. Their names describe the method for moving the fluid. A positive displacement pump causes a fluid to move by trapping a fixed amount of it then forcing (displacing) that trapped volume into the discharge pipe, that's why they are also known as volumetric pumps. On the other hand rotodynamic pumps also known as kinetic pumps or centrifugal pumps, use the concept of adding energy continuously to the fluid and than transforming this increase kinetic head into pressure head.

Piston pump is a positive displacement pump which can be further classified into three main categories, namely Radial piston pump, Bent axis piston pump and Swash plate axial piston pump. In the present work, the pump into consideration is a swash plate axial piston pump, generally called as an axial piston pump. It has a number of pistons (usually an odd number) arranged in a circular array within a housing which is commonly referred to as a cylindrical block, rotor or barrel. This cylinder block is driven to rotate about its axis of symmetry by an integral shaft that is, more or less, aligned with the pumping pistons.

Axial piston pumps can be further classified into two categories, fixed displacement and variable displacement piston pump. In fixed displacement pumps, the stroke of the piston can not be modified; on the other hand it can be modified in variable displacement piston pumps. Figure 1.1 shows a cross section cut of an axial piston pump. Different parts are also outlined in the figure and a small description is given bellow.

1.1.1 Variable displacement unit.

This unit is mounted only in variable displacement axial piston pumps. Its function is to modify the swash plate angle in order to modify pistons stroke, if the vector normal to the cam plane (swash plate) is set parallel to the axis of rotation, there is no axial movement of the pistons inside their cylinders. Thus there is no output flow. Swash plate angle, controls the piston stroke length and thus the pump output flow, from zero to maximum.

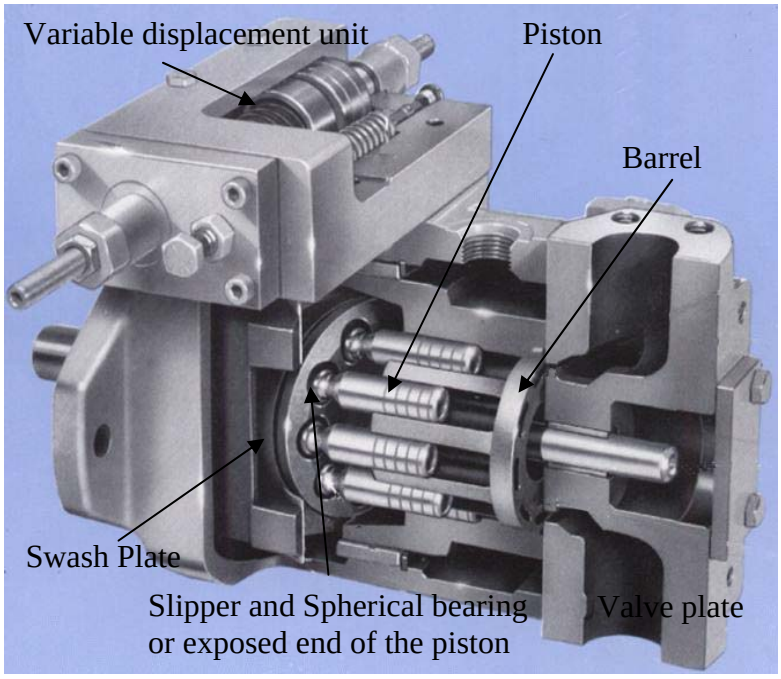

Figure 1.1 – Main Components with in an axial piston pump.

1.1.2 Barrel.

It is a cylindrical metallic block, as shown in the figure 1.1, inside which the pistons are allocated. It is connected with the pump main axis and therefore it turns with it, on one end, the barrel slides around the valve plate, while on the opposite end the slippers attached to the pistons slide around the swash plate.

1.1.3 Swash Plate.

The pumping pistons protrude from one end of the cylinder block (barrel). There are numerous configurations used for the exposed ends of the pistons but in all cases they bear against a plate, which is referred to as a swash plate. In variable displacement units, the plate is movable on the other hand in fix displacement unit it is not. For conceptual purposes, swash plate can be represented by a plane, the orientation of which, in combination with shaft rotation, provides the plate action that leads to piston reciprocation and thus pumping. The angle between a vector normal to the plate plane and the cylinder block axis of rotation, is called the swash plate angle, is one variable that

determines the volumetric displacement of the pump or the amount of fluid pumped per shaft revolution. In general, the value of swash plate angle is about 18^{o}.

1.1.4 Slipper.

The exposed end of the piston which is wearing against the swash plate is called slipper. Figure 1.2 represents a clearer picture of the top view of the slipper from the swash plate. There are various types of slippers found in different axial piston pumps, from the design point of view, it can be said that the existence of a non vented groove on the slipper surface is quite rear. Figure 1.2 represents the slipper design which is considered for the analysis in this project.

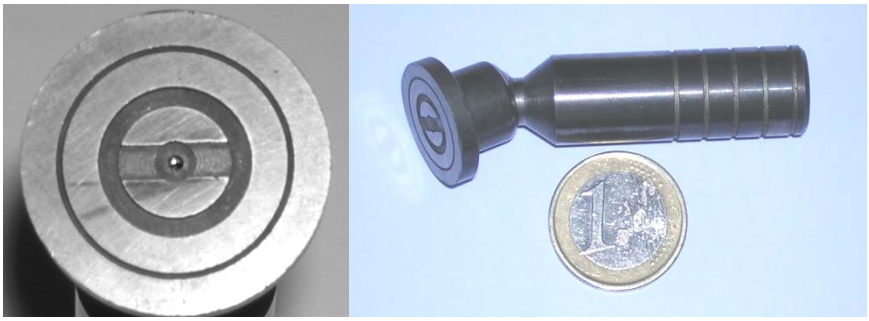

Figure 1.2 – Slipper top view and Piston-slipper assembly.

1.1.5 Piston.

A clear picture of single piston is shown in figure 1.2. Piston is a cylindrical block, hollow form the inside, one end of it is attached to the slipper through the spherical bearing. Another end is located inside the barrel. The presence of grooves cut on the outer piston surface is rear.

1.1.6 Pressure compensation.

In a typical pressure-compensated pump, the swash plate angle is adjusted through the action of a valve which uses pressure feedback so that the instantaneous pump output flow is exactly enough to maintain a designated pressure. If the load flow increases, pressure will momentarily decrease but the pressure-compensation valve will sense the decrease and then increase the swash plate angle to increase pump output flow so that the desired pressure is restored. When the operating pressure reaches, say 200 bar (20 MPa), the swash plate will tend to be driven towards zero angle (piston stroke nearly zero) so that the pump will produce enough flow to maintain the required pressure in the line while overcoming the leakages inherent of the pump. As demand increases the swash plate will be moved to a greater angle, piston stroke increases and the volume of fluid increases, if the demand slackens the pressure will tend to rise and the pumped volume will diminish as the pressure rises. At maximum system pressure the output flow is almost zero again. If the fluid demand increases, beyond the capacity of the pump's

delivery, the system pressure will drop near to zero. The swash plate angle will remain at the maximum allowed and the pistons will operate at full stroke. This continues until system flow-demand eases and the pump's capacity is greater than the demand.

1.2 Working Mechanism.

As the cylinder block (barrel) rotates, the exposed ends (slipper) of the pistons are constrained to follow the surface of the swash plate plane. Since the swash plate plane is at an angle to the axis of rotation, the pistons must reciprocate axially as they precess about the cylinder block axis. The axial motion of the pistons is sinusoidal. During the rising portion of the piston's reciprocation cycle, the piston moves toward the valve plate. Also, during this time, the fluid trapped between the buried end of the piston and the valve plate is vented to the pump's discharge port through one of the valve plate's semi-circular ports, (called kidney ports), the discharge port.

When the piston is at the top of the reciprocation cycle (commonly referred to as top-dead-center or just TDC), the connection between the trapped fluid chamber and the pump's discharge port is closed. Shortly thereafter, that same chamber becomes open to the pump's inlet port. As the piston continues to process about the cylinder block axis, it moves away from the valve plate thereby increasing the volume of the trapped chamber. As this occurs, fluid enters the chamber from the pump's inlet to fill the void. This process continues until the piston reaches the bottom of the reciprocation cycle, commonly referred to as bottom-dead-center or BDC. At bottom dead center, the connection between the pumping chamber and inlet port is closed. Shortly thereafter, the chamber becomes open to the discharge port again and the pumping cycle starts over. Further detailed description of different parts and working mechanism of the pump can be found in [1].

1.3 Motivation.

In the field of Fluid Power, piston pumps possess the most sophisticated designs, in fact, pistons pumps are the only ones capable of working at high pressures, besides possessing the best performance (efficiency) of the entire group of existing pumps. At present, there are two main companies that manufacture the pistons and pumps operating worldwide. These Companies are in Europe, Bosch - Rexroth and U.S. Oilgear Towler, and although it is true that they manufacture the whole range of existing pumps, according to the Bosch – Rexroth Company, the pumps that provide higher benefits are the Piston ones. However, it is noted that all the designs of piston pumps, are mostly based on the experience of the designers, thus there exist no mathematical tools for optimizing the design of the different parts of the pumps.

On the other hand, there are now companies like Oilgear Towler, who inserted slots (grooves) in the slippers and in the pistons, (two major parts of these pumps) but there is no scientific study to analyze its advantages or disadvantages. Indeed, early studies of the behavior of slippers with grooves were carried out experimentally by Böeinghof in

Germany, and by Hooke and Kakoulis in the UK. The groove they used had channels that connect the groove with the edges of the slipper, therefore such grooves were not able to create hydrostatic lift, just hydrodynamic lift and as a result, a bigger slipper was needed to counterbalance the piston force.
At present, some of the grooves carved on slippers and Pistons are not vented, (there are no channels connecting the groove with the slipper edges), but there are no studies explaining the advantages and drawbacks of the use of such grooves. There is therefore a need to understand mathematically the design of the different slipper configurations used in piston pumps, which would allow minimizing the leakage and maximizing the lift. There is a specific need to study the advantages and disadvantages due to the presence of the groove on the surface of different pump parts.

1.4 Project outlook.

It can be noticed from figure 1.1 that there are four sliding surfaces in the piston pump, where lubrication exist and leakage through these channels occur.

1. Slipper-swash plate gap.
2. Barrel-valve plate gap.
3. Piston-barrel chamber gap.
4. Spherical bearing.

In this project, our aim is to analyze each of these different sliding surfaces separately to understand its design constrains and the effect of the design parameters on the pump behavior. After having a better understanding of all the different parts of the piston pump, all Studies conducted in the previous stage are going to be linked using the continuity equation applied to the piston chamber, also fluid compressibility will be taken into account. The aim is to model the dynamic behavior of pressure and flow at the outlet of the pump. In order to achieve this work, the PhD has been divided in two main phases:

First phase **-** The work done during the first phase of the project is again divided into further sections to manifest the structure of the project more clearly. The first element considered during the first phase of the study is the slipper-swash plate gap, as it is known from previous studies, a considerable portion of the pump leakage occur through this element. The slipper behavior analysis will be divided into two parts, flat slipper [**Chapter 2**] and tilt slipper [**Chapter 3**], due to the major modification needed when creating the oil film computational domain. As a result of this modification, the computational technique required to simulate flow field for tilt slipper is much more complex than the one needed for flat slipper and therefore requires further attention. In both of these parts the different parameters (depth, width, position etc) of the groove design are analyzed briefly and the effect of these parameters on pressure, flow, force and torque are studied. As a result, the optimum dimensions of the grooves carved into the slipper is found to insure the best slipper performance. Due to the fact that in working condition slippers are not static, but they rotate around the barrel swash plate, the effect

of slipper dynamics is also studied and the vorticity inside the groove is further analyzed to understand the transfer of momentum inside the groove.

In the second section [**Chapter 4**], the flow losses in the barrel/valve plate gap are considered by performing a pressure/flow simulation in this gap and using the Reynolds equation of lubrication in cylindrical coordinates. From the calculated pressure, the force and torque are also studied and finally by using the temporal torque calculated by Bergada et al [2] barrel dynamics is also simulated by taking in to account spring forces, friction forces and damping coefficient.

In the next section [**Chapter 5**], we focus on studding the piston chamber gap. Since a huge amount of work has been done by Ivantysynova et al [3,4] regarding pressure distribution and leakage in the piston/barrel gap, a bit less effort is intended to be made to analyze piston chamber gap during this project. Nevertheless as it is seen that none of the previous researches considered the effect of grooves cut on pistons, this part of the project will focus in understanding its effect.

In **Chapter 6**, Reynolds equation of lubrication in spherical coordinates is applied to the spherical piston/slipper junction, since although expected to be small, the leakage and also the pressure distribution in the spherical junction is evaluated.

In each section, a computational model has been formulated in order to understand the performance of the different parts of the piston pump. Most of these models have been tested against experimental results in order to validate their accuracy. **Chapter 7** presents all the different experimental setups, which are used to obtain the experimental results during this project.

Second phase **-** In the second phase [**Chapter 8**] of the project, all these four components, studied in first phase has been combined together to analyze the total leakage and outflow ripple of the pump. An analytical model has been used to evaluate the leakage through each component based on certain assumptions which have been made on the experience of the studies done in Chapters 2-6. Thanks to the present study it is now possible to analyze the pump behavior when each of its components becomes old, (its surfaces wear out) and therefore the gaps becomes larger.

As a conclusion, it must be said that, in this project, a set of programs have been developed which allow a detailed analysis of an axial piston pump and the design of its component. One of the aims of the thesis is to evaluate, how the modifications of the design particularly affects the behavior of the pump as a whole. I believe, the work presented in this PhD thesis will result as a global leader on the issue of piston pumps, and it is expected to serve as a tool for the future design of pistons pumps as well as to improve the design of the current pumps. It is also necessary to emphasize that the work done in piston pumps can be easily extended to Pistons motors, since it is essentially the same machine.

References

1. Peter Rohner. Industrial Hydraulic control, 3rd editions, John wiley & sons 1988.

2. Bergada JM, Watton J, Kumar S. Pressure, flow, force and torque between the barrel and port plate in an axial piston pump. ASME Journal of dynamic systems, measurement and control, Jan 2008. Vol. 130. N 1. pp 011011-1/16

3. Wieczoreck U and Ivantysynova M. (2000) "CASPAR-A computer aided design tool for axial piston machines". Proceedings of the Power Transmission Motion and Control International Workshop, PTMC2000, Bath, UK. pp 113-126.

4. Wieczoreck U and Ivantysynova M. (2002) "Computer aided optimization of bearing and sealing gaps in hydrostatic machines-the simulation tool CASPAR". International Journal of fluid Power 3 (2002) Nº 1 pp 7-20.

2

Flat Slipper

This chapter presents static and dynamic characteristics of a piston pump slipper with a groove. Three dimensional Navier Stokes equations in cylindrical coordinates have been applied to the slipper/plate gap, including the groove. The results presented in this chapter include, pressure distribution, leakage, force and torque variations when groove dimensions and position are being modified, the effect of slipper tangential velocity and turning speed are also considered. Fluid momentum interchange inside the groove is studied, since vorticity inside the groove is analyzed under several working conditions. The CFD results are compared with the experimental ones, finding a good agreement for all of the cases studied. Flow is considered laminar and incompressible under all conditions and the slipper is considered parallel to the plate. Design instructions to optimize slipper/groove performance are also given.

2.1 Introduction.

The importance of understanding slippers behaviour is made relevant when is considered that most of the leakage in piston pumps and motors happens to be through slippers. Good performance of the machine is directly linked with smooth slipper/swash plate running, being necessary to avoid metal to metal contact and excessive film thickness. Therefore, volumetric, hydraulic and mechanic efficiencies in piston pumps and motors will be affected by slipper performance.

In the majority of the researches presented until now, the effect of the different pressure balancing grooves cut on pistons and slippers has been neglected, and although the groove effect on the flow and the pressure distribution is not expected to give a completely different pattern from previous knowledge using single-land slippers, the introduction of a groove brings a far more complicated mathematical approach when aiming to fully understand its behavior.

The main piston and slipper assembly used in this study is shown in figure 2.1, and is one of nine pistons from a pump which maximum volumetric displacement is 0,031 dm^3 /rev. It will be seen that the slipper design uses two full lands, an alternative being to machine additional slots across the second land to balance the groove and outlet pressure. The approach selected seems to be the corporate design philosophy of the particular pump manufacturer.

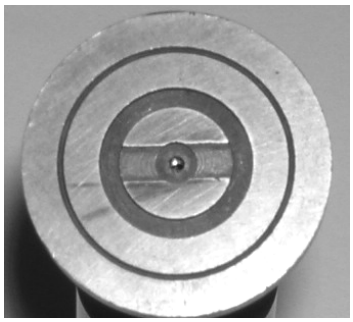

Figure 2.1 - Slipper studied in the present work.

There have been many publications in this general subject area over the past 30 years, many concerned with improving the slipper performance of piston pumps and motors. Fisher [1] studied the case of a slipper with single land on a rotating plate, in both cases, when the slipper was parallel and tilted with respect to the swash plate and the load capacity, restoring moment, and flow characteristics were studied. Fisher demonstrated that if a flat slipper tilts slightly so that the minimum clearance occurs at the rear; the hydrodynamic loads generated tend to return the slipper to the non tilted position. Fisher concluded that when the ratio of the angle of tilt to the angle at which the slipper would just touch the plate is higher than 0.675 then slipper equilibrium would be impossible since the load plus the dynamic force cannot be balanced by the hydrostatic force.

Böinghoff, [2] performed a deep study on slippers. He studied theoretically the static and dynamic forces and torques acting on a single piston, via analyzing carefully the slipper performance as it rotates around the swash plate, he also took into account the torque generated on the spherical bearing. Large quantities of experimental results where also generated, in which torque and leakage were evaluated for different position angles and turning speed. The effect of oil viscosity on the torques created was also taken into account. Pump leakage was studied for different swash plate angles and turning speeds. Leakage was found to be smaller at low speeds < 5 rad/s and low swash plate angles and increased with turning sped. He also studied experimentally the influence of slippers with different lands, focusing on torque and leakage at different turning speeds. It must be pointed out that although the slipper studied had four lands, just one of them can be considered as full land, the rest were vented. He found that torque remained pretty much constant with turning speed when 1 or 2 lands were used, and torque was quickly increasing with speed when using four lands. Leakage was found to be lower when decreasing the number of lands and for speeds higher than 10 rad/s.

Hooke [3] showed that a degree of non-flatness was essential to ensure the successful operation of the slipper and the non-flatness must have a convex profile. He concluded that the lift contribution due to spin had an effect of second order. The centripetal forces resulting from the speed of the pump had a tendency to tilt the slipper outwards thus reducing the clearance on the inside of the slipper path. He also pointed out that the friction on the piston ball played a major role in determining the behaviour of the slipper. In a further paper [4] Hooke studied more carefully the couples created by the slipper ball, finding that the major source of variation between slippers did not arise from differences on surface profile, but from differences in the friction in the ball-cup and piston-cylinder pairs. He concluded that ball-cup friction increased with pressure, and contact metal to metal may appear when lubrication was deficient.

Iboshi and Yamaguchi [5-7], working with single land slippers, found a set of equations based on the Reynolds equation of lubrication which gave the flow and the main moments acting on the slipper by taking into account the slipper displacement velocity and tilt. They found that there was a limit of fluid film lubrication for the specific supply pressure and rotational speed. They also defined a diagram checking the conditions under which metal to metal contact on the slipper may appear. It was pointed out that the friction of the spherical bearing affects significantly the tilt angles, and the rotational speed affects the central clearance of the slipper plate. Experimentally they found that the slipper plate clearance, under steady rotational conditions, was fluctuating.

Hooke [8] also studied more carefully the effect of non-flatness and the inlet orifice on the performance of the slipper. He gave a very good explanation of the equations used and the mathematical process to find them, finding the moments along the two main axes of the slipper. He found out that 2-5% of the load was being supported by hydrodynamic forces and tilt was necessary to produce the desired hydrodynamic lift. It was also found that the increase of the film thickness with reduction of slipper non-flatness was very small. In all geometrical conditions studied, it was found that slippers with no inlet orifices had larger clearances than slippers with orifices. However starvation effects and cavitations may appear. In [9] Hooke focused on the lubrication of over clamped slippers, the clamping ratio being defined as the relation between the hydrostatic lift acting on the slipper and the piston load. Typical over clamped ratios ranged between 1-10%. He noticed that to have successful slipper lubrication, the plate where the slipper slides must be well supplied with fluid. The tilt was found to be proportional to the non-flatness magnitude divided by the square root of the slipper central clearance. In this paper the Reynolds equation of lubrication for tilted slippers had been integrated numerically by finite difference method. In [10] Hooke analysed carefully the three different tilting couples acting on slipper, finding that the tilting couple due to friction at the slipper running face is much smaller than the ones created at the piston-cylinder, piston-slipper interfaces and the centrifugal one. All slippers tested had a single land. The slippers were found to operate relatively flat, clearances were highly dependent on the offset loads and the minimum clearance was found to be not particularly sensitive to the type of non-flatness magnitude.

Takahashi [11] studied the unsteady laminar incompressible flow between two parallel disks with the fluid source at the centre of the disks. Both the flow rate and the gap between disks were varied arbitrarily with time and independently of each other. The two dimensional Navier-Stokes equations were solved via spectral method. The theory presented gave light to the study of the complicated characteristics of the inertial forces.
Li et al [12] studied the lubrication of composite slippers on water based fluids. It was found out that the slipper plate clearance was smaller than when using hydraulic oil and it was essential that the surfaces of the slipper and plate should be highly polished in order to accomplish a successful slipper operation. Even for the best material combinations, problems were encountered when the system was run at high fluid pressures and low running speeds. When turning at speeds lower than 300 rpm, slipper plate metal to metal contact was found. The slipper plate clearance increased when increasing the slipper surface.

Koc et al [13] focused their work on checking whether under clamped flat slippers could operate successfully or whether a convex surface was required. A good understanding of the three couples acting on the slipper, previously defined by Hooke [4, 10], was essential. They took into account the work done by Kobayashi et al [14] on the measurements of the ball friction. They concluded that polishing of the running face of the slipper to a slightly convex form appeared to be essential for successful operation under all conditions. It was also found that the insertion of an inlet orifice at the centre of the slippers result in an increase of the central clearance, though tending to destabilize the slippers. Notice that the insertion of an inlet orifice seams to give opposite effects in references [8] and [13]. It must be bared in mind that in reference [8] the slipper used was having conical lands, while in reference [13] the sliding surface is slightly convex. The size of the central orifice in under clamped slippers appeared to be most critical for a successful operation. Harris RM [15], created a mathematical dynamic model for slipper-pads, in which lift and tilt could be predicted, the model was able to handle the effect of the possible contact with the swash plate. The simulation shows that slipper tilt is much higher at suction that at delivery and at delivery tilts increases with pump speed.

In [16,17] Koc and Hooke studied more carefully the effects of orifice size, finding that the under clamped slippers and slippers with larger orifice sizes run with relatively larger central clearances and tilt more than those of over clamped slippers with no orifice. Slippers with no orifice had greatest resistance to tilting couples and the largest minimum film thickness. One of the major effects of the orifices was to greatly reduce the slipper resistance to tilting couples. They pointed out that the use of two lands, an inner and outer land, brought more stability to the slipper. They also indicated that when a slipper incorporates a second land, the space between lands needs to be vented to avoid the generation of excessive hydrostatic lift, allowing the flow trapped between lands to escape. The direction and magnitude of the tilt was found to be directly dependent on the offsets imposed.

Tsua [18], analyzed in detail the slipper dynamics in a piston pump. As other authors before [1, 5], Tsua used the Reynolds equation of lubrication considering slipper spin and tangential velocity over the pump axis and integrated this equations by using Newmark-

β method. Pressure distribution found from the numerical scheme was later used to find out the force and torques over the slipper.

Wieczoreck, U. Ivantysynova [19-20] developed a package called CASPAR which uses the two dimensional equation of lubrication and the energy equation in differential form. Transient cylinder pressure has been computed by considering leakage in piston, slipper, and port plate. In addition, the clearance and tilt of the slipper was shown to vary over one revolution of the pump and a single land slipper plate was used in the theoretical and experimental analysis.

Manring [21, 22] analyzed the slipper by using classic lubrication equation based on pressure and volumetric flow rates, but the slipper he took into account had no groove. He found out that the minimum fluid film thickness between the bearing and the thrust surface is of the order of the surface roughness. Therefore, metal to metal contact might be possible. Kazama [23-25] formulated a time dependent mathematical model for slipper-swash plate model for the use of tap water under mixed and fluid film lubrication condition by considering the surface roughness and the revolution radius. He found that the radius of revolution of the pad influences the bearing performance because of the hydrodynamics wedge effect and the minimum power loss happened when the balance ratio become close to unity.

The performance of slippers with grooves was reported by [2, 8, 17, 26], where it was found that a groove brought stability to the slipper dynamics. In all these cases, the second land was vented and therefore the pressure on the groove was reported to be atmospheric. As a result the groove itself was not creating lift. It was also reported that for a given central clearance, reducing the number of lands give a reduction in leakage. It has to be noticed that in the present case the groove is not vented and therefore as it will later be demonstrated the second land and the groove will create hydrostatic and hydrodynamic lift. Analytical solution for slippers with multiple lands was outlined in [27, 28] and more clearly defined in [29], although the effect of tangential velocity was not considered. Reynolds equation of lubrication is applied to the slipper swash plate gap by considering the flow only in radial direction, which turn out to be accurate for flat slipper but while considering tilt slipper, flow tend to move into angular direction too, as a result this analysis does not produce very good result for higher tilts.

The equations developed in the full mathematical analysis of the slipper with groove are complex enough not to be solved analytically without further approximation. Another possible way to tackle such complex equations while retaining its accuracy is implementing a computational technique. There has been some previous efforts made in [11, 17 - 20, 23, 25, 30 - 33] to analyze the slipper through various computational techniques. Some of these works used spectral method [11, 18, 23] other have used finite difference method [17] through Reynolds equations.

Brajdic [30] analyzed the low friction pad bearing in two dimensions Cartesian coordinates system taking into account the compressibility of fluid. He showed the development of the fluid recirculation behaviour within the pocket. Helene [31] also

investigated a hybrid journal bearing in to two dimensional Cartesian coordinate system. She also took into account the turbulent flow conditional (Re up to 5000) by implementing k-ε model with logarithmic wall functions and pointed out that turbulent pressure pattern is less affected by recirculation zones. Braun [32] analyzed the effect of pocket depth by applying two dimensional Navier stokes equation to the slipper pocket gap and pointed out that the deep pockets show a lesser degree of coupling between the pocket flow and the clearance flow than the shallow pockets. Niels [33] formulated a numerical model based on Reynolds equation to minimize the friction in tilting pad and showed that a large amount of energy can be saved by using low length to width ration of the cavity.

If we focus on the problem a bit more conceptually rather than technically, the problem we are tackling here is similar in behaviour of three dimensional open cavities in cylindrical coordinates. The literature available for pressure/flow simulation in cavities is quite vast and the SIMPLE (semi implicit method for pressure linked equation) family algorithm [34] has been widely applied to this kind of simulation. Most of the work has been done for rectangular cavities [35-41] where Cartesian coordinates were applied. Literature available on cavities in cylindrical coordinates [42-44] is much less common. The cavities analyzed in [42-44] are 2-dimensional and the analysis done in [42, 44] is focusing in analyzing the heat transfer. Although the analysis performed in [43] considers the effect on flow performance when changing the sealing gaps, still the flow is axis-symmetric and therefore the cavity is considered as two dimensional. In the present study, the flow does not have any kind of symmetry, as a result a complete three dimensional analysis needs to be considered.

Despite the fact that exist some literature available in Cartesian coordinates, where dimensions and shape of cavities as well as clearances between plates were analyzed [38-41], no evidence has been found of a flow involving the complexities considered in the present study. For example, a 2d simulation in curvilinear coordinates using the stream function method was done in [38] where the Vorticity in triangular, circular and rectangular cavities were studied; the conclusion of the study was that for a given Reynolds number, triangular shape cavity created the smallest leakage, and for Reynolds numbers smaller than 100, the vortex created in all different cavities was positioned at the width centre of the cavity. The effect of upstream boundary layer thickness and the effect of the cavity dimensions on three dimensional rectangular cavities were studied in [39], it was found that the flow became increasingly unstable as the upstream boundary layer thickness decreased. Rectangular three dimension flow inside a cavity was also studied in [40], the paper focused on studding the Vorticity created inside the groove, they concluded that the corner Vorticity tended to increase flow transport. This paper also presented a graph of particle tracer explaining the vortex decay along the groove. In [41] the vortex created inside a rectangular cavity was studied when the lid was submitted to a sinusoidal displacement at different frequencies. It is also interesting to point out that all the previous studies presented regarded the flow as incompressible.

But despite the amount of work developed on slippers, no evidence has been found of any research focused on finding the leakage, pressure distribution, force and torque created by

a slipper with a non vented groove and considering spin and tangential velocity. Then such requirements can only be analyzed if three dimensional Navier Stokes equations in cylindrical coordinates are applied in the gap slipper swash/plate.

2.2 Governing Equations and Boundary Conditions.

Figure 2.2 shows a schematic drawing of the slipper and swash plate clearance, the two slipper-relative movements are also outlined. The shaded area presents the computational domain $\Omega\{\Omega : \square^3(r,\theta,z)\}$ with shown boundary $\Gamma\{\Gamma_{in},\Gamma_{out}\}$. Notice that the combination of tangential velocity and spin acting over the slipper, will create a flow field below the slipper which can not be considered symmetric in angular direction, even though the clearance between slipper-plate is constant at all points. Therefore it becomes necessary to consider a 3-dimentional cylindrical computational domain.

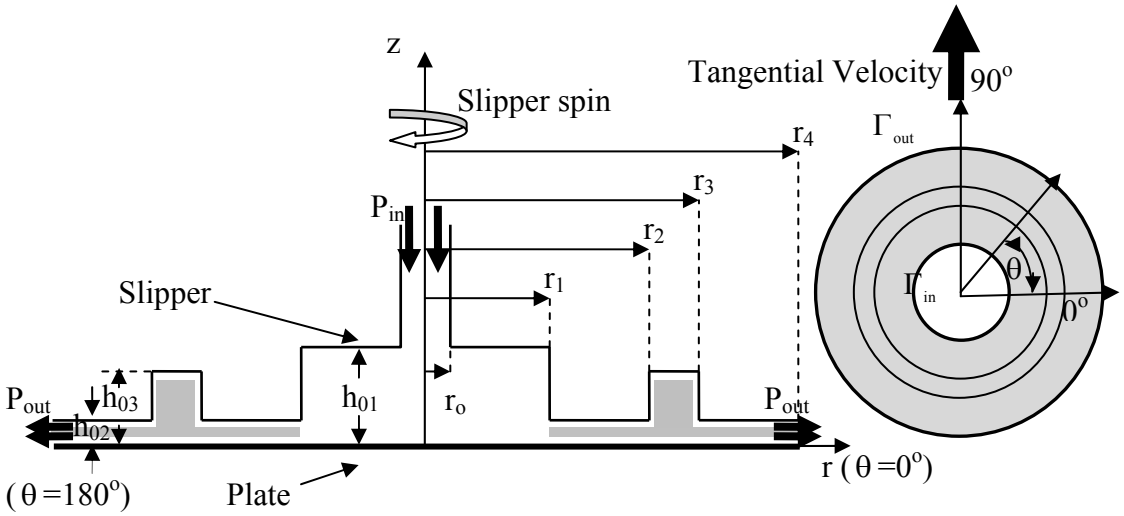

Figure 2.2 - A systematic diagram of computation domain.

The continuity equation and conservative form of Navier Stokes in cylindrical coordinates is given in Equations (2.1) and (2.2) respectively. Where $\phi\{V_r, V_\theta, V_z\}$ is considered as flux vector and the value of S_ϕ is given in Table- 2.1 for different ϕ.

$$\frac{1}{r}\frac{\partial(r.V_r)}{\partial r}+\frac{1}{r}\frac{\partial V_\theta}{\partial\theta}+\frac{\partial V_z}{\partial z}=0 \tag{2.1}$$

$$\rho\frac{\partial\phi}{\partial t}+\rho\left[\frac{1}{r}\frac{\partial}{\partial r}(r.V_r.\phi)+\frac{1}{r}\frac{\partial}{\partial\theta}(V_\theta.\phi)+\frac{\partial}{\partial z}(V_z.\phi)\right]=\mu\left[\frac{\partial}{\partial r}\left(\frac{1}{r}\frac{\partial(r.\phi)}{\partial r}\right)+\frac{1}{r^2}\frac{\partial^2\phi}{\partial\theta^2}+\frac{\partial^2\phi}{\partial z^2}\right]+S_\phi \tag{2.2}$$

Table 2.1 – The values of S_ϕ for different ϕ

ϕ	S_ϕ
V_r	$-\frac{\partial P}{\partial r}-\frac{2\mu}{r^2}\frac{\partial V_\theta}{\partial \theta}-\frac{\mu V_r}{r^2}+\frac{V_\theta^2.\rho}{r}$
V_θ	$-\frac{1}{r}\frac{\partial P}{\partial \theta}+\frac{2\mu}{r^2}\frac{\partial V_r}{\partial \theta}-\frac{\mu V_\theta}{r^2}-\frac{\rho V_r V_\theta}{r}$
V_z	$-\frac{\partial P}{\partial z}$

A no slipping boundary condition is imposed in all walls. The pressure at inlet and outlet boundaries is specified and the flow variables at inlet and outlet boundaries are specified by zero normal derivatives at each sub iteration step, as presented by equation 2.3.

$$P\big|_{\Gamma_{in}} = P_{in};\ P\big|_{\Gamma_{out}} = P_{out};\ \left.\frac{\partial\left(r.V_r\right)}{\partial r}\right|_{\Gamma_{in}\text{or }\Gamma_{out}} = 0;\ \left.\frac{\partial V_\theta}{\partial r}\right|_{\Gamma_{in}\text{or }\Gamma_{out}} = 0;\ V_z\big|_{\Gamma_{in}} = 0;\ \left.\frac{\partial V_z}{\partial r}\right|_{\Gamma_{out}} = 0; \qquad (2.3)$$

2.3 Solution Technique:

Equations (2.1) and (2.2) are discretized by control volume formulation over a staggered grid as defined in [45]. Four different control volumes for r-momentum, θ-momentum, z momentum and continuity are presented in Figure 2.3 with dependent neighbor variables. As can be seen velocities and pressure are staggered and therefore are the corresponding control volumes. In figure 2.3, all the neighbor velocities and effective pressures for each corresponding control volume are shown in terms of grid coordinates.

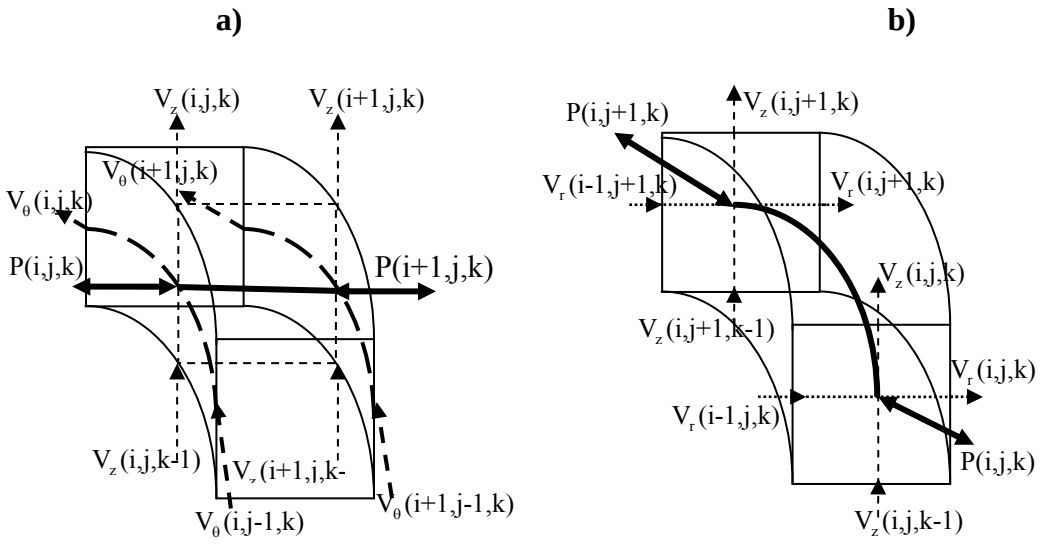

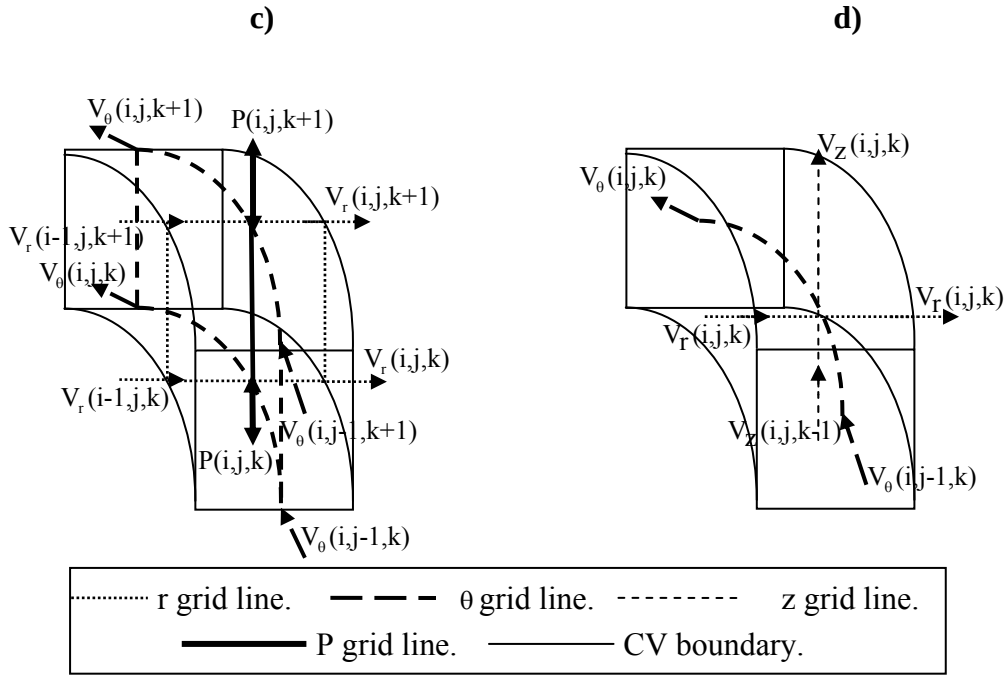

Figure 2.3 – four different control volumes with their neighbor dependent variables. (a) r-momentum control volume. (b) θ-momentum control volume. (c) z-momentum control volume. (d) Continuity control volume.

The grid size is uniform in r and θ direction but increases in the z direction when moving down towards groove bottom. Since in "z" direction the grid is not uniform, and the flow is considered incompressible, it was decided to put velocity grid lines in the centre of pressure grid lines, therefore velocity will represent the best approximation over the entire control volume when applied to momentum equation.

2.4 Source Term Linearization.

The Source terms of all momentum equations are linearized with a negative gradient to maintain the positivity of the coefficient according to equation (2.6).

$$S_\phi = S_{\phi.C} + S_{\phi.P}\,\phi \tag{2.6}$$

Table 2.2 – The Values of $S_{\phi.C}$ and $S_{\phi.P}$ for different ϕ

ϕ	$S_{\phi.C}$	$S_{\phi.P}$
V_r	$-\frac{\partial P}{\partial r} - \frac{2\mu}{r^2}\frac{\partial V_\theta}{\partial \theta} + \frac{V_\theta^2 \cdot \rho}{r}$	$-\frac{\mu}{r^2}$
V_θ	$-\frac{1}{r}\frac{\partial P}{\partial \theta} + \frac{2\mu}{r^2}\frac{\partial V_r}{\partial \theta} - \frac{\rho V_\theta}{r}\max[-V_r, 0]$	$-\frac{\mu}{r^2} - \frac{\rho}{r}\max[V_r, 0]$
V_z	$-\frac{\partial P}{\partial z}$	0

Among the negative-slope lines, the tangent to the curve represented by S_ϕ is usually the best choice. Steeper lines are acceptable but would normally lead to slower convergence. Less steep lines are undesirable, as they fail to incorporate the given rate of fall of S_ϕ with ϕ. By keeping all these points in mind, the value of $S_{\phi.C}$ and $S_{\phi.P}$ chosen are given in table 2.2. During each iteration cycle these values are recalculated from the new available data.

2.5 Discretization of generalized momentum equation.

To understand the physical flow phenomena and implement the computational technique more precisely, NVS equation can be treated as combination of different terms, Transient term, Convection term (T_1), Diffusion term (T_2) and Source term (S). As a result of this treatment, now different computation techniques can be implemented for each different term to attain more accuracy according to the understanding of the flow condition. In the present work, Transient term is treated by implicit scheme for faster convergence; an upwind scheme is implemented for the convection term to maintain the positivity of the coefficients; power law scheme is used as a shape function to integrate the diffusion term and source term is treated by implicit scheme. Equations (2.4) and (2.5) represent the convection and diffusion term.

$$T_1 = \rho\left[\frac{1}{r}\frac{\partial}{\partial r}\left(r.V_r.\phi\right)+\frac{1}{r}\frac{\partial}{\partial \theta}\left(V_\theta.\phi\right)+\frac{\partial}{\partial z}\left(V_z.\phi\right)\right] \tag{2.4}$$

$$T_2 = \mu\left[\frac{\partial}{\partial r}\left(\frac{1}{r}\frac{\partial(r.\phi)}{\partial r}\right)+\frac{1}{r^2}\frac{\partial^2\phi}{\partial\theta^2}+\frac{\partial^2\phi}{\partial z^2}\right] \tag{2.5}$$

The different terms of equation (2.2) are discretized by control volume formulation as described above over a staggered grid. Final discrete equation can be written in the form of equation (2.7) and its coefficients are given by equations (2.8) to (2.16),

$$a_p\Phi^*_p = \sum_{nb} a_{nb}\Phi^*_{nb} + b_\Phi \tag{2.7}$$

Where,

$$a_E = D_e + \left\| - F_e, 0\right\| \quad \text{where } D_e = \frac{\mu R_e \Delta\theta \Delta z}{\Delta r} \quad \& \quad F_e = \rho R_e V_e^r \Delta\theta \Delta z \tag{2.8}$$

$$a_W = D_w + \left\| F_w, 0\right\| \quad \text{where } D_w = \frac{\mu R_w \Delta\theta \Delta z}{\Delta r} \quad \& \quad F_w = \rho R_w V_w^r \Delta\theta \Delta z \tag{2.9}$$

$$a_N = D_n + \| - F_n, 0 \| \quad \text{where } D_n = \frac{\mu \, \Delta r \, \Delta z}{R_p \Delta \xi} \quad \& \quad F_n = \rho \, V_n^{\theta} \, \Delta r \, \Delta z \tag{2.10}$$

$$a_S = D_s + \| F_s, 0 \| \quad \text{where } D_s = \frac{\mu \, \Delta r \, \Delta z}{R_p \Delta \xi} \quad \& \quad F_s = \rho \, V_s^{\theta} \, \Delta r \, \Delta z \tag{2.11}$$

$$a_T = D_t + \| - F_t, 0 \| \quad \text{where } D_t = \frac{\mu \, R_p \, \Delta \theta \, \Delta r}{\Delta z} \quad \& \quad F_t = \rho \, R_p \, V_t^{z} \, \Delta \theta \, \Delta r \tag{2.12}$$

$$a_B = D_b + \| F_b, 0 \| \quad \text{where } D_b = \frac{\mu \, R_p \, \Delta \theta \, \Delta r}{\Delta z} \quad \& \quad F_b = \rho \, R_p \, V_b^{z} \, \Delta \theta \, \Delta r \tag{2.13}$$

$$a_P^o = \frac{\rho \, R_p \, \Delta \theta \, \Delta r \, \Delta z}{\Delta t} \tag{2.14}$$

$$b_{\Phi} = a_P^o \, \Phi_{p.old}^{*} + S_{\Phi.C} \, R_p \, \Delta \theta \, \Delta r \, \Delta z \tag{2.15}$$

$$a_P = a_E + a_W + a_N + a_S + a_T + a_B + a_P^o - S_{\Phi.P} \, R_p \, \Delta \theta \, \Delta r \, \Delta z \tag{2.16}$$

2.6 Different momentum equations.

Different momentum equations can be obtained from general momentum equation (2.7) for different values of ϕ as represented by equations (2.17, 18 and 19). These equations are written by implementing an under relaxation factor α_v as suggested by Patanker [34]. Pressure term is separated from $S_{\Phi.C}$, as it plays an important role in developing pressure correction formula. A value of 0.8 is suggested by Patanker [34] for these under relaxation factor. A value of 0.5 is used in the present work and no effort has been made to optimize this value.

$$\frac{a^{r}_{i,j,k}}{\alpha_v} V^{r*}_{i,j,k} = \sum_{nb} a^{r}_{nb} V^{r*}_{nb} + b_r + r \, \Delta\theta \, \Delta z \left(P^{*}_{i,j,k} - P^{*}_{i+1,j,k} \right) + \frac{(1-\alpha_v)}{\alpha_v} a^{r}_{i,j,k} V^{r*(n-1)}_{i,j,k} \tag{2.17}$$

$$\frac{a^{\theta}_{i,j,k}}{\alpha_v} V^{\theta*}_{i,j,k} = \sum_{nb} a^{\theta}_{nb} V^{\theta*}_{nb} + b_{\theta} + \Delta r \, \Delta z \left(P^{*}_{i,j+1,k} - P^{*}_{i,j-1,k} \right) + \frac{(1-\alpha_v)}{\alpha_v} a^{\theta}_{i,j,k} V^{\theta*(n-1)}_{i,j,k} \tag{2.18}$$

$$\frac{a^{z}_{i,j,k}}{\alpha_v} V^{z*}_{i,j,k} = \sum_{nb} a^{z}_{nb} V^{z*}_{nb} + b_z + r \, \Delta\theta \, \Delta r \left(P^{*}_{i,j,k-1} - P^{*}_{i,j,k+1} \right) + \frac{(1-\alpha_v)}{\alpha_v} a^{z}_{i,j,k} V^{z*(n-1)}_{i,j,k} \tag{2.19}$$

2.7 Pressure and velocity corrections

The momentum equation can be solved only when the pressure field is given or is somehow estimated. Unless the correct pressure is employed, the resulting velocity will not satisfy the continuity equation. So an improvement in guess pressure (P^*) is required which is denoted by P^c and is implemented in equation (2.20).

$$P = P^* + P^c \tag{2.20}$$

To estimate the change in behavior of velocity due to this pressure correction, corresponding velocity correction can be introduced in the similar manner, as represented in equation (2.21).

$$V^{\phi} = V^{\phi.*} + V^{\phi.c} \tag{2.21}$$

By implementing these corrections into momentum equations (2.17-19), equations for corrected velocities are developed. While developing these equations the term $\sum_{nb} a_{nb} V^c_{nb}$ is drooped from momentum equations to avoid coupling of all grid points while implementing these velocities into continuity equation. Equations (2.22-24) represent the velocity correction formulas.

$$V^r_{i,j,k} = V^{r*}_{i,j,k} + \frac{r\,\Delta\theta\,\Delta z}{a^r_{i,j,k}}\left(P^c_{i,j,k} - P^c_{i+1,j,k}\right) \tag{2.22}$$

$$V^{\theta}_{i,j,k} = V^{\theta*}_{i,j,k} + \frac{\Delta r\,\Delta z}{a^{\theta}_{i,j,k}}\left(P^c_{i,j+1,k} - P^c_{i,j-1,k}\right) \tag{2.23}$$

$$V^z_{i,j,k} = V^{z*}_{i,j,k} + \frac{r\,\Delta\theta\,\Delta r}{a^z_{i,j,k}}\left(P^c_{i,j,k-1} - P^c_{i,j,k+1}\right) \tag{2.24}$$

This corrected velocity field is implemented in continuity and a pressure correction formula is developed as described by Patanker [34], this method is named as SIMPLE (Semi-Implicit Method for Pressure-Linked Equation) based algorithm. Equation (2.25) represents the final pressure correction formula, which coefficients are given in equations (2.26-32).

$$A_p P^c_p = \sum_{nb} A_{nb} P^c_{nb} + B_p \tag{2.25}$$

Where,

$$A_E = \frac{\rho\left(R_p\,\Delta\theta\,\Delta z\right)^2}{\left(a_{r.P}\right)_e} \tag{2.26}$$

$$A_W = \frac{\left(R_p\,\Delta\theta\,\Delta z\right)^2}{\left(a_{r.P}\right)_w} \tag{2.27}$$

$$A_N = \frac{\left(\Delta r\,\Delta z\right)^2}{\left(a_{\theta.P}\right)_n} \tag{2.28}$$

$$A_S = \frac{\left(\Delta r\,\Delta z\right)^2}{\left(a_{\theta.P}\right)_s} \tag{2.29}$$

$$A_T = \frac{\left(R_p\,\Delta\theta\,\Delta r\right)^2}{\left(a_{z.P}\right)_t} \tag{2.30}$$

$$A_B = \frac{\left(R_p\,\Delta\theta\,\Delta r\right)^2}{\left(a_{z.P}\right)_b} \tag{2.31}$$

$$B_p = \left(R_e V_e^r - R_w V_w^r\right)\Delta\theta\,\Delta z + \left(V_n^\theta - V_s^\theta\right)\Delta r\,\Delta z + \left(V_t^z - V_b^z\right)R_P\,\Delta\theta\,\Delta r \tag{2.32}$$

When improving the guessed pressure using the calculated correction from equation (2.25), an under-relaxation factor α_p is implemented, as shown in equation (2.33).

$$P = P^* + \alpha_p P^c \tag{2.33}$$

Although the value of the under-relaxation factor suggested by Patanker [34] is 0.8, often, this value can be as low as a 0.1 as discussed by Anderson [46]. In the present work a very low value of α_p (0.01) is used to achieve convergence at the beginning of the simulation. After a few iterations, the rapidly varying component of error becomes negligible and error becomes a smooth function of spatial coordinates, therefore the value of the under-relaxation factor (α_p) is updated to 0.5 to increase the rate of convergence. Equation (2.34) represents the residue of the momentum equations. Mass residue (B_p), Momentum residue ($R_{p.\phi}$) and correction in pressure (P') are used as a convergence criteria.

$$R_{p.\phi} = a_{\phi.p} V_{\phi.p} - \sum_{nb} a_{\phi.nb} V_{\phi.nb} - b_\phi - (\Delta P)A_n \tag{2.34}$$

2.8 Results

2.8.1 Grid Independency test

As stated previously, in the present simulation a staggered grid is used. A diagram of pressure grid lines in r-z cross section for a given angular position is shown in figure 2.4. The grid size in r and θ direction is uniform but a logarithmic grid is used inside the groove in z direction, the grid is very fine near the groove edge and size increases towards groove bottom.

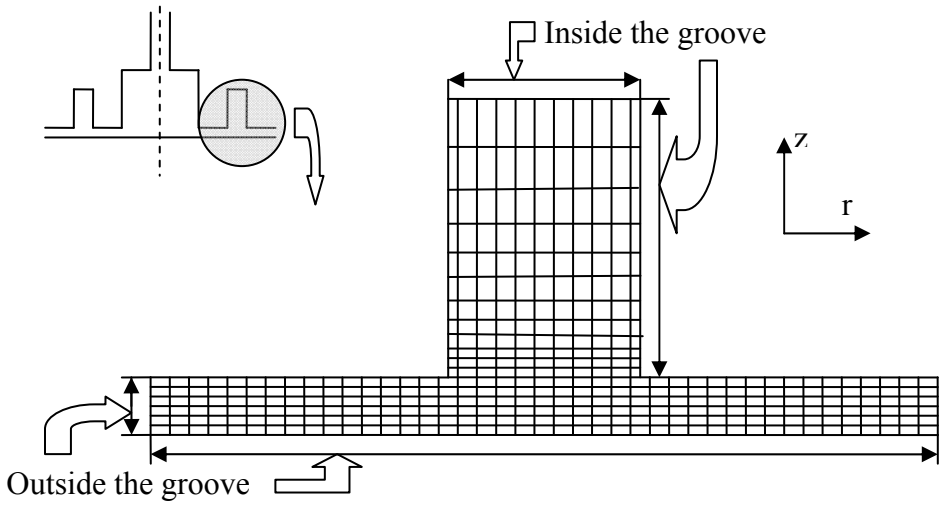

Figure 2.4 – Pressure Grid lines in r-z cross section plane at a angular position.

2D stream line plots are shown in figure 2.5 for different grid sizes inside the groove. Figure 2.5.a and 2.5.b correspond to 30-36-60 and 30-36-80 grid size in r-θ-z direction inside the grove and 312-36-20 outside the groove, the grid is maintained uniform in r-direction because this is the expected direction of the main flow and also the direction of the iteration, then, a non uniform grid in r-direction would deeply affect the convergence rate. Figure 2.5.c presents some results when grid refinement is in r direction, with 45-36-60 grid points inside the groove and 468-36-20 outside the groove to maintain uniform grid in r direction. Figure 2.5.d shows the results with 30-36-60 grid points inside the groove and 312-36-30 grid points outside the groove. From all four figures, it can be concluded that the solution is independent of the grid size chosen; therefore a common grid size of 30-36-60 points inside the groove and 312-36-20 points outside the groove is chosen for the rest of the simulation.

In dynamic conditions, the grid size in angular direction becomes important. Although the vortex inside the groove under dynamic conditions is three dimensional, for better visualization, in grid independency test, the vortex will be plotted in two dimensional r-z plane at a particular angular position, where magnitude of flow is highest. Figure 2.6 represents two stream line plots inside the groove in r-z plane at 90^o angular position of

slipper for 13 MPa, 1000 rpm and 20 microns clearance and at two different grid sizes in angular direction. The grid size for r and z direction is the same chosen in static case, while the grid in angular direction is refined from 36 points to 45 points. It can be concluded from figure 2.6 that, solution is independent from grid size, therefore 36 grid points in angular direction are chosen for the rest of the simulation.

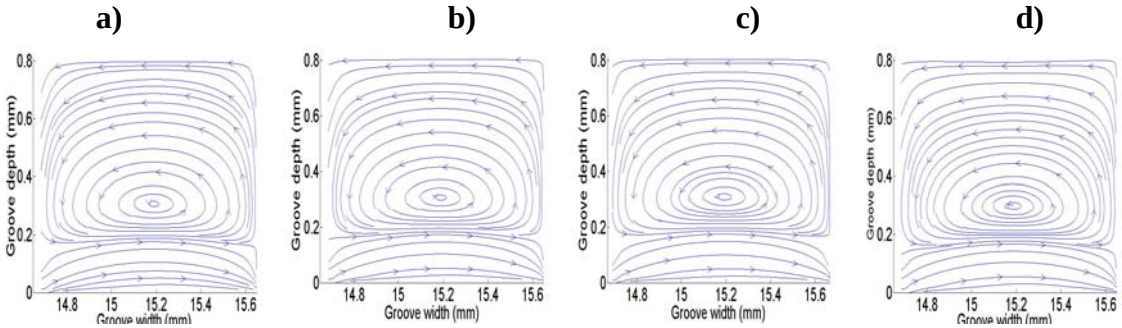

Figure 2.5 – Stream lines inside the groove for different grid size in static conditions at 13 MPa inlet pressure and 20 micron clearance.
(a). Groove in- [30-36-60], out-[312-36-20] (b). Groove in- [30-36-80], out-[312-36-20]
(c). Groove in- [45-36-60], out-[468-36-20] (d). Groove in- [30-36-60], out-[312-36-30]

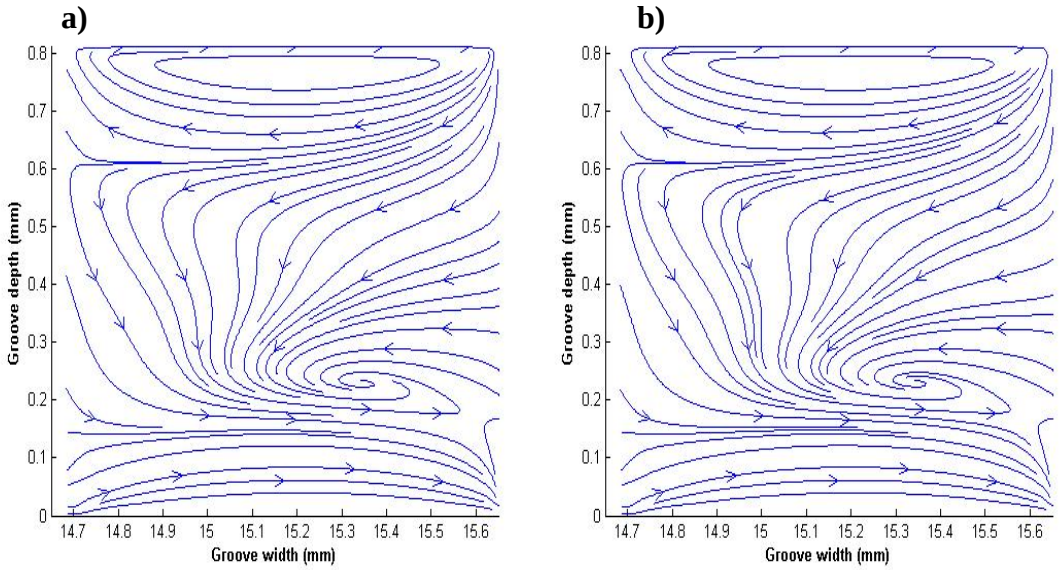

Figure 2.6 – Streamlines inside the groove at 90^{o} angular position (defined in figure 2.2) for different grid size at 13 MPa inlet pressure, 1000 rpm rotation and 20 microns clearance. (a) Groove in- [30-36-60], out-[312-36-20] (b) Groove in- [30-45-80], out-[312-45-20].

2.8.2 Analysis in static conditions.

To analyze the slipper performance in static conditions, several numerical simulations have been performed at different pressures (from 3 MPa to 15 MPa) for different

clearances (from 6.5 microns to 20 microns). Simulated pressure distributions and leakages have been compared with experiments which have been done by using test rig 1 presented in chapter 5. Several simulations have been performed, to analyze the effect of groove on slipper by modifying the groove dimension (width 1mm & 2 mm and depth up to 1 mm) and its position.

2.8.2.1 Pressure, force and torque.

When analyzing the pressure variation under static conditions, pressure is expected to be symmetric in angular direction due to the absence of any angular force which can produce movement of flow in angular direction. The results found by simulation, are shown in figure 2.7 for different inlet pressures and central clearances. Figure 2.7.b represents a 2-dimensional cross sectional cut through 90^o-180^o angular position of figure 2.7.a. Notice that the value of the pressure along the groove is approximately constant and is 42% of the value of inlet pressure, for the cases studied; such value is independent of inlet pressure and clearance as presented in figure 2.7.b.

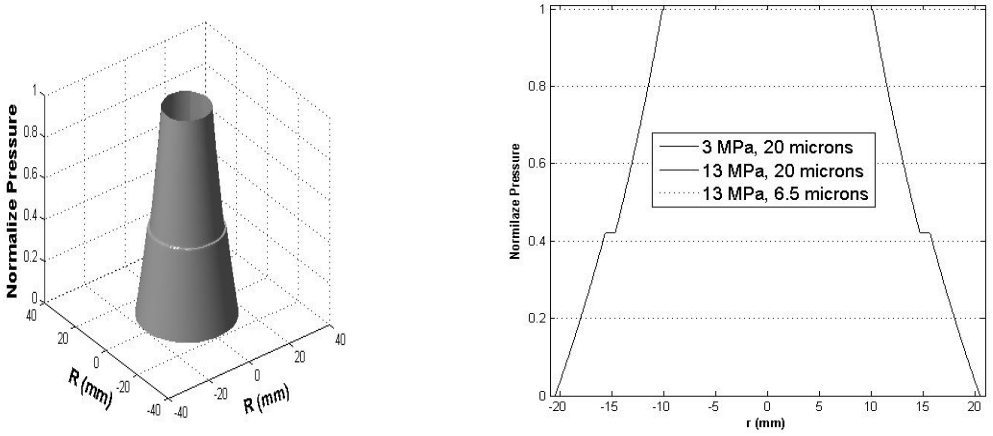

a) 3 MPa. 20 microns. b) Pressure plot at a 2-d cross section cut through 90^o-180^o angular position at different pressure and clearance.

Figure 2.7 – Normalize pressure graph at different inlet pressure and central clearance in static condition (CFD).

For static conditions, the force acting over the slipper is linearly dependent on pressure and does not depend on clearance. For the pressure range (3 to 13 MPa), studied in the present work, force over the slipper (without slipper pocket) can be given by equation 2.35. Due the fact that pressure is symmetric in angular direction, the torque acting on the slipper is null for all pressure boundary conditions and clearances.

$$F(N) = 380\, P_{in}(MPa) + 4.5 \qquad (2.35)$$

2.8.2.2 Slipper leakage.

Slipper leakage was measured experimentally by using the test rig 1 described in chapter 5; a comparison between the leakages obtained via computer simulation and experimentally is presented under static conditions and for a set of inlet pressures and clearances in figure 2.8. While dealing with such a tiny clearance, roughness plays an important role in determining the actual slipper-plate clearance. Surface roughness measurements are presented in figure 2.9 from where it is noticed that average variation in surface finish is typically 1 micron for both materials. Then the measured transducer clearance needs to be modified by the surface roughness in order to get the true clearance between slipper and plate, as defined in equation (2.36).

True clearance = Measured clearance + 2 * Average roughness of the surface (2.36)

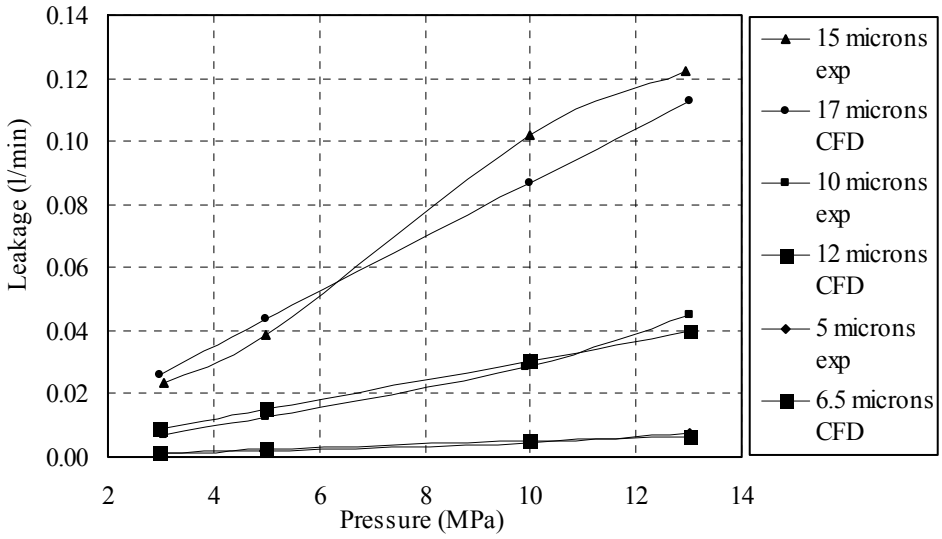

Figure 2.8 – Slipper leakage at different inlet pressure and central clearance (Comparison between CFD and experiment).

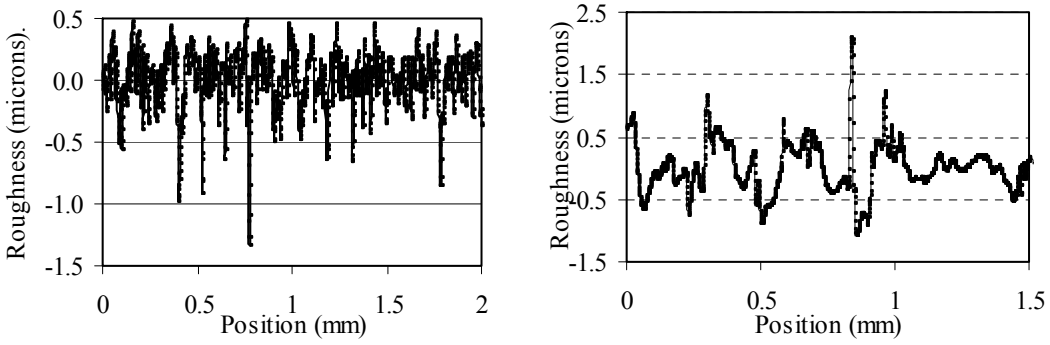

a) Aluminium base. b) Stainless Steel base.

Figure 2.9 - Surface Roughness of the aluminium base and the stainless steel slipper in the radial direction.

From the comparison, it can be seen that experimental results have a good agreement with computational ones, once the roughness of the surface is considered.

2.8.2.3 Effect of Groove dimensions and position.

The position of the grooves cut on slippers has never been studied before, although from the equations presented in [29] the effect of groove width and position could be analysed. In what follows it will be demonstrated that grove position and groove dimensions modify substantially the leakage across the slipper, force over the slipper will also suffer a huge modification. Figure 2.10 represents the value of the averaged normalized groove pressure and force on slipper at different groove positions and groove widths under static conditions.

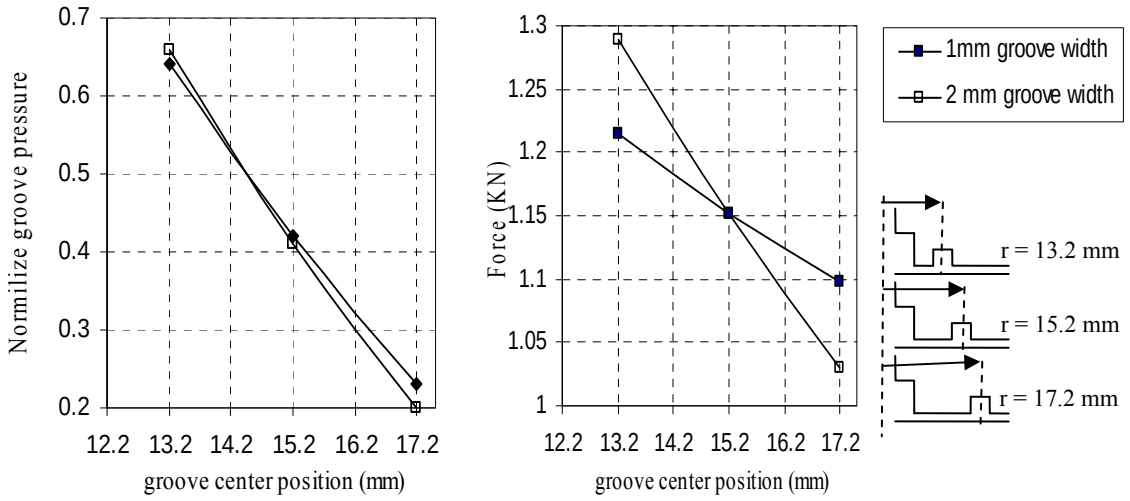

a) Normalized groove pressure. b) Force on slipper.

Figure 2.10 – Change in groove pressure and force at different groove position and groove width (CFD).

It can be seen from figure 2.10a that, the value of groove average pressure decreases as the groove moves towards the slipper outer boundary, this is well expected due to the fact that we have low pressure boundary condition at outer boundary. It is nevertheless to be noticed that, compared to a smaller groove, a groove with bigger width has slightly higher average pressure when it is nearer to inner boundary but a lower average pressure when it is nearer to outer boundary. The critical point happened to be at radius = 15 mm, which is the centre of the slipper land. Figure 2.10b, shows the lift force over the slipper for different groove positions and for two groove widths, grooves located at the slipper inner land will produce a much bigger lift than when grooves are located at the outer land. Notice that for the groove with of 2 mm, such force increase is about 13% versus the centred groove slipper.

Figure 2.11.a presents the leakage percentage increase versus a slipper with the groove centred and when the groove is located at different radial positions, with a groove width of 1mm. The graph clearly demonstrates that as the groove is positioned near the slipper pocked, leakage increases, while when the groove is moved towards the slipper external radius leakage will decrease, the percentage variation is independent of slipper inlet pressure. From figure 2.11.b can be seen that force in percentage versus a slipper with centred groove, increases when the groove is located near the slipper pocked, the percentage increase is independent on the inlet pressure.

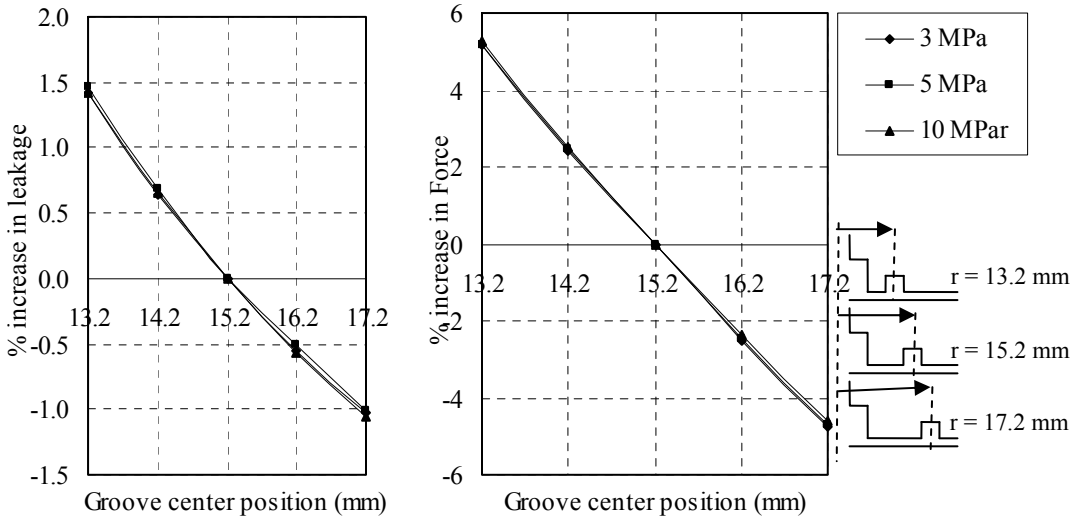

a) % increase in leakage. b) % increase in force.

Figure 2.11 – Percentage increase in leakage and force versus a slipper with centered groove at different groove position for groove width of 1mm (CFD).

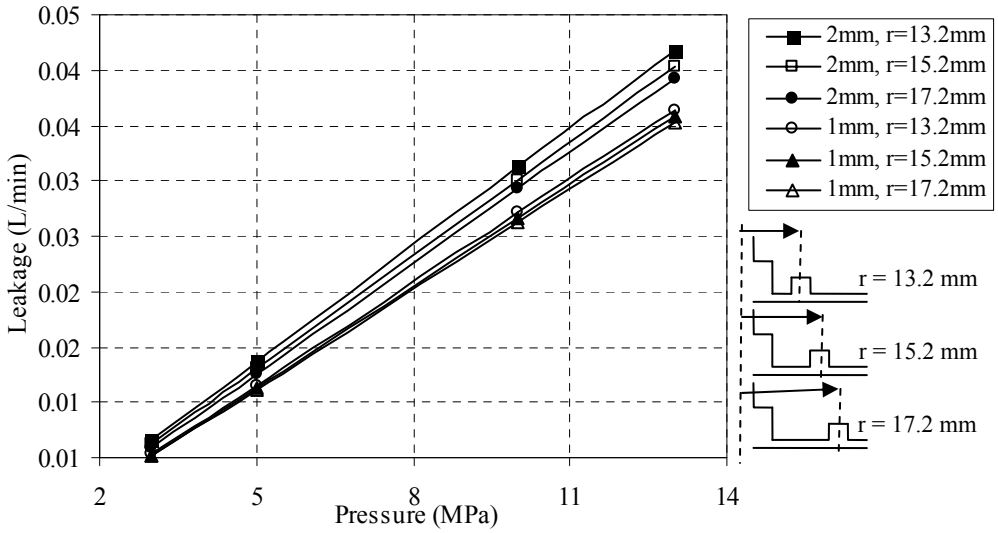

Figure 2.12 - Slipper Leakage at different groove widths (1 mm; 2 mm) and different groove positions. (CFD).

The effect of groove width at different groove positions on slipper leakage is presented in figures 2.12, where can be seen that when the groove central radius remains constant, an increase of groove width leads to an increase of leakage and as stated earlier, positing the groove towards the outer boundary leads to a lower slipper leakage.

Figure 2.13 presents the effect on leakage in percentage versus the non grooved slipper as groove depth is modified. It is clearly shown that for a given groove width and groove position, leakage increases with the increase of groove depth, although when depth overcomes a certain value (0.2mm in the present study), leakage will be nearly constant and independent on groove depth increase. The explanation of such behaviour is found latter when analyzing vorticity inside groove. Notice that at very low groove depths, slipper plate clearance slightly modifies leakage increase.

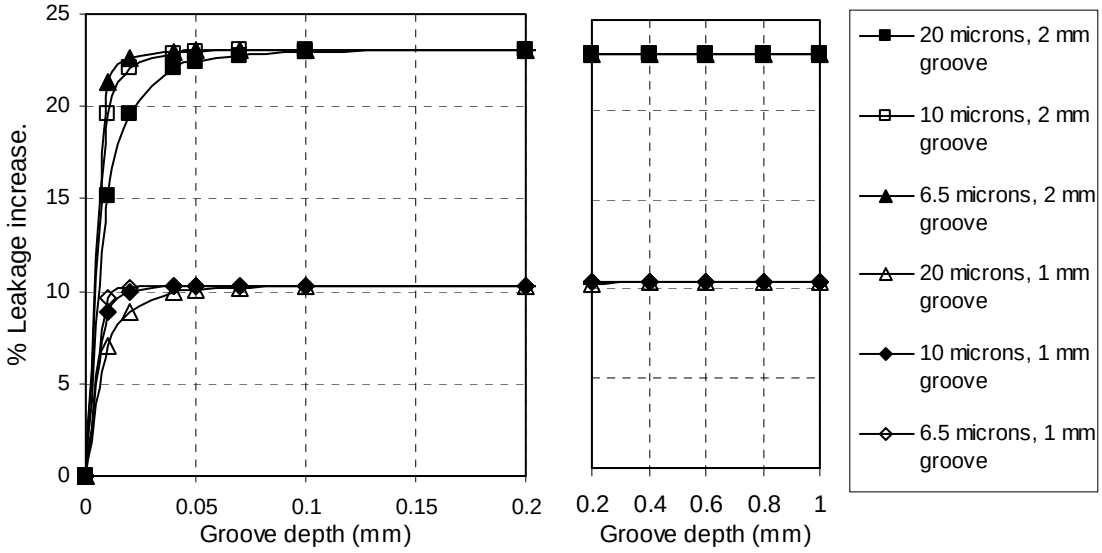

Figure 2.13 –Leakage increase in percentage versus non grooved slipper, for two different withds (1, 2 mm), inlet pressure 10 MPa and different clearance. Groove centered (CFD).

2.8.3 Analysis in dynamic conditions.

As in reality the slipper turns around the swash plate and also spins with respect to its own axis, to understand its dynamic behavior it will be necessary to consider such movement. Figure 2.14 shows a diagram of the two slipper rotations considered and existent in reality, with respect to slipper axis and with respect to the swash plate axis, the different angular positions considered over the slipper are also presented. The turning with respect to swash plate axis is much relevant than the spin and therefore the flow is expected to be deeply affected by its tangential velocity associated.

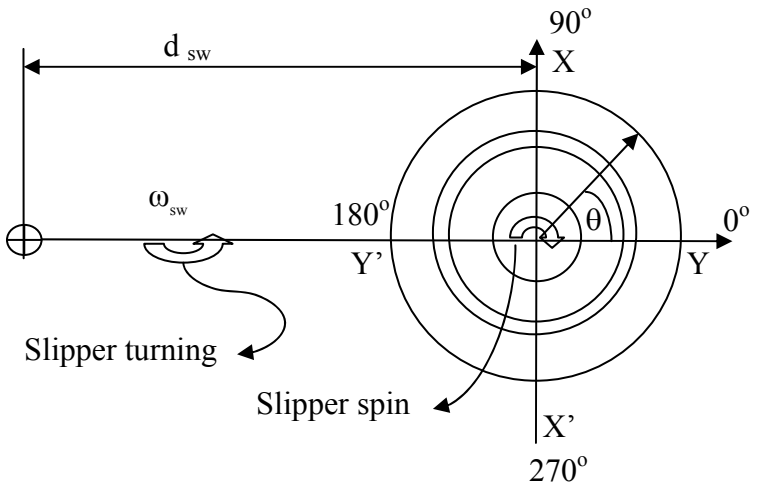

Figure 2.14 – Diagram of slipper turning speeds with respect to swash plat axis.
d_{sw} = 92 mm.

The experiments have been performed by using the test rig 1 presented in chapter 7. When using this test rig under dynamic conditions, it has to be considered the disk run out. Then, the clearance slipper/plate will need to be corrected by the disk run out. Numerical simulations have been performed at these corrected clearances to compare the leakage with the experiments. Although while doing experiments using test rig 1, it is not possible to maintain the fix gap between slipper and swash plate, nevertheless numerical simulations have been performed at fix clearances for different turning speeds (200 rpm to 1000 rpm) at different pressures (3 MPa to 13 MPa) to understand the effect of turning speed alone on the slipper performance.

2.8.3.1 Disk run out.

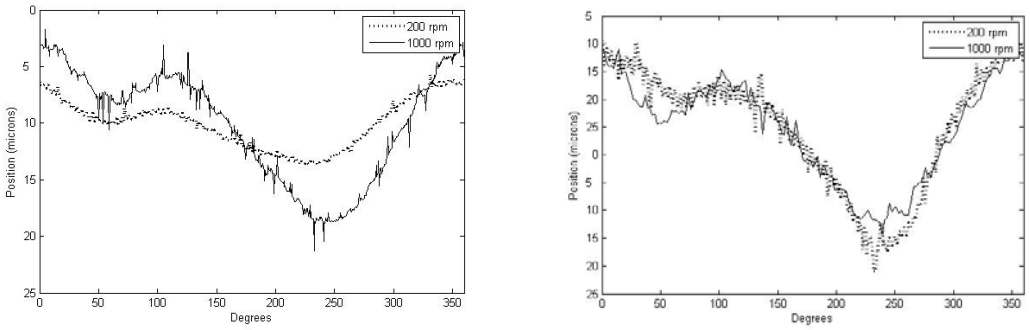

a) 3 MPa. b) 13 MPa.

Figure 2.15 - Disk run out at several pressures and tangential velocity (experimental).

During experimentation it was observed that disk run out depends on slipper inlet pressure and disk turning speed. The disk run out has been measured using the position transducer located at the slipper leading edge and figure 2.15 presents results at 3 MPa

and 13 MPa and for two rotational speeds of 200 rpm and 1000 rpm. It is noticed that at 3 MPa, the effect of rotational speed modifies substantially the disk run out; while at 13 MPa the disk run out is rather independent of turning speed. The maximum run out is found at low pressures and high speeds. Disk run out (for the cases studied) was found to be independent on the film thickness. During experimentation it was found that slipper plate clearance was increasing with the increase of inlet pressure. On section 2.8.3.3, the values of disk run out and disk displacement due to inlet pressure will be given and used to calculate the leakage.

2.8.3.2 Effect on pressure, force and torque.

In figure 2.7, it was presented the pressure distribution for several clearances and inlet pressures under static conditions, where it was noticed that for the cases studied, pressure distribution below the slipper was independent on slipper/plate clearance, therefore, it can be expected that under dynamic conditions, disk run out is not going to affect very much the pressure distribution below the slipper. On the other hand, leakage slipper plate it is expected to be highly dependent on disk run out.

Thanks to the experimental test rig 1, it was able to evaluate the pressure inside the slipper groove in four points separated 90 degrees from each other, and under all static and dynamic conditions, pressure inside the groove was found to be approximately constant on turning speed and mostly dependent on inlet pressure. In figure 2.16 the average simulated groove pressures for a set of turning speeds and slipper inlet pressures is compared with the experimental ones.

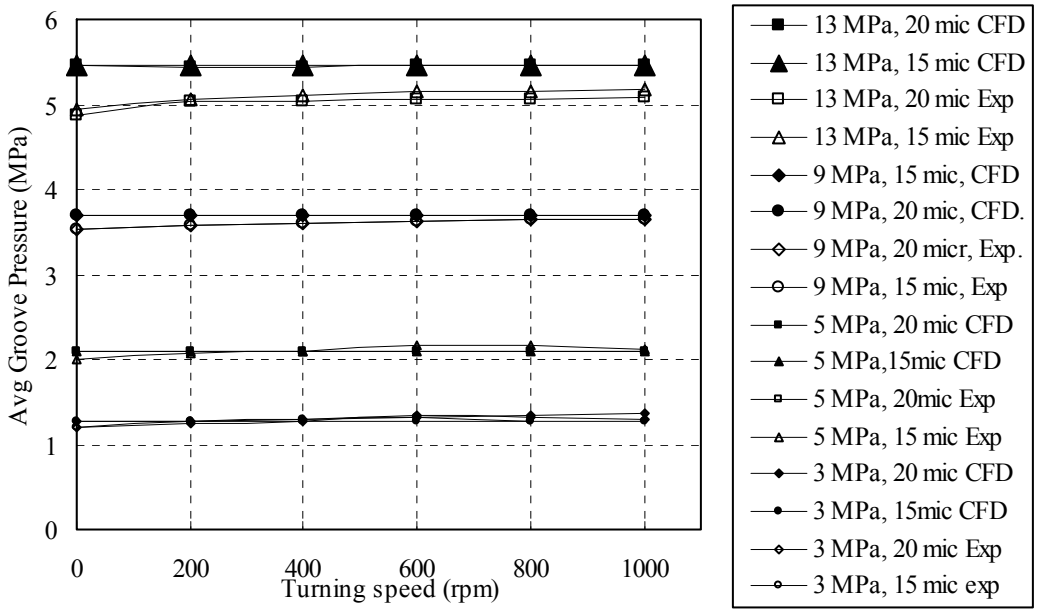

Figure 2.16 - Averaged groove pressure at different inlet pressure, central clearance and turning speed (comparison between CFD and experiment).

The results show a good concordance specially at low and medium slipper inlet pressures, nevertheless, such agreement decreases at high pressures, such discrepancies are well understood when taken into account that as inlet pressure increases leakage across the slipper also increases and shear stresses increase with leakage, the NVS equations consider shear stresses for a perfectly smooth surface, but in reality the slipper and plate surfaces have some roughness which was shown in figure 2.9 for the aluminium base and the stainless steel slipper, as a result pressure decay in slipper first land is higher in reality than the one found via CFD, specially at high pressure differentials.

To visualize the pressure distribution below the slipper under dynamic conditions, figure 2.17 is presented and represents pressure graphs at different turning speeds. It can be seen from figure 2.17.b, that at higher turning speed there exist in angular direction a pressure differential inside the groove of approximately 0.1 to 0.3 MPa, such pressure differential is negligible at low speeds. It is interesting to point out that at high turning speeds, the pressure measured experimentally at the four groove measuring points was fluctuating and therefore just the average pressure could be gathered.

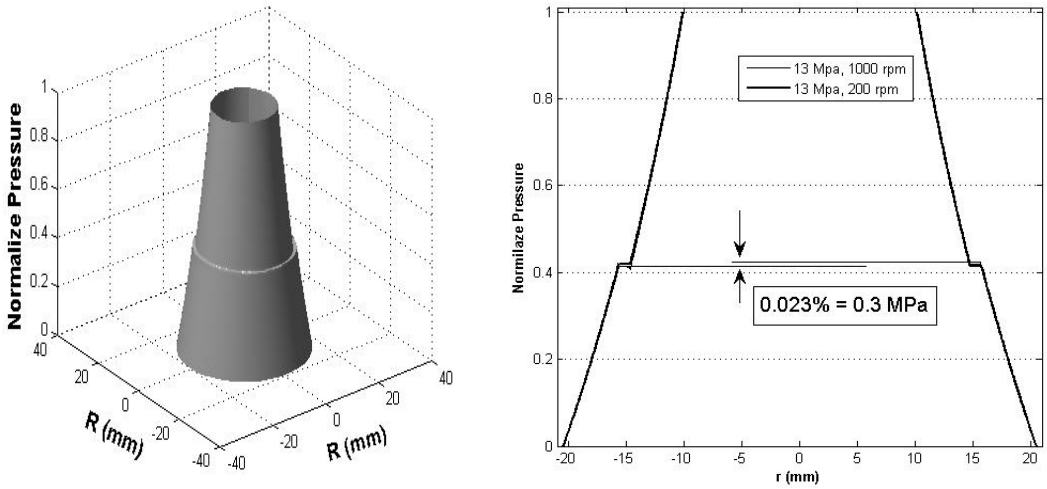

a) Turning = 1000 rpm. b) Pressure plot at a 2-d cross section cut through 90^o-180^o angular position at different turning speed.

Figure 2.17 - Simulated pressure three dimensional graphs at 13 MPa inlet pressure, 20 micron clearance and different turning speeds (CFD).

When comparing figure 2.17 and figure 2.7, it can be seen that pressure distribution bellow slipper is not much affected by tangential velocity; as a result force will remain nearly the same as in static conditions, represented by equation (2.35). For the cases studied the variation found was in the range of 0.02 % (3 Mpa, 1000 rpm) to 0.08 % (13 MPa, 1000 rpm).

Figure 2.18 presents for clearance of 20 microns, the torque at different turning speeds and pressures. It can be seen that, at low inlet pressures, torque is independent of

pressure, but as the pressure increases the torque becomes dependent on pressure and turning speed. The explanation of this phenomena can be found when noticing that the magnitude of flow due to pressure difference (Poiseulle flow) is at some point of the same order of magnitude as the flow due to slipper movement (Couette flow), there is then a mutual adjustment between these two flows, as a result, the direction and magnitude of flow change at different angular position as a function of turning speed and pressure, pressure distribution below the slipper and shear stresses are also affected by this effect. On the other hand, at low inlet pressure, the magnitude of Poiseulle flow is low with respect to Couette flow and flow pattern is manly determined by Couette flow. Nevertheless, the torques acting over a flat slipper, are of a fraction of a Newton.per meter

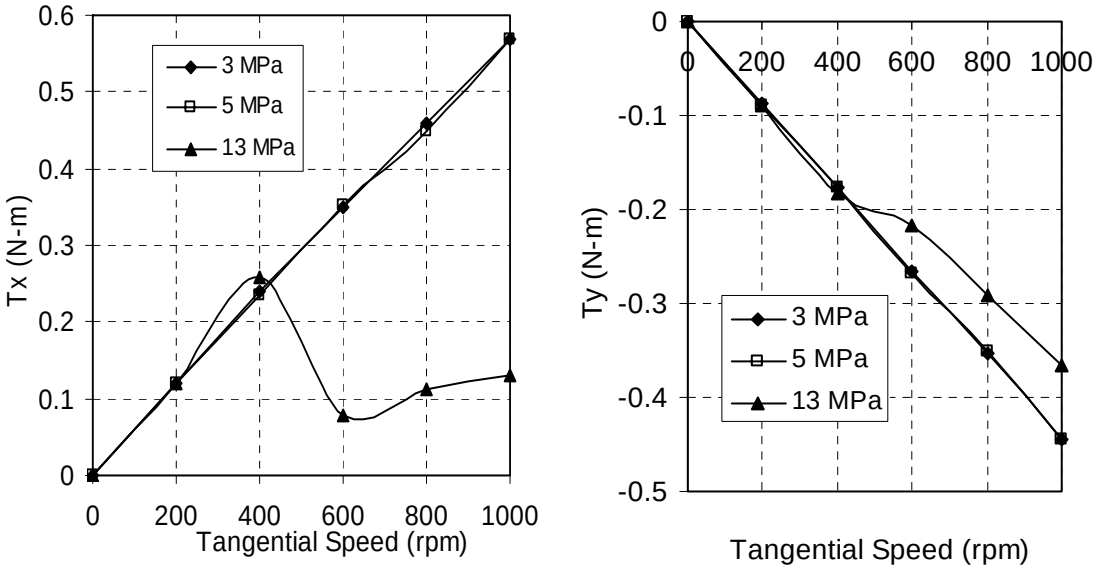

a) Torque Vs x-axis. b) Torque Vs y-axis.

Figure 2.18 – X and Y axis Torque at different turning speed and inlet pressure at 20 microns.

2.8.3.3 Effect on slipper leakage.

When measuring experimentally the slipper/plate leakage in dynamic conditions, needs to be considered the disk run out, since leakage strongly depends on central clearance between slipper and plate. Therefore for each turning speed and inlet pressure, the average clearance will have to be calculated to find out the real clearance slipper/plate. Figure 2.19.b represents the measured average plate run out for a set of inlet pressures and turning speeds. It seems that for a given pressure, the increase of turning speed slightly decreases the disk run out, but it is needed to point out that as the pressure increases the clearance will also increase, due to plate displacement when submitted under pressure. The clearance slipper/plate was measured statically and for a pressure of

3 MPa. Such distance was measured at the highest point of the disk run out, to make sure that this distance was the minimum possible between slipper and plate for the corresponding pressure. When the pressure was increased, the clearance slipper/plate also increased and this plate displacement was measured via measuring the change in amplitude of the disk run out versus the amplitude found at 3 MPa, presented in figure 2.14. Figure 2.19.a represents the plate displacement at different pressures.

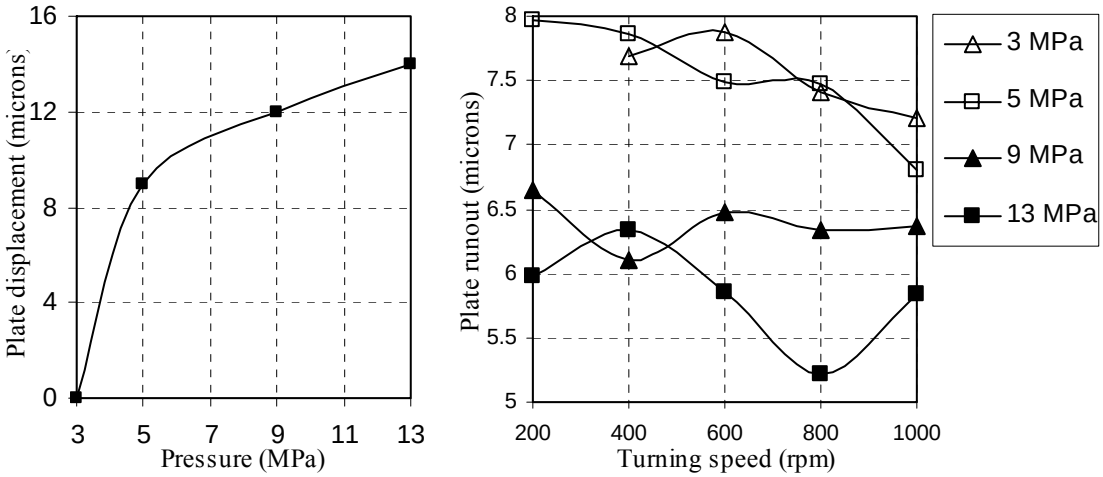

a) Plate displacement. b) Plate run out.

Figure 2.19 – Experimental plate run out and plate displacement at different turning speeds and inlet pressures.

To compare the experimentally measured leakage with the simulated one, the clearances need to be modified with plate run out and plate displacement, as presented in figure 2.19. Equation (2.37) represents this modification in static initial clearance in dynamics conditions.

$$\text{Modified clearance} = \text{initial clearance} + \text{plate run out} + \text{plate displacement} \quad (2.37)$$

Numerical simulations have been performed for each modified clearance to compare with experiments. Figure 2.20 represents the comparison between experimentally measured and simulated leakage at modified clearances, being the initial static clearance of 15 microns. The comparison shows a very good agreement.

Figure 2.21 presents the leakage calculated from CFD at fix gap and different turning speeds. It can be seen that, for a flat slipper at a fix clearance, turning speed does not affect the leakage. This is due to the fact that when the slipper turns around the pump swash plate, in half part of the slipper (0 to 180^0) flow is supported by the surface movement and on the other half part flow is opposed by surface movement and since the

slipper is flat, these effect cancel out each other and as a result the effective leakage remain constant with turning speed.

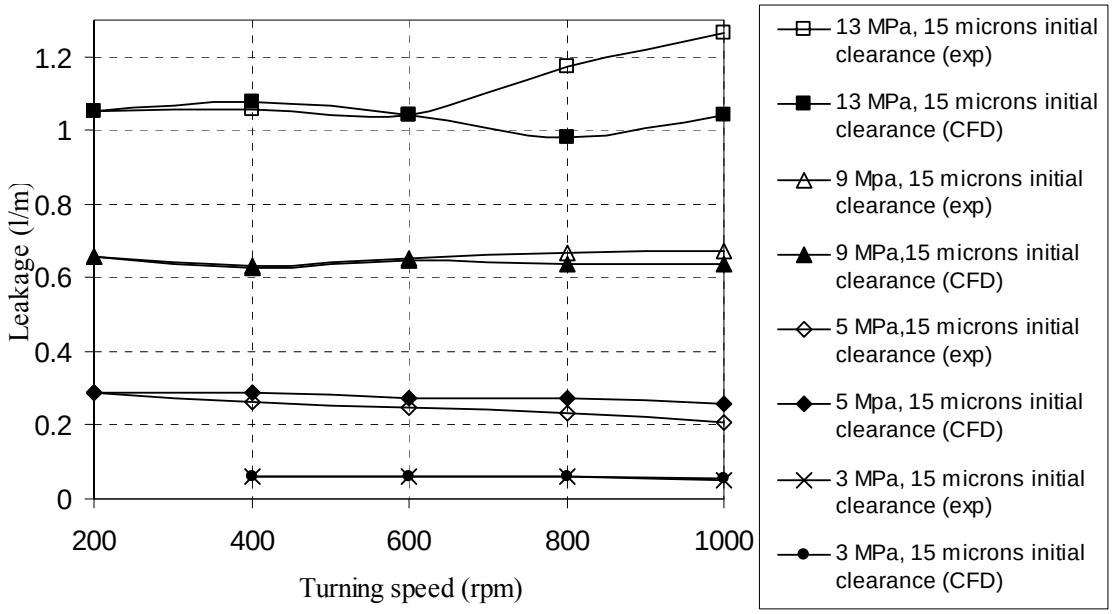

Figure 2.20 – Compression between experimentally measured and simulated leakage with modifies clearance at different pressure and 15 microns initial clearance.

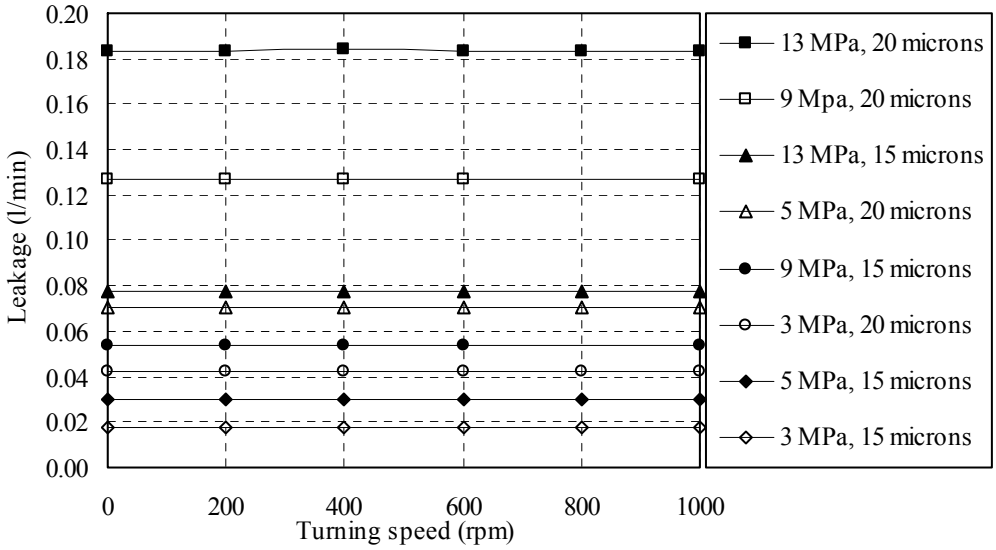

Figure 2.21 - Simulated leakages versus turning speed at different inlet pressure and central clearance (CFD).

Therefore it can be concluded that, in dynamic conditions leakage variation is due to plate run out and plate displacement, not because of turning speed.

2.8.4 Vorticity inside the groove.

It is assumed that a groove maintains a constant pressure all along, to understand this assumption it is necessary to study the momentum transfer of the fluid particles inside the groove, and such momentum transfer entirely depends on the Vorticity created inside the slipper groove. In the present section, Vorticity is analyzed in both static and dynamic conditions.

2.8.4.1 Vorticity under static conditions.

Under static conditions, the flow movement in the clearance slipper/plate is created by the pressure difference across the slipper and the Vorticity exist only in r-z plane (see figure 2.2), then, there is no need to transfer momentum along angular direction. Figure 2.22 represents the streamlines inside the groove in the r-z plane at different groove depths. It can be noticed, there exist an interaction between external flow and recirculating flow inside the groove and exist a big vortex at the groove bottom. Although not stated in figure 2.22, it is found that the position of this vortex is independent from inlet pressure and clearance, being the groove depth the most relevant parameter. It is noticed from figure 2.22 that there exists a saddle point at 0.2 mm in z direction versus the slipper face. The position of this saddle point remains constant regardless of groove depth or inlet pressure. Since the flow across the slipper and across the groove has to be the same, and for a given slipper/plate clearance the flow depends on the distance between the slipper face and the saddle point, and such distance remains constant for groove depths higher than 0.2 mm, it can be concluded that for the groove studied the leakage will remain constant if groove depths are higher than 0.2mm, understanding that pressure and slipper plate clearance remain constant. On the other hand, for groove depths lower than 0.2mm the leakage will sharply decrease, as presented in figure 2.13.

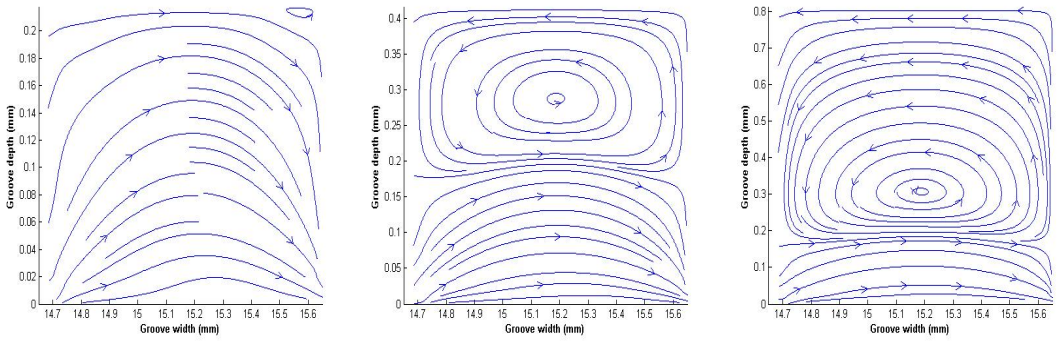

a) 0.2 mm groove depth. b) 0.4 mm groove depth. c) 0.8 mm groove depth.

Figure 2.22 – Streamlines in r-z plane in side groove at different groove depth in static conditions at 10 MPa, 20 microns clearance (CFD).

2.8.4.2 Vorticity under dynamic conditions.

In section 2.8.3.2, it has been demonstrated experimentally and via CFD that pressure inside the groove remains constant in angular direction regardless of slipper tangential

speed. The explanation of why pressure remains constant under dynamic conditions needs to be found in the extremely quick momentum interchange between fluid particles inside the groove. Such momentum interchange is enhanced by the action of recirculating fluid inside the groove which will now depend on slipper tangential velocity among other parameters.

The velocity on the slipper surface, at a given radius (r) and angular position (θ), due to slipper rotation with respect to swash plate axis is given by equations (2.38-39).

$$V_r = d_{sw}\ \omega_{sw}\ \sin(\theta) \tag{2.38}$$

$$V_\theta = d_{sw}\ \omega_{sw}\ \cos(\theta) + r\ \omega_{sw} \tag{2.39}$$

When analyzing the Vorticity in dynamic conditions, the flow inside the groove, which was recirculating in r-z plane in static conditions, is expected in dynamic conditions to recirculate in angular direction as well due to surface movement. Figure 2.23 represents a three dimensional streamlines flow pattern in slipper-swash plate gap at 13 MPa and 200 rpm rotation speed. It can be seen that in dynamic conditions, there exist two vortexes inside the groove, a primary vortex at groove bottom and a secondary vortex near groove entrance.

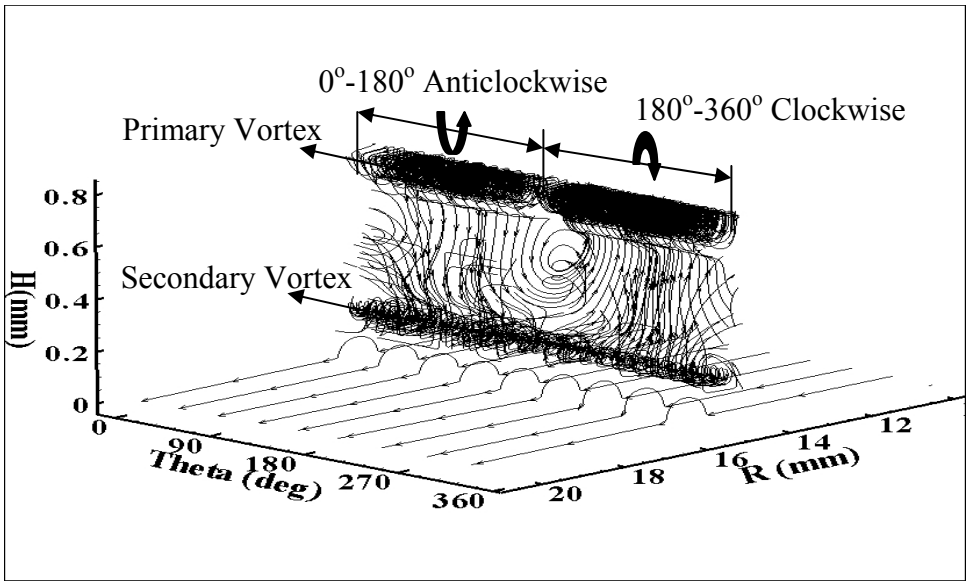

Figure 2.23 – streamlines plot at 13 MPa, 200 rpm and 20 microns clearance.

Primary vortex is created by the interaction between the flow coming into the groove and the no slipping boundary conditions at slipper walls. The primary vortex is displaced along the θ direction by the groove bottom surface movement defined in equation (2.39). The rotation of the primary vortex is directed by the radial component of slipper surface movement, given by equation (2.38). Since the radial movement of the groove bottom

surface is a sine wave, as a result, the primary vortex rotation will also change as a sine wave, therefore the vortex will rotate anticlockwise from 0^o to 180^o and clockwise from 180^o to 360^o angular position. This primary vortex is the most relevant one since exist at all angular positions and play the most important role in stabilizing the pressure.

Despite the fact that the secondary vortex is created by the mutual adjustment between the external flow and the primary vortex, the effect of the incoming flow is of higher relevance. As a result, the structure of the secondary vortex depends on the direction of slipper/plate flow, which depends upon inlet pressure and tangential speed (operating condition). Therefore the vortex dimensions and turning speed will be completely different at different angular positions. In some conditions the vortex might also disappear.

Before further analyzing the vortex, it is important to understand the direction and relative magnitude of the slipper/plate flow (radial flow) as a function of angular position at different inlet pressures and turning speeds. The structure of vortexes is determined by the magnitude and direction of the shear stresses which depend on velocity gradient. Figure 2.24 represents the normalized slipper/plate flow (radial flow) as a function of angular position at different tangential speeds (200 – 1000 rpm) and inlet pressures (3 and 13 MPa). It can be seen from figure 2.24 that depending upon inlet pressure and tangential speed, the direction of slipper/plate flow changes from positive (outward) to negative (inward) at different angular positions.

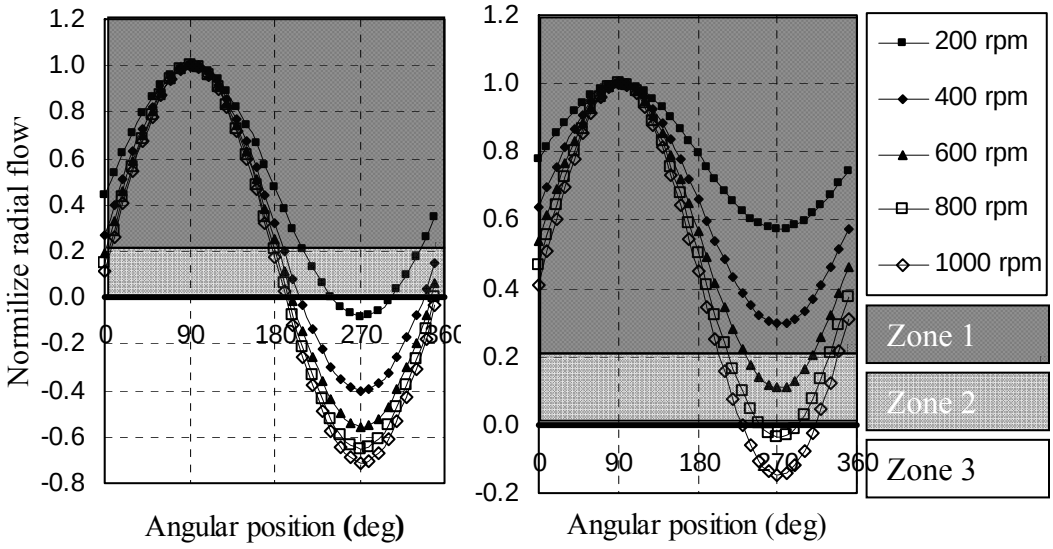

a) 3 MPa, 20 microns clearance. b) 13 MPa, 20 microns clearance.

Figure 2.24 – Normilize radial flow at different angular position of slipper.

By taking into account the mutual adjustment between Poiseulle and Couette flow, the slipper can be divided into three flow zones (see figure 2.24):

1. ***Zone 1 [Net radial flow = Poiseulle flow + Couette flow]*** **-** In this zone, the flow is radially outward. Poiseulle and Couette flows might be whether having the same direction (slipper leading edge) or opposite directions (slipper trailing edge), in any case the magnitude of Poiseulle flow at each angular position is much higher than the magnitude of Couette flow. Under such conditions, the velocity gradient at the groove face is at its highest, therefore the secondary vortex rotation speed will also be maximum. As a result it is expected that the momentum transfer between particles at different angular positions will also be higher. In this zone the secondary vortex is helping the primary vortex to stabilize the pressure inside the groove.

2. ***Zone 2 [Net radial flow = Poiseulle flow - Couette flow; & (Poiseulle flow > Couette flow)]*** **-** In this zone, Poiseulle and Couette flows have the same order of magnitude and opposite directions, as a result, the net flow is very small. The secondary vortex will be very weak and tending to disappear.

3. ***Zone 3 [Net radial flow = Poiseulle flow - Couette flow; & (Poiseulle flow < Couette flow)]*** **-** In this zone, Couette flow is radially inward and the magnitude of Couette flow is slightly higher than Poiseulle flow. Notice for example from figure 2.24.b, at 13 Mpa and 1000 rpm, that the magnitude of inward flow is about 15 % of the magnitude of outward flow of zone 1. Therefore inward net flow velocity in zone 3 is very weak; as a result the velocity gradient is not huge enough to create a secondary vortex.

As a conclusion figure 2.24 can be used to quickly visualize the existence of vortexes at different slipper groove angular positions for a set of inlet pressures and turning speeds. In zone 1 both vortexes exist and in zones 2 and 3 the secondary vortex is whether nonexistent or very weak.

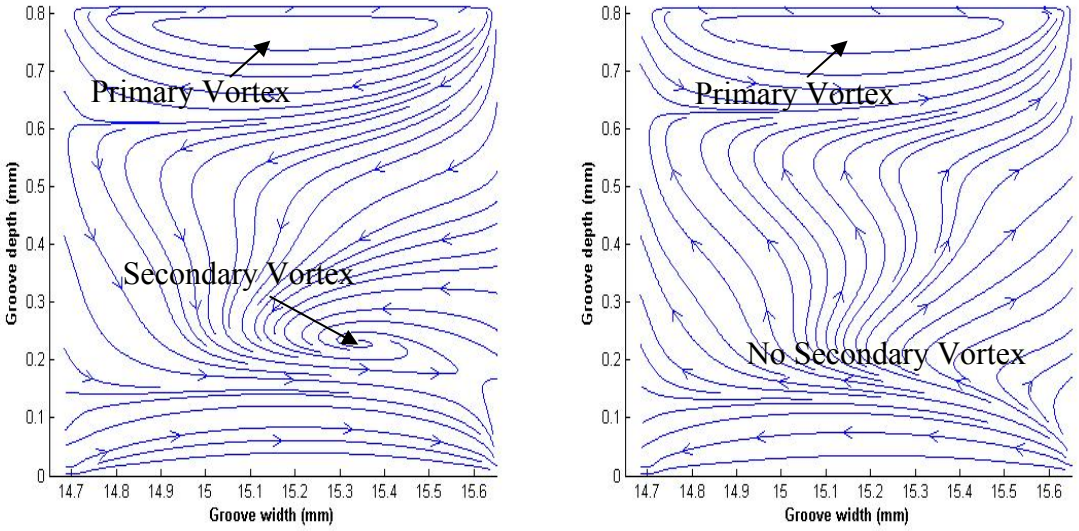

a) 90^{o} angular position (Zone 1). b) 270^{o} angular position. (Zone 3)

Figure 2.25 – Streamlines plot in r-z plane at different angular position for 13 MPa inlet pressure, 1000 rpm rotation and 20 microns clearance.

Figures 2.25 a,b present two dimensional streamlines plot inside the groove for a cross section cut of slipper at different angular positions (90^o and 270^o) at 13 Mpa and 1000 rpm. The nomenclatures of different vortexes are also shown in the figure. It can be noticed from figure 2.24 that at 13 Mpa and 1000 rpm, 90^o angular position corresponds to zone 1 and 270^o angular position corresponds to zone 3, therefore there exit both vortex (primary and secondary) at 90^o angular position but only primary vortex at 270^o angular position, therefore such figures corroborate the statement previously stated.

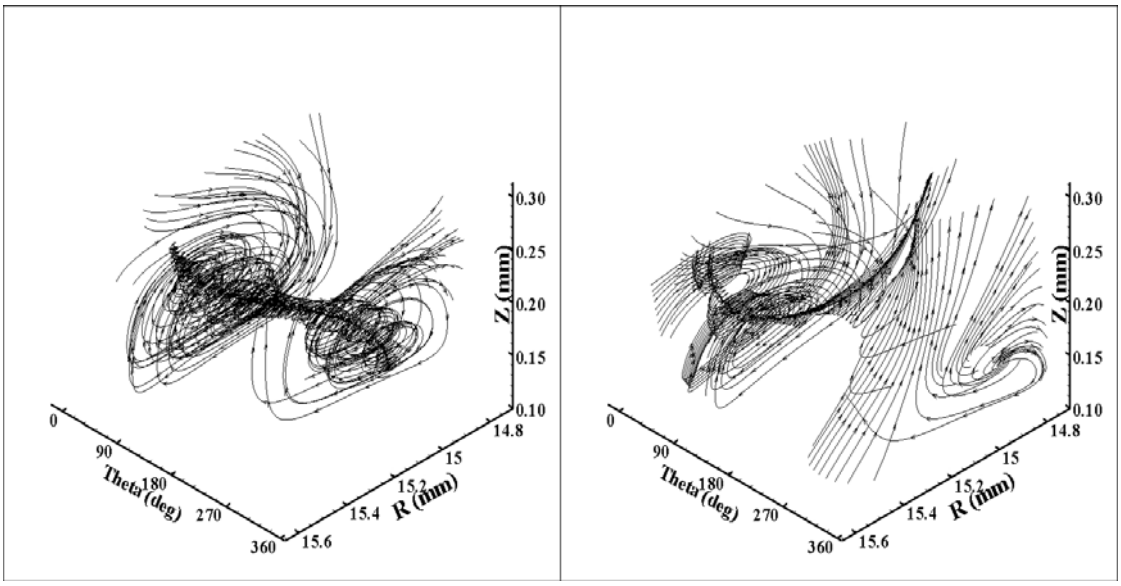

a) 13 MPa, 200 rpm, 20 microns. b) 3 MPa, 200 rpm, 20 microns.

c)13 MPa, 1000 rpm, 20 microns. d) 3 MPa, 200 rpm, 10 microns.

Figure 2.26 – Streamlines plot of secondary vortex inside the groove at different inlet pressure.

Figures 2.26 a, b represent a 3-D streamlines plot of secondary vortex inside the groove at two pressure boundary conditions, 3 and 13 MPa at 200 rpm. It can be seen that at 13

MPa inlet pressure and 200 rpm turning speed, the entire slipper is placed in zone 1, as a result the secondary vortex is appearing throughout all angular positions. On the other hand at 3 MPa inlet pressure and 200 rpm turning speed, the secondary vortex appears on the angular position (0^o to 200^o) which corresponds to zone 1 from figure 2.24a.

When comparing figure 2.26 a and 2.26 c, at 13 MPa it is noticed, the increase of turning speed from 200 rpm to 1000 rpm, will lead to the disappearance of the secondary vortex from angular position 200^o to 340^o, which corresponds to zone 2 and zone 3 (figure 2.24b).

When decreasing the clearance from 20 microns to 10 microns, at 3 MPa and 200 rpm, it can be noticed from figure 2.26 b and 2.26 d that the intensity of the vortex is lower, also the vortex appear a bit more near to groove face. Such behaviour can be understood by the fact that, at low clearance, the magnitude of flow is low, as a result velocity gradient is also going to be lower, which results into low vortex rotation.

2.9 Conclusions.

In static conditions, it is found that the normalized pressure inside the groove is independent of inlet pressure, force acting on the slipper and leakage are a linear function of pressure. Leakage strongly depends on clearance slipper/plate while slipper pressure distribution is for the cases studied, independent of clearance.

When modifying groove position, the displacement of the groove towards the slipper inner pocket (inner boundary) leads to increase in leakage and force acting over the slipper. If the groove central axis is maintained at the centre of the slipper land, an increase of groove width will bring an increase in force acting over slipper and leakage. When the groove is positioned near the outer boundary of the slipper, the narrower the groove width the higher the force on the slipper and the lower the leakage. Independently on the groove position and width, an increase in groove depth leads to an increase in leakage until reaching a certain depth, up to which leakage remains constant.
Slipper-plate relative movement under constant supply pressure is considered as dynamic conditions, under such conditions, the tangential speed has negligible effect on the force acting over the slipper. It creates nevertheless a small torque respect to the two slipper main axis. At higher speed, there exists a noticeable pressure differential inside the groove. Leakage is independent on turning speed.

Vorticity inside the slipper groove has been studied to analyze the momentum transfer inside the groove. In general two forced vortexes appear inside the groove. The primary one located at the groove bottom is the most responsible for maintaining the pressure along the groove in angular direction. This vortex exist under all working conditions, is created by mutual adjustment between slipper/plate flow and no slipping condition on slipper groove wall. A secondary vortex is also near the groove face. Its existence is due to interaction between slipper-plate flow and primary vortex. This secondary vortex

exists only in the region of higher velocity gradient. The work done in this chapter has been published in Computers and fluids journal [47].

Nomenclature

Γ	Computation domain boundary (m).
Ω	Computation domain (m^3).
ρ	Density of fluid (Kg/m^3).
μ	Dynamics viscosity (Kg/m/s).
ϕ	Flux vector (m/s).
ω_{sw}	Slipper turning speed around the plate main axis (rad/s).
A	Coefficient in pressure correction equation (m.s).
B	Mass conservation term in continuity. (Kg/s).
P	Pressure (Pa).
S_ϕ	Source term in momentum eq for corresponding ϕ ($Kg/m^2/s^2$).
V	Velocity (m/s).
a	Coefficient of discrete momentum equation (Kg/s).
b	Source term in discrete momentum equation ($Kg.m/s^2$).
dr, $d\theta$,dz	Grid size in r, θ and z direction (m, rad, m).
d_{sw}	Distance between slipper centre from swash plate centre (m).
h_{01}	Slipper pocket height from plate (m).
h_{02}	Slipper/plate clearance (m).
h_{03}	Groove bottom height from plate (m).
i, j, k	Grid coordinate in r, θ and z direction.
r, θ , z	Cylindrical coordinates vector (m, rad, m).
t	Time (s).

Subscript:

E,W,N,S,T,B	East, west, north, south, top and bottom direction.
in, out	Corresponding to Inlet and outlet boundary.
nb	Neighbour grid point of point p.
p	Grid point under consideration.
r, θ , z	Component of vector in r, θ and z direction.

Superscript:

*	Imperfect computed field.
‘	Correction in corresponding quantity.

References

1 Fisher, M.J. A theoretical determination of some characteristics of a tilted hydrostatic slipper bearing. B.H.R.A. Rep. RR 728 April 1962.

2 Böinghoff, O. Untersuchen zum Reibungsverhalten der Gleitschuhe in Schrägscheiben-Axialkolbenmascinen. VDI-Forschungsheft 584. VDI-Verlag. 1-46. 1977.

3 Hooke C.J. , Kakoullis Y.P. The lubrication of slippers on axial piston pumps. 5th International Fluid Power Symposium September 1978, B2-(13-26) Durham, England.

4 Hooke C.J. , Kakoullis Y.P. The effects of centrifugal load and ball friction on the lubrication of slippers in axial piston pumps. 6th International Fluid Power Symposium, 179-191, Cambridge, England. 1981

5 Iboshi N., Yamaguchi A. Characteristics of a slipper Bearing for swash plate type axial piston pumps and motors, theoretical analysis. Bulletin of the JSME, Vol 25, No 210, December 1982, 1921-1930.

6 Iboshi N., Yamaguchi A. Characteristics of a slipper Bearing for swash plate type axial piston pumps and motors, experiment. Bulletin of the JSME, Vol 26, No 219, September 1983. 1583-1589.

7 Iboshi N., Characteristics of a slipper Bearing for swash plate type axial piston pumps and motors, Design method for a slipper with a minimum Power loss in fluid lubrication. Bulletin of the JSME, Vol 29, No 254, August 1986.

8 Hooke C.J., Kakoullis Y.P. The effects of non flatness on the performance of slippers in axial piston pumps. Proceedings of the Institution of Mechanical Engineers, December 1983, Vol. 197 C, 239-247.

9 Hooke C.J., Li K.Y. The lubrication of overclamped slippers in axial piston pumps centrally loaded behaviour. Proceedings of the Institution of Mechanical Engineers 1988, Vol 202, No C4, 287-293.

10 Hooke C.J., Li K.Y. The lubrication of slippers in axial piston pumps and motors. The effect of tilting couples. Proceedings of the Institution of Mechanical Engineers 1989, Vol 203, part C, 343-350.

11 Takahashi K. Ishizawa S. Viscous flow between parallel disks with time varying gap width and central fluid source. JHPS International Symposium on Fluid Power, Tokyo, March 1989, 407-414.

12 Li K.Y., Hooke C.J. A note on the lubrication of composite slippers in water based axial piston pumps and motors. Wear, 147 1991, 431-437.

13 Koc. E., Hooke C.J., Li K.Y. Slipper balance in axial piston pumps and motors. Trans ASME, Journal of Tribology, Vol 114, October 1992, 766-772.

14 Kobayashi, S., Hirose, M., Hatsue, J., Ikeya M. Friction characteristics of a ball joint in the swashplate type axial piston motor. Proc Eighth International Symposium on Fluid Power, J2-565-592, Birmingham, England, 1988.

15 Harris RM. Edge KA. And Tilley DG. Predicting the behaviour of slipper pads in swashplate-type axial piston pumps. ASME Winter Annual Meeting. New Orleans, Louisiana. November 28-December 3, 1993, 1-9.

16 Koc E., Hooke C.J. Investigation into the effects of orifice size, offset and oveclamp ratio on the lubrication of slipper bearings. Tribology International, Vol. 29, No 4, 299-305, 1996.

17 Koc E. Hooke C.J. Considerations in the design of partially hydrostatic slipper bearings. Tribology International, Vol 30, No. 11, 815-823, 1997.

18 Tsuta, T. Iwamoto, T. Umeda T. Combined dynamic response analysis of a piston-slipper system and lubricants in hydraulic piston pump. Emerging Technologies in Fluids, Structures and Fluid/Structure Interactions. Vol 396 187-194 ASME 1999.

19 Wieczoreck, U. Ivantysynova M. CASPAR-A computer aided design tool for axial piston machines. Proceedings of the Power Transmission Motion and Control International Workshop, PTMC2000, Bath, UK. 2000, 113-126.

20 Wieczoreck U and Ivantysynova M. Computer aided optimization of bearing and sealing gaps in hydrostatic machines-the simulation tool CASPAR. International Journal of fluid Power 3 2002; 1:7-20.

21 Crabtree AB, Manring ND, Johnson RE. Pressure measurements for translating hydrostatic trust bearings. International Journal of Fluid Power 2005; Vol. 6 No 3.

22 R. E. Johnson, N. D. Manring. Translating circular thrust bearings. J. Fluid Mech. 2005; 530:197-212.

23 Kazama T., Yamaguchi A. Application of a mixed lubrication model for hydrostatic equipment. Tribology transactions of ASME. Oct 1993, Vol 115, pp:686-91.

24 Kazama T., Yamaguchi A., Fujiwara M. Motion of Eccentrically and dynamically loaded hydrostatic thrust bearing in mixed lubrication. Proceedings of the 5th JFPS International, 2002 - ISBN4-931070-05-3.

25 Kazama T. Numerical simulation of a slipper model for water hydraulic pumps/motors in mixed lubrication. Proceedings of the 6th JFPS International.

26 Kakoulis YP. Slipper lubrication in axial piston pumps. M.Sc. Thesis University of Birmingham; 1977.

27 Bergada JM and Watton J. A direct leakage flow rate calculation method for axial pump grooved pistons and slippers, and its evaluation for a 5/95 fluid application. 5th JFPS international Symposium on fluid power, Nara Japan, Nov 13, 2002.

28 Bergada JM and Watton J. Axial Piston pump slipper balance with multiple lands. ASME International Mechanical Engineering Congress and exposition, New Orleans Louisiana Nov 2002; Vol 2 No 39338.

29 Bergada JM, Haynes JM, Watton J. Leakage and groove pressure of an axial piston pump slipper with multiple lands. Tribol T 2008;5(4):469-82.

30 Brajdic-Mitideri P., Gosman A. D., Loannides E., Spikes H. A. CFD Analysis of a low friction pocketed pad bearing. Journal of Tribology, ASME 2005 Vol. 127, pp 803-12.

31 Helene M., Arghir M., Frene J. Numerical study of the pressure pattern in a two-dimensional hybrid journal bearing recess, laminar and turbulent flow results. Journal of tribology – ASME. Aprial 2003, Vol 125 pp:283-90.

32 Braun M.J., Dzodzo M. Effect of the feedline and the hydrostatic pocket depth on the flow pattern and pressure distribution. Tribology transactions of ASME. April 1995, Vol 117, pp:224-32.

33 Niels H., Santos F. Reducing friction in tilting pad bearing by the use of enclosed recesses. Journal of Tribology - ASME. Jan 2008, Vol 130.

34 Suhas V. Patankar, Numerical Heat Transfer and Fluid Flow. Taylor & Francis Group: Hemisphere Publishing Corporation; 1980.

35 C.A. Estrada, G. Alvarez and J.F. Hinojosa, Three-dimensional numerical simulation of the natural convection in an open tilted cubic cavity. Revista Mexicana De Fisica, Nov 2005; 52(2):111-119.

36 M. Zeng and W.Q. Tao, A comparison study of the convergence characteristics and robustness for four variants of SIMPLE-family at fine grid. Engineering Computations Nov 2003; Vol 20 No 3:320-340.

37 X. Shi, J.M. Khodadadi, Laminar fluid flow and heat transfer in a lid driven cavity due to thin film. Journal of heat transfer, ASME 2002; 124:1056-1063.

38 C.L. Chen, C.H. Cheng, Numerical study of flow and thermal behaviour of lid-driven flow in cavities of small aspect ratio. International journal for numerical methods in fluids 2006; 52:785-799.

39 H. Yao, R. K. Cooper, S. Raghunathan. Numerical Simulation Incompressible Laminar Flow Over Three Dimensional Rectangular Cavities. Journal of Fluid Engineering Nov 2004; 126:919-927.

40 Ching, T. P., Hwang, R. R. and Sheu, W.H. On End-Wall Corner Vortices in a Lid-Driven Cavity. ASME Journal of Fluid Eng. 1997; 119:201-204.

41 Iwatsu, R., Hyun J.M. and Kuwahara K. Numerical Simulation of Three Dimensional Flow in a Cubic Cavity with an Oscillating Lid. ASME-J Fluid Eng. 1993; 115:680-686.

42 S.H. Tasnim, S. Mahmud and P.K. Das. Effect of aspect ratio and eccentricity on heat transfer from a cylinder in a cavity. International journal of Numerical Method for Heat & Fluid Flow May 2002; Vol 12 No 7:855-869.

43 Z. Luan, M.M. Khonsari. Numerical simulation of the flow field around the ring of mechanical seals. Journal of Tribology, ASME July 2006; 128:559-565.

44 M. Molki, M. Faghri. Interaction between a buoyancy-driven flow and an array of annular cavities. Sadhana academy proceedings in engineering science 1999; 19:705-721.

45 Harlow FH, Welch JE. Numerical calculation of time-dependent viscous incompressible flow of fluid with free surface. Physics of Fluids 1965; 8(12): 2182.

46 Johan D. Anderson, Computational Fluid Dynamics, The Basic with Applications. Mc Graw Hill, Inc; 1995.

47 Kumar S., Bergada JM, Watton J. Axial piston pump grooved slipper analysis by CFD simulation of three dimensional NVS equation in cylindrical coordinates. Computer & Fluids (2009) Vol 38 N3 pp 648-663.

3

Tilt Slipper

This chapter presents the static characteristics of a piston pump slipper with a groove where slipper is tilted with respect to swash plate axis. Three dimensional Navier Stokes equations in cylindrical coordinates have been applied to the slipper/plate gap, including the groove. Equations have been transformed to an orthogonal domain from a non orthogonal domain and a SIMPLER based algorithm is developed to simulate flow field and analyze the slipper behavior in tilted conditions.

3.1 Introduction

In the previous chapter we studied the behavior of slipper while it was running parallel to swash plate, but in realistic running conditions, the slipper does not run parallel to the plate, it is therefore important to understand the behavior of slipper under tilted conditions.

The literature available in this field is quite vast and a detailed explanation of the previous research can be found in Chapter 2. When focusing on manly tilt slipper, Fisher [1] demonstrated that if a flat slipper tilts slightly so that the minimum clearance occurs at the trailing edge; the hydrodynamic loads generated tend to return the slipper to the non tilted position. Hooke and Kakoullis [2-3] showed that a degree of non-flatness was essential to ensure the successful operation of the slipper and found that the major source of slippers tilt fluctuation did not arise from differences on surface profile, but from differences in the friction between the slipper/piston spherical junction and piston/cylinder pairs. In [4] Hooke and Li focused on the lubrication of over-clamped slippers and demonstrated that the tilt was found to be proportional to the non-flatness magnitude divided by the square root of the slipper central clearance. In [5] they analysed carefully the three different tilting couples acting on slipper, finding that the tilting couple due to friction at the slipper running face is much smaller than the ones created at the piston/cylinder and slipper/piston interfaces. All slippers tested had a single land.

Iboshi and Yamaguchi [6-8], also worked with single land slippers in tilted condition. They pointed out that the friction of the spherical bearing affects significantly the tilt angles, and the rotational speed affects the central clearance of the slipper plate. Harris et al [9], created a mathematical dynamic model for slipper-pads, in which lift and tilt could be predicted, the model was able to handle the effect of the possible contact with the swash plate. The simulation showed that slipper tilt was much higher at suction that at delivery and at delivery tilt increased with pump turning speed.

Wieczoreck and Ivantysynova [10-11] developed a package called CASPAR which used the two dimensional Reynolds equation of lubrication and the energy equation in differential form for a single land slipper. The clearance and tilt of the slipper was shown to vary over one revolution of the pump. Niels and Ferreira [12] formulated a numerical model based on the Reynolds equation of lubrication, Cartesian coordinates, to minimize the friction in tilting pads and showed that a large amount of energy can be saved by using low length to width ratio of the cavity.

Analytical solution for slippers with multiple lands was outlined in Bergada and Watton [13-14] and more clearly defined in Bergada et al [15]. Reynolds equation of lubrication was applied to the slipper swash plate gap by considering the flow in radial direction, which turn out to be very accurate for flat slipper, for tilt slipper nevertheless and specially for high tilts, the analytical equations were not precise enough, due to the fact that the flow specially inside the groove, has an important tangential component. To overcome this problem, Kumar et al [16] applied the three dimensions Navier Stokes equations to the slipper plate gap with grooved slipper in non tilted conditions via Semi Implicit Pressure correction technique developed in Patanker [17]. As the simulation was done in three dimensions, the vorticity inside the groove could be understood. The present work, extend the model presented in [16] to tilted conditions. Under tilted conditions, the computational domain available for simulation is not orthogonal. As a result there is a need either to transform non orthogonal domain into orthogonal one or use a non orthogonal mesh and implement FEM (Finite element method) rather than FVM (finite volume method) technique. In general, finite element calculations are a bit more temporal expensive than the finite volume method ones, due to the involvement of all integral terms. For the present work, transformation option is chosen to implement the finite volume technique on a transformed orthogonal grid.

Coordinates transformations is a very basic subject in mathematics and its applications in computational fluid dynamics are also very common. In the field of computational fluid dynamics, transformation of non orthogonal boundary fitted grid into an orthogonal one is very common and there have been several techniques, which are used for this purpose such as Metrics and Jacobians formulation, derivative transformations etc. Boundary fitted grids have been quite frequently used to model the complex computational domain such as curved channel in Zhu et al [18], different type of ducts in Borges [19], flow between two slant walls in Koshizuka et al [20-22] and airfoils in Anderson [23] among others. Zhu et al [34] used a boundary fitted grid to simulate two dimensional shallow water flow in a curved open channel and transformed a physical non orthogonal curvilinear coordinates in to a generalized curvilinear orthogonal coordinates by using the

jacobian method to apply finite volume calculations. Borges [19] presented a computational inverse method to model the circular ducts computational domain. Koshizuka et al. [20-22] used a boundary fitted grid for the flow field simulation between two slant walls. They show, theoretically as well as numerically, that stability problem may occur when the mesh size of the adjacent cells differs by more than a factor of 3. In order to reduce mesh sensitivities Demirdzic et al [24], Koshizuka et al [20-22] and Takizawa et al [25] introduced the use of a physical component.

A derivative transformation method is used in the present work to model the non orthogonal boundary fitted grid in the slipper swash plate gap. A detail description of the technique implemented in the present work is found in Anderson [23], where a boundary fitted grid is transformed into an orthogonal grid for an airfoil. Transformed NVS equations in inertial cylindrical coordinates are applied to the slipper-plate gap. The effect of groove dimensions and position is considered for different tilted conditions. The flow slipper plate is considered to be laminar under all cases studied.

3.2 Mathematical Model

Fig 3.1 shows a schematic drawing of the slipper and swash plate clearance when slipper is tilted, the slipper relative movements is also outlined. The shaded area presents the domain $\Omega\{\Omega : \square^4(r,\theta,z,t)\}$ with shown boundary Γ {Γin, Γout}.

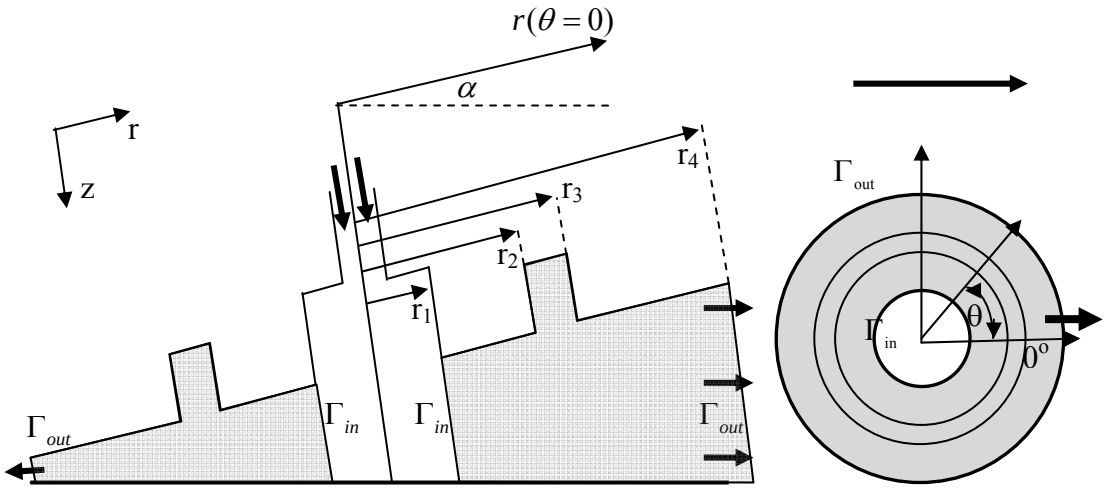

Fig. 3.1 - A systematic diagram of tilt slipper.

Notice that the clearance slipper/plate is different at different points and is represented by equation (3.1); as a result the flow field below the slipper can not be considered symmetric even in static conditions. Therefore it becomes necessary to consider a 3-dimentional cylindrical computational domain.

$$H = Ho + \alpha\, r\cos(\theta) \tag{3.1}$$

Three dimensional Navier Stokes equations in cylindrical coordinates have been applied to the slipper swash plate gap which is represented by equation (3.2) along with continuity (3.3) where $\phi\{V_r, V_\theta, V_z\}$ is considered as flux vector and the value of S_ϕ is given in Table- 3.1 for different ϕ.

$$\rho\frac{\partial\phi}{\partial t}+\rho\left[\frac{1}{r}\frac{\partial}{\partial r}(r.V_r.\phi)+\frac{1}{r}\frac{\partial}{\partial\theta}(V_\theta.\phi)+\frac{\partial}{\partial z}(V_z.\phi)\right]=\mu\left[\frac{\partial}{\partial r}\left(\frac{1}{r}\frac{\partial(r.\phi)}{\partial r}\right)+\frac{1}{r^2}\frac{\partial^2\phi}{\partial\theta^2}+\frac{\partial^2\phi}{\partial z^2}\right]+S_\phi \tag{3.2}$$

$$\frac{1}{r}\frac{\partial(r.V_r)}{\partial r}+\frac{1}{r}\frac{\partial V_\theta}{\partial\theta}+\frac{\partial V_z}{\partial z}=0 \tag{3.3}$$

A no slipping boundary condition is imposed on all walls. A Direchlet type pressure boundary condition is used at the inlet and outlet, regarding the flow variables at the inlet and outlet boundaries, they are specified by zero normal derivatives at each sub iteration step, as presented in equation (3.4).

Table 3.1 – The values of S_ϕ for different ϕ

ϕ	S_ϕ
V_r	$-\frac{\partial P}{\partial r}-\frac{2\mu}{r^2}\frac{\partial V_\theta}{\partial\theta}-\frac{\mu V_r}{r^2}+\frac{V_\theta^2.\rho}{r}$
V_θ	$-\frac{1}{r}\frac{\partial P}{\partial\theta}+\frac{2\mu}{r^2}\frac{\partial V_r}{\partial\theta}-\frac{\mu V_\theta}{r^2}-\frac{\rho V_r V_\theta}{r}$
V_z	$-\frac{\partial P}{\partial z}$

$$P\big|_{\Gamma_{in}}=P_{in};\ P\big|_{\Gamma_{out}}=P_{out};\ \left.\frac{\partial(r.V_r)}{\partial r}\right|_{\Gamma_{in}\text{or }\Gamma_{out}}=0;\ \left.\frac{\partial V_\theta}{\partial r}\right|_{\Gamma_{in}\text{or }\Gamma_{out}}=0;\ V_z\big|_{\Gamma_{in}}=0;\ \left.\frac{\partial V_z}{\partial r}\right|_{\Gamma_{out}}=0; \tag{3.4}$$

3.3 Computation Method

It can be seen from figure 3.1 that domain into consideration is not orthogonal. The axes are chosen in such a way that the physical domain is orthogonal inside the groove but not outside. To implement the control volume formulation developed by Patanker [17], it is necessary to have an orthogonal control volume. , as in his method, the diffusion flux across a control volume face, it is calculated in terms of ϕ value at two consecutive grid points, it is therefore crucial that the grid face is normal to the line joining the two grid

points. As a result, there is a need to transform non orthogonal physical domain into orthogonal computational domain.

In order to implement coordinates transformation, the total domain into consideration is divided into two parts, one inside the groove (Ω_{in}) which is already orthogonal and the rest outside the groove (Ω_{out}) which is required to be transformed into orthogonal domain. Different parts of the domain are shown in to figure 3.2.

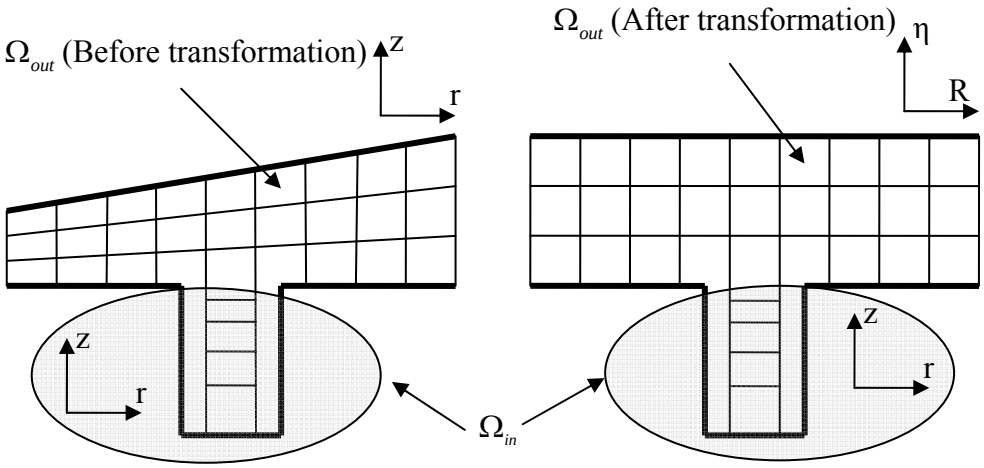

Figure 3.2 – Different domain and corresponding coordinates.

3.3.1 Coordinates transformation for domain outside the groove

For non orthogonal domain (Ω_{out}), all the equations (Navier Stokes and continuity) are needed to be transformed according to the transformation given in table 3.2 before implementing control volume formulation. The non orthogonal domain will be represented by $\Omega_p \left\{\Omega : \square^4 (r, \theta, z, t)\right\}$ namely the physical domain and the orthogonal domain will be represented by $\Omega_c \left\{\Omega : \square^4 (R, \xi, \eta, \tau)\right\}$ namely the computational domain.

Table 3.2 - $\Omega_p \left\{\Omega : \square^4 (r, \theta, z, t)\right\} \rightarrow \Omega_c \left\{\Omega : \square^4 (R, \xi, \eta, \tau)\right\}$

Physical domain.	Computational domain.
r	R
θ	ξ
z	$\dfrac{z}{(ho + \alpha\, r \cos\theta)}$
t	τ

Navier Stokes equation and continuity equations, which are represented by equations (3.2) and (3.3) on physical domain Ω_p are transformed into equations (3.5) & (3.6) on domain Ω_c. The value of source term S_ϕ corresponding to the value of ϕ is given in table 3.2. The details of the transformation are given in Appendix A1.

$$\rho\left[\frac{\partial\phi}{\partial\tau}+\frac{1}{R}\frac{\partial(RV_R\phi)}{\partial R}+\frac{1}{R}\frac{\partial(V_\xi\phi)}{\partial\xi}+\frac{1}{H}\frac{\partial(V_\eta\phi)}{\partial\eta}+\frac{\eta\alpha}{H}\left\{\sin\xi\frac{\partial(V_\xi\phi)}{\partial\eta}-\cos\xi\frac{\partial(V_R\phi)}{\partial\eta}\right\}\right]=$$
$$\mu\left[\frac{1}{R}\frac{\partial}{\partial R}\left(R\frac{\partial\phi}{\partial R}\right)+\frac{1}{R^2}\frac{\partial^2\phi}{\partial\xi^2}+\frac{1+(\eta\alpha)^2}{H^2}\frac{\partial^2\phi}{\partial\eta^2}+\frac{2\eta\alpha^2}{H^2}\frac{\partial\phi}{\partial\eta}+\frac{2\eta\alpha}{H}\left\{\frac{\sin\xi\,\partial^2\phi}{R\,\partial\xi\partial\eta}-\frac{\cos\xi\,\partial^2\phi}{\partial R\partial\eta}\right\}\right] \tag{3.5}$$

$$\left[\frac{1}{R}\frac{\partial(RV_R)}{\partial R}-\frac{\eta\alpha\cos\xi}{H}\frac{\partial V_R}{\partial\eta}\right]+\left[\frac{1}{R}\frac{\partial V_\xi}{\partial\xi}+\frac{\eta\alpha\sin\xi}{H}\frac{\partial V_\xi}{\partial\eta}\right]+\frac{1}{H}\frac{\partial V_\eta}{\partial\eta}=0 \tag{3.6}$$

Table 3.2 – Value of S_ϕ for different ϕ in computational domain Ω_c.

ϕ	S_ϕ
V_R	$\left[-\frac{\partial P}{\partial R}+\frac{\eta\alpha\cos\xi}{H}\frac{\partial P}{\partial\eta}\right]-\frac{\mu V_R}{R^2}+\frac{\rho V_\xi^2}{R}-\frac{2\mu}{R^2}\frac{\partial V_\xi}{\partial\xi}-\frac{2\mu\eta\alpha\,\sin\xi}{RH}\frac{\partial V_\xi}{\partial\eta}$
V_ξ	$\left[-\frac{1}{R}\frac{\partial P}{\partial\xi}-\frac{\eta\alpha\sin\xi}{H}\frac{\partial P}{\partial\eta}\right]-\frac{\mu V_\xi}{R^2}-\frac{\rho V_R V_\xi}{R}+\frac{2\mu}{R^2}\frac{\partial V_R}{\partial\xi}+\frac{2\mu\eta\alpha\sin\xi}{RH}\frac{\partial V_R}{\partial\eta}$
V_η	$-\frac{1}{H}\frac{\partial P}{\partial\eta}$

3.3.2 Source Term Linearization.

A detailed description of source term linearization can be found in section 2.2. The similar concept of negative gradient is applied while linearizing the source terms presented in table 3.2 and corresponding values of $S_{\phi.C}$ and $S_{\phi.P}$ are given into table 3.3.

Table 3.3 - $S_{\phi.C}$ and $S_{\phi.P}$ for different ϕ

ϕ	$S_{\phi.C}$	$S_{\phi.P}$
V_r	$\left[-\frac{\partial P}{\partial R}+\frac{\eta\alpha\cos\xi}{H}\frac{\partial P}{\partial\eta}\right]+\frac{\rho V_\xi^2}{R}-\frac{2\mu}{R^2}\frac{\partial V_\xi}{\partial\xi}-\frac{2\mu\eta\alpha\,\sin\xi}{RH}\frac{\partial V_\xi}{\partial\eta}$	$-\frac{\mu}{R^2}$
V_θ	$\left[-\frac{1}{R}\frac{\partial P}{\partial\xi}-\frac{\eta\alpha\sin\xi}{H}\frac{\partial P}{\partial\eta}\right]+\frac{2\mu}{R^2}\frac{\partial V_R}{\partial\xi}+\frac{2\mu\eta\alpha\sin\xi}{RH}\frac{\partial V_R}{\partial\eta}-\frac{\rho V_\xi}{R}\max[-V_R,0]$	$-\frac{\mu}{R^2}-\frac{\rho}{R}\max[V_R,0]$
V_z	$-\frac{1}{H}\frac{\partial P}{\partial\eta}$	0

3.3.3 Discritization of generalized momentum equation

As described earlier, for better understanding of the flow phenomena and to implement the computational technique more precisely, NVS equation is divided into combination of different terms, Transient term, Convection term (T_1), Diffusion term (T_2) and Source term (S). As a result of this treatment, now different time steps can be used for each different term to attain more accuracy according to the requirement of the flow condition.

In the present work, the transient term is treated by implicit scheme for faster convergence; an upwind scheme is implemented for the convection term to maintain the positivity of the coefficients, central difference scheme is implemented for the diffusion term and the source term is treated by implicit scheme. Convection and diffusion terms are represented by equation (3.7) and (3.8).

$$T_1 = \rho\left[\frac{1}{R}\frac{\partial\left(RV_R\phi\right)}{\partial R}+\frac{1}{R}\frac{\partial\left(V_\xi\phi\right)}{\partial\xi}+\frac{1}{H}\frac{\partial\left(V_\eta\phi\right)}{\partial\eta}+\frac{\eta\alpha}{H}\left\{\sin\xi\frac{\partial\left(V_\xi\phi\right)}{\partial\eta}-\cos\xi\frac{\partial\left(V_R\phi\right)}{\partial\eta}\right\}\right] \tag{3.7}$$

$$T_2 = \mu\left[\frac{1}{R}\frac{\partial}{\partial R}\left(R\frac{\partial\phi}{\partial R}\right)+\frac{1}{R^2}\frac{\partial^2\phi}{\partial\xi^2}+\frac{1+(\eta\alpha)^2}{H^2}\frac{\partial^2\phi}{\partial\eta^2}+\frac{2\eta\alpha^2}{H^2}\frac{\partial\phi}{\partial\eta}+\frac{2\eta\alpha}{H}\left\{\frac{\sin\xi\,\partial^2\phi}{R\,\partial\xi\partial\eta}-\frac{\cos\xi\,\partial^2\phi}{\partial R\partial\eta}\right\}\right] \tag{3.8}$$

Different terms of equation (3.5) are discretized by control volume formulation over a staggered grid as described above. The final discrete equation can be written in the form of equation (3.9) and its coefficients are given by equations (3.10) to (3.33).

$$\frac{a_p}{\alpha_v}\Phi_p^* = \sum_{nb} a_{nb}\Phi_{nb}^* + b_\Phi + \frac{(1-\alpha_v)}{\alpha_v}a_{\phi.p}\Phi_{p.old}^* \tag{3.9}$$

Where:

$$C_1 = \frac{\rho\,\eta_P\,\alpha\,R_P\,\Delta\xi\,\Delta R}{2} \tag{3.10}$$

$$F_e = \rho\,R_e\,V_e^R\,H_P\,\Delta\xi\,\Delta\eta \qquad D_e = \frac{\mu\,R_e\,H_P\,\Delta\xi\,\Delta\eta}{\Delta R} \tag{3.11}$$

$$a_E = D_e + \max\left(-F_e, 0\right) + C_1\left[\max\left(\cos\xi, 0\right)\max\left(-V_b^R, 0\right) + \max\left(-\cos\xi, 0\right)\max\left(-V_t^R, 0\right)\right] \tag{3.12}$$

$$F_w = \rho R_w V_w^R H_P \Delta\xi \Delta\eta \qquad D_w = \frac{\mu R_w H_P \Delta\xi \Delta\eta}{\Delta R} \tag{3.13}$$

$$a_W = D_w + \max(F_w, 0) + C_1\left[\max(-\cos\xi, 0)\max(V_b^R, 0) + \max(\cos\xi, 0)\max(V_t^R, 0)\right] \tag{3.14}$$

$$F_n = \rho V_n^\xi H_P \Delta R \Delta\eta \qquad D_n = \frac{\mu H_P \Delta R \Delta\eta}{R_P \Delta\xi} \tag{3.15}$$

$$a_N = D_n + \max(-F_n, 0) + C_1\left[\max(\sin\xi, 0)\max(-V_t^\xi, 0) + \max(-\sin\xi, 0)\max(-V_b^\xi, 0)\right] \tag{3.16}$$

$$F_s = \rho V_s^\xi H_P \Delta R \Delta\eta \qquad D_s = \frac{\mu H_P \Delta R \Delta\eta}{R_P \Delta\xi} \tag{3.17}$$

$$a_S = D_s + \max(F_s, 0) + C_1\left[\max(-\sin\xi, 0)\max(V_t^\xi, 0) + \max(\sin\xi, 0)\max(V_b^\xi, 0)\right] \tag{3.18}$$

$$D_t = D_b = \frac{\mu \Delta R R_P \Delta\xi}{H_P \Delta\eta} \qquad F_t = \rho V_t^\eta \Delta R R_P \Delta\xi \qquad F_b = \rho V_b^\eta \Delta R R_P \Delta\xi \tag{3.19}$$

$$a_T = D_t\left[1 + (\eta_t \alpha)^2\right] + \max(-F_t, 0) \tag{3.20}$$

$$a_B = D_b\left[1 + (\eta_b \alpha)^2\right] + \max(F_b, 0) \tag{3.21}$$

$$C_2 = \frac{\mu \eta_P \alpha R_P}{2} \tag{3.22}$$

$$a_{ET} = C_1 \max(-\cos\xi, 0)\max(-V_t^R, 0) - C_2 \cos\xi R \Delta\xi \tag{3.23}$$

$$a_{WT} = C_1 \max(\cos\xi, 0)\max(V_t^R, 0) + C_2 \cos\xi R \Delta\xi \tag{3.24}$$

$$a_{NT} = C_1 \max(\sin\xi, 0)\max(-V_t^\xi, 0) + C_2 \sin\xi \Delta R \tag{3.25}$$

$$a_{ST} = C_1 \max(-\sin\xi, 0)\max(V_t^\xi, 0) - C_2 \sin\xi \Delta R \tag{3.26}$$

$$a_{EB} = C_1 \max(\cos\xi, 0) \max\left(-V_b^R, 0\right) + C_2 \cos\xi \, R \, \Delta\xi \tag{3.27}$$

$$a_{WB} = C_1 \max\left(-\cos\xi, 0\right) \max\left(V_b^R, 0\right) - C_2 \cos\xi \, R \, \Delta\xi \tag{3.28}$$

$$a_{NB} = C_1 \max\left(-\sin\xi, 0\right) \max\left(-V_b^\xi, 0\right) - C_2 \sin\xi \, \Delta R \tag{3.29}$$

$$a_{SB} = C_1 \max(\sin\xi, 0) \max\left(V_b^\xi, 0\right) + C_2 \sin\xi \, \Delta R \tag{3.30}$$

$$a_P^o = \frac{\rho \, R_p \, \Delta\xi \, \Delta R \, \Delta\eta}{\Delta\tau} \tag{3.31}$$

$$b_\Phi = a_P^o \, \Phi_{p.old}^* + S_{\Phi.C} \, R_p \, \Delta\xi \, \Delta R \, \Delta\eta \tag{3.32}$$

$$a_P = \sum_{nb} a_{nb} + a_P^o - S_{\Phi.P} \, R_p \, \Delta\theta \, \Delta r \, \Delta z \tag{3.33}$$

It can be noticed that in equation (3.9), a under relaxation factor α_v is implemented to attain convergence.

3.3.4 Different momentum equations

Different momentum equations can be obtained from general momentum equation (3.9) for different values of ϕ as represented in equations (3.34, 35 and 36).

$$a^r_{i,j,k} V^{R*}_{i,j,k} = \sum_{nb} a_{nb} V^{R*}_{nb} + R_{m(i)} \Delta\xi \left[\left(P^*_{i,j,k} - P^*_{i+1,j,k} \right) H^R_{i,j} \Delta\eta + \frac{\eta_k \alpha \cos\xi_j \Delta R}{4} \left(P^*_{i,j,k+1} + P^*_{i+1,j,k+1} - P^*_{i,j,k-1} - P^*_{i+1,j,k-1} \right) \right] \tag{3.34}$$

$$a^\xi_{i,j,k} V^{\xi*}_{i,j,k} = \sum_{nb} a_{nb} V^{\xi*}_{nb} + \Delta R \left[\left(P^*_{i,j,k} - P^*_{i,j+1,k} \right) H^\xi_{i,j} \Delta\eta - \frac{\eta_k \alpha \sin\xi^m_j \Delta\xi}{4} \left(P^*_{i,j,k+1} + P^*_{i,j+1,k+1} - P^*_{i,j,k-1} - P^*_{i,j+1,k-1} \right) \right] \tag{3.35}$$

$$a^\eta_{i,j,k} V^{\eta*}_{i,j,k} = \sum_{nb} a_{nb} V^{\eta*}_{nb} + \left(P^*_{i,j,k+1} - P^*_{i,j,k} \right) R_i \Delta\xi \Delta R \tag{3.36}$$

3.3.5 Pressure and velocity correction

The momentum equation can be solved only when the pressure field is given or is somehow estimated. Unless the correct pressure is employed, the resulting velocity will

not satisfy the continuity equation. Therefore an improvement in guess pressure (P^*) is required which is denoted by P^c and is implemented in equation (3.37).

$$P = P^* + P^c \tag{3.37}$$

To estimate the change in behavior of velocity due this pressure correction, corresponding velocity correction can be introduced in the similar manner, as represented in equation (3.38).

$$V^{\phi} = V^{\phi.*} + V^{\phi.c} \tag{3.38}$$

By implementing these corrections into the momentum equations (3.34-36), equations for corrected velocities are developed. While developing these equations the term $\sum_{nb} a_{nb} V^c_{nb}$ is drooped to avoid coupling of all grid points while implementing these velocities into continuity equation. Equations (3.39-41) represent the corrected velocity formulas.

$$V^R_{i,j,k} = V^{R*}_{i,j,k} + \frac{R_{m(i)}\Delta\xi}{a^r_{i,j,k}}\left[\left(P^c_{i,j,k} - P^c_{i+1,j,k}\right)H^R_{i,j}\Delta\eta + \frac{\eta_k \alpha \cos\xi_j \Delta R}{4}\left(P^c_{i,j,k+1} + P^c_{i+1,j,k+1} - P^c_{i,j,k-1} - P^c_{i+1,j,k-1}\right)\right] \tag{3.39}$$

$$V^{\xi}_{i,j,k} = V^{\xi*}_{i,j,k} + \frac{\Delta R}{a^{\xi}_{i,j,k}}\left[\left(P^c_{i,j,k} - P^c_{i,j+1,k}\right)H^{\xi}_{i,j}\Delta\eta - \frac{\eta_k \alpha \sin\xi^m_j \Delta\xi}{4}\left(P^c_{i,j,k+1} + P^c_{i,j+1,k+1} - P^c_{i,j,k-1} - P^c_{i,j+1,k-1}\right)\right] \tag{3.40}$$

$$V^{\eta}_{i,j,k} = V^{\eta*}_{i,j,k} + \frac{R_i \Delta\xi \Delta R}{a^{\eta}_{i,j,k}}\left(P^c_{i,j,k+1} - P^c_{i,j,k}\right) \tag{3.41}$$

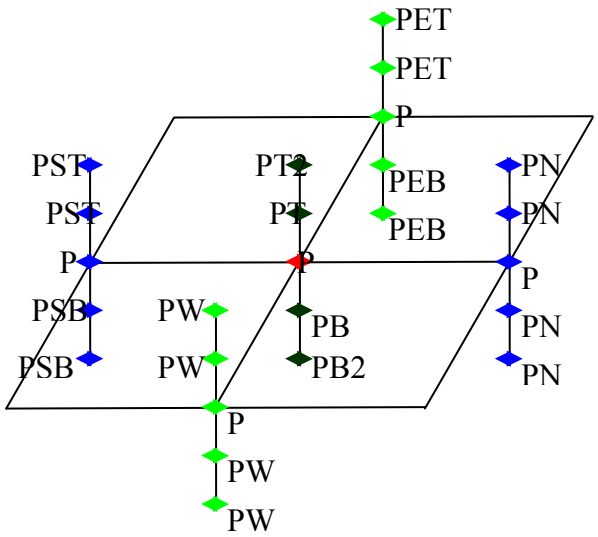

Figure 3.3 – Nomenclature of Pressure correction neighbor points.

These velocities are implemented into the continuity equation (3.5) to obtain the pressure correction formula. Equation (3.42) represents the discrete continuity equation in terms of

pressure correction. It can be noticed from equation (3.42) that pressure correction at one point depends upon 24 neighbor points. Nomenclature of these 24 neighbor points is represented by figure 3.3.

$$
\begin{aligned}
&\left[H_{i,j}\Delta\xi\Delta\eta \left(\frac{R_{m(i)}^2 \Delta\xi}{arp_{i,j,k}} \left\{ \left(P^c_{i,j,k} - P^c_{i+1,j,k} \right) H^R_{i,j} \Delta\eta + \frac{\left(P^c_{i,j,k+1} + P^c_{i+1,j,k+1} - P^c_{i,j,k-1} - P^c_{i+1,j,k-1} \right)}{4} \eta_k \alpha \cos\xi_j \Delta R \right\} \right.\right. \\
&\left.\left. - \frac{R_{m(i-1)}^2 \Delta\xi}{arp_{i-1,j,k}} \left\{ \left(P^c_{i-1,j,k} - P^c_{i,j,k} \right) H^R_{i-1,j} \Delta\eta + \frac{\left(P^c_{i-1,j,k+1} + P^c_{i,j,k+1} - P^c_{i-1,j,k-1} - P^c_{i,j,k-1} \right)}{4} \eta_k \alpha \cos\xi_j \Delta R \right\} \right) \right] \\
&- \frac{R_i \cos\xi_j \Delta R (\Delta\xi)^2 \eta_k \alpha}{4} \left(\begin{array}{l}
\left(P^c_{i,j,k+1} - P^c_{i+1,j,k+1} \right) \dfrac{H^R_{i,j} R_{m(i)} \Delta\eta}{arp_{i,j,k+1}} + \dfrac{\eta_{k+1} \alpha \cos\xi_j R_{m(i)} \Delta R}{arp_{(i,j,k+1)}} \dfrac{\left(P^c_{i,j,k+2} + P^c_{i+1,j,k+2} - P^c_{i,j,k} - P^c_{i+1,j,k} \right)}{4} \\
\left(P^c_{i-1,j,k+1} - P^c_{i,j,k+1} \right) \dfrac{H^R_{i-1,j} R_{m(i-1)} \Delta\eta}{arp_{i-1,j,k+1}} + \dfrac{\eta_{k+1} \alpha \cos\xi_j R_{m(i-1)} \Delta R}{arp_{(i-1,j,k+1)}} \dfrac{\left(P^c_{i-1,j,k+2} + P^c_{i,j,k+2} - P^c_{i-1,j,k} - P^c_{i,j,k} \right)}{4} \\
\left(P^c_{i+1,j,k-1} - P^c_{i,j,k-1} \right) \dfrac{H^R_{i,j} R_{m(i)} \Delta\eta}{arp_{i,j,k-1}} - \dfrac{\eta_{k-1} \alpha \cos\xi_j R_{m(i)} \Delta R}{arp_{(i,j,k-1)}} \dfrac{\left(P^c_{i,j,k} + P^c_{i+1,j,k} - P^c_{i,j,k-2} - P^c_{i+1,j,k-2} \right)}{4} \\
\left(P^c_{i,j,k-1} - P^c_{i-1,j,k-1} \right) \dfrac{H^R_{i-1,j} R_{m(i-1)} \Delta\eta}{arp_{i-1,j,k-1}} - \dfrac{\eta_{k-1} \alpha \cos\xi_j R_{m(i-1)} \Delta R}{arp_{(i-1,j,k-1)}} \dfrac{\left(P^c_{i-1,j,k} + P^c_{i,j,k} - P^c_{i-1,j,k-2} - P^c_{i,j,k-2} \right)}{4}
\end{array} \right) \\
&+ \left[H_{i,j}\Delta R\Delta\eta \left(\left\langle \left(P^c_{i,j,k} - P^c_{i,j+1,k} \right) \frac{H^\xi_{i,j} \Delta R\Delta\eta}{ayp_{i,j,k}} + \frac{\eta_k \alpha \sin\xi^m_j R_i \Delta R\Delta\xi}{ayp_{i,j,k}} \left(\frac{P^c_{i,j,k-1} + P^c_{i,j+1,k-1} - P^c_{i,j,k+1} - P^c_{i,j+1,k+1}}{4} \right) \right\rangle \right.\right. \\
&\left.\left. - \left\langle \left(P^c_{i,j-1,k} - P^c_{i,j,k} \right) \frac{H^\xi_{i,j-1} \Delta R\Delta\eta}{ayp_{i,j-1,k}} + \frac{\eta_k \alpha \sin\xi^m_{j-1} R_i \Delta R\Delta\xi}{ayp_{i,j-1,k}} \left(\frac{P^c_{i,j-1,k-1} + P^c_{i,j,k-1} - P^c_{i,j-1,k+1} - P^c_{i,j,k+1}}{4} \right) \right\rangle \right) \right] \\
&+ \frac{R_i \Delta R\Delta\xi \eta_k \alpha \sin\xi_j}{4} \left(\begin{array}{l}
\left(P^c_{i,j,k+1} - P^c_{i,j+1,k+1} \right) \dfrac{H^\xi_{i,j} \Delta R\Delta\eta}{ayp_{(i,j,k+1)}} + \dfrac{\eta_{k+1} \alpha \sin\xi^m_j R_i \Delta R\Delta\xi}{ayp_{(i,j,k+1)}} \dfrac{P^c_{i,j,k} + P^c_{i,j+1,k} - P^c_{i,j,k+2} - P^c_{i,j+1,k+2}}{4} \\
\left(P^c_{i,j-1,k+1} - P^c_{i,j,k+1} \right) \dfrac{H^\xi_{i,j-1} \Delta R\Delta\eta}{ayp_{(i,j-1,k+1)}} + \dfrac{\eta_{k+1} \alpha \sin\xi^m_{j-1} R_i \Delta R\Delta\xi}{ayp_{(i,j-1,k+1)}} \dfrac{P^c_{i,j-1,k} + P^c_{i,j,k} - P^c_{i,j-1,k+2} - P^c_{i,j,k+2}}{4} \\
\left(P^c_{i,j+1,k-1} - P^c_{i,j,k-1} \right) \dfrac{H^\xi_{i,j} \Delta R\Delta\eta}{ayp_{(i,j,k-1)}} - \dfrac{\eta_{k-1} \alpha \sin\xi^m_j R_i \Delta R\Delta\xi}{ayp_{(i,j,k-1)}} \dfrac{P^c_{i,j,k-2} + P^c_{i,j+1,k-2} - P^c_{i,j,k} - P^c_{i,j+1,k}}{4} \\
\left(P^c_{i,j,k-1} - P^c_{i,j-1,k-1} \right) \dfrac{H^\xi_{i,j-1} \Delta R\Delta\eta}{ayp_{(i,j-1,k-1)}} - \dfrac{\eta_{k-1} \alpha \sin\xi^m_{j-1} R_i \Delta R\Delta\xi}{ayp_{(i,j-1,k-1)}} \dfrac{P^c_{i,j-1,k-2} + P^c_{i,j,k-2} - P^c_{i,j-1,k} - P^c_{i,j,k}}{4}
\end{array} \right) \\
&+ \left[\left(\frac{P^c_{i,j,k}}{azp_{(i,j,k+1)}} + \frac{P^c_{i,j,k}}{azp_{(i,j,k-1)}} - \frac{P^c_{i,j,k+1}}{azp_{(i,j,k+1)}} - \frac{P^c_{i,j,k-1}}{azp_{(i,j,k-1)}} \right) \left(R_i \Delta R\Delta\xi \right)^2 \right] + M_B = 0
\end{aligned}
\tag{3.42}
$$

The final pressure correction equation can be written in the form of equation (3.43) and its coefficients are given by equations (3.44-68).

$$A_p P_p^c = \sum_{nb} A_{nb} P_{nb}^c + B_p \tag{3.43}$$

Where,

$$A_{PET2} = \frac{\eta_{k+1}\eta_k R_{m(i)} R_i \left(\alpha \cos\xi_j \Delta R \Delta\xi\right)^2}{16\, arp_{(i,j,k+1)}} \tag{3.44}$$

$$A_{PEB2} = \frac{\eta_{k-1}\eta_k R_{m(i)} R_i \left(\alpha \cos\xi_j \Delta R \Delta\xi\right)^2}{16\, arp_{(i,j,k-1)}} \tag{3.45}$$

$$A_{PE} = \frac{H_{i,j} R^2_{m(i)} \Delta\eta \left(\Delta\xi\right)^2}{arp_{i,j,k}} - \left(A_{PET2} + A_{PEB2}\right) \tag{3.46}$$

$$A_{PWT2} = \frac{\eta_{k+1}\eta_k R_{m(i-1)} R_i \left(\alpha \cos\xi_j \Delta R \Delta\xi\right)^2}{16\, arp_{(i-1,j,k+1)}} \tag{3.47}$$

$$A_{PWB2} = \frac{\eta_{k-1}\eta_k R_{m(i-1)} R_i \left(\alpha \cos\xi_j \Delta R \Delta\xi\right)^2}{16\, arp_{(i-1,j,k-1)}} \tag{3.48}$$

$$A_{PW} = \frac{H_{i,j} R^2_{m(i-1)} \Delta\eta \left(\Delta\xi\right)^2}{arp_{i-1,j,k}} - \left(A_{PWT2} + A_{PWB2}\right) \tag{3.49}$$

$$A_{PNT2} = \frac{\eta_{k+1}\eta_k \sin\xi^m_j \sin\xi_j \left(\alpha R_i \Delta R \Delta\xi\right)^2}{16\, ayp_{(i,j,k+1)}} \tag{3.50}$$

$$A_{PNB2} = \frac{\eta_{k-1}\eta_k \sin\xi^m_j \sin\xi_j \left(\alpha R_i \Delta R \Delta\xi\right)^2}{16\, ayp_{(i,j,k-1)}} \tag{3.51}$$

$$A_{PN} = \frac{H^{\xi}_{i,j} H_{i,j} \left(\Delta R \Delta\eta\right)^2}{ayp_{i,j,k}} - \left(A_{PNT2} + A_{PNB2}\right) \tag{3.52}$$

$$A_{PST2} = \frac{\eta_{k+1}\eta_k \sin\xi^m_{j-1} \sin\xi_j \left(\alpha R_i \Delta R \Delta\xi\right)^2}{16\, ayp_{(i,j-1,k+1)}} \tag{3.53}$$

$$A_{PSB2} = \frac{\eta_{k-1}\eta_k \sin\xi^m_{j-1} \sin\xi_j \left(\alpha R_i \Delta R \Delta\xi\right)^2}{16\, H_{i,j}\, ayp_{(i,j-1,k-1)}} \tag{3.54}$$

$$A_{PS} = \frac{H^{\xi}_{i,j-1} H_{i,j} \left(\Delta R \Delta \eta\right)^2}{ayp_{i,j-1,k}} - \left(A_{PST2} + A_{PSB2}\right) \tag{3.55}$$

$$A_{PT2} = A_{PET2} + A_{PWT2} + A_{PNT2} + A_{PST2} \tag{3.56}$$

$$A_{PB2} = A_{PEB2} + A_{PWB2} + A_{PNB2} + A_{PSB2} \tag{3.57}$$

$$A_{PEB} = \frac{\eta_k \alpha \, \Delta R \, \Delta \eta \cos\xi_j \left(\Delta \xi\right)^2}{4} \left(\frac{H_{i,j} R^2_{m(i)}}{arp_{i,j,k}} + \frac{H^{R}_{i,j} R_{m(i)} R_i}{arp_{i,j,k-1}} \right) \tag{3.58}$$

$$A_{PET} = -A_{PEB} \tag{3.59}$$

$$A_{PWB} = -\frac{\eta_k \alpha \, \Delta R \, \Delta \eta \cos\xi_j \left(\Delta \xi\right)^2}{4} \left(\frac{H_{i,j} R^2_{m(i-1)}}{arp_{i-1,j,k}} + \frac{H^{R}_{i-1,j} R_{m(i-1)} R_i}{arp_{i-1,j,k-1}} \right) \tag{3.60}$$

$$A_{PWT} = -A_{PWB} \tag{3.61}$$

$$A_{PNT} = \frac{\eta_k \alpha R_i \, \Delta \xi \, \Delta \eta \left(\Delta R\right)^2}{4} \left(\frac{\sin\xi^{m}_{j} H_{i,j}}{ayp_{i,j,k}} + \frac{\sin\xi_j H^{\xi}_{i,j}}{ayp_{(i,j,k+1)}} \right) \tag{3.62}$$

$$A_{PNB} = -A_{PNT} \tag{3.63}$$

$$A_{PST} = -\frac{\eta_k \alpha R_i \, \Delta \xi \, \Delta \eta \left(\Delta R\right)^2}{4} \left(\frac{\sin\xi^{m}_{j-1} H_{i,j}}{ayp_{i,j-1,k}} + \frac{\sin\xi_j H^{\xi}_{i,j-1}}{ayp_{(i,j-1,k+1)}} \right) \tag{3.64}$$

$$A_{PSB} = -A_{PST} \tag{3.65}$$

$$A_{PT} = \frac{\eta_k \alpha \cos\xi_j \Delta R \Delta \eta \left(\Delta \xi\right)^2}{4} \left[H_{i,j} \left(\frac{R^2_{m(i-1)}}{arp_{i-1,j,k}} - \frac{R^2_{m(i)}}{arp_{i,j,k}} \right) + R_i \left(\frac{H^{R}_{i,j} R_{m(i)}}{arp_{i,j,k+1}} - \frac{H^{R}_{i-1,j} R_{m(i-1)}}{arp_{i-1,j,k+1}} \right) \right]$$
$$+ \frac{\eta_k \alpha R_i \left(\Delta R\right)^2 \Delta \eta \Delta \xi}{4} \left[H_{i,j} \left(\frac{\sin\xi^{m}_{j}}{ayp_{i,j,k}} - \frac{\sin\xi^{m}_{j-1}}{ayp_{i,j-1,k}} \right) + \sin\xi_j \left(\frac{H^{\xi}_{i,j-1}}{ayp_{(i,j-1,k+1)}} - \frac{H^{\xi}_{i,j}}{ayp_{(i,j,k+1)}} \right) \right] + \frac{\left(R_i \Delta R \Delta \xi\right)^2}{azp_{(i,j,k+1)}} \tag{3.66}$$

$$A_{PB} = -A_{PT} + \frac{\left(R_i \Delta R \Delta \xi\right)^2}{azp_{(i,j,k+1)}} + \frac{\left(R_i \Delta R \Delta \xi\right)^2}{azp_{(i,j,k-1)}} \tag{3.67}$$

$$A_P = \sum_{nb} A_{nb} \tag{3.68}$$

3.3.6 Final implementation.

It can be seen from figure 3.2 that we have two different types of computational domains for inside and out side the groove. The computational domain inside the groove is already orthogonal and no further transformation is required. As a result equations (2.1 & 2.2) are applied for it and a similar technique described in chapter 2 is implemented for control volume formulation. On the other hand, physical domain outside the groove is non orthogonal, the equivalent orthogonal computational domain has to be obtained via axis transformation, as given in table3.2. The transformed equations (3.2 & 3.3) has to be applied for computation domain and the technique described in section (3.3 to 3.6) is used for control volume formulation.

It can be noticed that in both of these cases second order accuracy has been maintained throughout the formulation. An under relaxation technique has been implemented while solving momentum and pressure correction equations. A value of 0.1 has been used as under relaxation factor in each of the momentum equations. For pressure correction, a very low value of under relaxation factor (0.01) is used to achieve convergence at the beginning of the simulation. After a few iterations, the rapidly varying component of error becomes negligible and error becomes a smooth function of spatial coordinates, therefore the value of under relaxation factor is updated to 0.05 to increase the rate of convergence.

Residue of momentum equations, residue of continuity and the value of pressure correction have been used as convergence parameters. By using the simulation program which is developed according to the above specified instructions, first, several numerical test were performed at different grid sizes to ensure the grid independence of the solution. Pressure distribution, force, torque and leakage were tested for a set of different pressure boundary conditions (from 3 to 10 MPa), different clearances (15, 20, 25 and 30 microns) and for a set of tilts (from 0^o to 0.042^o). For two different tilts, 0.03 and 0.02 degrees and a central clearance of 20 μm, the effect of groove dimensions and positions have been analyzed and compared with the flat slipper case [16]. Computational results were compared with experimental ones, showing a good agreement. Slipper dimensions are to be found in section 4.

3.4. Results static

3.4.1. Grid Independency test

As stated previously, in the present simulation a staggered grid is used. The grid size in r and θ direction is uniform but a logarithmic grid is used inside the groove in z direction, the grid is very fine near the groove edge and size increases towards groove bottom. Figure 3.4 represent 2-D stream line plots inside the groove at 180^o angular position

(slipper trailing edge), two different grid sizes with ($25\times60\times60$ and $30\times72\times80$) grid points inside the groove were used, an inlet pressure of 5 MPa and 0.01 degree tilt were evaluated. It is clear from figure 3.4 that the solution remains the same for both grid sizes therefore $25\times60\times60$ grid size will be chosen for the rest of the simulations. The same comparison has been done at different angular positions for different tilt, obtaining identical results for the two meshes chosen.

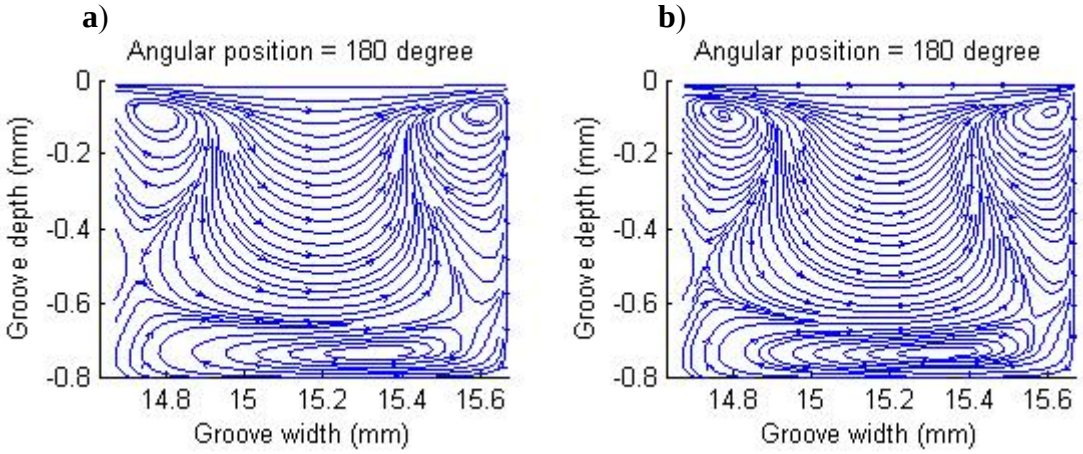

Figure 3.4 - 2-D stream lines plot inside the groove for different grid size at 5 MPa inlet pressure, 0.02 degree tilt and 30 micron central clearance. a). Groove in- [25-60-60], out-[259-60-25] b). Groove in- [30-72-80], out-[312-72-30]

3.4.2 Pressure, force and torque.

When analyzing the pressure variation under static conditions, pressure is expected to be asymmetric in angular direction due to the asymmetry created by the tilt. Although it is found (experimentally and via CFD) that the magnitude of this pressure differential in angular direction, with grooved slipper is much smaller (0.03 MPa for 10 MPa inlet pressure, 15 microns central clearance, and 0.042 degree tilt) than for slipper without groove (0.3 MPa for the same conditions). Figure 3.5 represents the pressure distribution below the slipper with and without groove at 10 MPa inlet pressure 0.042 degrees tilt, and for two different clearances (15 and 25 microns). It can be noticed from the figure 3.5 that the groove brings stability in the pressure distribution along the angular direction. The explanation of such pressure stabilization can be found while analyzing the momentum transfer inside the groove.

It is also important to be noticed from figure 3.5 that pressure distribution below the slipper it is as much affected by the slipper/plate central clearance as it is with tilt. It has also been noticed that as the central clearance increases, the effect of the tilt becomes less relevant and the slipper tends to behave like a flat slipper, the effect of tilt for a given central clearance becomes less important in the presence of a groove.

Figure 3.6 compares the average pressure inside the groove found experimentally and via CFD simulation, as a function of inlet pressure and slipper tilt. It can be noticed that the

average pressure inside the groove decreases as tilt increases, although the decrease is less than 0.4 MPa even for the highest inlet pressure and highest tilt studied. The explanation of such pattern can be understood by the fact that as tilt increases, the distortion into the flow field domain also increase then a higher momentum interchange occur inside the groove, which tends to maintain the pressure drop inside the groove rather constant. Due to the effect of shear stresses in the first slipper land, as tilt increases, the average pressure to be expected in the groove must decrease.

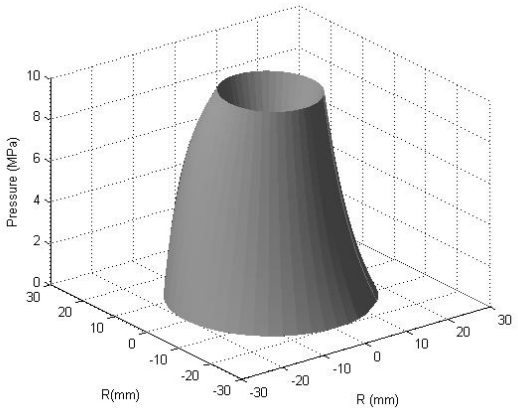

a) No groove slipper (15 microns clearance).

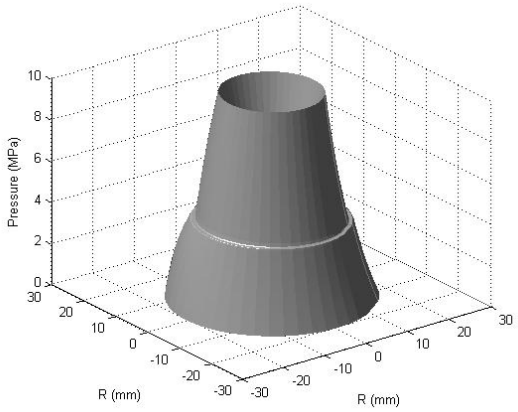

b) Groove slipper (15 microns clearance).

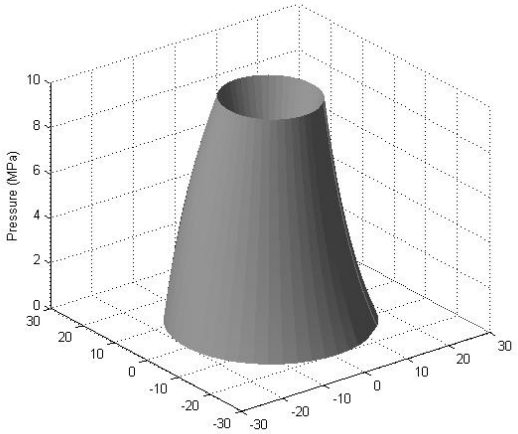

c) No groove slipper (25 microns clearance).

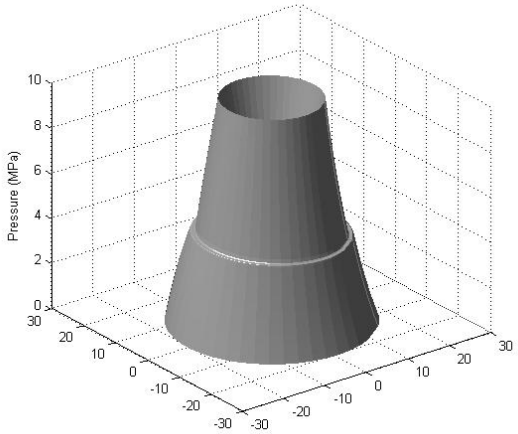

d) Groove slipper (25 microns clearance).

Figure 3.5 – Pressure three dimensional graphs at 10 MPa inlet pressure and 0.042 degrees tilt and two different central clearances, 15μm and 25μm.

Figure 3.6 shows a good agreement between experimental and simulation results, especially at low and medium slipper inlet pressure, nevertheless, such agreement decreases at high pressures. Such discrepancies are well understood when taken into account that an increase in inlet pressure leads to an increase in leakage across the slipper which means increase in shear stresses. As the NVS equations consider shear stresses for a perfectly smooth surface, but in reality the slipper and plate surfaces have some

roughness, the resulting pressure decay in slipper first land is higher in reality than the one found via CFD, especially at high inlet pressures.

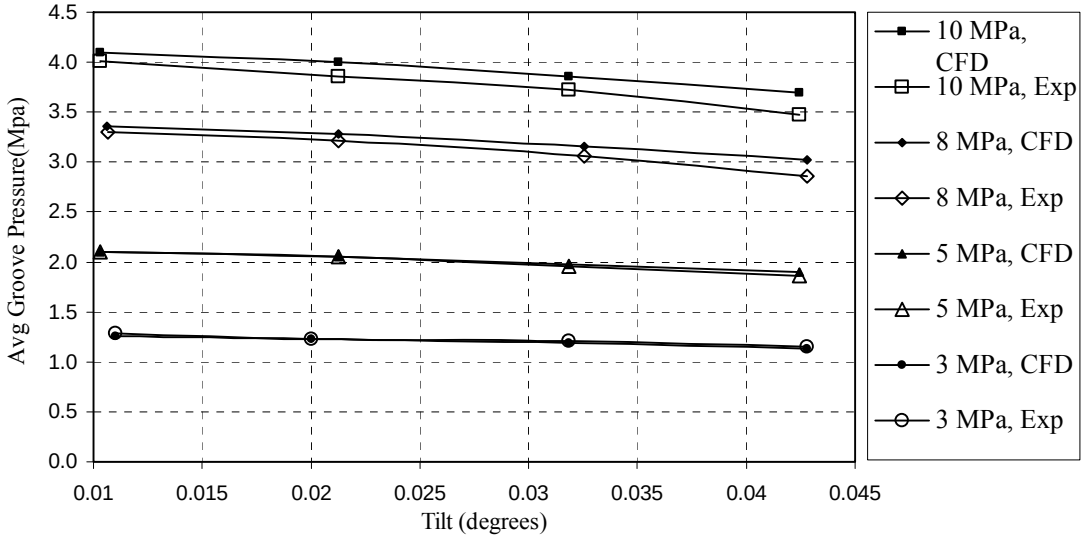

Figure 3.6 – Average groove pressure with tilt at different inlet pressure at 20 microns central clearance (Comparison between experiments and CFD).

Figure 3.7 represents the percentage decrease of the force acting perpendicular over the slipper, as a function of slipper tilt and for different inlet pressures and central clearances. The decrease in force as tilt increases can be understood by the fact that the average groove pressure decreases with tilt. For a narrow slipper/plate central clearance, the effect of tilt is more severe, so it is the decrease in force. The percentage decrease in force, it is independent of the slipper inlet pressure.

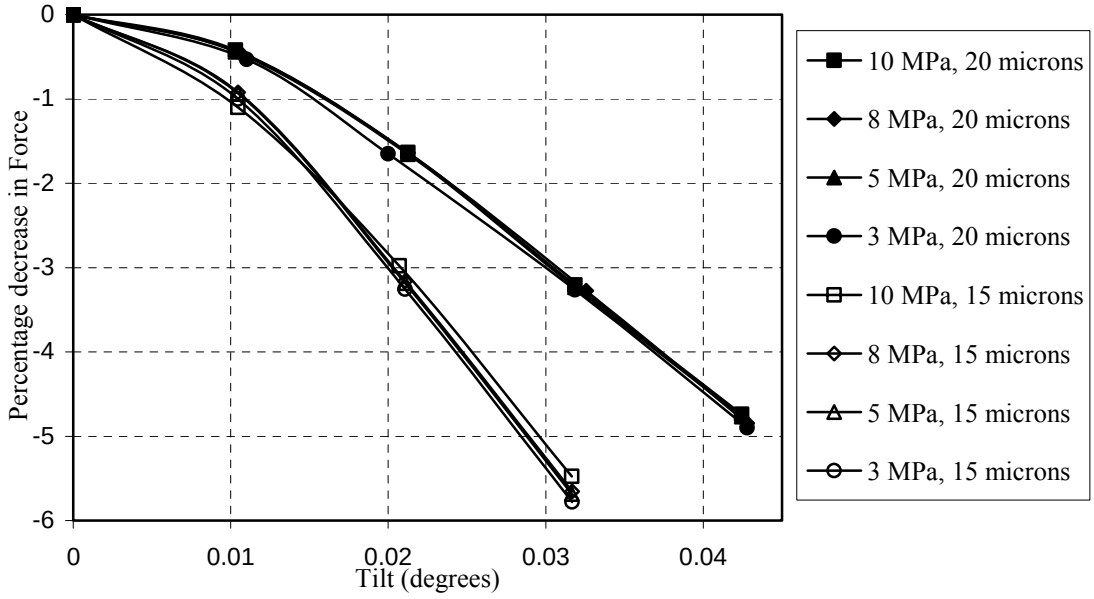

Figure 3.7 – Percentage decrease in the force with respect to non tilted slipper with tilt at different inlet pressure and central clearances.

As can be seen from figure 3.5, exist non symmetrical pressure distribution along the slipper angular position, this fact will result in the creation of a torque versus the slipper y-axis. Figure 3.8 represents the torque over the slipper y-axis as a function of tilt at different inlet pressures and clearances, this torque tends to balance the slipper tending to return it to the flat position, as previously defined by Fisher [1]. It can be noticed that the magnitude of the torque increases with the increase of tilt. The torque has a sharper increase in magnitude for higher inlet pressures and for lower clearances. In static conditions, the pressure is symmetric with respect to x-axis, therefore the torque with respect to x-axis is null.

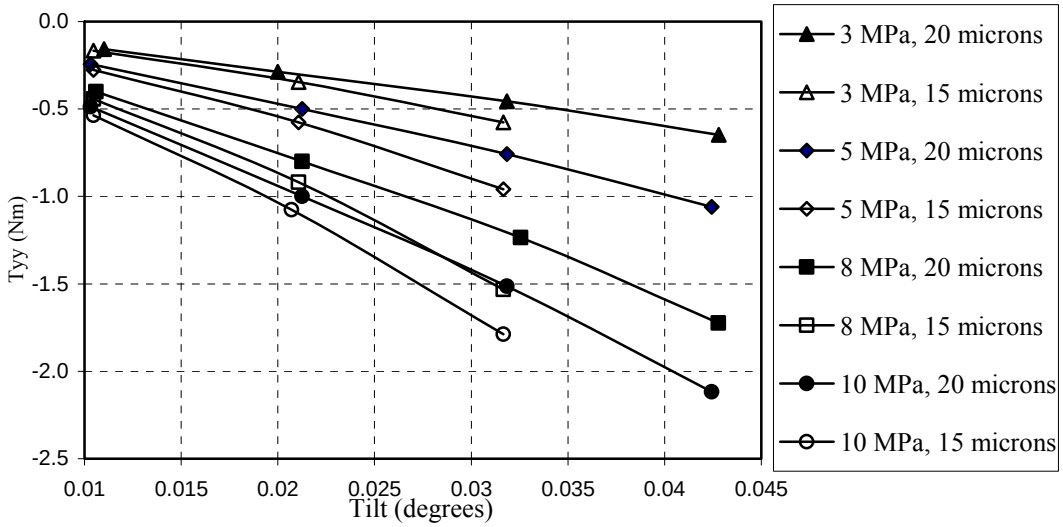

Figure 3.8 – Torque versus y-axis as a function of tilt and for different inlet pressures and central clearances, CFD results.

3.4.3 Slipper leakage.

Slipper leakage was measured experimentally by using the test rig described in chapter 7. A comparison between the leakages obtained via computer simulation and experimentally is presented under static conditions and for a set of inlet pressures and clearances in figure 3.9. While dealing with such a tiny clearance, roughness plays an important role in determining the actual slipper-plate clearance. Surface roughness measurements are already presented in chapter 2, figure 2.9 from where it is noticed that average variation in surface finish is typically 1 micron for both materials. Then the measured transducer clearance needs to be modified by the surface roughness in order to get the true clearance between slipper and plate, as defined in equation (3.69).

True clearance = Measured clearance + 2 * Average roughness of the surface (3.69)

From figure 3.9, it is noticed that leakage slightly increases with slipper tilt. The reason behind such increment can be understood when noticed that as tilt increases the overall

flow resistance created by the slipper slightly decreases. When comparing the experimental and computational results, it is seen a very good agreement.

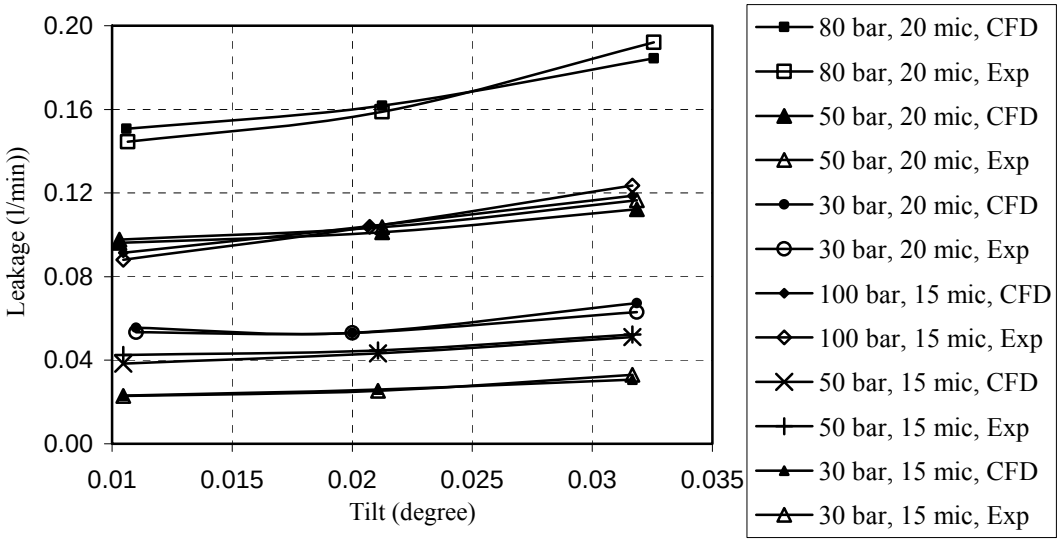

Figure 3.9 – Slipper leakage with tilt at different inlet pressure and central clearance (Comparison between CFD and experiment).

3.4.4 Effect of Groove dimensions and position.

The effect of modifying the depth of the groove and its position on the slippers has been very well explained for the slipper running parallel to the plate in chapter 2 although no evidence of such research work has been found in the literature when the slipper is running under tilted conditions. The necessity to analysing the effect of groove dimensions and position in the present chapter arises, when understanding that the groove plays a more important stabilization role under tilted conditions than when slipper is sitting flat, and in reality, slippers run tilted.

Figure 3.10 represents the variation of leakage and force versus the flat slipper case with original groove, for two groove widths and several groove positions around the slipper central diameter, tilt and no tilt conditions are also being evaluated, central clearance 20 μm. It can be noticed, when comparing tilt versus no tilt conditions that the variation pattern in leakage and forces remain quite the same, but the effect is more severe under tilted conditions. It can be stated that leakage and force decrease as the groove moves towards the slipper outer diameter. The percentage variation of leakage is much higher for tilt slippers than for flat ones, but the percentage variation in force is smaller for the tilt case than for the flat case. An increase of the groove width produces a high variation in force and leakage, then, when the groove is placed near the outer slipper diameter, the wider the groove the higher the percentage decrease in force and leakage will be. When the groove is placed near the slipper central pocked diameter, the effect on the force and leakage percentage variation is the opposite, as the groove width increases, the higher the

force and leakage increase will be. The same effect, although less relevant, was found for flat slippers with a groove in chapter 2.

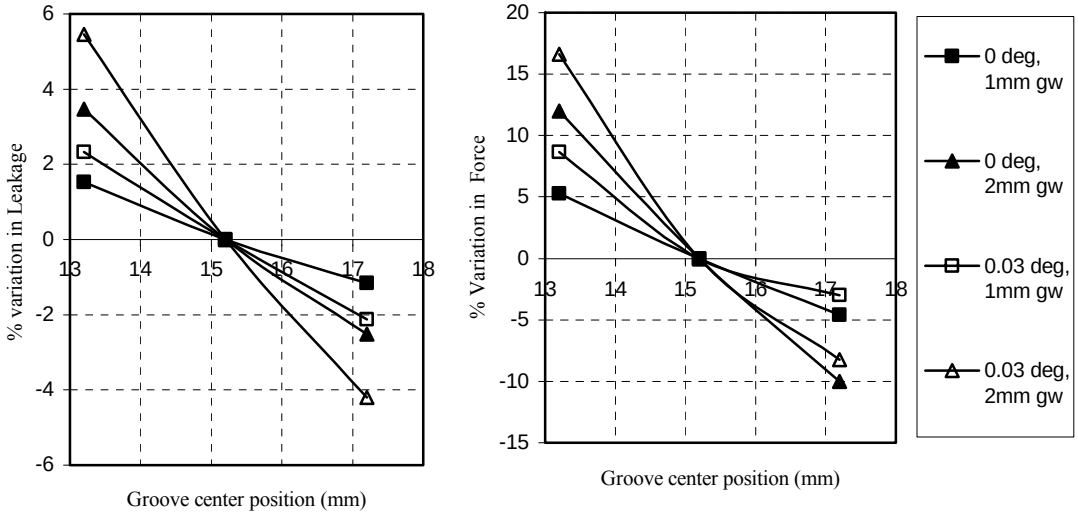

Figure 3.10 – Leakage and force variation with groove position in tilted and non tilted conditions at 1 and 2 mm groove width, versus the original groove flat position slipper at 20 microns central clearance.

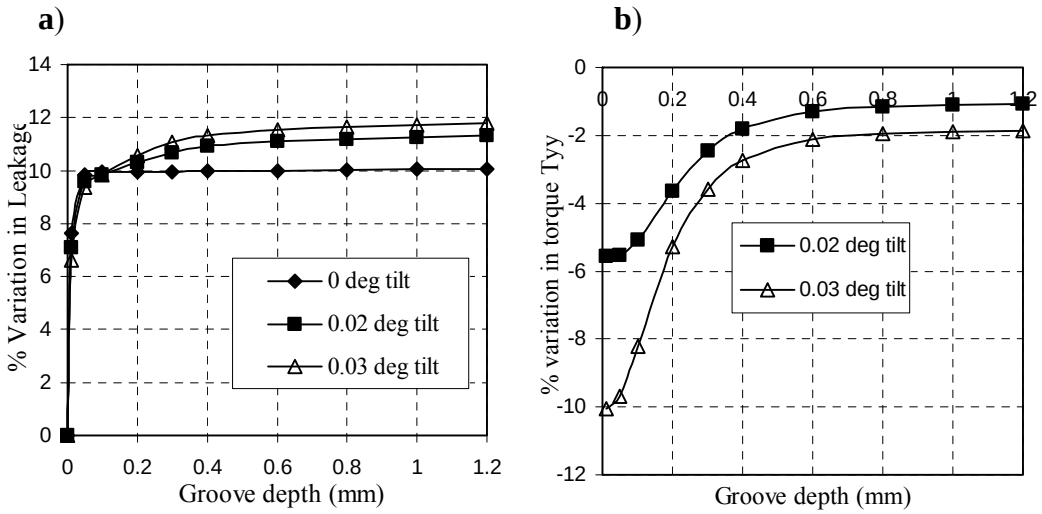

Figure 3.11 – Effect of groove depth on leakage and torque at different tilts and 20 microns central clearance. a) Percentage variation in Leakage. b) Percentage variation in y-direction torque.

Figure 3.11 a, b, presents the effect of groove depth on leakage and y-directional torque, (torque along the y axis) in percentage versus the flat slipper case, at 20 microns central clearance. It is seen that under tilted conditions, leakage increases with the increase of the

groove depth. A higher depth than for the flat case, it is required to obtain a constant leakage across the slipper, this required depth, increases with the increase of tilt, though tending to an asymptotic value, figure 3.11a. The torque acting on the slipper increases with the increase of groove depth, tending also to an asymptotic value, the higher the slipper tilt, the smaller the variation of the torque will be with the increase of groove depth. Since in fact, as tilt increases, the torque created along the slipper lands becomes more relevant, therefore, the torque variation due to the increase of groove depth has a smaller effect on the overall torque.

3.4.5 Vorticity inside the groove.

The vorticity inside the groove when slipper is placed parallel to the swash plate was explained in chapter 2. The same result is found in the present work, figure 3.12 compares the work done in chapter 2 and the one done in this chapter. Notice that the groove position in figures 3.12.a, b is upside down due to matrix formulation in different simulation codes.

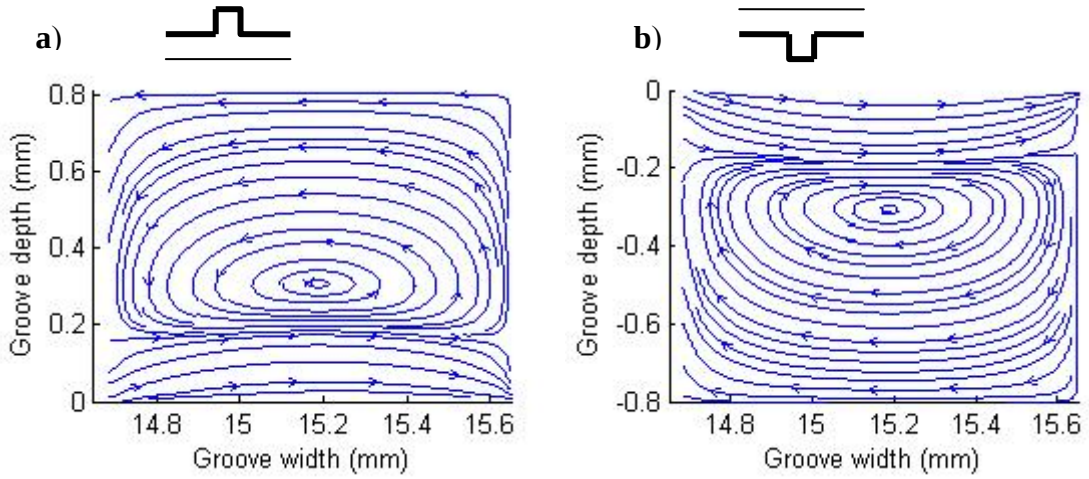

Figure 3.12 – Streamlines in r-z plane inside the groove, groove depth 0.8mm, 10 MPa, 20 microns clearance, Flat slipper CFD Results.
a) Flat slipper vorticity from Kumar [32]. b) Flat slipper vorticity from present work.

Vorticity in tilted conditions is found to be far more complex than for the flat slipper case. The flow inside the groove is highly angular. Figures 3.13-15 present the three dimensional stream line plots at 30 microns central clearance for different inlet pressures and slipper tilts. The working conditions are, figure 3.13; 9 MPa inlet pressure, and 0.02 degrees tilt, figure 3.14; 5 MPa inlet pressure and 0.02 degrees tilt, figure 3.15; 5 MPa inlet pressure and 0.03 degrees tilt. To better understand the vortexes and its evolution, figures 3.16-18 present the 2D stream lines plots corresponding to figures 3.13-15. As can be seen, there exist three vortexes, one at the entrance of the groove (Entrance Vortex), a second at the groove exit (Exit Vortex) and a third at the groove bottom (Bottom Vortex).

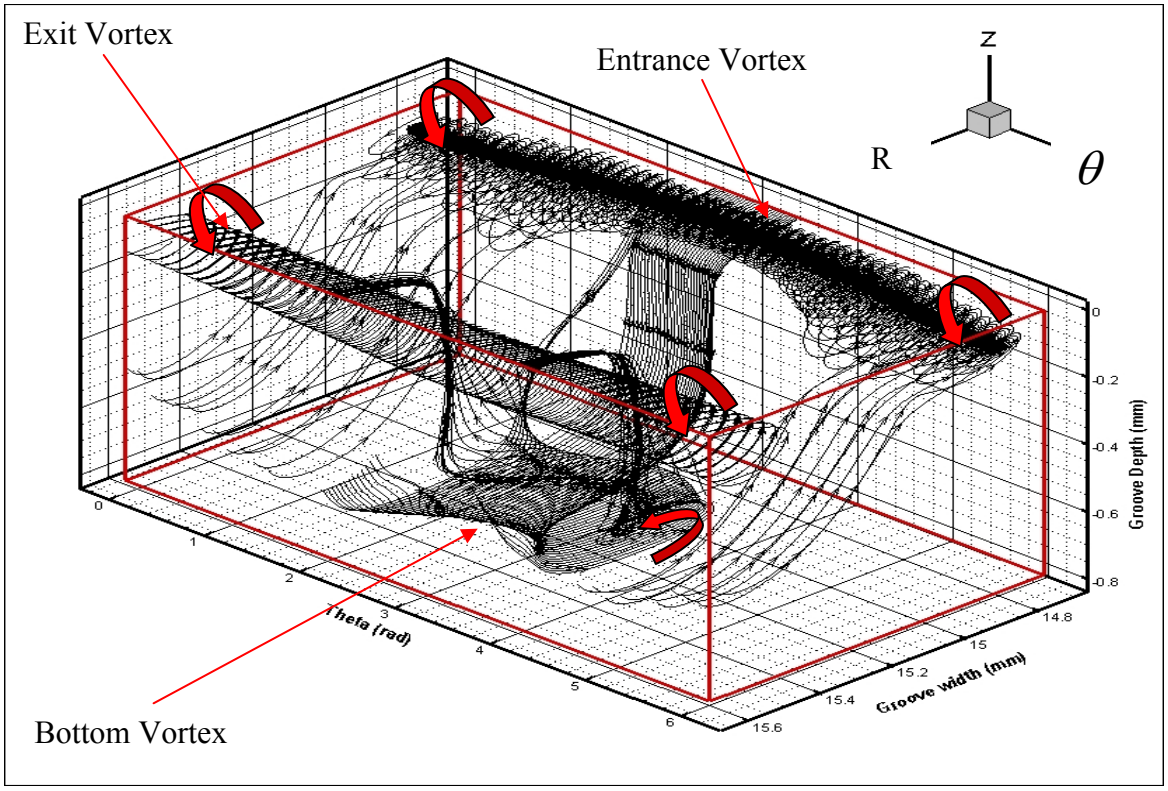

Figure 3.13 – 3-D stream line plot inside slipper groove at 9 MPa inlet pressure, 0.02 degree tilt and 30 microns central clearance.

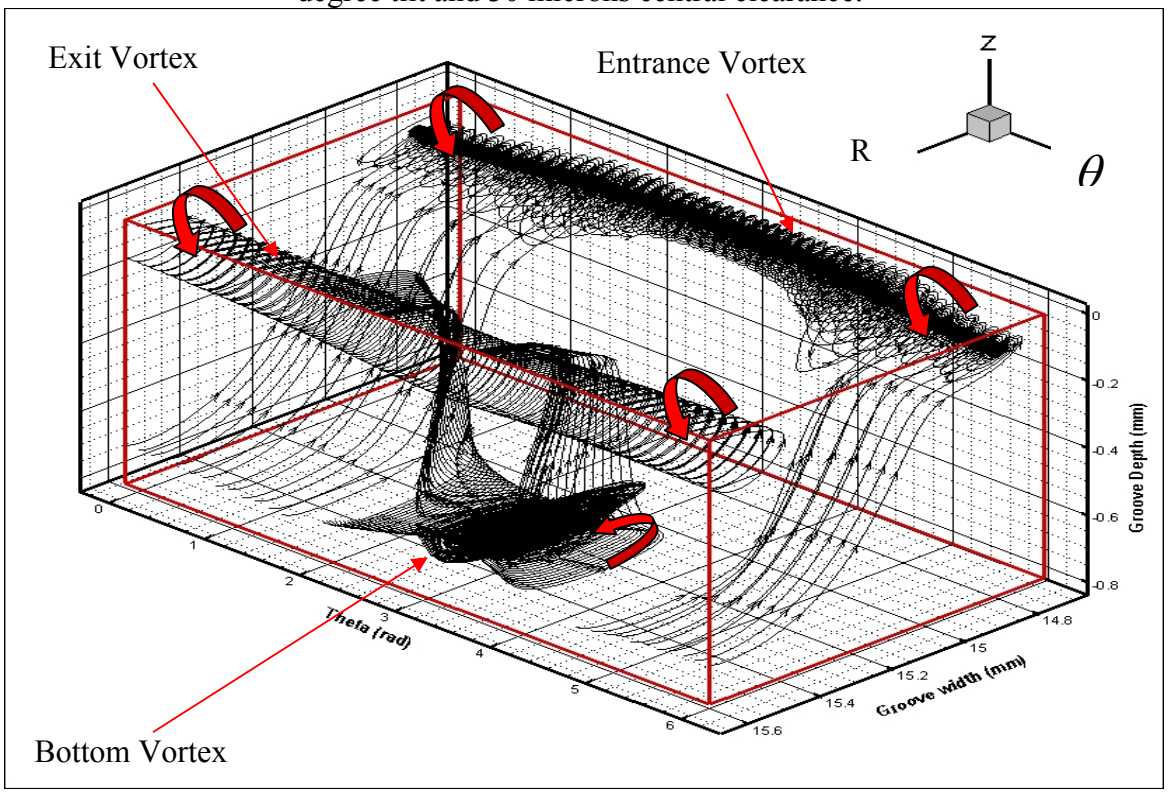

Figure 3.14 - 3-D stream line plot inside the groove at 5 MPa inlet pressure, 0.02 degree tilt and 30 microns central clearance.

It can be noticed from figures 3.13-15 that the top two vortexes exist throughout the angular positions (0^o – 360^o). The entrance vortex tends to move towards the outer radius and towards the bottom of the groove, when moving from 180^o angular position to 0^o angular position. Such displacement is very much effected by the tilt effect which is more clearly seen when comparing figures 3.14 and 3.15. The vortex displacement can be understood by the fact that when moving from 180^o towards 0^o angular position, higher amount of flow tends to enter inside the groove, then the available slipper/plate gap is higher, such flow increase push the entrance vortex towards the groove bottom and towards a higher radius position, while tending to increase its diameter.

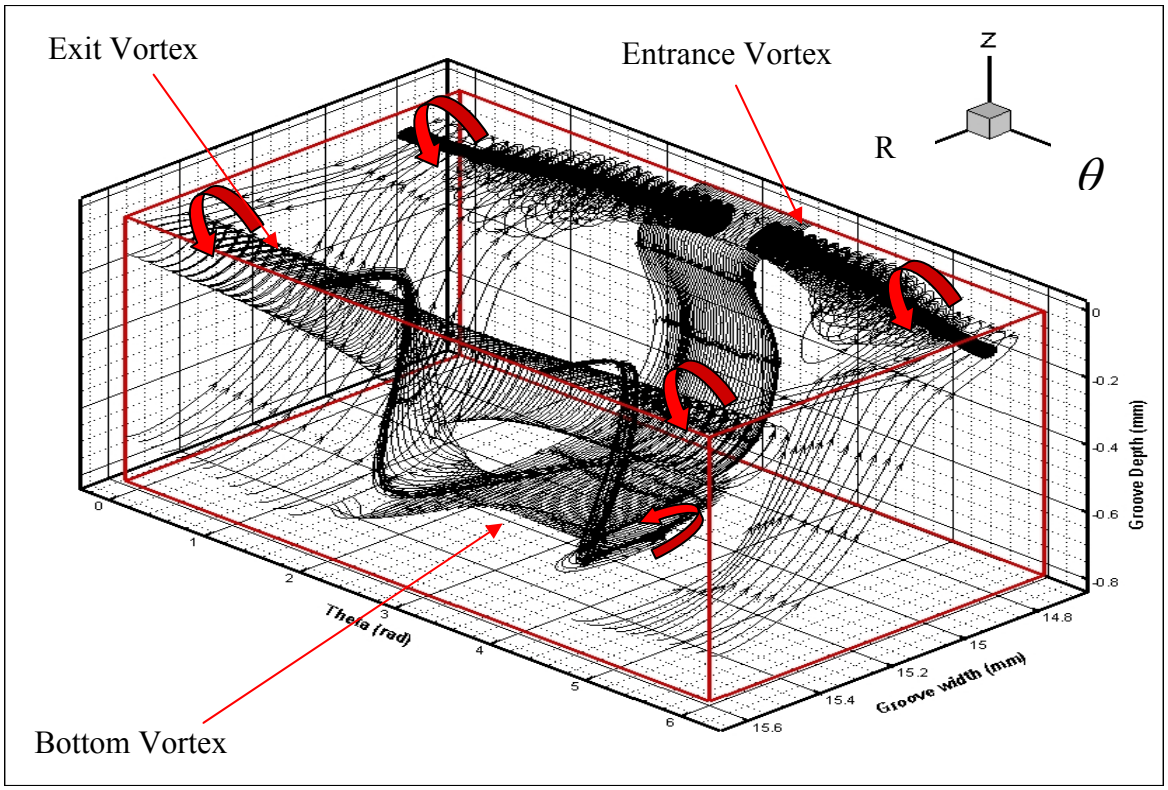

Figure 3.15 - 3-D stream line plot inside the groove at 5 MPa inlet pressure, 0.03 degree tilt and 30 microns central clearance.

It has also been noticed that an increase of pressure and or tilt, produce an increase of the entrance vortex turning speed. Regarding the entrance vortex diameter along the groove angular position, from figures 3.13-14, it is stated that the higher the inlet pressure the bigger the vortex diameter will be, this effect is more clearly seen from figures 3.16a and 17a. An increase of tilt brings a decrease on the vortex diameter, especially at slipper 180^o, figures 3.14-15, see also figures 3.17a and 18a, since around this angular position, the leakage flow will be at its minimum. For slipper angular position between 160^o-0^o, see figures 3.17c and 18c, the entrance vortex diameter increase with the increase of tilt, then for the cases studies.

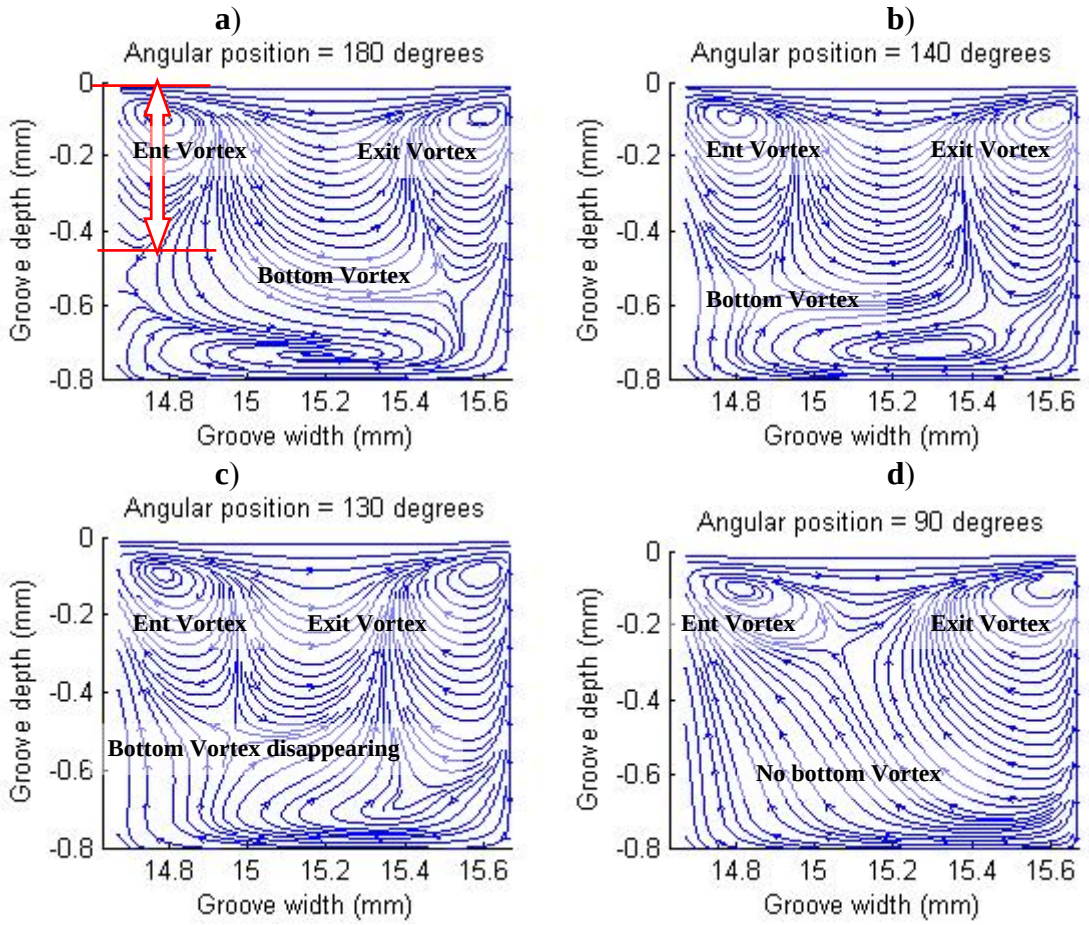

Figure 3.16 -2-D stream line plots inside slipper groove at different angular positions for 9 MPa inlet pressure, 0.02 degree tilt and 30 microns central clearance.

When studying the exit vortex, figures 3.13-15, the first thing to be noticed is that for the cases studies, such vortex maintain its shape rather constant along its 360^{o}, regardless of slipper tilt and inlet pressure. Nevertheless it must be pointed out, that for clarity the part of the exit vortex shown in figures 3.13-15 is just the central core, therefore to understand the evolution of such particular vortex, it is needed to focus to figure3.16, from where it is seen that the central core position is very much constant along the slipper angular position, yet the vortex itself increases very much in size when moving from 180^{o} to 0^{o}. Regarding the exact vortex variation with tilt and pressure, it can be seen from figures 3.17a and 3.18a, that a tilt increase brings a small decrease in vortex diameter, especially at 180 degrees, while a pressure increase create a negligible effect on the exit vortex, figures 3.16 and 3.17.

The evolution of exit and entrance vortexes is fully linked with the evolution of the bottom vortex. The bottom vortex exists along an angular position when huge momentum transfer between particles is needed. This is why at low tilts and low pressures the bottom vortex length is smaller than higher tilts and pressures. As stated in figures 3.16-18, at 5 MPa, 0.02^{o} tilt, figure 3.17, the bottom vortex disappear at around 140^{o} angular position,

being the total vortex length 80°. When maintaining the tilt and having a pressure of 9 MPa, figure 3.16, the bottom vortex length increases to 100°, and for 5 MPa inlet pressure, 0.03° tilt, figure 3.18, the total vortex length, increase to 120°, it therefore exist from 120° to 240°. The conclusion is, that the bottom vortex job is to maintain a constant pressure along the groove bottom, this is why the vortex transfers momentum to a longer distances when needed, this is for higher tilt and or higher pressure. For the cases studies the effect of tilt on the bottom vortex is more relevant than the effect of the pressure.

A very interesting point regarding the bottom vortex is the movement of the vortex central core. At slipper 180°, leakage flow comes into the groove, pushing the bottom vortex towards the groove inner radius; the vortex at this angular position is rather tiny and close to the groove bottom, figure 3.14. As the bottom vortex moves along the groove angular positions, the vortex central core moves from the groove inner radius towards the groove outer radius, creating a horse shoe shape, figure 3.15. As soon as the vortex reaches the groove outer radius, changes its direction in 90° and the flow leaves the groove. Regarding the bottom vortex dimensions, at 180° it is noticed, the vortex is small, as the vortex moves in angular direction, its dimension first increases and then, just before changing direction and leaving the groove, the vortex abruptly decreases its diameter and disappears.

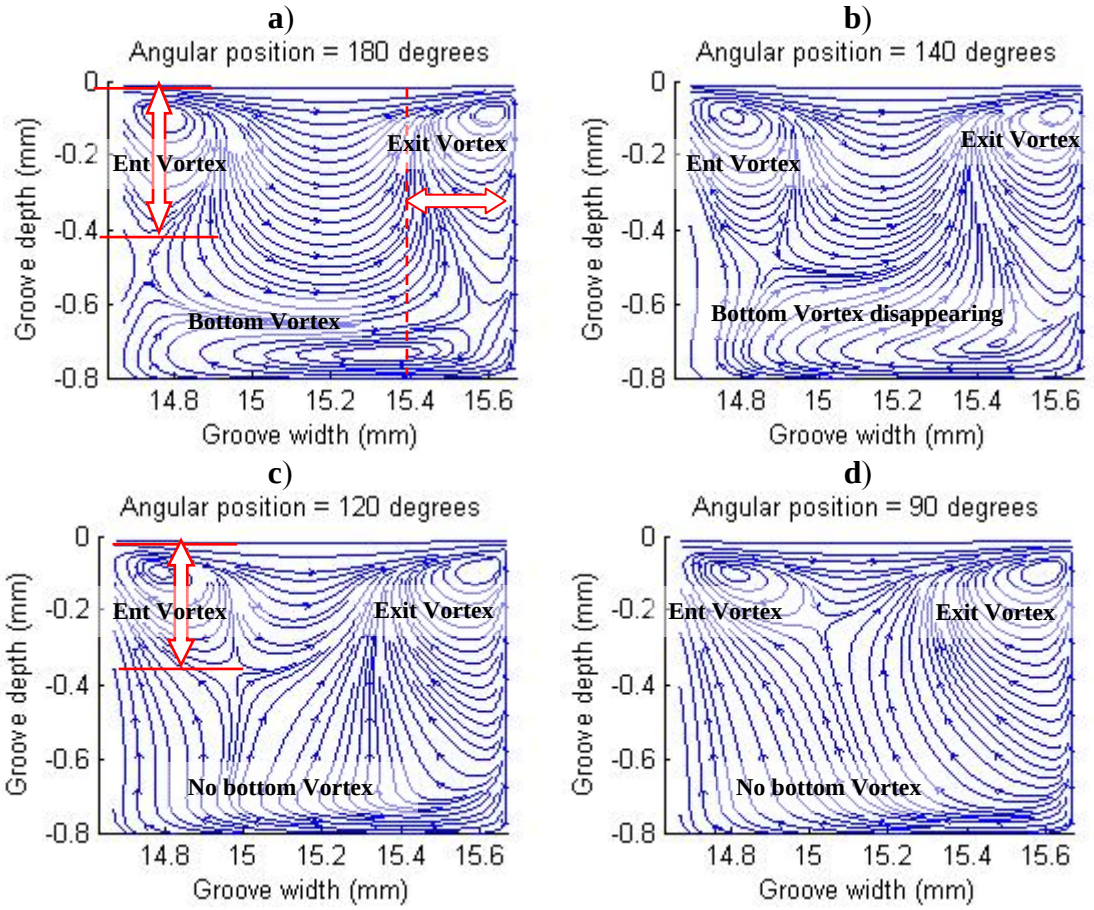

Figure 3.17 - 2-D stream line plot inside the groove at 5 MPa inlet pressure, 0.02 degree tilt and 30 microns central clearance.

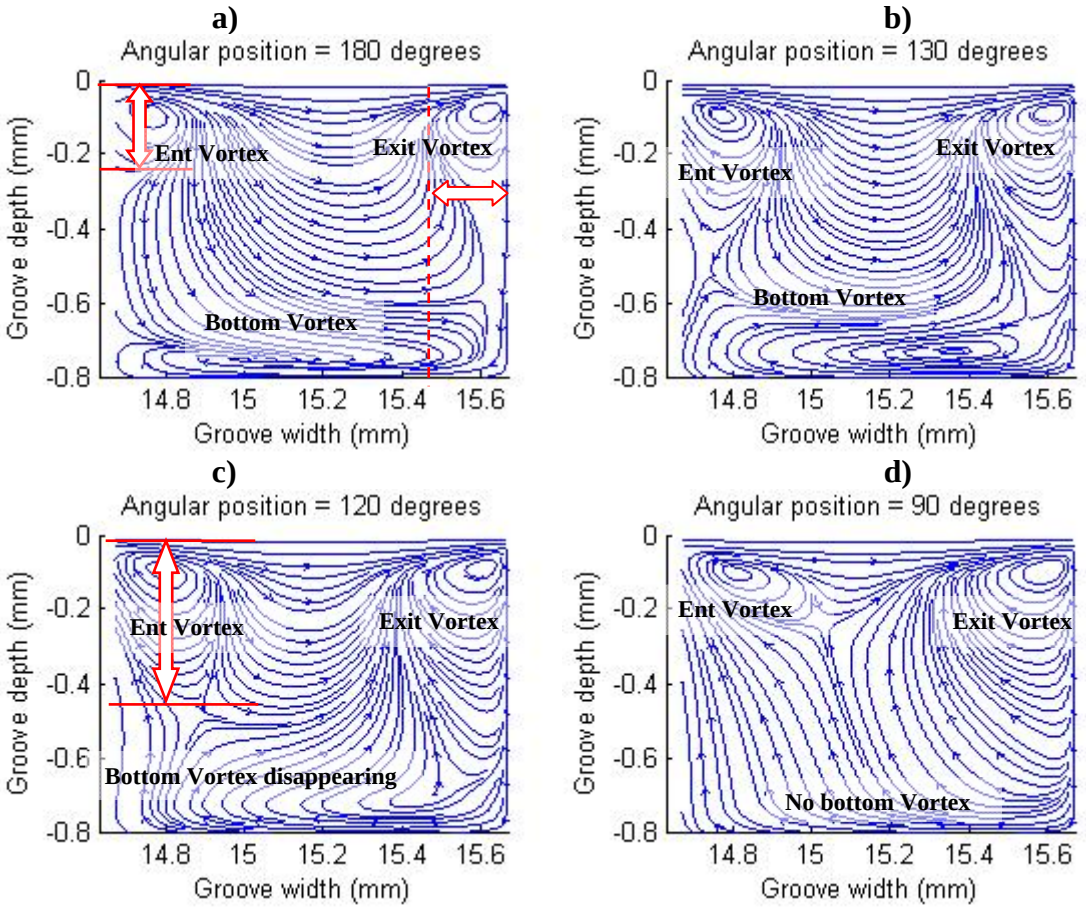

Figure 3.18 - 2-D stream line plot inside the groove at 5 MPa inlet pressure, 0.03 degree tilt and 30 microns central clearance.

3.4. 5.1 Transformation of Vortex from flat to tilted conditions

To understand the transformation of vortexes from flat slipper (Fig 3.12.b) to tilt slipper (Fig 3.16.a-18.a), a simulation has been performed at a very low tilt (0.0005^{o}), being a two dimensional streamline plot at 180 degrees angular position presented in figure 3.19.

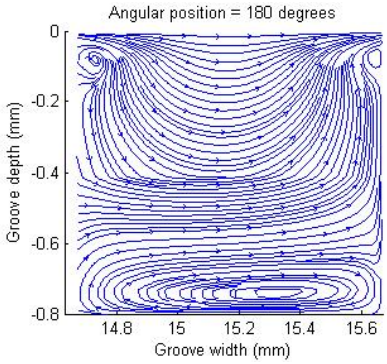

Figure 3.19 - 2-D stream line plot inside the groove at 5 MPa inlet pressure, 0.0005 degrees tilt and 30 microns central clearance.

It can be noticed from this figure that, when slipper is tilt, flow tends to enter inside the groove to a higher depth (0.5mm for the present case) compared to flat slipper whre the flow entered to a depth of 0.2mm and therefore, the bottom vortex is being pushed towards the groove bottom, appearing two edge vortexes on both sides of the groove. As tilt increases, the edge vortexes become more important and the size of bottom vortex become much narrower. Due to the fact that, as tilt increases, a higher momentum transfer is required to maintain a stable pressure along the groove, the angular extension in which the bottom vortex appears, tends, as explained in 3.4.5, to increase with the tilt. See figures 3.14 and 3.15.

3.5 Result in dynamic conditions.

When considering the dynamic conditions, from computational point of view, two movements are possible. First when slipper is fixed and swash plate is turning and second when slipper is turning and swash plate is fixed. Due to the difference in the reference frame for such movements, non-inertial and inertial respectively, Navier stokes equation need to be used accordingly.

Figure 3.20 shows a diagram of these two cases, showing the direction of movement with respect to the swash plate axis, the different angular positions considered over the slipper are also presented.

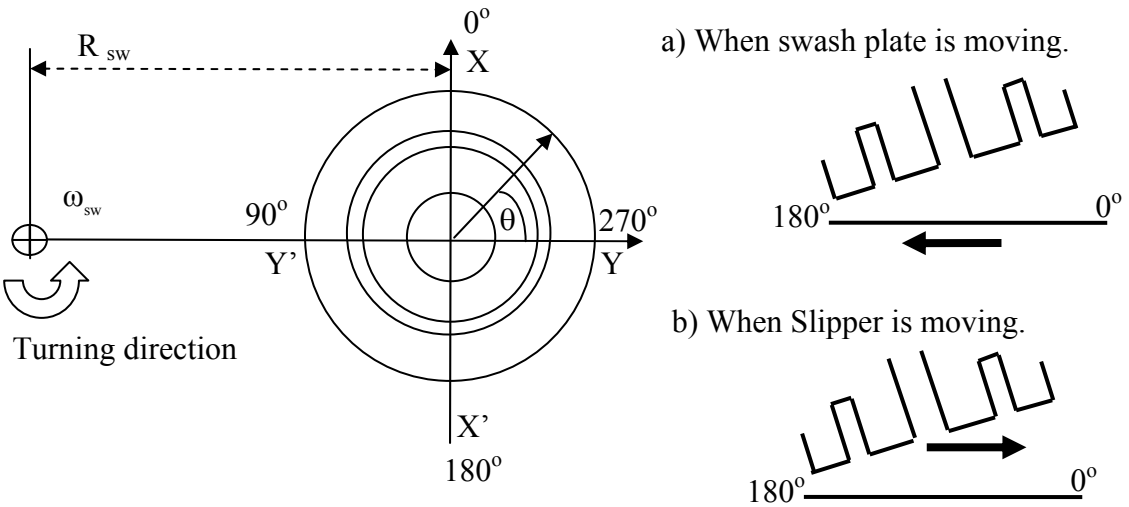

Figure 3.20 – Systematic diagram of slipper with two different dynamic cases (R_{sw} = 92mm) [a] When swash plate is moving (non-inertial reference frame). [b] When slipper is moving (inertial reference frame).

In the first case, when slipper is fixed and swash plate is moving, the axis of the computational domain is considered to be attached to the slipper centre, movement of swash plate can be introduced by velocity boundary conditions. Therefore the problem

can be treated in an inertial frame of reference and corresponding NVS equation (3.70) is applied to the domain.

$$\rho\left[\frac{\partial u}{\partial t}+u\cdot\nabla u\right]=\mu\,\Delta u+S \tag{3.70}$$

On the other hand, in reality, the slipper rotates around the swash plate axis. In this case, the coordinate axis has been attached to slipper centre, which makes the reference frame as non inertial, this case corresponds NVS equation (3.71), which considers Coriolis and centripetal forces.

$$\rho\left[\frac{\partial u}{\partial t}+u\cdot\nabla u+2\,\omega\times u+\omega\times\left(\omega\times R\right)\right]=\mu\,\Delta u+S \tag{3.71}$$

3.5.1. Solution technique and Boundary Conditions.

Case I (when swash plate is moving) – In this case axis can be attached to the centre of the fixed slipper and problem can be treated in a inertial reference frame. Three dimensional Navier stokes equations in cylindrical coordinates have been applied to the slipper plate gap and the domain has been transformed from non orthogonal to orthogonal by using derivative transform over a boundary fitted grid as explained in section 3.3. The inlet-outlet boundary conditions for this case are given by equation (3.72).

$$P\big|_{\Gamma_{in}}=P_{in};\ P\big|_{\Gamma_{out}}=P_{out};\ \left.\frac{\partial\left(r.V_r\right)}{\partial r}\right|_{\Gamma_{in}\text{or }\Gamma_{out}}=0;\ \left.\frac{\partial V_\theta}{\partial r}\right|_{\Gamma_{in}\text{or }\Gamma_{out}}=0;\ V_z\big|_{\Gamma_{in}}=0;\ \left.\frac{\partial V_z}{\partial r}\right|_{\Gamma_{out}}=0; \tag{3.72}$$

No slipping boundary conditions at walls are represented by equation (3.73 & 74).

$$V_r\big|_{\text{Slipper wall}}=0 \qquad V_r\Big|_{\text{swash plate wall}}=-\left[R_{sw}\ \omega_{sw}\ \text{Cos}\left(\theta\right)\right] \tag{3.73}$$

$$V_\theta\big|_{\text{Slipper wall}}=0 \qquad V_\theta\Big|_{\text{swash plate wall}}=R_{sw}\ \omega_{sw}\ \text{Sin}\left(\theta\right)-r\,\omega_{sw} \tag{3.74}$$

Case II (When slipper is moving) – In this case, the axis are attached to slipper center which is rotating with respect to swash plate axis. It is necessary to consider the problem in non inertial reference frame and include the coriolis and centripetal forces in Navier Stokes Equation as represented by equation (3.71). The contribution of these forces in r and θ momentum equation is given by T_r and T_θ, as represented by equation (3.75 & 76). A similar coordinate transformation is done as explained in section 3.3 by including the two terms T_r and T_θ in momentum equations.

$$T_r=-\left[2\,\omega_{sw}\ v+R_{sw}\ \omega_{sw}^2\right] \tag{3.75}$$

$$T_\theta = 2\,\omega_{sw}\,u \tag{3.76}$$

The inlet-outlet boundary conditions remain the same as represented by equation (3.72). No slipping boundary conditions at walls need to be modified according to equations (3.77 & 78).

$$V_r\big|_{\text{Slipper wall}} = 0 \qquad V_r\big|_{\text{swash plate wall}} = R_{sw}\,\omega_{sw}\,\text{Cos}(\theta) \tag{3.77}$$

$$V_\theta\big|_{\text{Slipper wall}} = 0 \qquad V_\theta\big|_{\text{swash plate wall}} = -R_{sw}\,\omega_{sw}\,\text{Sin}(\theta) + r\,\omega_{sw} \tag{3.78}$$

In both cases the transformed equations have been integrated by control volume formulation. The discrete Navier stokes equation is coupled with continuity by using Semi Implicit Pressure Correction technique developed by Patankar [17].

3.5.2 Vorticity.

When doing simulation under tilt dynamic conditions, it was not possible to achieve a full convergence. Figure 3.21 represents the residue of u-momentum equation at different iterations level for 5MPa inlet pressure, 0.02 deg tilt, 200 rpm turning speed, 30 microns central clearance. It is clear from figure that after a certain number of iterations, residue starts fluctuating. A possible explanation for such behaviour is, it might be possible that steady state does not exist under tilt dynamic conditions.

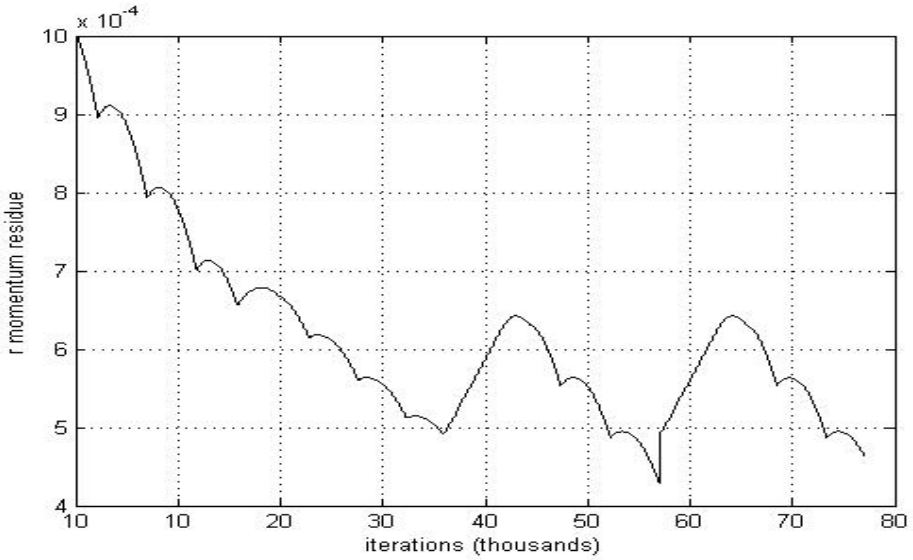

Figure 3.21 – Residue of u-momentum equation at different iterations, 5MPa inlet pressure, 0.02 deg tilt, 200 rpm turning speed, 30 microns central clearance.

To understand the possibility of the existence of steady state, two dimensional stream lines have been plotted at different iteration levels. Figure 3.22 represents some of such

two dimensional stream line plots inside the groove at 5MPa inlet pressure, 0.02 deg tilt, 200 rpm turning speed, 30 microns central clearance and 90^{o} angular position. It is clear from the figure that Vorticity inside the groove appears not to be constant under tilt dynamic conditions which give further confidence to the point made earlier that flow inside the groove is time dependent under tilt dynamic conditions.

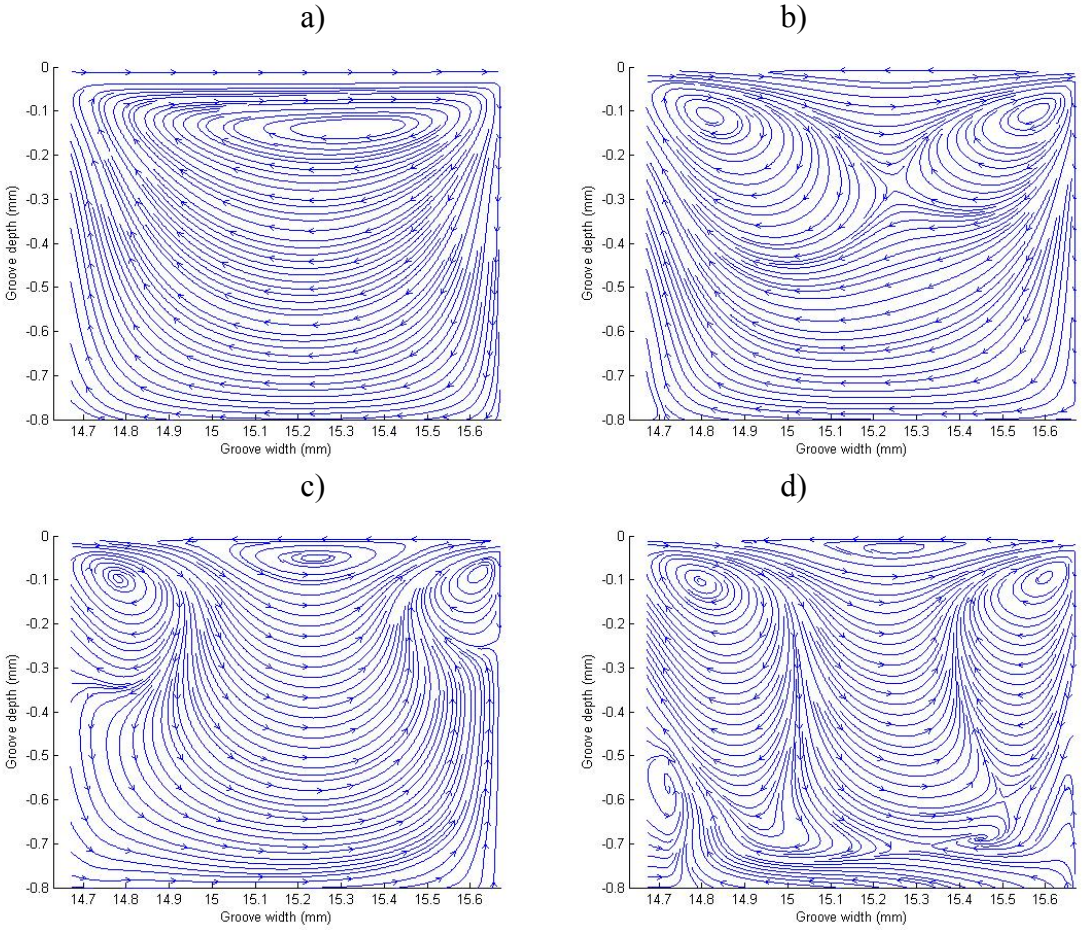

Figure 3.22 – 2D stream line plot inside the groove at different iteration level, 5MPa inlet pressure, 0.02 deg tilt, 200 rpm turning speed, 30 microns central clearance at 90^{o} angular position. [a] 20,000 iterations. [b] 35,000 iterations. [c] 55,000 iterations. [d] 80,000 iterations.

Assuming that the flow in slipper plate clearance is time dependent, it is not possible to analyze the Vorticity inside the groove by the simulation code develop during this project under tilt dynamic conditions, as the simulation code is design to handle steady state problems. It has to be pointed out that it is possible to convert the steady state code into transient one but such attempt has not been made due to the fact that it takes 10 to 15 days to achieve the full convergence under tilt static conditions from the simulation code on a normal Personal Computer. Converting the code into transient will increase this time further and will make the simulation impractical. Therefore it might be better choice to develop a transient code using unstructured grid and finite element method rather than boundary fitted grid and finite volume method. It has to be said that no security can be

given regarding that such code will produce a faster result than the code based on boundary fitted grid.

It has already been stated that the simulation tool developed during this project is designed to handle steady state problems therefore a fully trusted analysis of a tilted slipper under dynamic conditions is not possible. On the other hand, it has been found, when analysing pressure distribution, torque, force and leakage outside the groove at different iteration level that these quantities are much weaker function of time compared to the flow inside the groove. Therefore it can be understood that the flow inside the grooves is highly dependent on time but the flow out side the groove is a much weaker function of time. As a result, even though the simulation code is designed to handle steady states problems it is still possible to get a very good idea about the behaviour of slipper characteristic (pressure, force, torque and leakages) under tilt dynamic conditions from the code developed in this project, although such dynamic results can not be seen as completely trustable.

The simulations have been performed under different operating conditions (3 to 9Mpa inlet pressure, 200 to 1000 rpm swash plate turning speed, 0.2 to 0.5 degrees tilt) by using the steady state code. The stopping point for the simulations has been chosen when the residues start fluctuating and the simulation results have been compared to the corresponding experimental results.

3.5.3 Disk run out (Experimental).

The experimentation has been performed by using the test rig described in chapter 7. As mentioned earlier. Due to the transducers attached to the slipper, the experiments can only be performed while considering swash plate rotation. From the experimental setup, it is possible to measure the pressure inside the groove, disk run out and leakage through the slipper-plate gap for different turning speeds, tilts, central clearances and inlet pressures. The disk run out has been measured using the position transducer located at the slipper leading edge and figure 3.23 presents results at 3 MPa and 13 MPa and for two rotational speeds of 200 rpm and 1000 rpm.

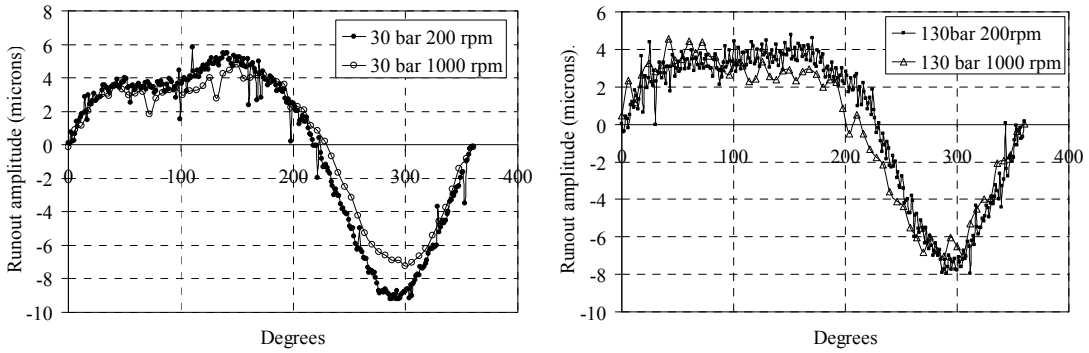

Figure 3.23 - Run out amplitude at two different pressures and turning speeds at 0.05 degree tilt

Please notice that disk runout was already introduced in chapter 2, yet, the test rig used to perform the tilt dynamic experiments, although essentially the same test rig, had some mechanical improvements in comparison with the test rig used to perform the dynamic flat slipper experiments presented in chapter 2. This is why in the present chapter the disk runout is again presented and it is clearly seen when comparing figures 3.23 with 2.15 that thanks to the test rig mechanical improvements, disk runout was now reduced.

Therefore, for each turning speed and inlet pressure an average dynamic clearance due to disk run out needs to be calculated. The average dynamic clearance has been calculated by calculating the average flow over one cycle. For laminar flow case, flow rate is proportional to the cubic of clearance, as given in Bergada [15].

$$Q_o = k\, H_o^3 \tag{3.79}$$

Assuming the run out over one cycle as sinusoidal, the average flow over one cycle can be given as: see Bergada et al [15].

$$Q = \frac{k}{2\pi}\int_0^{2\pi}\left(H_o + A_o \sin\theta\right)^3 d\theta = Q_o\left[1+\frac{3}{2}\left(\frac{A_o}{H_o}\right)^2\right] \tag{3.80}$$

From equations (3.79) and (3.80), an average dynamic clearance can be given as:

$$H = H_o\sqrt[3]{1+\frac{3}{2}\left(\frac{A_o}{H_o}\right)^2} \tag{3.81}$$

Equation (3.81) will be used to modify the theoretical slipper/plate distance, in order to compare the CFD results with the experimental ones.

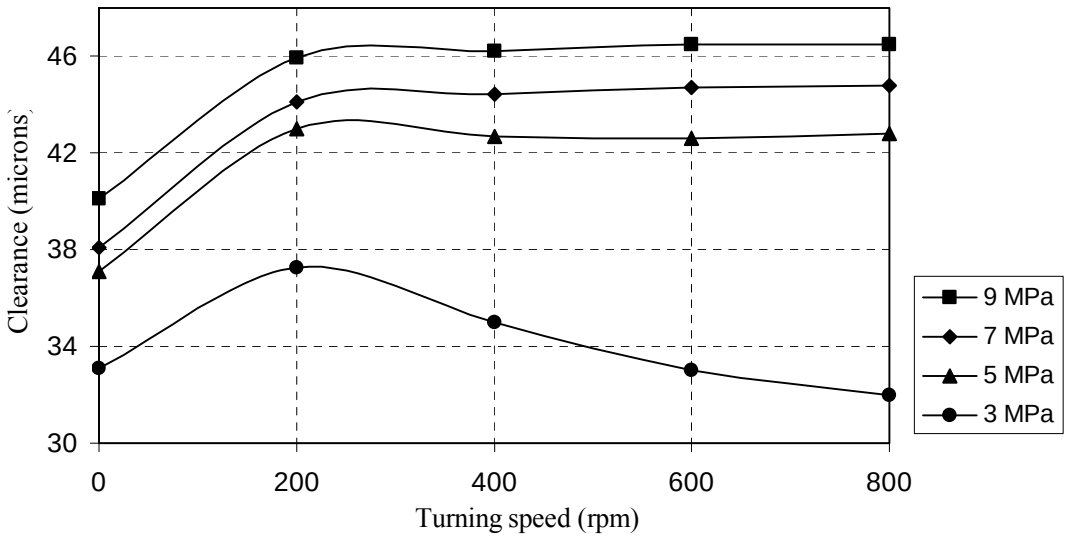

Figure 3.24– Average calculated clearance considering disk run out at 0.05 degree tilt at different turning speeds and inlet pressures.

Figure 3.24 represent the average dynamics clearance which has been calculated from measured temporal run out (presented for a particular pressure and turning speed in figure 3.23) by using equation (3.81). It seems that for a given pressure, once the plate starts turning, clearance between slipper and plate increases, a further increase in turning speed, tends to slightly decrease the disk run out, but it is needed to point out that as the pressure increase the clearance will also increase.

3.5.4 Effect of swash plate turning on pressure, force and torque.

The experimental test rig was able to evaluate the pressure inside the slipper groove in four points separated 90 degrees from each other, and under dynamic conditions pressure differential inside the groove was found to be approximately constant on turning speed and just dependent on inlet pressure and tilt.

In figure 3.25 the average simulated groove pressure for a set of turning speeds and slipper inlet pressures, corresponding to the clearances shown in figure 3.24, is compared with the average groove pressure measured experimentally.

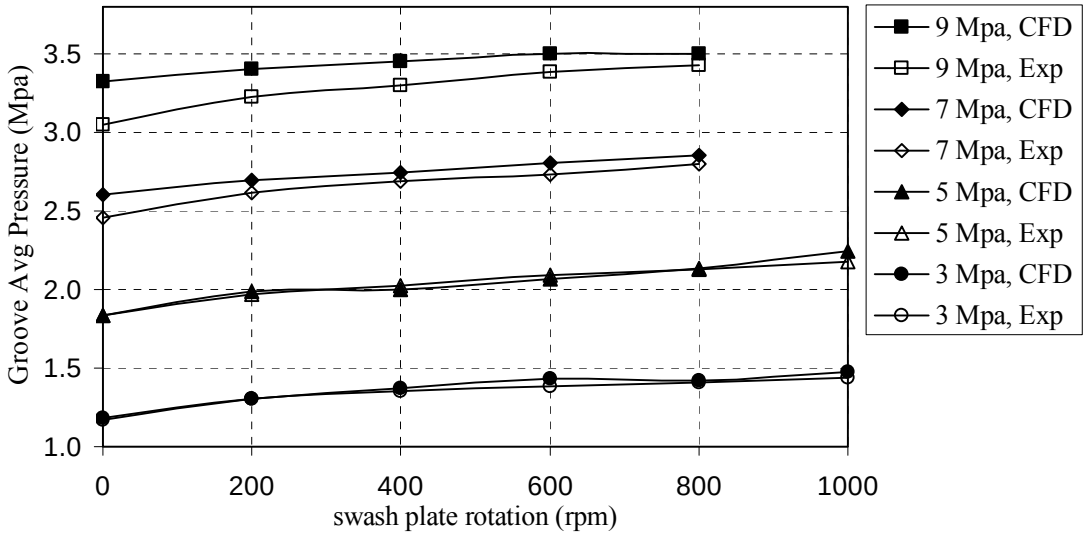

Figure 3.25 - Averaged groove pressure at different inlet pressure and turning speed at 0.05 deg tilt (comparison between CFD and experiment). Central clearance = corresponding to figure 3.24

The results show a good concordance specially at low and medium slipper inlet pressures, nevertheless, such agreement decreases at high pressures, such discrepancies are well understood when taken into account that as inlet pressure increase leakage across the slipper also increases and shear stresses increase with leakage, the NVS equations consider shear stresses for a perfectly smooth surface, but in reality the slipper and plate surfaces have some roughness, as a result pressure decay in slipper first land is higher in reality than the one found via CFD, specially at high pressure differentials.

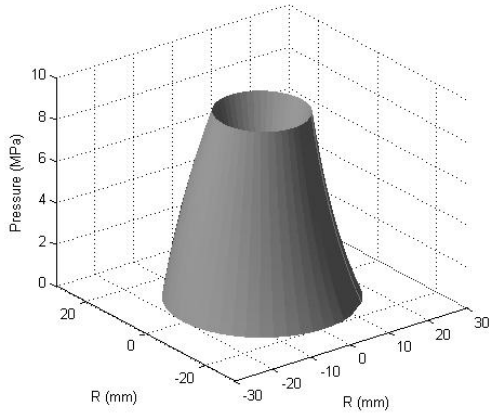

a) 200 rpm, no groove, 30 microns.

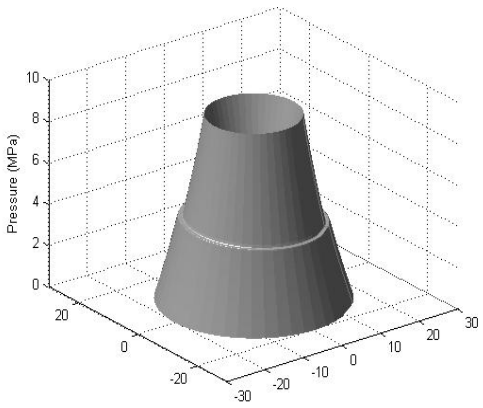

b) 200 rpm, 0.8mm groove, 30 microns.

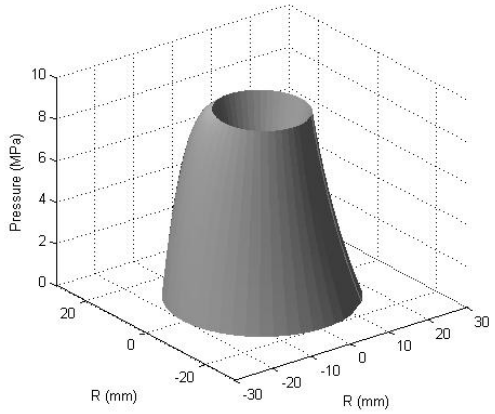

c) 1000 rpm, no groove, 30 microns.

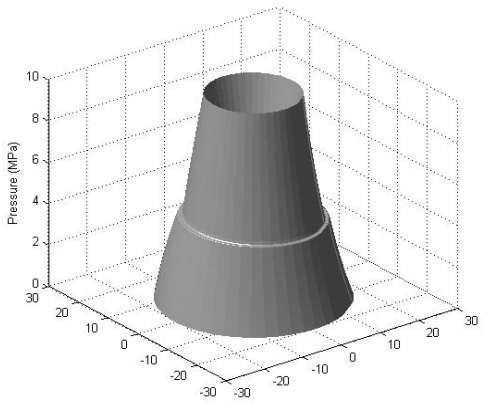

d) 1000 rpm, 0.8mm groove 30 microns.

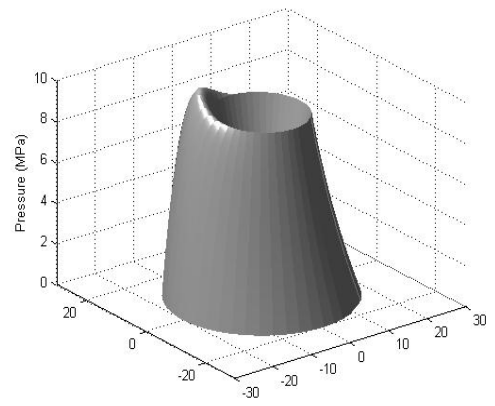

e) 1000 rpm, no groove, 20 microns.

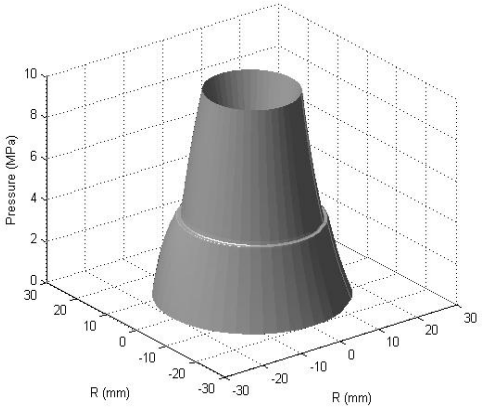

f) 1000 rpm, 0.8mm groove, 20 micron

Figure 3.26 - Pressure three dimensional graphs at two different turning speeds and clearances at 9 MPa and 0.025 degree tilt. (CFD).

To visualize under dynamic conditions, the pressure distribution below the slipper, figure 3.26 is presented and represents pressure three dimensional graphs at two different turning speeds (200-1000 rpm), clearances of (20-30 microns) at 0.025 degrees tilt in

groove and non grooved conditions. When comparing figure 3.26.a-b to 3.26.c-d, it can be noticed that an increase in turning speed tends to destabilize the pressure distribution below slipper but the effect of this destabilization is more severe in absence of the groove. When comparing figure 3.26.c-d to 3.26.e-f, it can be noticed that the effect of disk turning speed is more severe at lower clearances. It is clear from the figure 3.26 that groove brings stability in the slipper pressure distribution. Force on the slipper increases with turning speed, as shown in Figure 3.27, which can be understood when visualizing figure 3.26.b and 3.26.d, then, as turning speed increases, there exist a higher pressure distribution regime below slipper trailing edge, which result into higher force.

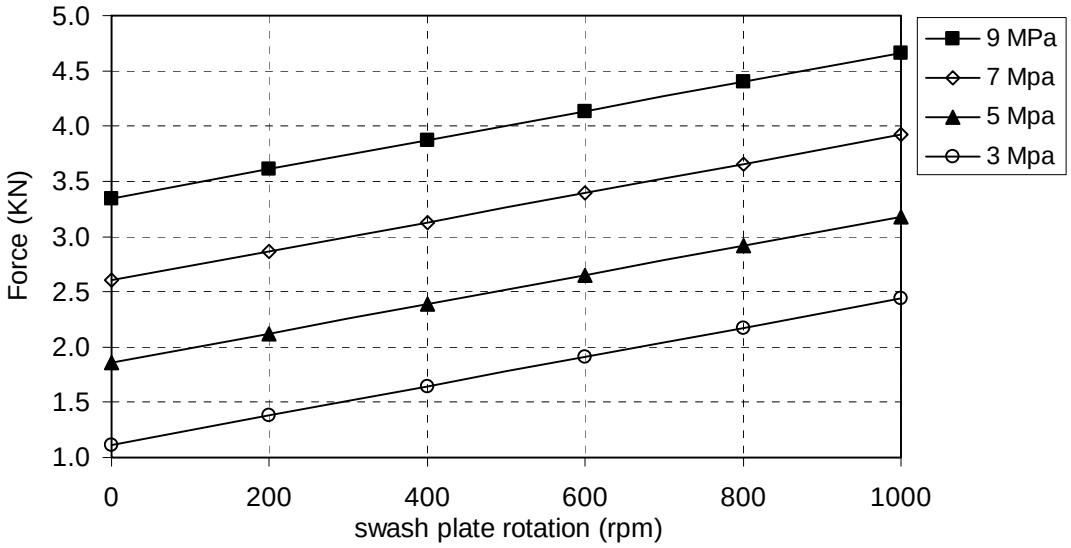

Figure 3.27 –Force acting on the slipper at different turning speed and inlet pressure at 0.04 deg tilt and 25 microns central clearance. (CFD).

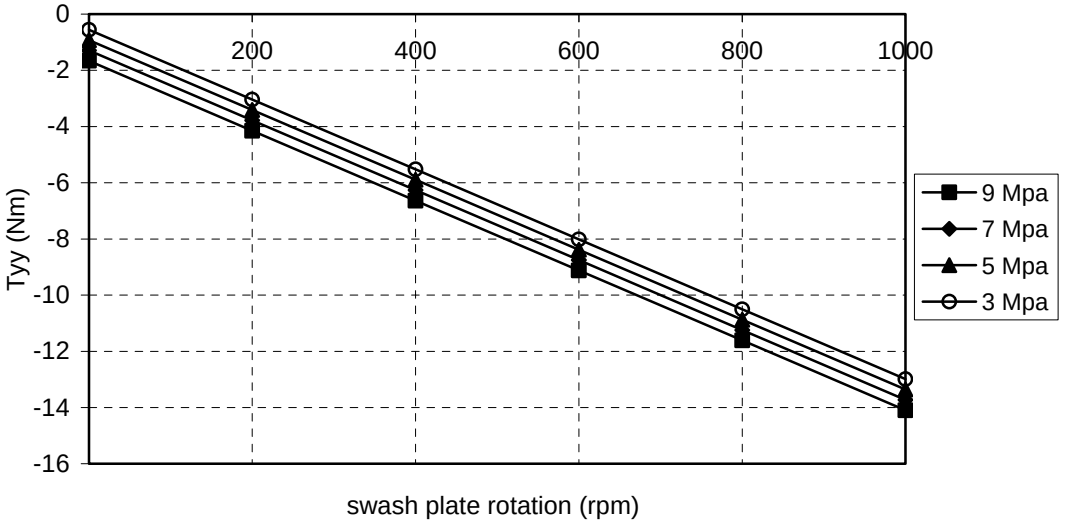

Figure 3.28 –Y axis Torque at different turning speed and inlet pressure at 0.04 deg tilt and 25 microns central clearance.

Figure 3.28 represents the torque versus Y-axis at different turning speeds for different inlet pressures and 0.04 degrees tilt. It can be noticed that the magnitude of the torque is increasing with turning speed increase, which can be understood when realised that the pressure differential along the angular direction also increases with turning speed. It can also be noticed that there is a slight increase in torque with inlet pressure which is well understood by the fact that the increase in inlet pressure also results into an increase in angular pressure differential although such increase is very tiny; this is why the torque increase is also very tiny.

3.5.5 Effect of swash plate rotation on slipper leakage.

It is clear from previous research that leakage is a strong function of slipper plate clearance. As a result it is important to consider disk run out while comparing experimental leakage to the simulated one. A set of numerical simulations have been performed for each clearance presented in figure 3.24, given as a function of turning speed and inlet pressure, and used to compare with experimental data. Figure 3.29 represents the comparison between experimentally measured and simulated leakage corresponding to its clearances.

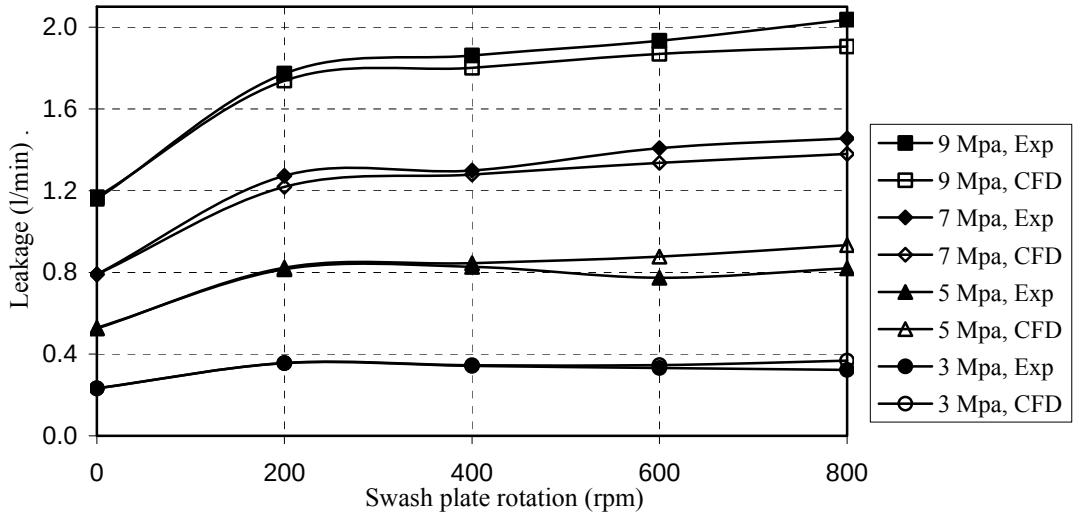

Figure 3.29 – Compression between experimentally measured and simulated leakage at different turning speed, inlet pressure and 0.05 degree tilt, clearances corresponding to figure 3.24.

The comparison shows a very good agreement. It is important to notice that while comparing the leakage with experiments, clearances between slipper and plate have not been modified by surface roughness as it had been done with static case. The reason behind such calculation is that, in dynamic conditions, due to disk run out, the magnitude on total clearance is much higher that surface roughness (typically 1 micron).

It can be noticed from figure 3.29 that leakage through the gap slipper/plate, is following the similar trend as the clearance between slipper and plate which supports the argument of strong dependency of leakage on clearance. To understand the effect of turning speed

more precisely, it is important to simulate the leakage at a fix gap, as presented in figure 3.30.

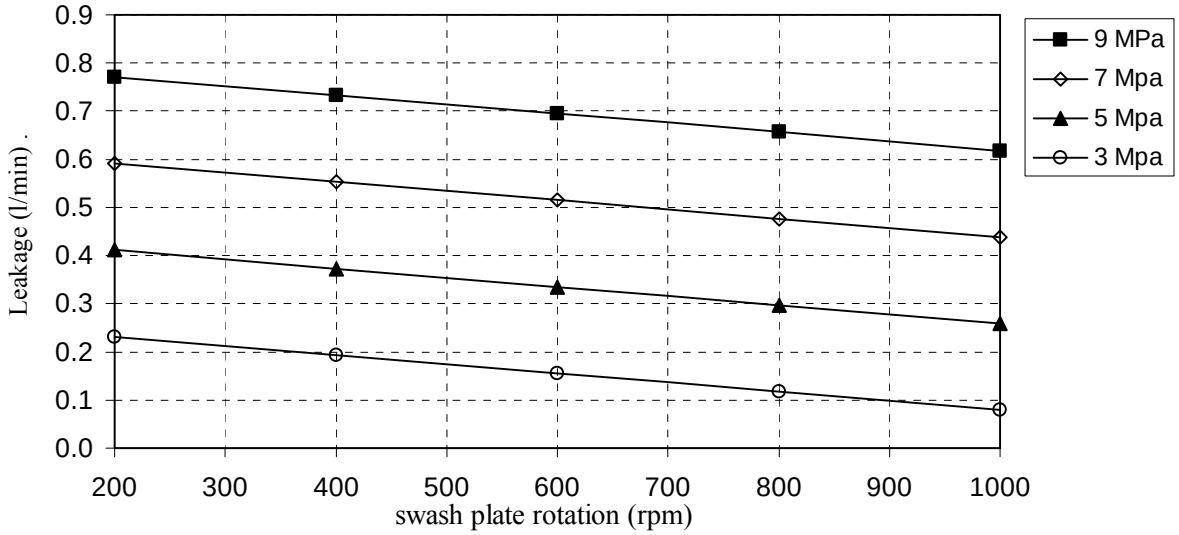

Figure 3.30 - Simulated leakages versus turning speed at different inlet pressure at 0.03 deg tilt.

Figure 3.30 presents the variation of leakage with turning speed, for a fixed given central clearance and tilt. It is noticed, leakage decreases with turning speed, which can be understood by the fact that slipper leading edge (higher clearance) has an inward flow due tangential velocity, on the other hand slipper trailing edge (lower clearance) has an outer flow. As the clearance is higher on leading edge, higher inward flow enters the slipper than the flow leaving it, decreasing the overall leakage.

3.6 Conclusions.

Under tilted static conditions, pressure is found to be very stable along the angular direction in presence of the groove. The maximum pressure differential across the slipper radius, for inlet pressure 10 MPa, 0.042^{o} tilt and 15μm central clearance, decreases from 0.3 MPa to 0.03 MPa due to the presence of a groove.

Groove pressure differential increases when central clearance decreases. Average pressure inside the groove decreases with the increase of tilt. Percentage decrease in force acting on the slipper is found to be independent of inlet pressure although highly dependent on slipper/plate central clearance. At lower clearance, the force decrease with tilt increase is more severe.

As the slipper tilt is considered along the X-axis, the torque with respect to X-axis is found to be zero. On the other hand there exists Y directional torque. The magnitude of the Y torque is found to be increasing with the increase of tilt.

Slipper leakage is found to be a strong function of clearance as it was found in Kumar et al [16] for flat slipper. In fact, slipper leakage is a function of the clearance to the power 3, see Bergada et al [15] among other authors. Slipper leakage increases with the increase of tilt.

When modifying the groove position, the displacement of the groove towards the slipper inner pocket (inner boundary) leads to an increase in leakage and force acting over the slipper, as it was found in Kumar et al [16], but the effect under tilted conditions is more severe than for the flat slipper case.

Under tilt conditions, it is found, there exist three vortexes inside the groove, two at groove top edges and one at the bottom of the groove. The existence of the bottom vortex depends on tilt and inlet pressure. At higher tilt and higher pressure, the angular length of the bottom vortex increases. The bottom vortex appears in the locations where a huge momentum interchange between particles is needed. The two small vortexes appearing at the groove top edges remain rather constant in shape along the slipper groove, tilt and inlet pressure have a second order effect on the top vortexes.

Under tilt dynamic conditions, flow inside the groove is found to be highly time dependent, on the other hand flow outside the groove is a very weak function of time, which made it possible to do the approximate analysis for pressure, force, torque and leakage by using a steady state code. It has been found that an increase in turning speed tends to destabilize the pressure distribution below slipper but the effect of this destabilization is more severe in absence of the groove. The effect of disk turning speed is more severe at lower clearances. Force and torque are found to be increasing with increase in turning speed but leakage tends to decrease with increase in turning speeds.

Nomenclature:

Γ	Computation domain boundary (m).
Ω	Computation domain (m^3).
ρ	Density of fluid (Kg/m^3).
μ	Dynamics viscosity (Kg/m/s).
ϕ	Flux vector (m/s).
A_o	Runout amplitude (mm).
P	Pressure (Pa).
S_ϕ	Source term in momentum Eq for corresponding ϕ ($Kg/m^2/s^2$).
V	Velocity (m/s).
Ho	Slipper/plate central clearance (m).

H	Generic slipper/plate clearance (m).
r, θ, z	Cylindrical coordinates vector (m, rad, m).
R, ξ, η	Transformed cylindrical coordinates vector (m, rad, non dimensional).
α	slipper tilt.
t	Time (s).

Subscript:

r, θ, z	Component of vector in r, θ and z direction.
R, ξ, η	Component of vector in R, ξ and η direction.

References

1 Fisher, M.J. A theoretical determination of some characteristics of a tilted hydrostatic slipper bearing. B.H.R.A. Rep. RR 728 April 1962.

2 Hooke C.J. , Kakoullis Y.P. The lubrication of slippers on axial piston pumps. 5th International Fluid Power Symposium September 1978, B2-(13-26) Durham, England.

3 Hooke C.J. , Kakoullis Y.P. The effects of centrifugal load and ball friction on the lubrication of slippers in axial piston pumps. 6th International Fluid Power Symposium, 179-191, Cambridge, England. 1981

4 Hooke C.J., Li K.Y. The lubrication of overclamped slippers in axial piston pumps centrally loaded behaviour. Proceedings of the Institution of Mechanical Engineers 1988, Vol 202, No C4, 287-293.

5 Hooke C.J., Li K.Y. The lubrication of slippers in axial piston pumps and motors. The effect of tilting couples. Proceedings of the Institution of Mechanical Engineers 1989, Vol 203, part C, 343-350.

6 Iboshi N., Yamaguchi A. Characteristics of a slipper Bearing for swash plate type axial piston pumps and motors, theoretical analysis. Bulletin of the JSME, Vol 25, No 210, December 1982, 1921-1930.

7 Iboshi N., Yamaguchi A. Characteristics of a slipper Bearing for swash plate type axial piston pumps and motors, experiment. Bulletin of the JSME, Vol 26, No 219, September 1983. 1583-1589.

8 Iboshi N., Characteristics of a slipper Bearing for swash plate type axial piston pumps and motors, Design method for a slipper with a minimum Power loss in fluid lubrication. Bulletin of the JSME, Vol 29, No 254, August 1986.

9 Harris RM. Edge KA. And Tilley DG. Predicting the behaviour of slipper pads in swashplate-type axial piston pumps. ASME Winter Annual Meeting. New Orleans, Louisiana. November 28-December 3, 1993, 1-9.

10 Wieczoreck, U. Ivantysynova M. CASPAR-A computer aided design tool for axial piston machines. Proceedings of the Power Transmission Motion and Control International Workshop, PTMC2000, Bath, UK. 2000, 113-126.

11 Wieczoreck U and Ivantysynova M. Computer aided optimization of bearing and sealing gaps in hydrostatic machines-the simulation tool CASPAR. International Journal of fluid Power 3 2002; 1:7-20.

12 Niels H., Santos F. Reducing friction in tilting pad bearing by the use of enclosed recesses. Journal of Tribology - ASME. Jan 2008, Vol 130.

13 Bergada JM and Watton J. A direct leakage flow rate calculation method for axial pump grooved pistons and slippers, and its evaluation for a 5/95 fluid application. 5th JFPS international Symposium on fluid power, Nara Japan, Nov 13, 2002.

14 Bergada JM and Watton J. Axial Piston pump slipper balance with multiple lands. ASME International Mechanical Engineering Congress and exposition, New Orleans Louisiana Nov 2002; Vol 2 No 39338.

15 J.M. Bergada, J. Watton, J.M.Haynes and D. Ll. Davies. The hydrostatic /hydrodynamic behaviour of an axial piston pump slipper with multiple lands. Meccanica. DOI:10.1007/s11012-009-9277-0.

16 S. Kumar, JM Bergada, J. Watton, "Axial piston pump grooved slipper analysis by CFD simulation of three dimensional NVS equation in cylindrical coordinates." Computer &Fluids 38 (2009) 648-663.

17 Subhas V. Patankar, Numerical Heat Transfer and Fluid Flow. Taylor & Francis Group: Hemisphere Publishing Corporation; 1980.

18 Zhu ML., Shimizu Y., Nishimoto N., Calculation of curved open channel flow using physical curvilinear non-orthogonal coordinates. Int J. Numer. Meth. Fluids 2004, Vol 44, pp:55-70.

19 Borges JE. Computational method for the design of ducts. Computer & Fluids 2007, Vol 36, pp:480-83.

20 Koshizuka S., Oka Y., Kondo S. A staggered differencing technique on boundary fitted curvilinear grid for incompressible Navier Stokes equation written with physical components. 3rd Int. Symp. on computational fluid dynamics Nagoya, Japan 1989.

21 Koshizuka S., Oka Y., Kondo S. A boundary fitted staggered difference method for incompressible flow using Riemann geometry. Proceeding of the 1st Int. conference on super computing in nuclear applications, Mito, Japan 1990.

22 Koshizuka S., Oka Y., Kondo S. A staggered differencing technique on boundary fitted curvilinear grid for incompressible flows along curvilinear or slant walls. Journal of computer mechanics 1990, Vol 7, pp:123-36.

23 Johan D. Anderson, Computational Fluid Dynamics, The Basic with Applications. Mc Graw Hill, Inc; 1995.

24 Demirdzic I., Gosman AD., Issa RI, Peric M., A calculation procedure for turbulent flow in complex geometries. Computer & Fluid 1987, Vol 15, pp:251-73

25 Takizawa A., Koshizuka S., Kondo S. Generalization of physical component boundary fitted coordinates (PCBFC) method for the analysis of free surface flow. International journal of numerical method in fluid 1992, Vol 15, pp:1213-37.

4

Barrel and port plate

This chapter analyses the pressure distribution, leakage, force and torque between the barrel and the port plate of an axial piston pump by simulating Reynolds equations of lubrication by FDM (finite difference method). The overall mean force and torques over the barrel are evaluated from simulated pressure and it shows that the torque over the XX axis is much smaller than the torque over the YY axis. A detailed dynamic analysis is then studied by using the temporal torque calculated by Bergada et al [27].

4.1 Introduction.

It is known that an axial piston barrel experiences small oscillations due to the forces acting over it. Cavitation also occurs in many cases, sometimes damaging the plate and barrel sliding surfaces and therefore reducing the volumetric and overall efficiency of the pump. More importantly, the resulting failure of the pump is often a critical issue in modern industrial applications. Piston pumps and motors are not fully understood in analytical detail, since problems related to cavitation, mixed friction and barrel dynamics, among others, are yet to be resolved via explicit methods. This chapter attempts to bridge this gap by simulating Reynolds equation of lubrication, in connection with an important area of barrel/port plate leakage flow and associated torque dynamics.

Helgestad et al [1] studied theoretically and experimentally the effect of using silencing grooves on the temporal pressure and leakage fluctuation in one piston cycle. Triangular and rectangular silencing grooves versus port plate 'ideal timing' and standard port plate were compared. For a range of operating conditions, the choice of triangular entry grooves was deduced to be the most appropriate. Martin and Taylor [2] analysed in detail the start and finish angles for the pressure and tank grooves to have ideal timing. As in [1] graphs are presented to understand the temporal pressure and flow in a single piston, but leakage flow was not considered. The results showed that triangular silencing grooves were more appropriate in all cases except when the pump parameters are fixed; in such case ideal timing main grooves were preferable. Edge et al [3] presented an improved analysis able to evaluate piston temporal pressure and flow, the improvement being based

on taking into account the rate of change of momentum of the fluid during port opening. As in previously reported work, triangular silencing grooves were shown to be most appropriate for a piston pump operating over a wide range of working conditions. With regard to cavitation erosion, they defined the most severe region to be at the end of the inlet port and at the start of the delivery port.

Jacazio and Vatta [4] studied the pressure, hydrodynamic force and leakage between the barrel and plate. The study used Reynolds equation of lubrication, integrating it when considering pressure decay in the radial direction and including rotational speed. They found equations for the pressure distribution and lift force which showed the dependency of these parameters with rotational speed. Yamaguchi [5] demonstrated that a port plate with hydrostatic pads allows fluid film lubrication over a wide range of operating conditions. When analysing the barrel dynamics he took into account the spring effect of the shaft and by changing some physical parameters he determined the most likely cases for metal to metal contact between barrel and valve plate to occur. Yamaguchi [6] experimentally studied the barrel and plate dynamics, using position transducers, and used 4 different plates for experimentation, three of them with a groove, one without a groove and no outer pad. He found that the gap between the barrel and plate oscillates, the oscillation having a large peak and an intermediate smaller peak. For any kind of fluid used, it was found that the film thickness and amplitude increased with increasing inlet pressure.

Matsumoto and Ikeya [7] experimentally studied the friction, leakage and oil film thickness between the port plate and cylinder for low speeds. They found that the friction force was almost constant with rotational speed, but strongly depended on supply pressure and static force balance. In a further paper, Matsumoto and Ikeya [8] focussed more carefully on the leakage characteristics between the cylinder block and plate, again for low speed conditions. The results showed that the fluctuation of the tilt angle of the barrel and the azimuth of minimum oil film thickness depended mainly on the high pressure side number of pistons. Kobayashi and Matsumoto [9] studied the leakage and oil film thickness fluctuation between a port plate and barrel. They integrated numerically the Reynolds equation of lubrication, taking into account the pressure distribution in both the radial and the tangential direction. The flow, barrel tilt and barrel/port plate clearance versus angular position were determined at very low rotational speeds. Weidong and Zhanlin [10] studied the temporal leakage flow between a barrel and plate and between piston and barrel, and considered separately the leakage from each barrel groove and the effect of the inlet groove. Barrel tilt was not taken into consideration. Yamaguchi [11, 12] gives an overview of the different problems found when considering tribological aspects of pumps. When assessing the plate and cylinder block performance, he points out the effect of the leakage for different fluid viscosities when the port plate has or has not a hydrodynamic groove. It was found that the use of a groove stabilizes the leakage for different fluid viscosities.

Manring [13] evaluated the forces acting on a cylinder block and its torque over the cylinder main axis. He considered the pressure distribution at the pump outlet as constant and the decay along the barrel lands as logarithmic, independent of the barrel tilt and

turning speed. In a further study [14] he also investigated various port plate timing geometries within an axial piston pump. It was found that a constant area timing groove design had the advantage of minimizing the required discharge area of the timing groove, the linearly varying timing groove design having the advantage of utilizing the shortest timing groove length, and the quadratic timing groove design had no particular advantages over the other two. Zeiger and Akers [15] considered the dynamic equations of the swash plate which were linked with piston chamber pressures. They defined first the temporal piston chamber pressure, taking into account the area variation at the inlet and outlet groove entrance. The torque over the swash plate was dynamically and statically evaluated, finding that the torque average changed mainly with the swash plate angle, turning speed and outlet pressure. They compared simulation and experimental results finding a good correlation, although leakage was not evaluated. In a further study [16] they presented a model consisting of a second order differential equation of the swash plate motion and two first-order equations describing the flow continuity into the pump discharge chamber and into the swash plate control actuator.

One of the first studies focussing on the understanding of the operating torques on a pump swash plate was undertaken by Inoue et al [17, 18]. They found theoretically that the exciting torque acting on the swash plate had a saw tooth shape. They also measured the torque on the swash plate finding that it had two peaks while the exciting one had a single peak. They defined the second peak as the one appearing when the system reached its natural frequency. Manring and Johnson [19] defined the dynamic equations of the swash plate in an axial piston pump, such equations having regard to the effect of the two actuators which maintain the swash plate in position. Wicke et al [20] simulated the dynamic behaviour of an axial piston pump using the program *bathfp*. They focussed the study on understanding the influence of swash plate angle variation on the piston forces and the yoke moment around the turning axis They found that an increase of swash plate angle increased the risk of cavitation in the cylinder chamber at the beginning of the suction port, and also decreased the time averaged yoke moment and increased peak to peak variations. In the paper by Manring [21], he further analyzed the dynamic torque acting on the swash plate. As in a previous study he did not consider the swash plate inertia and damping. He noticed that piston and slipper inertia tends to destabilize the swash plate position, although the most important term which created torque onto the swash plate was due to piston pressure. Gilardino et al [22] defined the dynamic equations which gives the torque onto the swash plate and including the torque created by the displacement control cylinders.

In Ivantysynova et al [23] a new method of prediction of the swash plate torque based on the software CASPAR is presented and which calculates the non isothermal gap flow and pressure distribution across all piston pump gaps. The study defined a direct link between the dynamic torque acting on the swash plate and the small groove dimension located at the entrance and exit of the valve plate main groove. Manring [24] studied the forces acting on the swash plate in an axial piston pump and took into account “secondary swash-plate angle” as well as the primary swash plate angle. He demonstrated that the use of a secondary swash plate angle will require a control and containment device that is capable of exerting a thrust load in the swash plate horizontal axis direction. In a further

study [25] he examined the control and containment forces for a cradle-mounted, axial-actuated swash plate, showing that an axial-actuated swash plate tends to keep the swash-plate well seated within the cradle during all operating conditions. Bahr et al [26] used the swash plate dynamic equations, found in previous papers, to create a dynamic model of a pressure compensated swash plate axial piston pump with a conical cylinder block. They implemented the equations of the compensating unit to create a full model of the pump. The equations were integrated using Matlab Simulink, finding that the lateral moment acting on the swash plate fluctuates in a periodic fashion and contains nine harmonics and a negative mean value.

Despite the amount of papers published, evidence has not been found regarding a full investigation of the described effects, and this chapter considers this task in a methodical way by considering pressure distribution, leakage, force and torque distribution and then adding barrel dynamics.

4.2 Governing equations

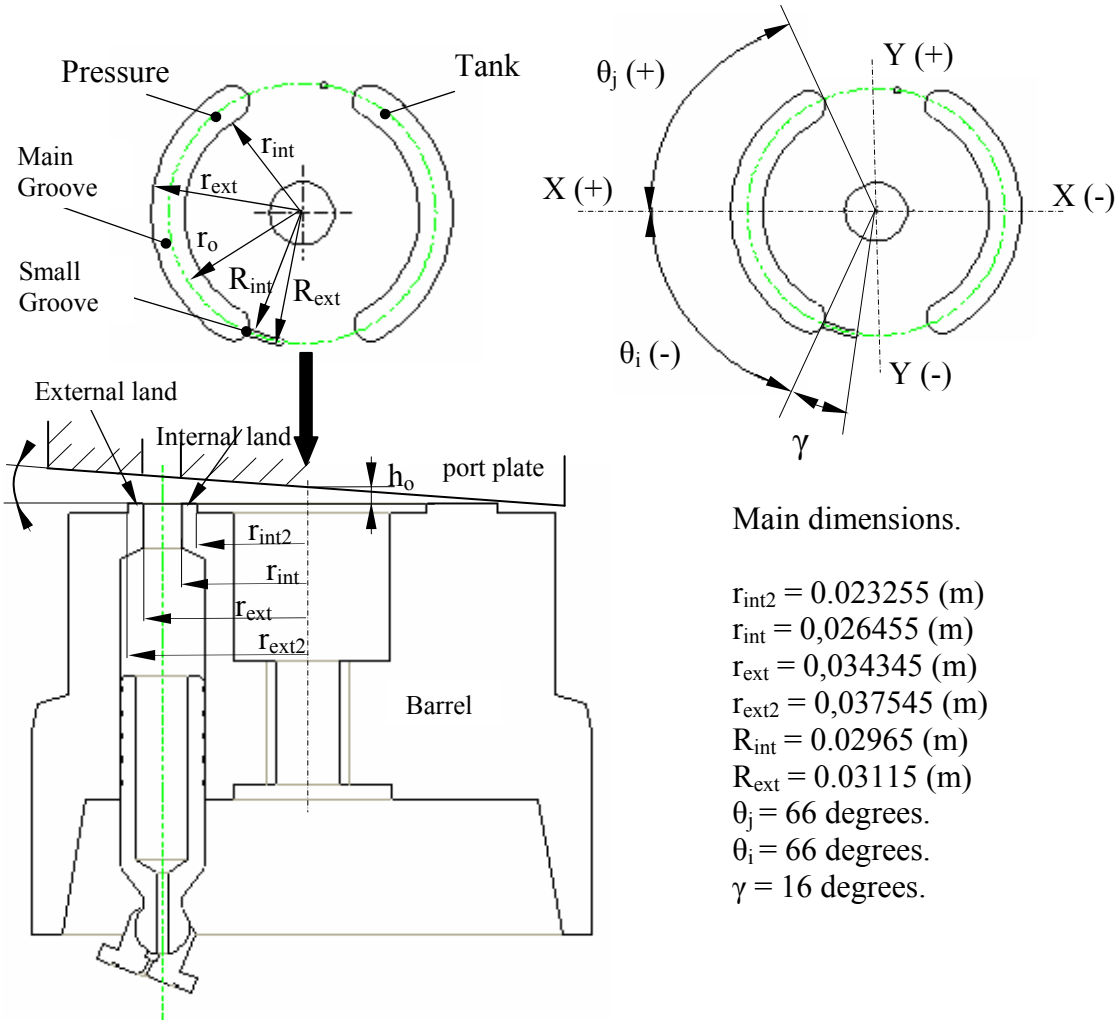

Main dimensions.

r_{int2} = 0.023255 (m)
r_{int} = 0,026455 (m)
r_{ext} = 0,034345 (m)
r_{ext2} = 0,037545 (m)
R_{int} = 0.02965 (m)
R_{ext} = 0.03115 (m)
θ_j = 66 degrees.
θ_i = 66 degrees.
γ = 16 degrees.

Figure 4.1 - Barrel/port plate configuration

Figure 4.1 represents the barrel and port plate face of an axial piston pump, one of the pistons being drawn for clarification. The port plate transfers the flow rate from the external connecting ports via two large kidney-shaped slots machined in the port plate inner face, one at the pump inlet and the other at the pump outlet. These port plate slots, often called grooves, are shown in figure 4.1 where the main dimensions and the central axes are also shown. Notice that a timing groove is placed at the entrance of the main groove on the pressurised side. The entrance to each piston in the barrel is via an associated small kidney shaped port referred to later as the 'piston groove', that is, there are 9 piston grooves machined on the face of the barrel. The sign convention is that the positive side of the 'X' axis is towards the left side of the 'Y' axis, and the barrel is slightly tilted with respect to the port plate with a tilt angle 'α'. The port plate is secured to the main body of the pump with four bolts and the barrel is pushed towards the port plate by a spring located at the bottom of the barrel, and not shown in figure 1. This fixing mechanism therefore carries an additional load induced by the torque created by the pressure differential across the pump when in operation. Since laminar flow exists then the flow field in barrel port plate gap can be analyzed by Reynolds equation as given in equation (4.1).

$$\frac{\partial}{\partial r}\left(r\, h^3 \frac{\partial p}{\partial r}\right) = 6\mu\omega r \frac{\partial h}{\partial \theta} \tag{4.1}$$

When solving this differential equation, two pressure boundary conditions are needed. These boundary conditions are the pressure at the internal and external part of each land, pressures which happen to be the pump internal pressure and the tank pressure, as presented in figure 4.1.

4.3 Computational method

A numerical solution of the original differential equations has also been undertaken specifically for this study of flow through the gap between the barrel and the port plate. A second order finite difference technique has been implemented to equation (4.1). The matrix form of resulting algebraic system of equations has been solved by using Tri diagonal matrix algorithm (TDMA). A parabolic flow profile presented by equation (4.2) has been used to calculate leakage from simulated pressure field.

$$Q = \frac{1}{12\ \mu}\frac{\partial P}{\partial r} H^3\ r\ \Delta\theta \tag{4.2}$$

Regarding the mesh selection, it is important to point out that the mesh created in the θ direction along the main groove lands has a step size much bigger than the step size needed in the θ direction along the timing groove lands. This is due to the fact that the land for the barrel plate in the radial direction associated with the main groove is much smaller than the one associated with the timing groove. Therefore although the flow will be mostly radial in both cases, the effect of barrel rotation will be more intense along the small groove lands. Nevertheless, it was found that the radial direction pressure drop in

both cases was much bigger than the tangential pressure drop. To increase the accuracy of the results at every cell, the average pressure of all four grid points was used.

4.4 Results

Numerical simulations have been performed for a set of inlet pressures (15 MPa to 40 MPa) at different rotation speeds (1440 rpm and 2000 rpm) and clearances (1-10 microns) Leakages, forces and torques are calculated from simulated pressure. By using the torque presented by Bergada et al [27] barrel dynamics have been simulated by using MATLAB Simulink model.

4.4.1 Pressure distribution.

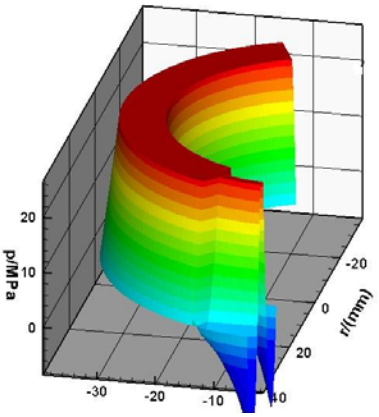

a) 2 microns, 1440 rpm and 25 MPa

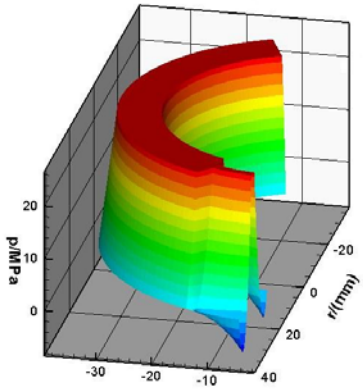

b) 3 micron, 1440 rpm and 25 MPa

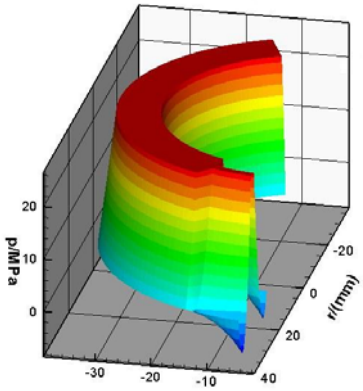

c) 3 microns, 2000 rpm and 25MPa

Figure 4.2 - Pressure distribution along the main and small grooves for a set of different parameters.

Figure 4.2 represent the pressure distribution along the main groove and timing groove lands for different clearance and turning speeds. At this point it is interesting to reflect on the work by Edge et al [3] who found that the most severe region for cavitation erosion was at the end of the inlet port and the start of the delivery port, as predicted by solution shown in figure 4.2. From figure 4.2a) and 4.2b) it is shown that cavitation at the entrance of the timing and main groove is more likely to appear as the clearance is reduced.

The pressure asymmetry is accentuated as the central clearance decreases, and it is also accentuated as the inlet pressure decreases. It is important to notice that as the turning speed increases, the pressure distribution asymmetry increases as well and will tend to create a low pressure area at both sides of the groove entrance. Therefore it can be said that according to the simulation, cavitation at the entrance of the timing and main groove is more likely to appear when working under low pressures, small clearances, and high turning speeds.

4.4.2 Leakage in the main groove and the timing groove.

Figure 4.3 represents the leakage for different central clearances 'ho', where for each clearance the maximum angle α possible has been used. Figure 4 a) shows the leakage from the main groove and figure 4.3b shows the leakage from the timing groove

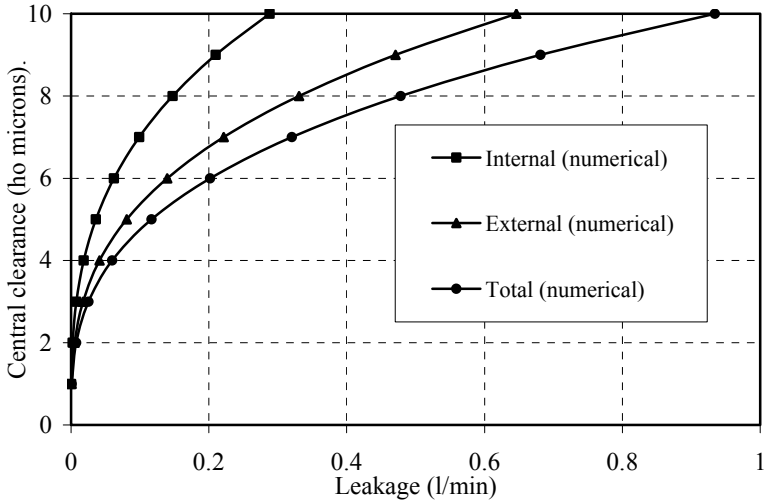

a) Main groove

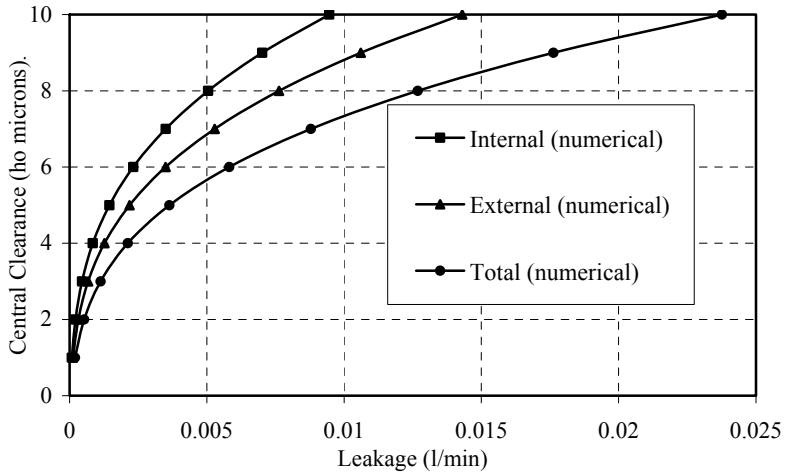

b) Timing groove

Figure 4.3 - Leakage between the barrel and plate for different central clearances and for maximum α at each clearance. Internal pressure 25 MPa

Although not presented, the leakage variation with pressure differential is linear as expected for both grooves. From these graphs it is clearly noticed that leakage is much higher on the external land than on the internal one. Leakage also has the tendency to reach an asymptotic value as the barrel-plate distance increases. When comparing figures 4.3 a) and 4.3 b) it can be said that the leakage due to the timing groove is less than 5% of the main groove leakage. The reason why the timing groove leakage is so small is because the land between the groove and the exterior is much bigger than in the main groove.

4.4.3 Force acting on the barrel.

Figure 4.4 represent the overall force four or five pistons are under pressure. The reality is that values will fluctuate between the two total limits. When computing the overall force due to the main groove, timing groove and cylinder pressure in figure 4.4, it is shown that the timing groove plays a very small role. Therefore, all changes in force due parameters other than pressure will be negligible. It can be said that the inclusion of the small groove would bring an increase of force of typically 10% for the case studied. It is very important to point out that when considering the force due to the cylinders, it is noticed that when the fifth piston is under pressure the total force over the barrel is much more balanced than when just 4 cylinders operate, in fact, the fluctuation of the total force when acting 4 or five pistons is of almost 40% of the total force acting over the barrel.

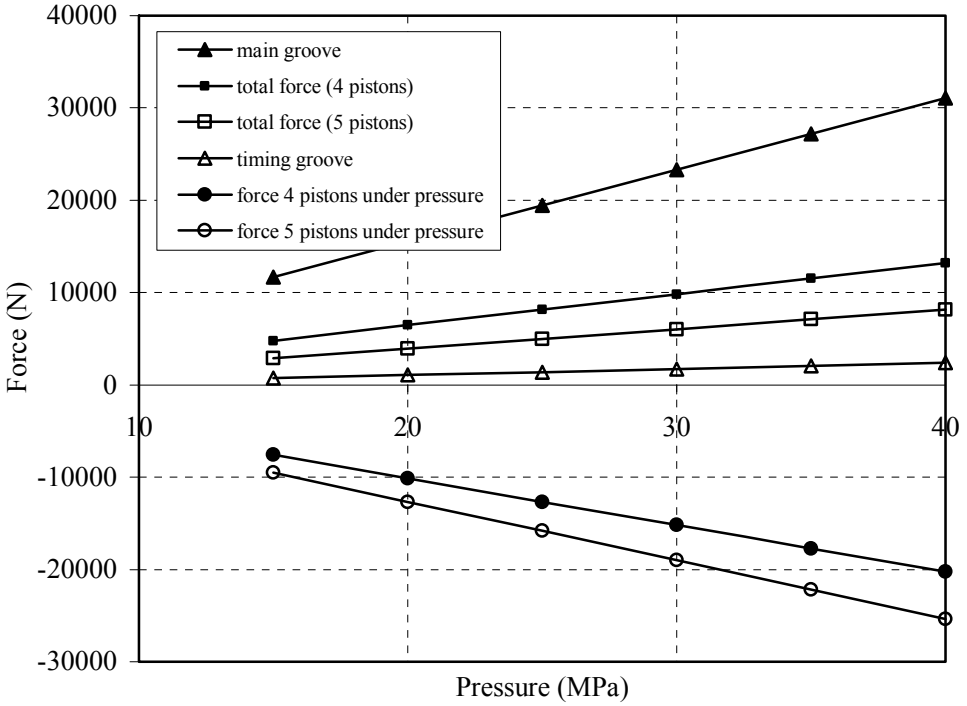

Figure 4.4 - Mean force over the pump barrel for a set of pressure differentials.

4.4.4 Mean torques about the XX and YY axes.

Perhaps the most interesting aspect of this study regarding average steady state conditions is the fact that torque over the "X" and "Y" axes can now be clearly and explicitly defined.

Consider first the torque about the XX axis, figure 4.5 represent the torque due to main groove and timing groove with respect to XX axis where it is noticed that the maximum torque over the "X" axis will be found for the highest turning speeds and smallest clearances.

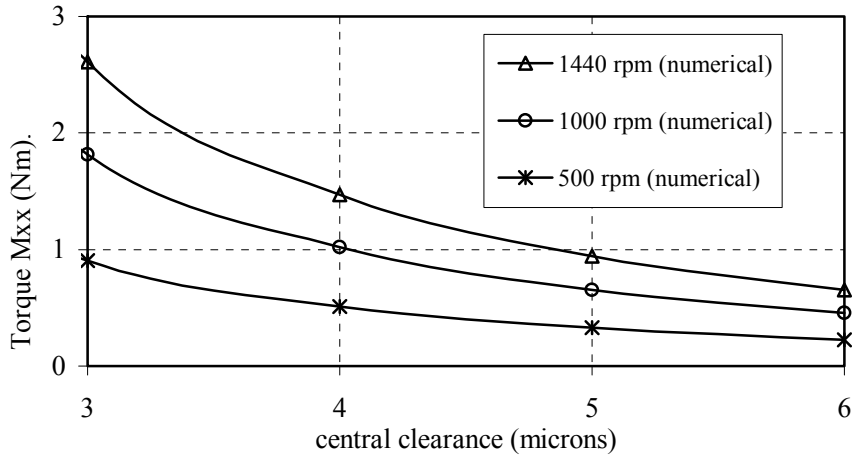

a) main groove

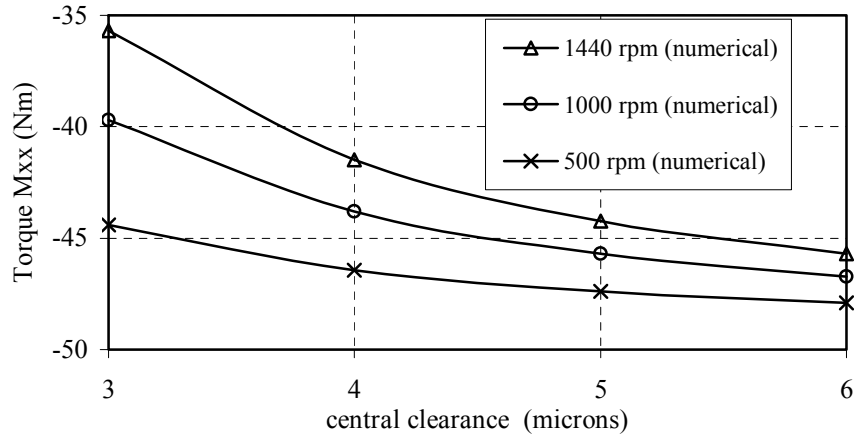

b) timing groove

Figure 4.5 - Mxx Torque due to the main and timing groove effect, maximum tilt, 25MPa.

To be analytically appropriate, the minimum clearance has been set to 3μm since cavitation exists in the small groove below this clearance, even though the area of cavitation is very small as previously discussed. It has to be pointed out that the torque increases with the central clearance for the timing groove and will be numerically greater

than the effect due to the main groove. Note also that the torque due to the main groove is not zero due to the effect of angular velocity which distorts the pressure distribution around the groove. It is also noticed that the main groove torque acts in the opposite direction to the timing groove torque; the main groove torque is mainly created by the effect of rotational speed, but the timing groove torque is mainly created by the static pressure.

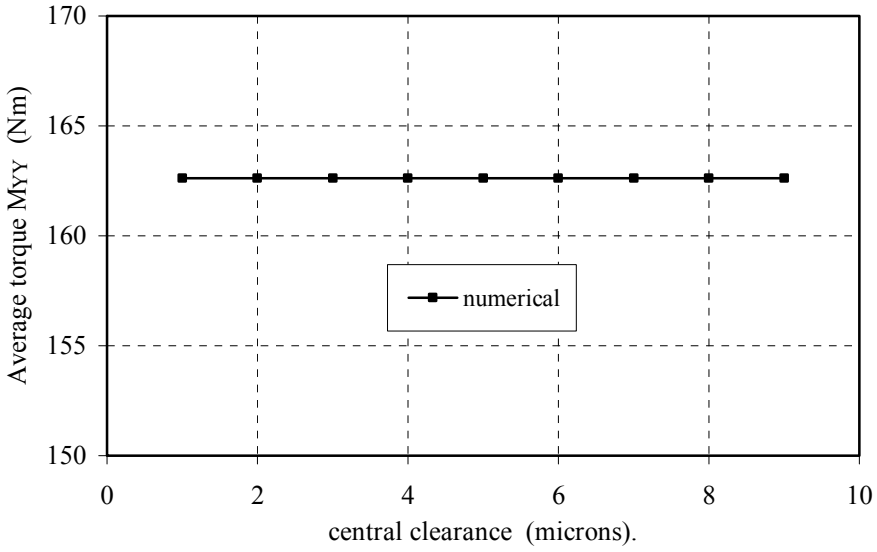

1) Main groove

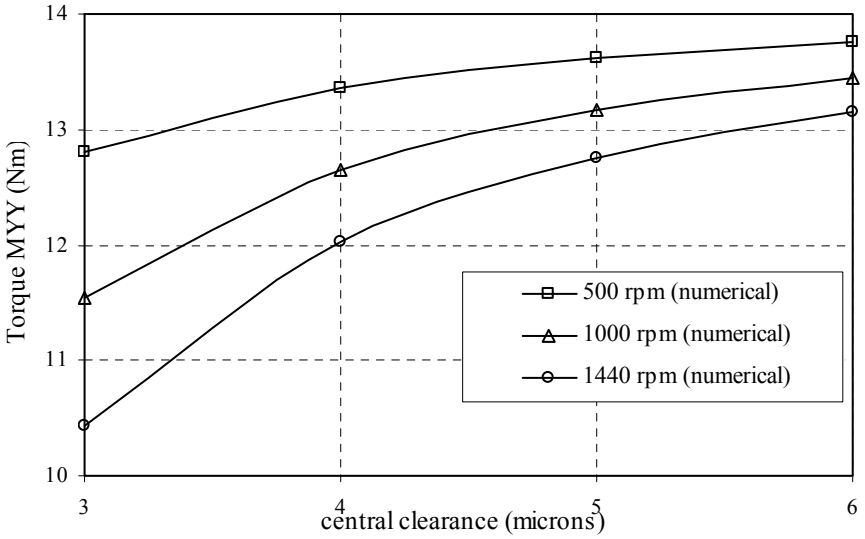

b) timing groove

Figure 4.6 - Myy torque due to the main and timing groove effect, maximum tilt, 25MPa.

Consider next the torque about the YY axis, Figure 4.6 shows the torque Myy for the main groove and the timing groove versus tilt angle and for a set of central clearances. These have been represented in a consistent way to those for Mxx, but it is clear that the contribution from the main groove is substantially constant for a particular pump pressure. Figure 4.6a shows that the effect of central clearance change is negligible.

It is important to note when considering the main groove, that the contribution from the pistons varies with angular position. Therefore figure 4.6a shows the average torque evaluated over a rotation of 40^o. The timing groove effect is of course substantially lower than the main groove effect although Myy does increase with increasing central clearance and decreases with increasing speed. This effect is perfectly understandable once it is understood what happens with the pressure distribution on both lands of the timing groove when modifying the barrel turning speed and or the central clearance. As the rotational speed decreases and/or the clearance increases, the pressure distribution across and along the timing groove lands tends to be higher and more symmetrical, giving a higher value for the torques about both axis. Figures 4.5b and 4.6b clearly indicate that the maximum torques due to the timing groove occur at the lowest speed and highest central clearance.

4.4.5 Torque dynamics.

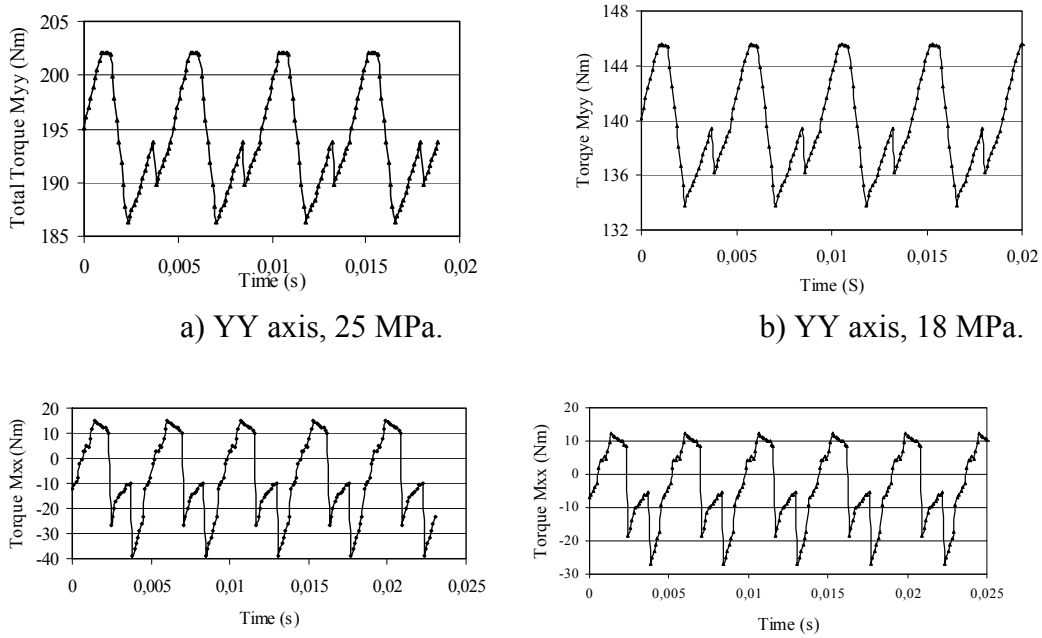

a) YY axis, 25 MPa. b) YY axis, 18 MPa.

c) XX axis, 25 MPa. d) XX axis, 18MPa.

Figure 4.7 - Dynamic torque variation about each axis (1440 rpm, 18 and 25MPa, ho = 4μm, α = 0.006104 degrees.)

Until this point, pressure, leakage, force and torque versus the main barrel axis have been evaluated in the absence of piston motion effects by just considering average values. However as the barrel turns around the pump main axis, then in fact the area under pressure will depend on the number and position of the pistons appropriate to the geometry. Therefore the leakage, force and torque over the two main axes will vary with barrel position. This dynamics torque has been calculated by Bergada et al [27] by taking into account different angular position of pistons during the one complete cycle. Figure

4.7 represents the temporal net dynamic torque over the barrel, calculated by Bergada et al [27].

4.4.6 Barrel dynamics.

Once the torques M_{XX} and M_{YY} acting over the barrel swash-plate system are known, the theoretical dynamic barrel position versus the barrel main axis can be calculated by implementing different models. In the present work two models have been implemented in order to simulate barrel dynamics.

Figure 4.8 shows the measured temporal barrel position (measured by Dr. Josep M Bergada) obtained using the test rig 2 defined in chapter 7, and after the run-out signal has been removed. This figure shows several peaks of frequencies around 216 Hz and others which have frequencies around 1100 Hz. Such peaks will be discussed later.

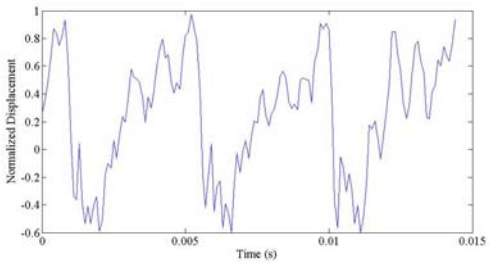

Figure 4.8 - Experimental position dynamics, XX axis, 18 MPa

4.4.6.1 Model 1 – This model considers a constant friction torque which is created due to metal to metal contact. The independent dynamic equations over the XX and YY axes may be approximated as follows:

$$I_x \ddot{\delta} + B_x \dot{\delta} + K_x(\delta - \delta_0) + F_{forces_x} * \text{sign}(\dot{\delta}) = M_{XX} \tag{4.3}$$

$$I_y \ddot{\alpha} + B_y \dot{\alpha} + K_y(\alpha - \alpha_0) + F_{forces_y} * \text{sign}(\dot{\alpha}) = M_{YY} \tag{4.4}$$

When using equation (4.3), being the input torque the Mxx given in figure 4.7, the temporal barrel position will be found from the simulink diagram defined in figure 4.9. A similar kind of simulink model is needed when using equation (4.4).

The damping coefficient for the barrel piston assembly may be considered small, but it is highly dependent on oil temperature. Friction forces exist on the barrel face and the barrel circumference, and act mainly against the turning movement of the barrel, and can be considered small when studying the barrel XX, YY axis acceleration. Also the torsional spring constant, although unknown, has to play an important role when studying the

barrel dynamics and inertia effects will need to be considered. A mean value defined in Bergada et al [27] for inertia (Ixx = Iyy = 0,0127 Kg m^2) is used for the simulink model.

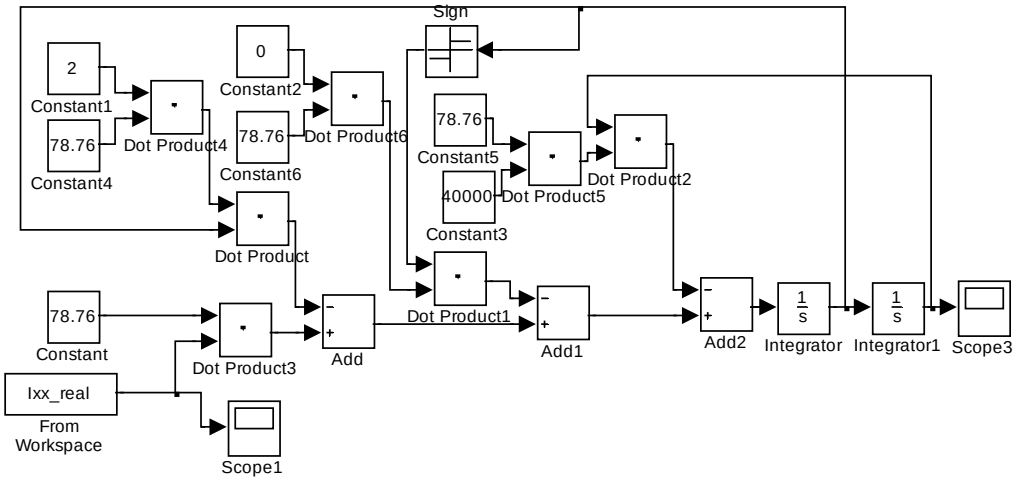

Figure 4.9 - Matlab simulink representation of equation (4.3).

The simulated barrel dynamic gap position from simulink is presented in figures 4.10 and shows the small effect of the damping coefficient on the dynamic behaviour. Notice that, as expected, an increase in the damping coefficient will reduce the fluctuation therefore reducing the magnitudes of both peaks. When comparing figure 4.10 with 4.8 it is seen that the general shape is very similar although the high frequency peaks of about 1100 Hz do not appear in the simulation results.

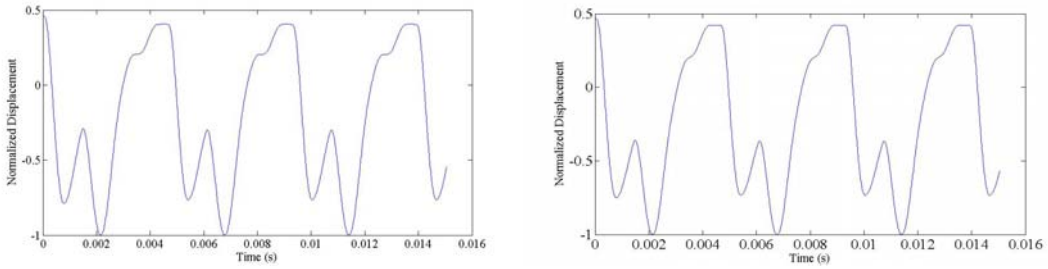

a) Damping coefficient 25 $\left[\frac{\text{Nm}}{\text{rad s}^{-1}}\right]$. b) Damping coefficient 30 $\left[\frac{\text{Nm}}{\text{rad s}^{-1}}\right]$

Figure 4.10 Computed gap position dynamics, XX axis. Frictional torque 3Nm.

It is noticed that the experimental result are very noisy and this is attributed to high frequency fluid dynamic effects not included in the mathematical model. This frequency of 1250Hz is possibly created by the fluid momentum change during port opening, as reported by Edge et al [3], and may very well explain some of the peaks of the experimental results obtained. Nevertheless, the experimental trends show clearly the peak created by the torque increase as each piston groove faces the timing groove, having a good agreement with the theory presented. It is to be noticed that experimental and simulated results have the same frequency, the pumping frequency.

4.4.6.2- Model 2 – To try to find out the origin of the high frequency peaks, a second mathematical model was created. This model considers the friction torque as a function of displacement. The independent dynamic equations over the XX and YY barrel axes may be approximated as follows:

$$I_x \ddot{\delta} + B_x \dot{\delta} + K_x(\delta - \delta_0) + \overbrace{\frac{E A_0}{L_0} r^2}^{M_E} \max(|\delta| - \delta_L; 0) = M_{XX} \tag{4.5}$$

$$I_y \ddot{\alpha} + B_y \dot{\alpha} + K_y(\alpha - \alpha_0) + \overbrace{\frac{E A_0}{L_0} r^2}^{M_E} \max(|\alpha| - \alpha_L; 0) = M_{YY} \tag{4.6}$$

Elastic metal to metal forces exist between the barrel face and the port plate; they act in opposite direction than the input torque and depend on the Young modulus, the area of contact and the distance the barrel penetrates into the plate. Although such elastic forces can in general be considered small when studying the barrel XX, YY axis acceleration, they play a relevant role regarding the barrel dynamics. Notice that in these equations, the term evaluating the elastic metal to metal force, acts just when the barrel tilt is higher than the maximum existing tilt for the working conditions at each case.

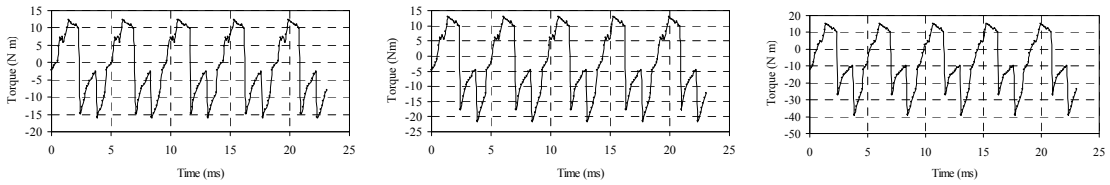

a) b) c)

Figure 4.11 - several input torques Mxx at different pump output pressures.
a) 15 MPa; b) 17.5 MPa; c) 25 MPa.

Figure 4.11 presents three input perturbation torques Mxx, generated along the XX axis, for three different pump output pressures, 15, 17.5 and 25 MPa. Introducing these torques as inputs in equation (4.5), and via using the Matlab Simulink package, several dynamic barrel fluctuations as a function of the damping coefficient B, spring torsional constant K and the elastic metal to metal reaction torque M_E were found and presented in figure 4.12.

From these results it is noticed that if the spring torsional constant, which depends on the barrel spring and the pump main axis is big enough, the barrel will be able to follow the input torque generated by the pump. The effect of elastic forces created in the barrel/port plate surface enhances the perturbation peaks, in fact, the metal to metal elastic forces play a decisive role when studding the barrel dynamics, as it is seen from figures 4.12 a,b,c. Notice that, the simulated results shown in figure 4.12, resembles very closely the experimental ones presented in figure 4.8, specially when considering the small peaks of high frequency.

It is therefore demonstrated that the frequencies of around 1100 Hz, are in fact appearing when the pump barrel has a very high stiffness, able to follow the small torque perturbations created by the pump along the XX axis; such huge stiffness appears at high pressures and high temperatures, showing that under this conditions the barrel response is very fast. Also under these conditions metal to metal elastic forces play a very relevant role in the barrel dynamics. It is demonstrated that when the elastic torque is considered, the fluctuation peaks amplitude increase, fig 16 b, c and e, f, clearly showing that elastic metal to metal forces need to be considered when aiming to understand the full barrel dynamics. In reality, elastic barrel/plate forces can be quite different along time, then the metal to metal forces, depend on the random contact between surfaces. This explains why the measured frequencies of the fluctuation peaks are not constant, although oscillate around 1100 Hz.

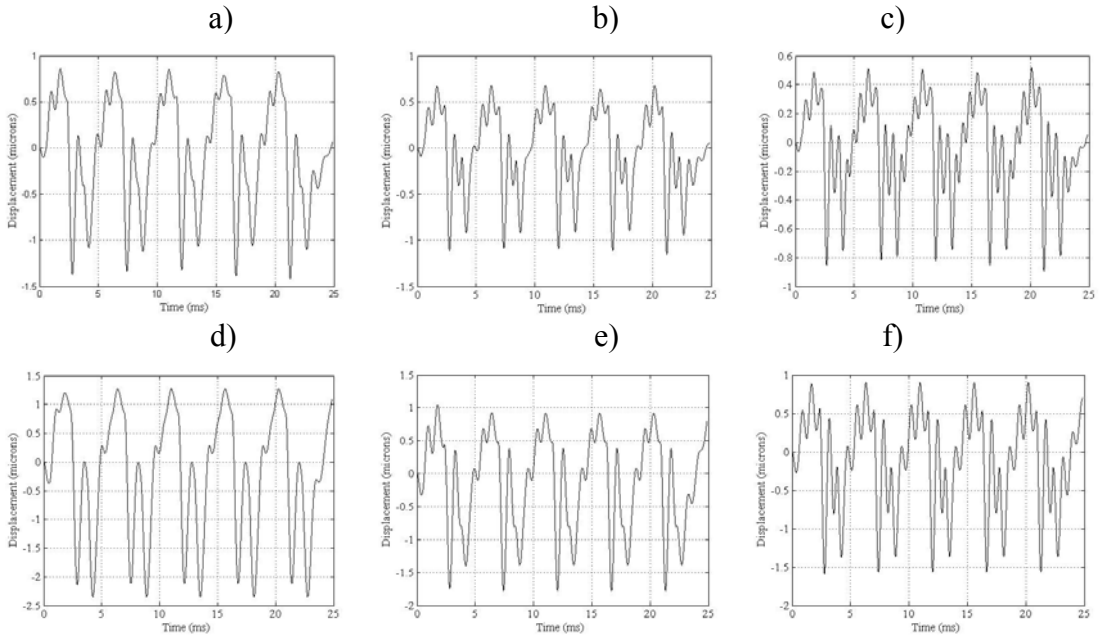

Figure 4.12 - several barrel dynamics via Simulink modelisation for different parameters.
[a] 15MPa, B=35, $K = 6\times10^5$, $M_E = 0$. [b] 15MPa, B=35, $K = 6\times10^5$, $M_E = 1.68\times10^5$
[c] 15MPa, B=35, $K = 6\times10^5$, $M_E = 5.6\times10^5$.[d] 17.5MPa, B=35, $K = 4\times10^5$, $M_E = 0$
[e] 17.5 MPa, B=20, $K = 6\times10^5$, $M_E = 0$. [f] 17.5 MPa, B=20, $K = 6\times10^5$, $M_E = 1.68\times10^5$

The effect of barrel damping coefficient is presented in figure 4.12, d, e, f, where it is noticed that a decrease of the damping coefficient (which happens when the oil temperature increases), has a similar effect than an increase of the elastic metal to metal torque, both enhance the barrel fluctuations amplitude. The system response is much relevant at high pressures and high temperatures, since the fluctuations in the input torques are increasing in amplitude with the increase of pressure and the damping coefficient decreases as temperature increases.

4.5 Conclusions.

Reynolds equation of lubrication has also been applied to the gap between the barrel and port plate by using finite difference method. Leakage was found to be greater across the external land than the internal land, for the same operating pressure, and typically by a factor of 2 whether it be related to pressure or central clearance. As expected, the small timing groove produced a significantly lower leakage than the main groove and could probably be neglected from a total flow loss point of view. It was found that cavitation in pumps is more likely to appear for smaller clearances, smaller output pressures and bigger turning speeds.

The effect of precisely defining piston position was shown to be crucial when calculating the total force on the barrel, the total force reducing as the number of active pistons changes from 4 to 5 during one cycle. This was shown to be due to the balance between piston pressure effects and groove effects, the former becoming more dominant as the number of pistons active changes from 4 to 5.

The total static torque is dominated by the contribution about the YY axis as anticipated from other work and simple considerations of the pumping mechanism. Individual torque contributions were shown to increase with pressure in almost a linear manner, the torque effect of the combined grooves being larger than the opposing torque due to piston pressure.

Both dynamic torques acting over the barrel XX and YY axes were taken from Bergada et al [27] and were introduced into a Simulink model to evaluate the barrel temporal position. In particular, the importance of precise modelling of the flow continuity mechanism was shown to be crucial in predicting the correct waveform shapes.

The results clearly show the torque increase as each piston groove is connected to the timing groove, as established by the theory presented. This was in spite of the requirement to extract the required data from a noisy signal due to barrel run-out. A good correlation between simulated and experimental results was found.

The fluctuation wave will present two main peaks, a small one related to the torque created when each piston enters in contact with the timing groove, and a main one created when each piston leaves the pressure kidney port, its frequency is 216 Hz. Along with the main fluctuation wave, appear another wave of a frequency around 1000-1100 Hz, this second fluctuation wave is more clearly seen when the system stiffness is high, system stiffness depends on the pump spring constant, pump central axis constant, and elastic/plastic metal to metal reaction forces, therefore as pressure increases, film thickness decreases, metal to metal contact increases, and these small perturbation peaks more clearly appear. The damping coefficient also plays an important role regarding the barrel dynamics, since as temperature increases, the damping coefficient decreases, allowing the barrel to move more freely, this is why at high temperatures and high pressures, the fluctuation wave is more clearly seen. The elastic/plastic metal to metal forces enhances the perturbation peaks increasing their amplitude.

Nomenclature.

A_0	metal to metal contact area between the barrel and the port plate (m^2).
B	barrel damping coefficient (Nm/rad s^{-1}).
E	Young modulus (N/m^2).
F_{force}	barrel frictional torque (Nm).
h	barrel general height (m).
h_o	barrel central height (m).
I	barrel moment of inertia, versus a generic angle (kg m^2).
K	spring torsional constant acting over the barrel (Nm).
L_0	port plate width (m).
M_{XX}	torque versus the barrel X axis (Nm).
M_{YY}	torque versus the barrel Y axis (Nm).
p	general pressure (N/m^2).
p_{ext}	pump inlet (tank) pressure (N/m^2).
p_{int}	pump outlet pressure (N/m^2).
Q	generalised leakage flow (m^3/s).
r	barrel generic radius (m).
r_{int}	internal radius of the main groove (m).
r_{ext}	external radius of the main groove (m).
R_{int}	internal radius of the timing groove (m).
R_{ext}	external radius of the timing groove (m).
r_m	average radius between land borders (m).
r_o	groove central radius (m).
t	time (s).
α	barrel tilt angle perpendicular to Y axis (rad).
α_0	barrel initial angular position, perpendicular to Y axis (rad).
α_L	maximum barrel tilt angle perpendicular to Y axis for a given working conditions (rad).
δ	barrel tilt angle perpendicular to X axis (rad).
δ_0	barrel initial angular position, perpendicular to X axis (rad).
δ_L	maximum barrel tilt angle perpendicular to X axis for a given working conditions (rad).
γ	small groove angle (rad).
μ	fluid dynamic viscosity (Kg/m s).
θ	barrel angle (rad).
ω	barrel angular velocity (rad/s).

References

1. Helgestad BO, Foster K, Bannister F K. Pressure Transients in an Axial Piston Hydraulic Pump. Proceedings of the Institution of Mechanical Engineers, Vol 188 No 17 / 74. 1974, 189 – 199.

2. Martin MJ and Taylor B. Optimised Port Plate Timing for an Axial Piston Pump. 5th Int Fluid Power Symposium. Cranfield, England. September 13 – 15 1978, B5 – 51-66.

3. Edge KA and Darling J. The Pumping Dynamics of Swash Plate Piston Pumps. ASME. J Dynamic Systems, Measurement, and Control. June 1989, Vol. 111, 307-312.

4. Jacazio G and Vatta F. The Block-lift in Axial piston Hydraulic Motors. The ASME / ASCE Bioengineering, Fluids Engineering and Applied Mechanics Conference. June 22-24 , 1981, Boulder, Colorado USA, 1-7.
5. Yamaguchi A. Formation of a Fluid Film between a valve plate and a Cylinder Block of piston Pumps and Motors. (2nd Report, A Valve Plate with Hydrostatic Pads). Int Journal of the Japan Society of Mechanical Engineers. Vol 30 No. 259 1987, 87-92.

6. Yamaguchi A. Bearing/seal characteristics of the film between a valve plate and a cylinder block of axial piston pumps: Effects of fluid types and theoretical discussion. The Journal of Fluid Control. Volume 20 Issue 4 May 1990, 7-29.

7. Matsumoto K and Ikeya M. Friction and leakage characteristics between the valve plate and cylinder for starting and low speed conditions in a swashplate type axial piston motor. Trans of the Japan Society of Mechanical Engineers, part C. Vol 57,1991, 2023-2028.

8. Matsumoto K and Ikeya M. Leakage characteristics between the valve plate and cylinder for low speed conditions in a swashplate-type Axial Piston Motor. Trans of the Japan Society of Mechanical Engineers, part C. Vol 57, 1991, 3008-3012.

9. Kobayashi S and Matsumoto K. Lubrication between the valve plate and cylinder block for low speed conditions in a swashplate-type axial piston motor. Trans of the Japan Society of Mechanical Engineers, part C. Vol 59, 1993,182-187.

10. Weidong G and Zhanlin W. Analysis for the real flow rate of a swash plate axial piston pump. Journal of Beijing University of Aeronautics and Astronautics. Vol 22, 2 1996, 223-227.

11. Yamaguchi A. Tribology of Hydraulic Pumps. ASTM Special technical publication. No 1310, 1997, 49-61.

12. Yamaguchi A, Sekine H, Shimizu S, Ishida S. Bearing / seal characteristics of the Oil film between a valve plate and a cylinderblock of axial pumps. JHPS 18-7, 1987, 543-550.

13. Manring ND. Tipping the cylinder block of an axial-piston swash-plate type hydrostatic machine. ASME Journal of Dynamic Systems Measurement and Control. Vol. 122 March 2000, 216-221.

14. Manring ND. Valve-plate design for an Axial Piston pump operating at low displacements. ASME J of Mechanical Engineering. Vol 125 March 2003, 200-205.

15. Zeiger G and Akers A. Torque on the Swashplate of an Axial Piston Pump. Journal of Dynamic Systems, Measurement and Control. ASME. Vol 107, September 1985, 220-226.

16. Zeiger G and Akers A. Dynamic analysis of an axial piston pump swashplate control. Proc of the Institution of Mechanical Engineers. Vol 200 No. C1,1986, 49-58.

17. Inoue K and Nakasato M. Study of the operating moment of a swash plate type axial piston pump. First report, effects of dynamic characteristics of a swash plate angle supporting element on the operating moment. The Journal of Fluid Control, Vol 22, Issue 1, 1994, 30-46.

18. Inoue K and Nakasato M. Study of the operating moment of a swash plate type axial piston pump. Second report, effects of dynamic characteristics of a swash plate angle supporting element on the cylinder pressure. Journal of Fluid Control Vol 22 Issue 1,1994, 7-29.

19. Manring ND and Johnson RE. Modeling and designing a variable-displacement open-loop pump. Journal of Dynamic Systems Measurement and Control, June 1996, Vol 118, 267-271.

20. Wicke V, Edge KA, Vaughan D. Investigation of the effects of swash plate angle and suction timing on the noise generation potential of an axial piston pump. FPST-Vol 5, Fluid Power Systems and Technology 1998, ASME, 1998, 77-82.

21. Manring ND. The control and containment forces on the swash plate of an axial piston pump. Journal of Dynamic Systems Measurement and Control, Dec1999 Vol 121, 599-605.

22. Gilardino L, Mancò S, Nervegna N, Viotto F. An experience in simulation the case of a variable displacement axial piston pump. Forth JHPS International Symposium 1999, paper 109, 85-91

23. Ivantysynova M, Grabbel J, Ossyra JC. Prediction of Swash Plate Moment Using the Simulation tool CASPAR. Proceedings of IMECE 2002 ASME International Mechanical Engineering Congress & Exposition. November 17-22, 2002, New Orleans, Louisiana USA. IMECE2002-39322, 1-9.

24. Manring ND. The control and containment forces on the swash plate of an axial piston pump utilizing a secondary swash-plate angle. Proceedings of the American Control Conference. Anchorage, AK-USA May 8-10 2002, 4837-4842.

25. Manring ND. Designing a Control and Containment device for a Cradle-mounted, Axial-Actuated Swash Plates. Jl of Mechanical Design. Sept 2002, Vol 124, 456-464.

26. Bahr MK, Svoboda J, Bhat RB. Vibration analysis of constant power regulated swash plate axial piston pumps. J of Sound and Vibration, 2003 -259(5),1225-1236.

27. Bergada JM, Watton J, Kumar S. Pressure, flow, force and torque between the barrel and port plate in an axial piston pump. Journal of dynamic systems, measurement and control, Jan 2008, Vol 130. N 1. pp 011011-1/16

5

Piston and Cylinder Clearance

In this chapter, we studied the effect of the number of grooves and their location over the piston surface, regarding piston force, torque, leakage and piston stability. A finite volume based Reynolds equation model has been formulated for the piston-cylinder clearance which considers the piston eccentricity and the relative tangential movement between piston and barrel. Different configurations of the grooves have been evaluated in search of finding minimum leakage, minimum appearance of cavitation and maximum restoring torque. Design instructions to optimize the piston behavior are also given. The flow is considered as laminar under all working conditions. The Fluid used is hydraulic oil ISO 32.

5.1 Introduction.

In the fluid power field, among the most efficient pumps are to be found the piston ones, piston dynamics plays a fundamental role in two critical processes related to fluid flow in these pumps. The first is the flow leakage through the radial clearance, which may cause considerable reduction in the pump efficiency. The second process is the viscous friction associated, with the lubricant film in the radial clearance, eventually friction metal to metal might appear. Therefore the geometry of the pistons used affects the mechanical and volumetric efficiency of the pump and its long term performance. The pistons used in these machines differ from different manufactures, then some of them cut grooves along the piston length and others don't. The present chapter clarifies the effect of the grooves being cut on piston surface.

Figure 5.1 represents a picture of the piston considered in this chapter and a two dimensional schematic diagram of it. It is important to notice from figure 1, that the piston into consideration has several grooves on the sliding surface, the aim of which is to increase stability, decrease friction and increase lateral forces.

The first studies about the groove balancing effect were conducted experimentally by Sweeney [1], who examined the pressure distribution in the piston-cylinder clearances and established a relationship existing between the leakage flow and the geometry of the clearance. Sadashivappa et al [2] examined also experimentally the pressure distribution in the clearance piston-cylinder and concluded that the eccentricity of the piston affected the performance of the piston by influencing the frictional and leakage aspects.

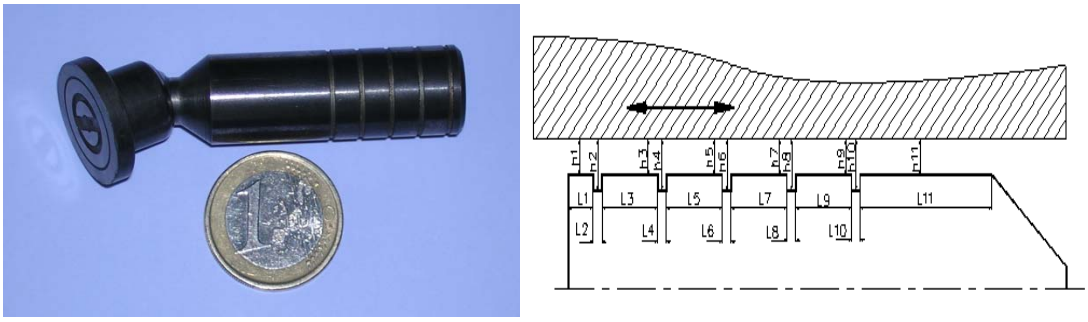

a) Piston considered in this project. b) 2-D schematic diagram of the piston.

Figure 5.1 - Piston geometry

Some attempts have been pursued to find the flow and pressure distribution theoretically taking into account the effect of the grooves, Milani [3] applied the continuity equation to link the Poiseuille equation in each land, and considered a constant pressure in each groove. The same method was used by Borghi et al [4, 5], although they applied it to a single groove tapered spool. In both cases relative movement between piston and cylinder was not considered, yet eccentricity was taken into account. Blackburn et al [6] and Merrit [7] established an analytical formulation for the pressure distribution and forces in narrow clearances. They assumed that the pressure distribution in narrow gaps was not affected by peripheral flow rates; they made an easy estimation of the sticking phenomena effects.

In any case, the most precise way to find out the leakage and pressure distribution would be via using the two dimensional Reynolds equation of lubrication. The main difficulty here is that the equation needs to be integrated numerically. Such work although when grooves were not considered was undertaken by Ivantysynova [8, 9] which found the dynamic pressure distribution and leakage between piston and barrel considering piston tilt, piston displacement and heat transfer. Elastohydrodynamic friction was also considered.

Fang et al [10] carried out a numerical analysis in order to obtain the metal contact force between the piston and cylinder and he concluded that exist mixed lubrication between the piston and cylinder, being independent on pump operation conditions such as supply pressure or the rotation speed. Prata et al [11] performed a numerical simulation for a piston without grooves, by using finite volume method, considering both the axial and the radial piston motion and explained the effect of the operating conditions on the stability of the piston.

On the other hand, the study of the machine element surfaces with grooves and narrow gaps is more generic and has a mature foundation in literature. Berger et al [12] investigated the effect of the surface roughness and grooves on permeable wet clutches by using a finite element approach and considering the modified Reynolds and force balance equations. They concluded that friction and groove width significantly influence the engagement characteristics as torque, pressure and film thickness, on the other hand groove depth did not have a significant affect on engagement characteristics. Razzaque et al [13] applied a steady-state Reynolds type equation with inertia consideration to a coolant film entrapped between a grooved separator-friction plate pair of a multi disk wet clutch arrangement. Razzaque used finite difference technique to simulate pressure distribution and flow field for different groove shapes such as rounded, trapezoidal, and V-section at different angular orientations, and found that among the profiles studied, the rounded groove performed better under the leakage and force point of view, nevertheless the use of inclined grooves caused less viscous torque and, hence, less power loss.

Lipschitz et al [14] used the Finite Difference Method to study a radial grooved thrust bearing operation and showed that rounded bottom grooves were superior to flat bottom grooves regarding the load carry capacity. Basu [15] justified the validity of the radial groove approximation when simulating parallel grooves in face seals. He used both FDM (Finite Difference Method) and FEM (Finite Element Method) and found that FDM was considerably faster. Kumar et al [16] investigated the effect of the groove in slipper-swash plate clearance, by doing finite volume formulation for a three dimensional Navier stokes equation in cylindrical coordinates. They demonstrated that the presence of the groove stabilized the pressure distribution in the clearance slipper swash plate. The grooves position was having a considerable effect on the force acting over the slipper.

An interesting amount of work has been undertaken until now, considering the geometric shape of the groves, friction parameters and its effect on the operating conditions in order to improve the piston performance, but despite all the work undertaken by previous researchers, there has never been studied, the effect of the number of grooves cut on the piston surface and specially the effect of modifying their position, including as well the piston tilt and its relative movement versus the cylinder. In this chapter, it is being investigated the piston performance by modifying the number of grooves and their position, pressure distribution in the clearance piston-cylinder, leakage force and torque acting over the piston will be discussed, also the locations where cavitation is likely to appear will be presented, discussing how to prevent cavitation from appearing via using grooves.

5.2 Mathematical model and solution technique.

In the literature [8-15], Reynolds equation of lubrication is considered a good approach to investigate the fluid flow inside a thin film. In the present work, the Reynolds equation of lubrication (5.1) in Cartesian coordinates is also applied to the piston-cylinder clearance. For a given generic piston location inside the cylinder, piston-cylinder clearance is

variable and a function of the coordinate axis $\{\theta, L\}$, see figure 5.2, being its calculation vital for the simulation of the pressure field.

$$\frac{1}{R^2}\frac{\partial}{\partial\theta}\left(\frac{h^3}{\mu}\frac{\partial p}{\partial\theta}\right)+\frac{\partial}{\partial L}\left(\frac{h^3}{\mu}\frac{\partial p}{\partial L}\right)=6\left(V_{S\theta}\frac{1}{R}\frac{\partial h}{\partial\theta}+V_{SL}\frac{\partial h}{\partial L}+2\frac{\partial h}{\partial t}\right) \tag{5.1}$$

Figure 5.3 represents the cross sectional cut, perpendicular to the piston central axis, of the piston-cylinder assembly, the figure represents the clearance piston-cylinder for two different given lengths {L (0, L_t)}, where L is greater or smaller than L_1 (position of the intersection of piston and cylinder axis).

The Length of the piston inside the barrel as a function of the piston-slipper position as the slipper slides around the swash plate (θ_{sw}) is given by equation (5.2).

$$L_t = L_0 + R_{sw}\tan\beta\left(1-\cos\theta_{sw}\right) \tag{5.2}$$

To simulate the pressure distribution in the clearance piston-cylinder, first it is important to evaluate the clearance as a function of the known variables. Equation 5.3 represents the relationship between piston diameter (D_p), cylinder diameter (D_c), length of the piston inside barrel (L_t), minimum edge clearance (Ec_1 & Ec_2) and piston tilt from barrel axis (α), see figure 2. When knowing the values of D_p, D_c, L_t, Ec_1 and Ec_2, the tilt (α) can be evaluated numerically from equation (5.3).

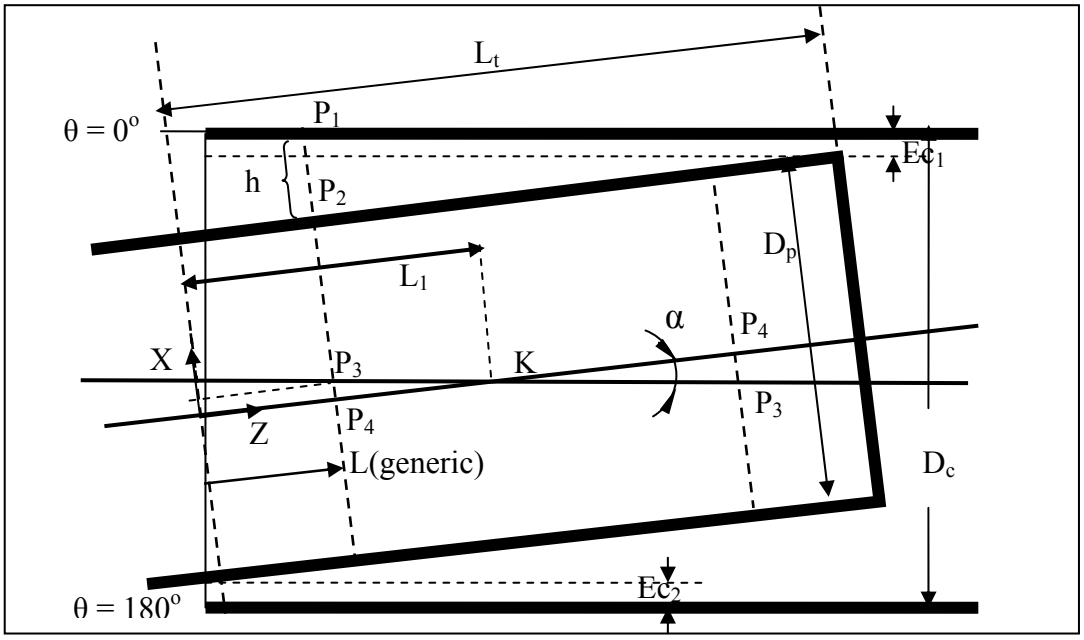

Figure 5.2 – Piston cylindrical clearance (Longitudinal view).

Once the tilt (α) is known, the gap piston barrel at any point can be calculated from equations (5.4-5.7). Equation 5.4 relates the piston minimum edge clearance Ec_2, piston

tilt (α), piston diameter and cylinder diameter with the piston length between the origin of the coordinates system and the intersection piston axis with cylinder axis, see figure 5.2. Equations 5.5 and 5.6 uses the information calculated until this moment to find out the X and Y coordinates of the point (P_1) given by the intersection between the ellipse curve presented in figure 5.3 which represents the cylinder boundary, and a generic straight line which central position is the piston central axis, the straight line is defined as a function of a generic angle θ. The intersection point (P_2) is the point between the same straight line and the piston diameter. Once (P_1) and (P_2) are found, the straight distance between them is given by equation 5.7.

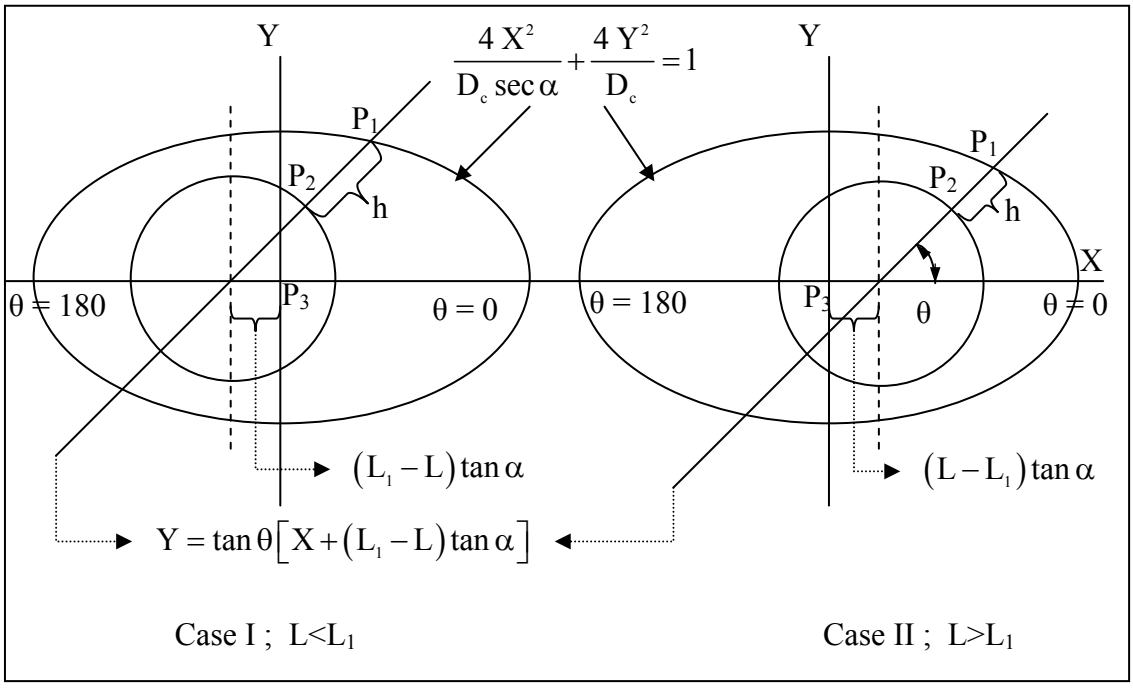

Figure 5.3 – Piston cylinder clearance (Cross sectional view) with coordinate geometric equations used to calculate clearance.

$$Ec_1 + \left(L_t - \frac{D_p}{2}\tan\alpha \right)\sin\alpha + D_p \sec\alpha + Ec_2 - D_c = 0 \tag{5.3}$$

$$L_1 \sin\alpha + \frac{D_p}{2}\sec\alpha + Ec_2 = \frac{D_c}{2} \tag{5.4}$$

$$X_1 = \frac{-(L_1 - L)\tan\alpha\,\tan^2\theta \pm \sqrt{\left(\frac{D_c \tan\theta}{2}\right)^2 + \left(\frac{D_c \cos\alpha}{2}\right)^2 - \left\{(L_1 - L)\sin\alpha\,\tan\theta\right\}^2}}{\cos^2\alpha + \tan^2\theta} \tag{5.5}$$

$$Y_1 = \tan\theta\left[X_1 + (L_1 - L)\tan\alpha\right] \tag{5.6}$$

$$h = \sqrt{\left[X_1 - \left\{r\cos\theta - (L_1 - L)\tan\alpha\right\}\right]^2 + \left[Y_1 - r\sin\theta\right]^2} \tag{5.7}$$

Reynolds equation of lubrication (Eq 5.1) has been integrated over a uniform staggered mesh by using finite volume technique described by Patanker [17]. Dirichlet type pressure boundary conditions are specified at inlet and outlet boundary and a no slipping boundary condition is imposed on the walls, as defined in equations 5.8 and 5.9.

$$V_{S\theta} = 0 \tag{5.8}$$

$$V_{SL} = R_{SW}\omega_{SW}\tan\beta\sin\theta_{sw} \tag{5.9}$$

A Couette - Poiseuille type velocity distribution profile is assumed at any point of the clearance piston-cylinder, then, once the pressure distribution in the clearance piston-cylinder will be determined, to calculate piston-cylinder leakage equation (5.10) will be used.

$$Q = \int_0^{2\pi}\int_0^{h}\left\{\frac{1}{2\mu}\frac{\partial p}{\partial L}\left(X^2 - h\,X\right) + V_{SL}\frac{X}{h}\right\} R\,d\theta\,dX \tag{5.10}$$

Using the methodology presented here, a set of computational tests were developed, all tests used 30 MPa pump outlet pressure, clearances piston-cylinder were of 3, 15 and 20 microns, and pump turning speeds ranged from 200 rpm to 1000 rpm. Results from the simulation will be discussed in the next section.

5.3. Results.

5.3.1 Clearance and Grid independency test.

Following the instructions given in the previous section and specifically from equation 5.7, the calculated piston-cylinder clearance is presented in figure 5.4, two different cases are considered, when no groove exists on the piston surface and when five equiv-distance grooves are being cut on the piston surface, for a groove depth of 8 microns and a piston cylinder central clearance of 3 microns. The clearance presented in figure 5.4 has been calculated for each case and configuration of the grooves studied, being this the first step to find out the simulated pressure and flow field between piston and cylinder. Notice that a groove depth of 8 microns is chosen in figure 5.4.b, to clarify the effect of the tilt on groove clearance. A real groove depth of 0.8mm has been used in all simulations performed.

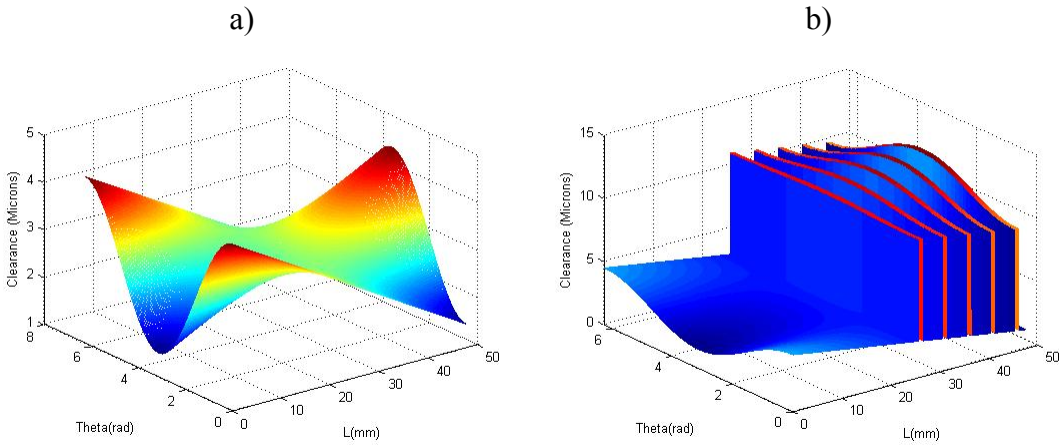

Figure 5.4 – clearance piston barrel gap, with and without groove, 3 microns piston-cylinder central clearance, 1.5 microns edge clearance. [a] No groove. [b] 5 groove. (8 microns groove depth)

For the CFD model created a uniform grid in both directions (θ, L) was chosen. Grid independency test has been performed on two different grid sizes (360-1000) and (720-1600). Figure 5.5 presents the resulting pressure distribution for a five grooved piston, at 30MPa inlet pressure, 3 microns central clearance, 1.5 micron minimum edge clearances (Ec_1, Ec_2) and 0.8mm groove depth. It can be concluded from figure 5.5 that solution is independent of the grid size and therefore a common grid size (360-1000) is chosen for the rest of the simulation in the present work.

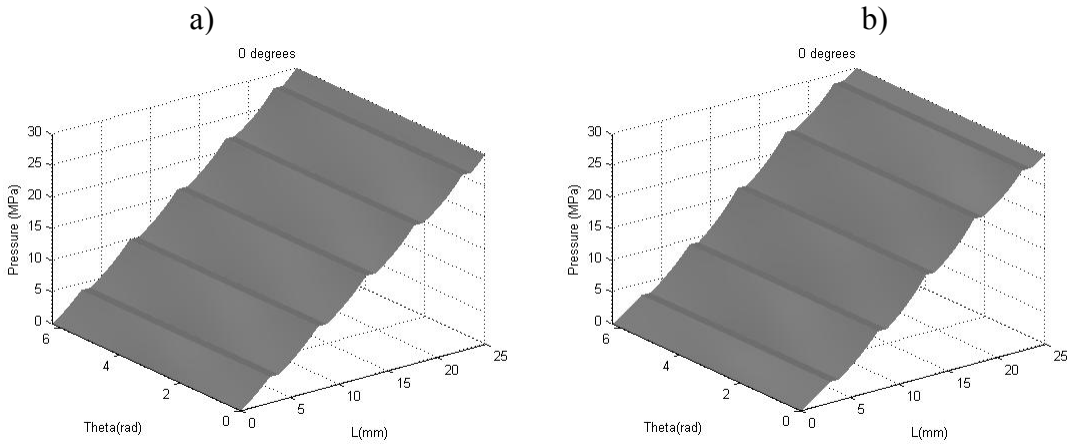

Figure 5.5 – Pressure distribution in piston barrel gap at 30MPa inlet pressure, 3 microns central clearance, 1.5 micron edge clearances. [a] 800-360 grid. [b] 1600-720 grid.

In order to validate the model, it was decided to compare the results given by the analytical expression, for the flow between two axisymetric cylinders and considering relative movement between them, equation to be found in literature [18- chapter 6], and

presented here as equation (5.11), with the computational results. Figure 5.6 represents the leakage versus piston relative movement, comparison between simulated and analytical results calculated from equation (5.11), at 30 Mpa pressure differential across the cylinder length, 10 microns clearance piston cylinder. Figure 5.6 shows a prefect agreement between numerical and analytical results, giving confidence to the model presented. The leakage shown in figure 5.6 when there is no relative movement is due to Poiseuille flow.

$$Q = -\frac{\Delta p}{\Delta L}\frac{\pi}{8\mu}\left(\frac{D_c^2}{4}-\frac{D_p^2}{4}\right)^2 + \frac{V_{SL}+\frac{\Delta p}{\Delta L}\frac{\pi}{4\mu}\left(\frac{D_c^2}{4}-\frac{D_p^2}{4}\right)}{\ln\left(\frac{D_p}{D_c}\right)}\pi\left[\frac{D_p^2}{8}-\frac{D_c^2}{8}+\frac{D_p^2}{4}\ln\left(\frac{D_c}{D_p}\right)\right] \qquad (5.11)$$

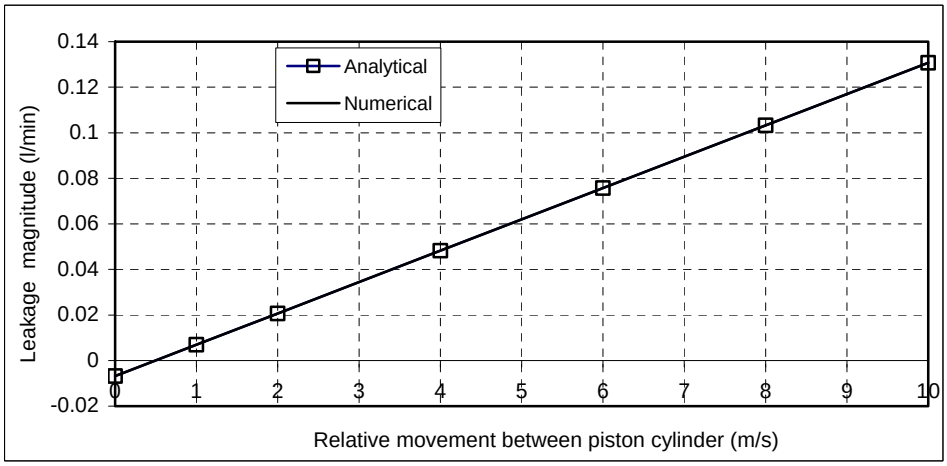

Figure 5.6 – Leakage between piston-cylinder clearance versus piston relative movement, 30Mpa pressure differential, 10 microns central clearance, piston centered, comparison between numerical and analytical results.

5.3.2 Different groove configurations studied.

In order to understand the effect of groove positioning, eight different types of pistons, as shown in figure 5.7, were used to evaluate the piston performance. The nomenclature used is: G0 no groove, G1o one groove located at the outer edge, G1i one groove at inner edge, G2 two grooves, one at the inner edge and other at the outer edge, G5, five grooves placed at equiv distance from each other, $G1_{2i}$ one groove at the inner edge and located at the 2nd groove position, Gc_1 is the same configuration as $G1_{2i}$ with an extra groove located at the piston stroke length, Gc_2 is the same configuration as the $G1_{2i}$ with two extra grooves located at the piston stroke length. Piston stroke length is defined as the length of the piston which is moving in and out of the cylinder. All grooves cut on the piston surface, have a width of 0.8mm and a depth of 0.8mm since these are the original dimensions of the grooves being cut by the manufacturer. Nevertheless the grooves cut

on the piston stroke length (see configurations Gc_1 and Gc_2 in figure 5.7) have a groove depth of 0.2mm and a width of 0.2mm.

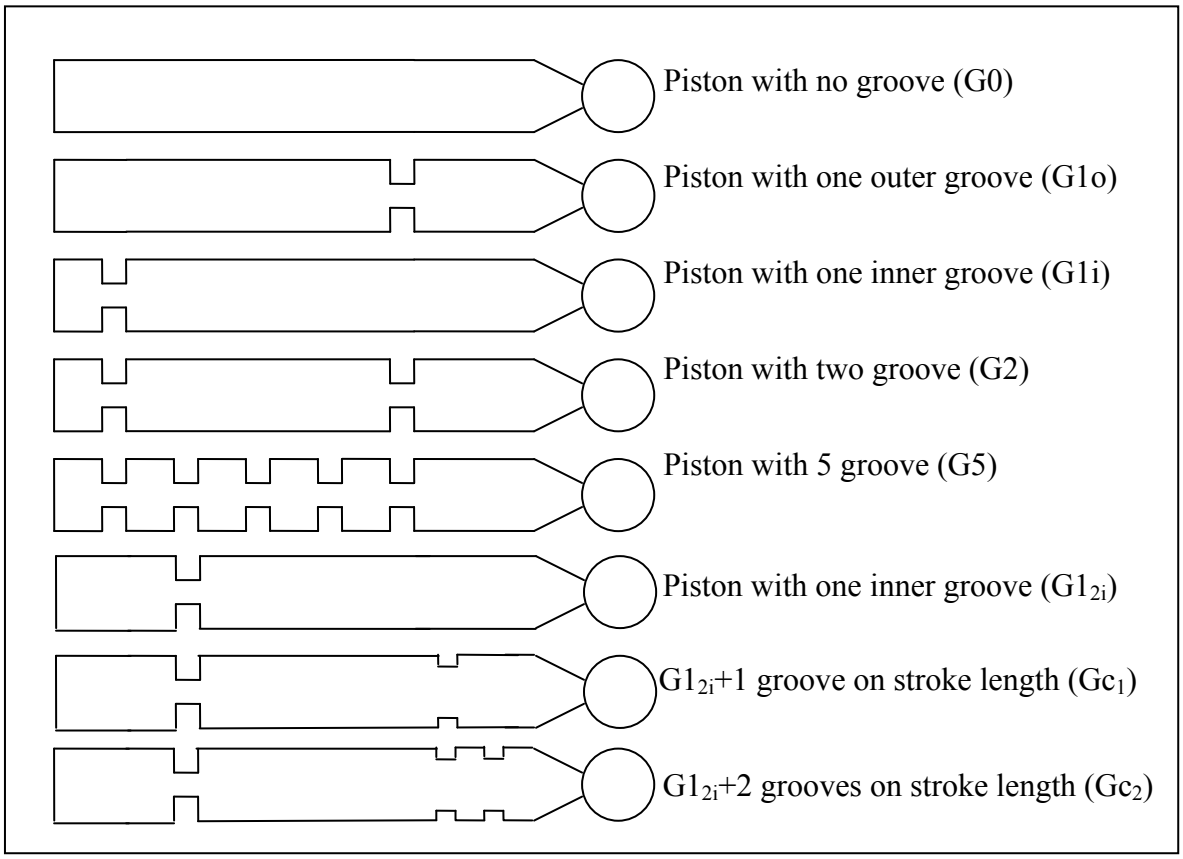

Figure 5.7 – Eight different types of piston studied.

It must be recalled when viewing figure 5.7, that the five main grooves cut on the piston surface, remain inside the cylinder for all swash angular positions, just the one or two grooves cut on the piston stroke length will come in and out of the cylinder, depending on the swash plate angular position. These one/two extra grooves do not exist in the original manufactured piston shown in figure 5.1, and its use will be discussed in a further section.

5.3.3 Pressure distribution.

Figure 5.8 represents the simulated pressure distribution in the piston-cylinder clearance for a piston without grooves and at different piston angular positions on swash plate, inlet pressure 30Mpa when connected to high pressure side and 0.15Mpa when connected to tank side, 1000 rpm pump turning speed, 10 microns central clearance and 5 microns piston eccentric displacement. Piston is connected to high pressure side from 0^o to 180^o piston angular positions and to the tank side (low pressure side) from 180^o to 360^o piston angular positions. Piston is moving in upward direction while connected to high pressure side and in downward direction when connected to the tank side.

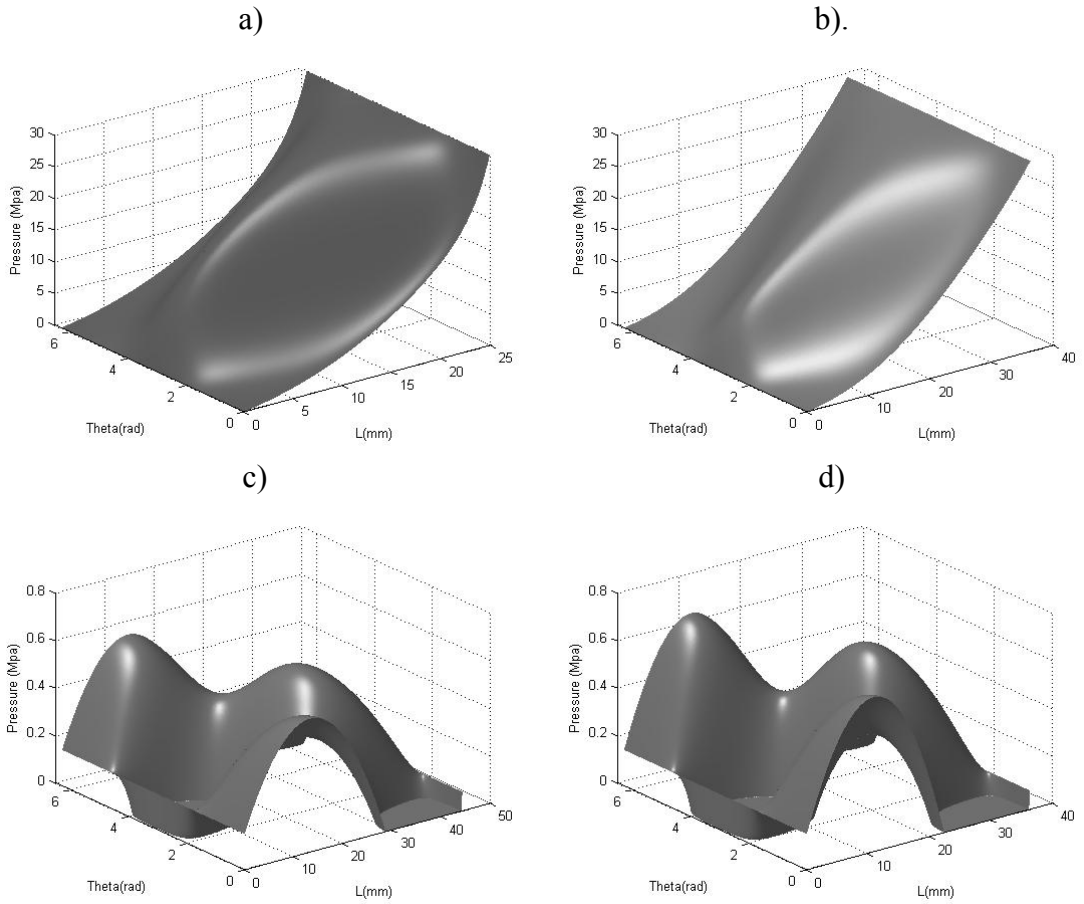

Figure 5.8 – Pressure distribution between piston cylinder gaps at 1000 rpm rotation speed for different piston angular positions on swash plate, piston without grove, central clearance 10 microns, edge clearance 5 microns. [a] 0 degree, 30Mpa. [b] 90 degrees, 30Mpa. [c] 225 degrees, 0.15Mpa. [d] 270 degrees, 0.15Mpa.

It has to be noticed from figures 5.8.c, d that negative pressure has been put to zero in order to see more clearly the area where cavitation is likely to appear. It can be seen that cavitation appears when the piston is connected to tank and the area where cavitation appears is at its highest at 270^{o} piston angular position, this happens because the piston velocity is negative and is at its maximum for this particular piston angular position. Therefore during the cylinder incoming flow period it would be strongly desirable, to minimize the effect of cavitation in order to increase the life of the piston. The existence of cavitation is found in regions where piston-cylinder clearance is at its minimum, on both ends of the piston inside the cylinder. Although it not presented in the present here, the area under the influence of cavitation increases as the pump turning speed increases.

Another thing to be noticed from figure 5.8, is that the pressure peaks appearing in figure 8a, b produce a negative y-directional torque (see figure 5.2), trying to restore the piston eccentric displacement, which arises from the differences in the friction of ball-cup and piston-cylinder pairs [19, 20].

Figure 5.9 represent the pressure distribution between piston cylinder gap in similar operating conditions as figure 5.8, except, at low clearance (3 microns central, 1.5 microns edge) and low turning speed (400rpm). As it can be seen via comparison of figure 5.8 and 5.9, at low clearances pressure tends to become more unstable. It can be noticed when comparing figure 5.8c, d to figure 5.9c, d that turning speed has a strong effect on cavitation. Such effect is found to be even stronger under low clearances.

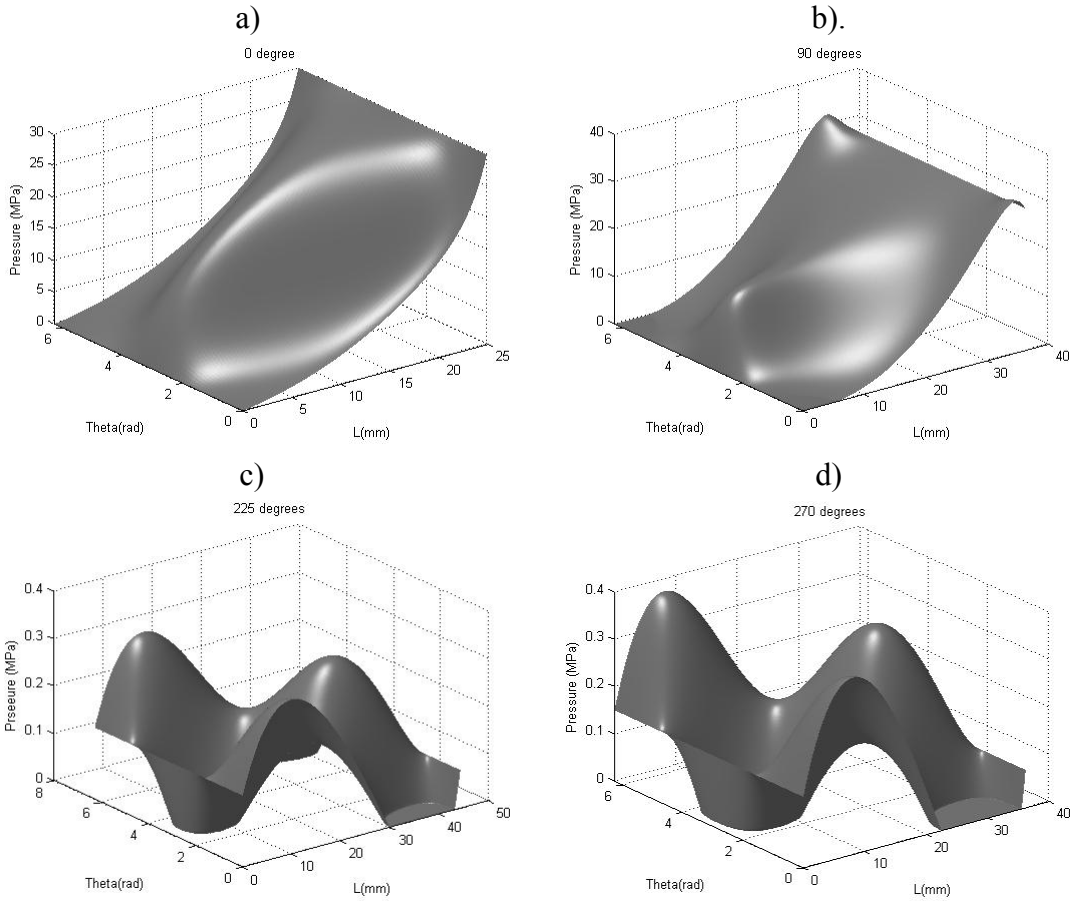

Figure 5.9 – Pressure distribution between piston cylinder gaps at 400 rpm rotation speed for different piston angular positions on swash plate, piston without grove, central clearance 3 microns, edge clearance 1.5 microns. [a] 0 degree, 30Mpa. [b] 90 degrees, 30Mpa. [c] 225 degrees, 0.15Mpa. [d] 270 degrees, 0.15Mpa.

Figure 5.10 presents the pressure distribution in the piston-cylinder clearance for different piston groove configurations at 30 Mpa inlet pressure, 1000 rpm and 90^{o} piston angular position on swash plate. This particular piston angular position has been chosen because the piston sliding velocity is at its maximum and therefore the pressure peaks are expected to be at its highest. It is clear from the figure that, grooves stabilize the pressure distribution along the angular direction of the piston. Such pressure distribution will result into more packed and stiff piston-cylinder system which will give a higher resistance to any movement created by external forces such as friction force. It can be noticed from figure 5.10.b that when a groove is located at each piston side, the pressure

distribution along the piston length is rather stable; such stability is nearly achieved when just a single groove is placed on the outer side of the piston, figure 5.10 d. Therefore for stabilization purpose and pressure distribution point of view, it would be desirable to locate the grooves towards the edges of the piston rather than placing them in the center.

a) G5

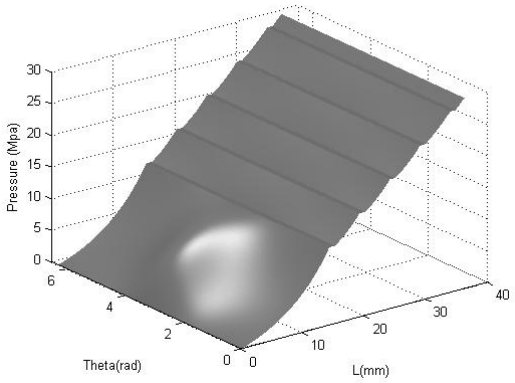

b) G2

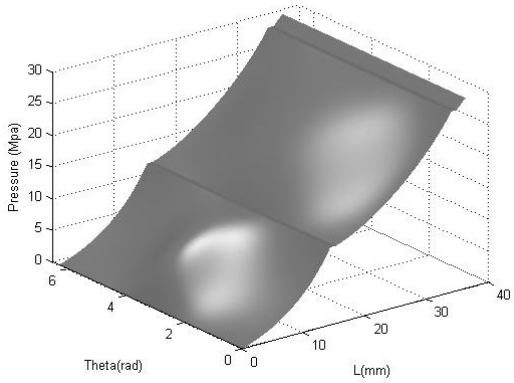

c) G1i

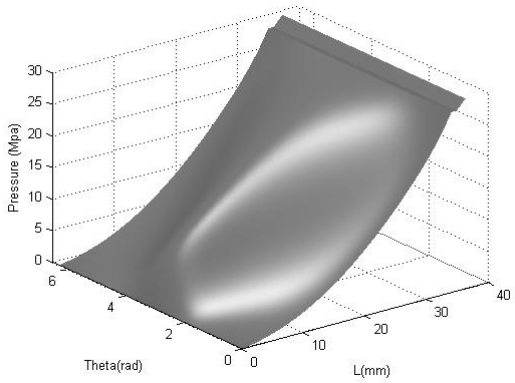

d) G1o

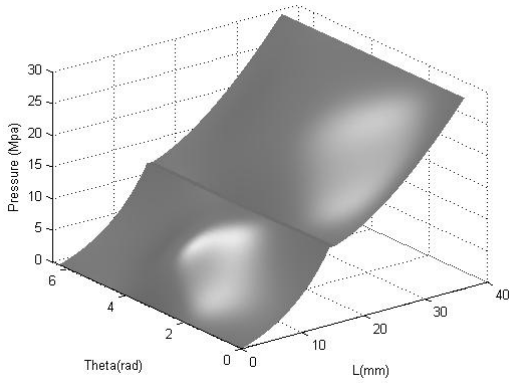

e) $G1_{2i}$

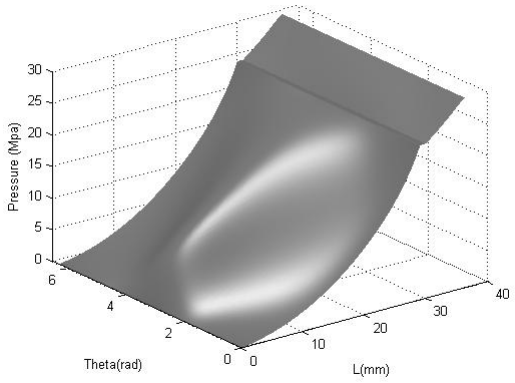

Figure 5.10 – Pressure distribution in the piston-cylinder clearance at 30 MPa inlet pressure, 1000 rpm rotation speed, 90^{o} piston angular positions on swash plate, 10 microns central clearance, 5 microns edge clearance, different pistons groove configurations.

Although not presented here, another important consideration to be noticed is, in presence of the grooves, the pressure distribution in piston-cylinder clearance is less dependent on the piston tilt. In reality, as the minimum edge clearance changes over time (tilt changes over time), for a piston without grooves the pressure distributions will be very much time dependent. On the other hand when considering the same piston dynamic movements and using a piston with grooves, the pressure distribution variation will be much less time dependent. Notice that in figure 5.10, the configuration G0, piston without groove is not presented since such configuration can be found in figure 5.8.b.

5.3.4 Effect of the grooves regarding cavitation.

As can be seen from figures 5.8.c, d, in the absence of grooves, there is an important part of the piston, which is under the influence of cavitation; on the other hand in the presence of grooves, the effect of the cavitation tends to be reduced, as can be seen in figure 5.11.

Figures 5.11 a,b, have the same characteristics as figure 5.8d 30 MPa inlet pressure, 10 microns central clearance, 5 microns edge clearance, 270 degrees of piston on the swash plate. The difference is that in figure 10 a, the piston configuration G5 is used, while on figure 10 b, configuration G2 is presented. It is noticed, the five groove configuration, G5, reduces more effectively the appearance of cavitation.

a) b)

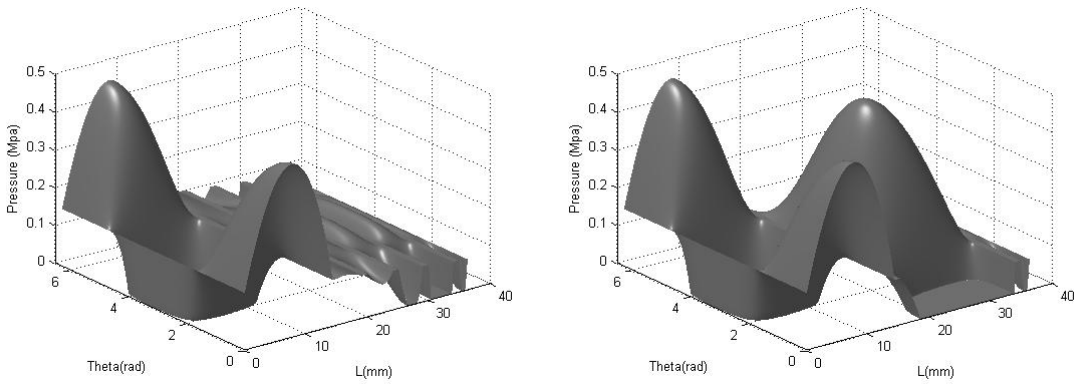

Figure 5.11 – Pressure distributions in piston cylinder clearance when piston is connected to tank side, 10 microns central clearance, 5 micron edge clearance, 270^{o} piston angular position, 1000 rpm pump turning speed. [a] Configuration G5. [b] Configuration G2.

Figures 5.12 a, b, have the same characteristics as figure 5.9d, since both graphs are at 400 rpm, it can now be seen more clearly than in figure 5.11 that the presence of grooves drastically reduce the appearance of cavitation, as previously explained, cavitation is more severe for low clearances and high turning speeds, being the turning speed effect more relevant.

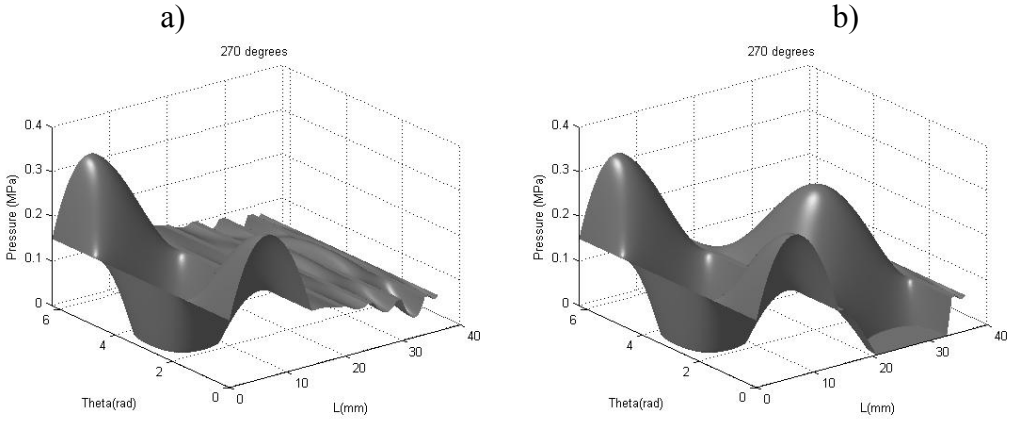

Figure 5.12 – Pressure distributions in piston cylinder clearance when piston is connected to tank side, 3 microns central clearance, 1.5 micron edge clearance, 270^{o} piston angular position, 400 rpm pump turning speed. [a] Configuration G5. [b] Configuration G2.

It is a standard procedure to avoid putting grooves on the piston stroke length, but according to the models developed, it would be desirable to put maybe a very shallow groove on piston stroke length, in order to be able to minimize the cavitation in this particular position. Figure 5.13 and 5.14 presents the pressure distribution between piston-cylinder clearance, for such piston configurations (Gc_1 and Gc_2) and under the same operating conditions as the ones used in figure 5.11 and 5.12 respectively. It is clear from figure 5.13a and 5.14a that putting 1 shallow groove on the piston stroke length reduces the appearance of cavitation; increasing the number of grooves to two, figure 5.13b and 5.14b, will produce a more stable pressure all around the angular position.

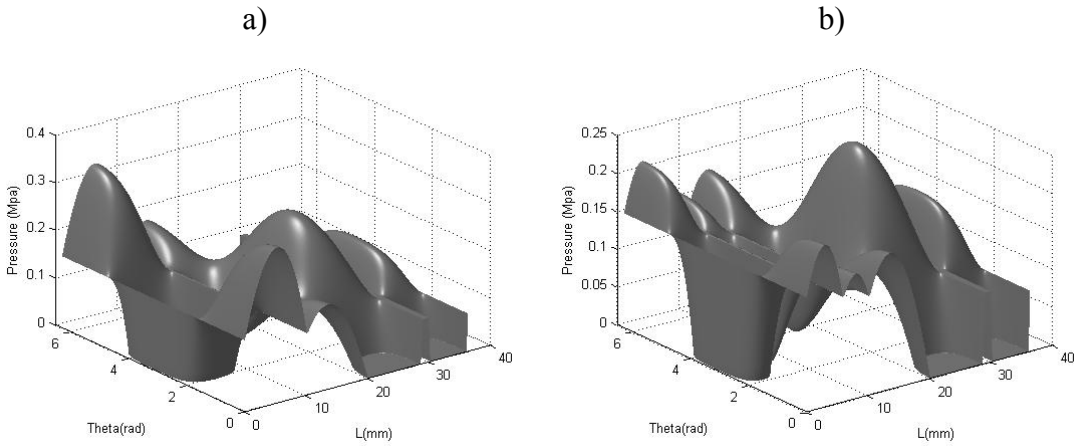

Figure 5.13 – Pressure distributions in piston cylinder clearance when piston is connected to tank side, 10 microns central clearance, 5 micron edge clearance, 270 degrees piston angular position, 1000 rpm pump turning speed. [a] Configuration Gc_1. [b] Configuration Gc_2.

Despite the shape of the grooves has not been considered in this study, we are confident to say that using shallow V-shape grooves on the piston stroke length would bring very

similar results to the ones presented in figure 5.13, such grooves would facilitate the incoming and outgoing of the piston into the cylinder.

It is important to notice from figures 5.9, 5.11-5.14 that, the position of the grooves on piston surface is very relevant, since it completely modifies the pressure distribution in the piston-cylinder clearance. The use of a groove located on the second groove position, is the configuration which appears to be reducing more effectively the appearance of cavitation, compare figure 5.11.b and 5.13.b. On the other hand, the grooves located on the central part of the piston have no effect regarding cavitation improvement.

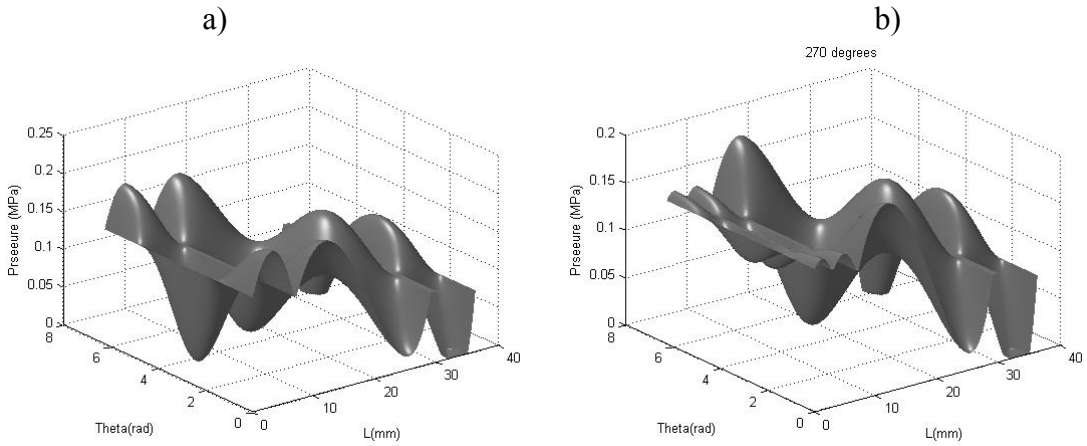

Figure 5.14 – Pressure distributions in piston cylinder clearance when piston is connected to tank side, 3 microns central clearance, 1.5 micron edge clearance, 270 degrees piston angular position, 400 rpm pump turning speed. [a] Configuration Gc_1. [b] Configuration Gc_2.

5.3.5 Effect of the grooves on total piston force and y-directional torques.

Initially, the different groove configurations will be studied when maintaining the piston perfectly aligned with the cylinder, under such conditions, it is understood that the force acting over the piston will be symmetrical, maintaining the piston always in the central position, the higher the force due to pressure distribution will be, the tighter the piston will be held in its central position, therefore the piston resistance to the external forces, such as friction forces will be maximum. Then the total force on piston surface can be treated as a measure of the system stiffness.

Figure 5.15 presents the percentage increase in total force exerted by the pressure acting on piston surface, with respect to the non grooved piston configuration, the operating conditions are: 30 MPa inlet pressure, 3 microns central clearance, 400 rpm pump turning speed and when piston axis is parallel to cylinder axis (α=0). It can be seen that grooves placed towards the inner edge of the piston contribute to the force magnitude and produce 1.5% higher force on piston surface with respect to the non grooved piston. On the other hand, grooves placed towards the outer edge reduce the total force on the piston. Such

statement, it is found to be independent of pump turning speed. It is important to clarify that figure 5.15 presents the percentage increase in force when the piston is connected to the higher pressure side (0^o-180^o) as the total force acting on the piston surface is much higher than the force when piston is connected to the tank side.

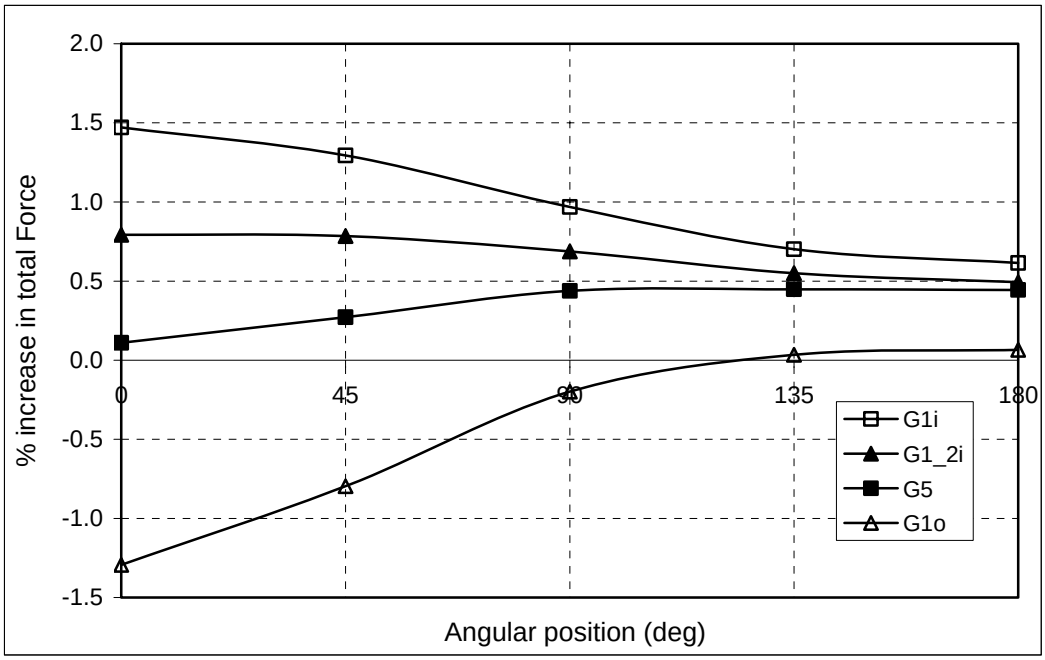

Figure 5.15 – Percentage increase in total force with respect to no groove piston at 400 rpm, 30MPa inlet pressure, 3 microns central clearance, eccentric displacement = 0.

When the piston is tilt versus the cylinder axis, the force acting over the piston surface will create a restoring torque which can be seen as a stabilizing parameter. In figure 5.16, it is represented the y-directional torque acting on the piston versus swash plate angular position, for different turning speeds and groove configurations. It can be seen that, in most of the cases, the value of the torque is negative, which means that the torque acts over the piston in such a way that it tries to rotate it in clock wise direction to restore its central position. Although when grooves are placed near outer edge (G2, G1o), the y-direction torque does become positive, which means the pressure torque acts in such a way that it tries to tilt the piston even further, which is totally undesirable. Therefore configuration G2 and G1o are unacceptable under the restoring torque point of view.

From figure 5.16, configuration G5, which is the way the original piston was designed, does not produce enough restoring torque, being the torque from 0^o to 60^o angular position less than 5Nm, nevertheless this configuration is the only one which creates higher torque at higher turning speeds. Configuration G1i and G0 produce good torque on low turning speeds but fail to do it on high turning speeds. Configuration $G1_{2i}$, creates a restoring torque which is pretty independent of pump turning speeds and will result into the most stable configuration.

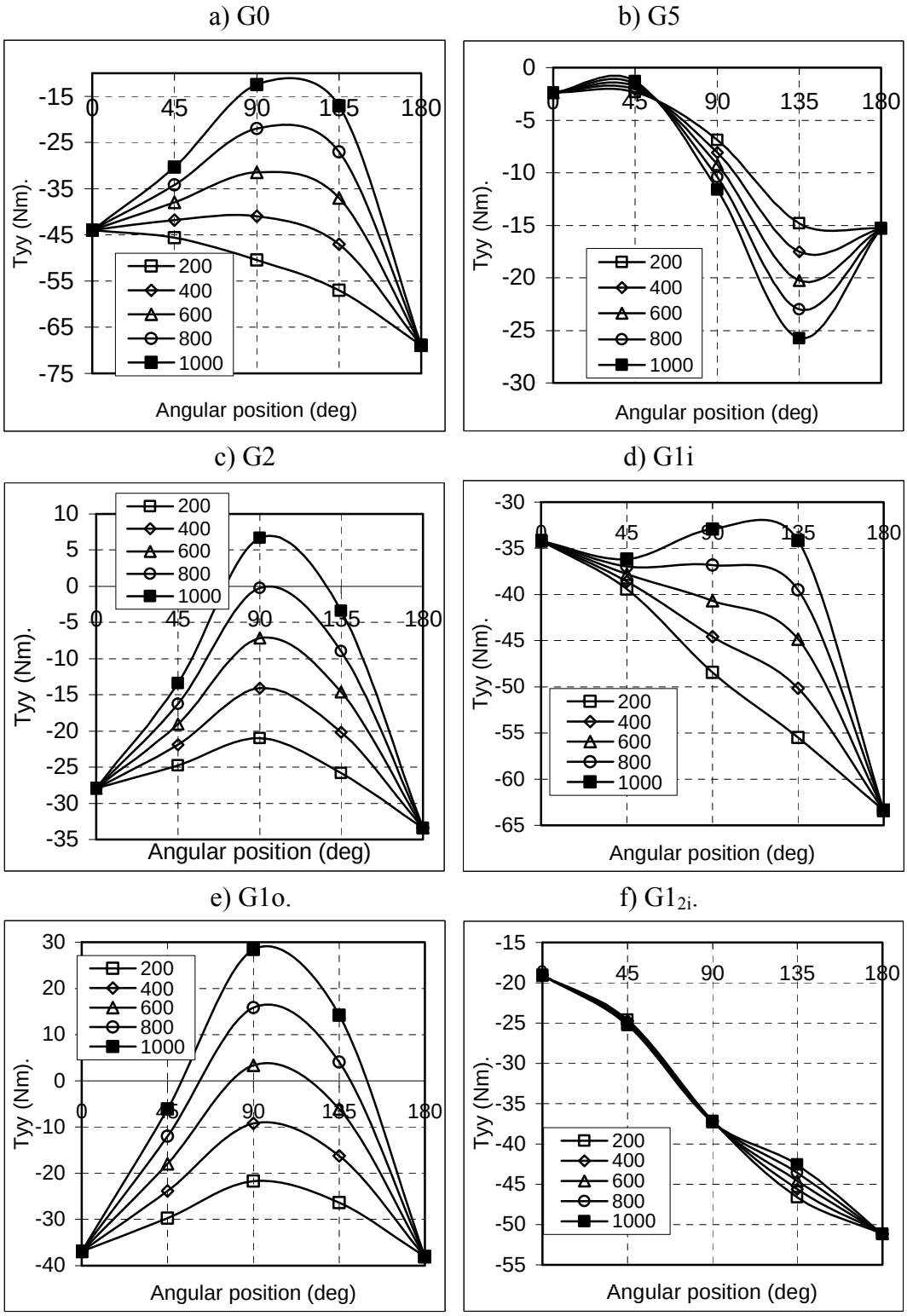

Figure 5.16 – Tyy with respect to piston swash plate angular position at different pump turning speed at 30 Mpa inlet pressure, 3 microns central clearance, 1.5 micron edge clearance. [a] No groove piston. [b] 5 groove piston. [c] 2 groove piston. [d] 1 inner groove piston. [e] 1 outer groove piston. [f] 1 inner groove located at 2nd groove position.

5.3.6 Effect of the grooves on leakage.

Figure 5.17, represents the leakage in the piston-cylinder assembly versus swash plate angular position for a non grooved piston and maintaining an edge clearance of 1.5 microns for all swash plate angular positions, being the maximum clearance when piston is centered of 3 microns. Two different pump turning speeds of 200 and 1000 rpm are considered. It can be seen that when piston is connected to the higher pressure side, the leakage is found to be negative for most of the cycle, (leakage flowing towards the cylinder chamber), this is due to the fact that Couette flow which is link with piston velocity, is higher that Poiseuille flow. Similar results were found in literature [8-9].

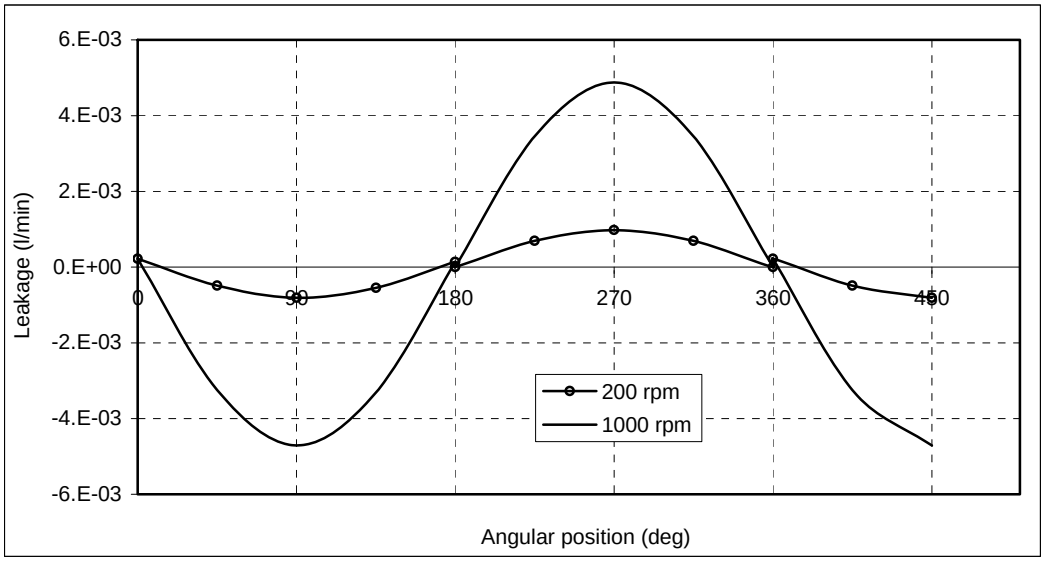

Figure 5.17 – Leakage piston-cylinder clearance at 30MPa inlet pressure versus piston angular position on swash plate for non groove piston, 1.5 microns edge clearance. 3 microns central clearance, 200-1000 rpm pump turning speed.

Figure 5.18 shows again the leakage at different swash plate angular positions for 10 microns piston-cylinder central clearance, 1000 rpm pump turning speed and different piston eccentric displacements (piston tilt), piston without grooves and piston with five grooves. It can be seen from figure 5.18a that piston tilt affects the leakage when piston moves from lower death center to upper death center (0^o-180^o), as tilt increases the leakage curves fall, increasing the leakage towards cylinder chamber, as a result it is expected the overall leakage of piston-cylinder for one full revolution, to be decreasing with the increase of piston tilt, figure 5.19 will clarify this point. Notice as well in figure 5.18, the effect of piston tilt is just relevant when the piston is connected to the high pressure port, indicating that the tilt influences mostly the Poiseuille flow. The peaks at 180^o and 360^o, found in figures 5.18a, b are due to Poiseuille flow when the piston is at its upper and lower death center. Another thing to be noticed from figure 5.18b is that, piston tilt has no effect on leakage when grooves have been cut on piston surface.

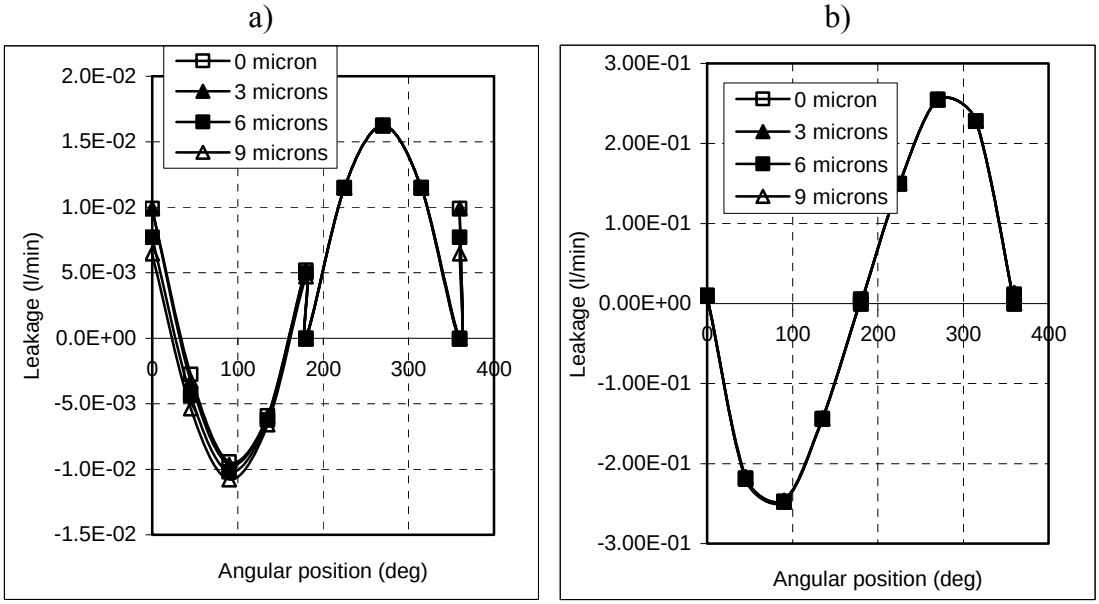

Figure 5.18 – Leakage piston-cylinder clearance at 30MPa inlet pressure versus piston angular position on swash plate, 10 microns central clearance, 1000 rpm pump turning speed, at different piston eccentric displacement. [a] G0. [b] G5.

It must be recalled that the overall leakage in a full cycle will be positive; the leakage flow direction is towards tank. The overall leakage can be found when integrating the temporal leakage presented in figure 5.18 as a function of angular position.

Figure 5.19a presents the overall leakage between piston-cylinder gap versus piston eccentric displacement for 10 microns central clearance and different piston groove configurations G0, G5, $G1_{2i}$. It is noticed, as already established in figure 5.18, that increase in piston tilt decreases the overall leakage slightly, and such decrease is more relevant for piston without grooves. As the number of grove cut on the piston increases, the piston-cylinder overall leakage tends to be constant and independent of piston tilt. Nevertheless, as expected as the number of the grooves being cut on piston surface increases the overall leakage increases.

To see more clearly the effect of piston eccentric displacement (tilt) on leakage, two given piston clearances of 15 and 20 microns and two turning speeds of 200 and 1000 were evaluated, inlet pressure was 30 MPa and the angular position of the piston on swash plate was 45 degrees, results are presented in figure 5.19.b. It can be seen that as the piston eccentric displacement increases, the leakage tends to decrease. The leakage decrease with piston eccentric displacement is higher for higher clearances. One of the most important characteristic of figure 5.19.b is, the leakage at this particular point (45^o angular position of piston on swash plate) is positive and in figure 5.18 same leakages at 10 microns central clearance was reported as negative. This is due to the face that as the clearances increase Poiseuille flow become more relevant than Couette flow, therefore the overall leakage towards tank will be much higher than the smaller clearance.

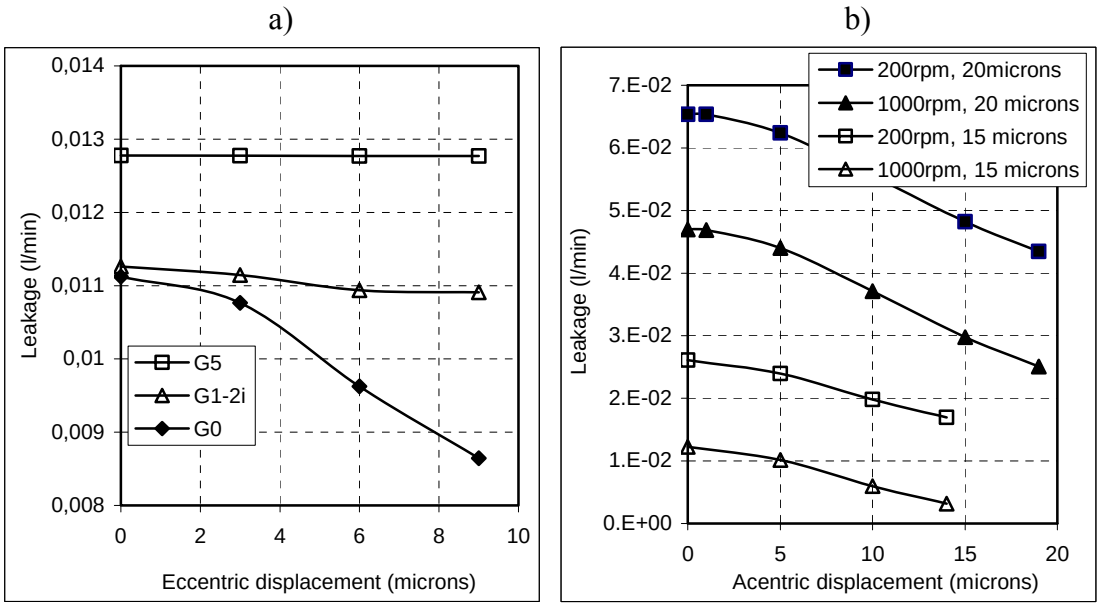

Figure 5.19 – Leakage piston cylinder versus piston eccentric displacement. [a] overall leakage at 10 microns central clearance, different groove configurations. [b] Temporal leakage for non groove piston at 45^{o} swash plate angular position at two different clearance and turning speed.

It is important to point out that in figure 5.19b, leakages have a higher value for low turning speeds and high clearances. In figure 5.17 it was explained that leakages had a higher value for higher turning speeds and in figure 5.19b it seams that the opposite is being said. The explanation of this is that as clearance increases, the Poiseuille flow becomes more relevant than Couette flow, then even when the piston moves from the lower death centre towards the upper death centre the leakage piston-cylinder flows in direction to tank, its sign is positive, as pump turning speeds increases the Couette flow gains relevance although Poiseuille flow is still dominant, the resulting flow will therefore be positive but the magnitude will be smaller than the one found at pump high turning speeds.

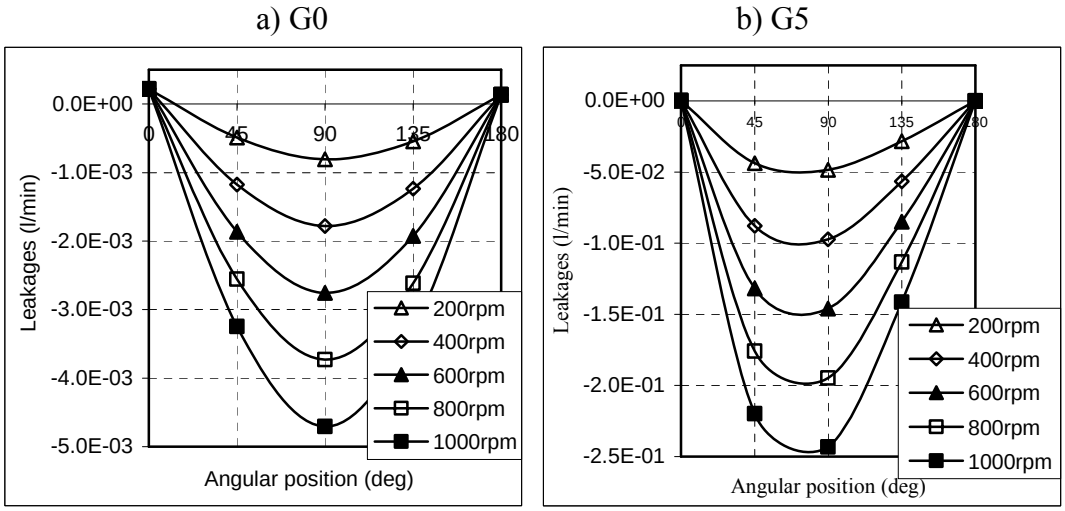

c) G1-2i

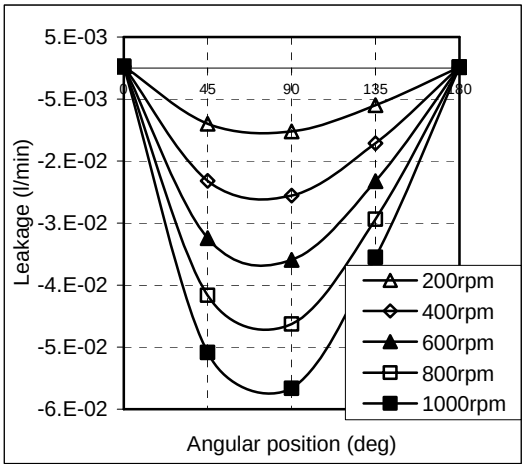

Figure 5.20 – Leakage between piston-barrel gap with respect to piston swash plate angular position at different swash plate turning speed at 30 Mpa inlet pressure, 1.5 micron edge clearance, 3microns central clearance. [a] No groove piston. [b] 5 groove piston. [c] 1 inner groove away from inner edge.

Figure 5.20 presents the leakage versus swash plate angular position for different groove configurations at 30MPa inlet pressure, 3 microns central clearance and different turning speeds. Notice that the graph focuses on the leakage when the piston goes from the lower death center to the upper death center, since under these conditions Couette and Poiseuille flows are relevant. It can be noticed for this figure that the increase in leakage is higher as number of grooves increases. As expected, leakage increase as the turning speed increases.

5.4. Conclusions.

1. The use of grooves cut on the piston surface brings stability to the piston, since it increases piston stiffness.
2. The grooves located on the central part of the piston, appear not to be useful regarding the pressure stabilization, torque, force or even cavitation point of view.
3. To avoid cavitation, it is important to consider the inclusion of grooves at the piston stroke length and near to the piston pressure side. In fact, wherever it is expected cavitation to appear, the use of a groove will tent to prevent cavitation from appearing.
4. Regarding the restoring torque point of view, configurations G2 and G1o are undesirable, configuration $G1_{2i}$ (one groove at the inner edge at second groove position) seams to be the best location from restoring torque point of view, since the magnitude of the restoring torque produced by the pressure distribution is quite high and rather independent of turning speed.
5. For a piston without grooves, leakage piston-cylinder decreases as the piston tilt increases, the decrease is more relevant at higher clearances.

6. As the number of grooves being cut on piston surface increases, the effect of piston tilt becomes less relevant regarding the piston cylinder overall leakage. As already established in literature, the increase in number of grooves will bring an increase in leakage.
7. Among the configurations studied, $G1_{2i}$ is the one bringing the best performance because it produces higher restoring torque at all pump turning speeds, leakage is fairly independent of piston tilt and although overall leakage is slightly higher that the non groove configuration, it is much lower than the configuration G5.

Nomenclature

D_p	Piston diameter [m].
D_c	Cylinder diameter [m].
Ec_1, Ec_2	Minimum edge clearances [m].
h	Piston-barrel clearance [m].
L_t	Length of the piston inside cylinder at time t [m].
L_o	Length of the piston inside cylinder at t=0 [m].
L_1	Piston cylinder axis intersection point position [m].
p	Pressure [Pa].
Q	Leakage through piston-cylinder clearance [l/min].
R	Piston radius [m].
R_{sw}	Swash Plate radius [m].
t	time [s].
$V_{s\theta}$	Angular surface velocity of piston [m/s].
V_{SL}	Longitudinal surface velocity of piston [m/s].
X_1, Y_1	Coordinates of a generic point on cylinder surface.
X, Y	Generic coordinates axis in figure 3.
θ , L	Generic coordinates axis.
θ_{SW}	Angular position on swash plate [rad].
β	Swash plate angle [rad].
α	Piston tilt to cylinder axis [rad].
μ	Viscosity of the fluid [Kg/s/m].
ω_{SW}	Swash plate rotation [rad/s].

References:

1. Sweeney D.C., Preliminary investigations of hydrolic lock. *Engineering, 1951*, 172, 513-16.

2. Sadashivappa K., Singaperumal M., Narayanasamy K., "Piston eccentricity and friction force measurement in a hydraulic cylinder in dynamic conditions considering the form deviations on a piston". Mechatronics 2001, 11pp251-66.

3. Milani M. Design hydraulic locking balancing grooves. *Proceedings Institution of Mechanical Engineers* 215, Part I, 2001. pp 453-465.

4. Borghi M, Cantore G., Milani M. and Paoluzzi P, Numerical analysis of the lateral forces acting on spools of hydraulic components. FPST5, Fluid Power Systems and Technology, ASME, 1998.

5. Borghi M, Hydraulic locking-in spool-type valves: tapered clearances analysis. *Proceedings Institution of Mechanical Engineers* 215, Part I, 2001 pp157-168.

6. Blackburn J.F., Reethof G. and Shearer J. L., Fluid power control, 1960 (MIT Press – John wiley, New York).

7. Merrit H. E., Hydraulic control systems, 1967 (John Wiley New York).

8. Ivantysynova M; Huang C. Investigation of the Flow in Displacement Machines Considering Elastohydrodynamic Effect. *Proceedings of the 5th JFPS International Symposium on Fluid Power*, November 13, Nara 2002 Japan Vol. 1 pp 219-229.

9. Ivantysynova M; Lasaar R. An Investigation into Micro – and Macrogeometric Design of Piston Cylinder Assembly of Swash plate machines. *International Journal of Fluid Power* 5 2004 No 1 pp 23-36.

10. Fang, Y. and Shirakashi, M., Mixed lubrication characteristics between the piston and cylinder in hydraulic piston pump motor. J. of Tribology Transactions of ASME, 1995. Vol:117, Issue:1, pp80-85.

11. Prata AT, Fernandes JRS, Fagotti F, Dynamic analysis of piston secondary motion for small reciprocating compressors, J. of Tribology Transactions of ASME, 2000. Vol:122, Issue:4, pp752-760.

12. Berger E. J., Sadeghi F., Krousqrill C.M., Finite element modeling of engagement of rough and grooved wet clutches. J. of Tribology Transactions of ASME, 1996. Vol:118, Issue:1, pp137-146.

13. Razzaque M. M., Kato T., Effects of Groove Orientation on Hydrodynamic Behavior of Wet Clutch Coolant Films, Transactions of the ASME, 1999. Vol. 121, pp56-61.

14. Lipschitz, A., Basu, P., and Johnson, R. P., 1991, "A Bi-Directional Gas Thrust Bearing," STLE *Tribology Transactions,* Vol. 34, No. 1, pp. 9-16.

15. Basu, P., 1992, "Analysis of a Radial Groove Gas Face Seal," STLE *Tribology Transactions,* Vol. 35, No. 1, pp. 11-20.

16. S. Kumar, JM Bergada, J. Watton, ”Axial piston pump grooved slipper analysis by CFD simulation of three dimensional NVS equation in cylindrical coordinates.” Computer &Fluids 38 (2009) 648-663.

17. Subhas V. Patankar, Numerical Heat Transfer and Fluid Flow. Taylor & Francis Group: Hemisphere Publishing Corporation; 1980.

18. David Pnueli, Chaim Gutfinger, Fluid Mechanics. Cambridge university press1992.

19. Hooke C.J., Kakoullis Y.P. The lubrication of slippers on axial piston pumps. 5th International Fluid Power Symposium September 1978, B2-(13-26) Durham, England.

20. Hooke C.J., Kakoullis Y.P. The effects of centrifugal load and ball friction on the lubrication of slippers in axial piston pumps. 6th International Fluid Power Symposium, 179-191, Cambridge, England. 1981.

6

Spherical Bearing

In this chapter, we present the expression for the pressure distribution and leakage, for spherical bearing clearance while considering a very simplified model via implementing Reynolds equation of lubrication in spherical coordinates to the bearing gap. Ball and bearing are considered as constrict which result into a uniformly symmetric gap. Flow is considered as laminar.

6.1 Introduction

A spherical bearing is a common device used in pumps to permit rotation about a central point in two orthogonal directions, offer an unequaled combination of high load capacity, high tolerance to shock load and self aligning ability and play an important role in pump performance. A great amount of research work has been done on spherical bearing in piston pumps. Mainly the different researchers focused on studding the friction piston ball – slipper. Figure 6.1 represent a schematic diagram of spherical piston – slipper bearing under consideration in this work.

Hooke at al [1] studied experimentally the couples acting on the slipper ball, they concluded that lubrication is under all conditions deficient, appearing metal to metal contact. Friction increases with pressure and small slipper plate tilt angles. Ball friction causes the piston to rotate. Kobayashi et al [2] studied experimentally the friction torque characteristics between the piston ball and the slipper. Different surface coatings, clearances and surface roughness were analyzed. They found that friction torque increased with the pressure, tending to an asymptotic value, an increase on the swash plate angle created a decrease on the friction torque, the friction torque decreased as clearance increased; there was also a slight decrease on friction torque with increase of oil temperature. The use of different surface roughness did not prove any significant change on friction torque. The measurements on leakage showed a small leakage decrease when slipper spin increased.

Böinhoff [3] performed a first analytical study on the spherical bearing friction. Hooke et al [4] pointed out that friction on a piston ball plays a major role in determining the behaviour of the slipper. In [5, 6] Iboshi and Yamaguchi pointed out that friction on the spherical bearing affects significantly the slipper tilt angles, rotational speed affects the central clearance slipper-plate. It must be said that those results agree very well with Hooke`s considerations. In [7] Hooke et al analysed carefully the three different tilting couples acting on the slipper, finding that the tilting couple due to friction at the slipper running face, is much smaller than the ones created at the piston – cylinder, piston – slipper interfaces.

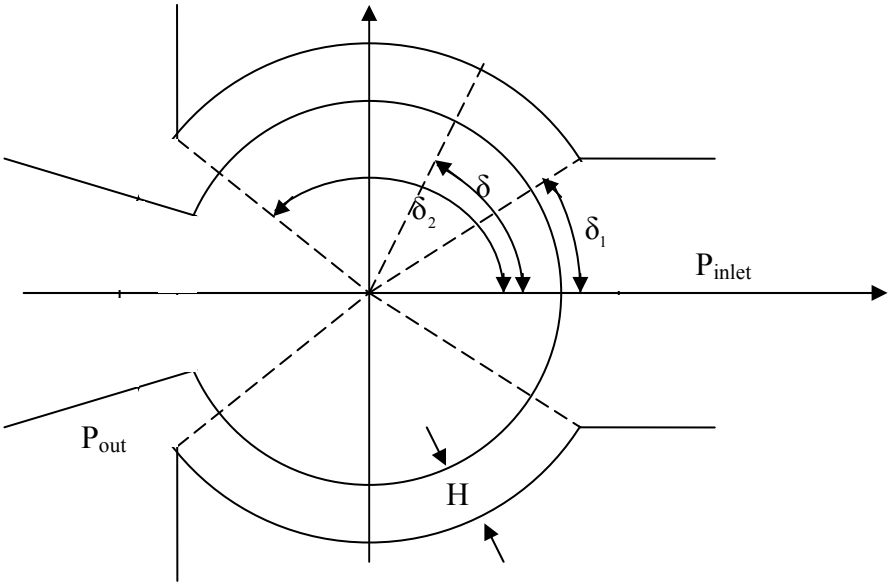

Figure 6.1 – Schematic diagram of spherical piston – slipper bearing.

Spherical bearing was also experimentally studied in a ball-piston pump by Abe at al [8, 9], the work was mainly focused on the friction coefficient, although piston velocity, and pressure contact between sphere and cam were also evaluated, they had a first attempt on explaining pressure distribution on the spherical bearing. Different shapes of pistons with restricting holes were evaluated. Elastohydrostatic lubrication of piston balls and slipper bearings was studied by Kobayashi et al [10], in fact, most of the work was focused in presenting the slipper swash plate gap and the leakage as a function of the slipper main land length and the slipper central hole. It was found that minimum film thickness and leakage through slipper tended to reach an asymptotic value with the increase of the slipper land length. The transformed Reynolds equation of lubrication in spherical coordinates was accomplished by Meyer [11], the integration of such equation gives the pressure distribution along the sphere. It is quite clear from the literature available that a lot of research work has been done on spherical bearing and the window for the further research is quite narrow. Therefore a very simple model of spherical bearing has been considered. Ball and bearing are considered as constrict. A similar model has been already developed by Bergada [12] using two different approaches, one assuming the

Poiseuille flow profile in the spherical bearing clearance and calculating the leakage from it and the second, by direct integration of Reynolds equation in spherical coordinates. In both cases an expression for leakage and pressure distribution is developed. The second technique used by Bergada [12] is implemented in this chapter and the same expressions for pressure and leakage are found.

6.2 Governing equations

The Reynolds equation of lubrication in spherical coordinates (given by equation 6.1 for the system represented in figure 6.1) is applied to the spherical bearing clearance.

$$\frac{\partial}{\partial\delta}\left(H^3 \sin\delta \frac{\partial p}{\partial\delta}\right) = 0 \tag{6.1}$$

The Dirichlet type pressure boundary conditions are used as given in equation 6.2.

$$P\big|_{\delta=\delta_1} = P_{inlet}, \quad P\big|_{\delta=\delta_2} = P_{out} \tag{6.2}$$

As the spherical ball and the pocket are assumed to be concentric, the variation of H versus angular position δ is zero and the equation 6.1 is integrated directly, finding the pressure distribution in spherical bearing clearance as a function of angular position δ, given by equation 6.3.

$$P = P_{inlet} - \left(P_{inlet} - P_{out}\right)\frac{\ln\left[\dfrac{\tan\left(\delta/2\right)}{\tan\left(\delta_1/2\right)}\right]}{\ln\left[\dfrac{\tan\left(\delta_2/2\right)}{\tan\left(\delta_1/2\right)}\right]} \qquad \vee \quad \delta_1 \le \delta \le \delta_2 \tag{6.3}$$

Flow is considered to be Laminar under all working condition therefore a Poiseuille flow profile is used to calculate the leakage in the spherical bearing clearance, given in equation (6.4).

$$Q = \frac{\pi\left(P_{inlet} - P_{out}\right)\left(R_0 \dfrac{H^3}{6} + \dfrac{H^4}{12}\right)}{\mu\left(R_0 + \dfrac{H}{2}\right)\ln\left[\dfrac{\tan\left(\delta_2/2\right)}{\tan\left(\delta_1/2\right)}\right]} \tag{6.4}$$

6.3 Results

Figure 6.2 present the pressure distribution versus the angular position δ at different inlet pressure. It can be seen that the pressure distribution is found to be logarithmic for the

case study. It is already clear from equation 6.3, that the pressure distribution does not depend on clearance. Figure 6.3 present the leakage as function of clearance at different inlet pressure. As seen from the graph or equation 6.4, leakages are third order function of clearance.

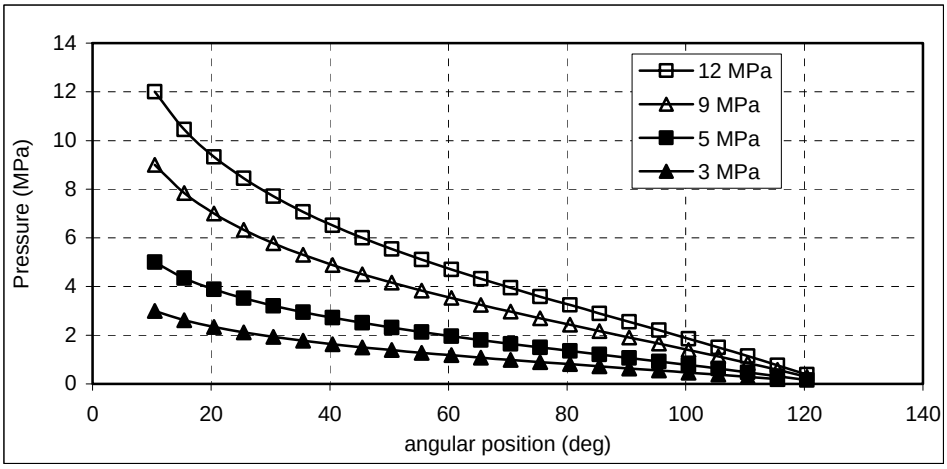

Figure 6.2 – Pressure distribution in verses angular position at different inlet pressure.

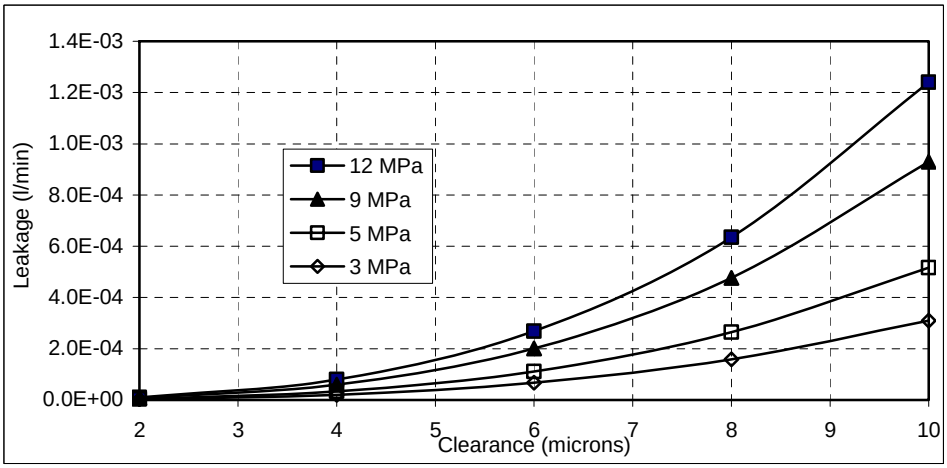

Figure 6.3 – Leakage variation versus clearance at different inlet pressure.

6.4 Conclusions.

The results presented in this chapter, have been already well established in literature and have already been published, for example in reference [12]. The purpose behind these presentation is, we required to have the leakage analysis for each component of the pump to calculate the out flow ripple therefore the expression 6.4 is used to calculate leakage in spherical bearing when simulating the outflow ripple of the pump.

Nomenclature.

H	Spherical bearing clearance (m)
p	Generic pressure in spherical bearing clearance (Pa).
δ	Generic angular position (rad).
δ_1	Bearing entrance angular position (rad).
δ_2	Bearing exit angular position (rad).
R_o	spherical ball radius (m).
P_{inlet}	Inlet pressure (Pa)
P_{out}	Out let pressure (Pa).
μ	viscosity of the fluid.
Q	Leakage in the spherical bearing clearance. (m^3/s).

References

1. Hooke C.J. , Kakoullis Y.P. The effects of centrifugal load and ball friction on the lubrication of slippers in axial piston pumps. 6th International Fluid Power Symposium, 179-191, Cambridge, England. 1981.

2. Kobayashi, S., Hirose, M., Hatsue, J., Ikeya M. Friction characteristics of a ball joint in the swashplate type axial piston motor. Proc Eighth International Symposium on Fluid Power, J2-565-592, Birmingham, England, 1988.

3. Böinghoff, O. Untersuchen zum Reibungsverhalten der Gleitschuhe in Schrägscheiben-Axialkolbenmascinen. *VDIForschungsheft* 584. VDI-Verlag. 1977. pp 1-46.

4. Hooke C.J., Kakoullis Y.P. The lubrication of slippers on axial piston pumps. *5th International Fluid Power Symposium September* 1978, B2-(13-26) Durham, England.

5. Iboshi N., Yamaguchi A. Characteristics of a slipper Bearing for swash plate type axial piston pumps and motors, theoretical analysis. *Bulletin of the JSME,* Vol 25, No 210, December 1982, pp 1921-1930.

6. Iboshi N; Yamaguchi A. Characteristics of a slipper Bearing for swash plate type axial piston pumps and motors, experiment. *Bulletin of the JSME,* Vol 26, No 219, September 1983. pp 1583-1589.

7. Hooke C.J., Li K.Y. The lubrication of slippers in axial piston pumps and motors. The effect of tilting couples. *Proceedings of the Institution of Mechanical Engineers* 1989, Vol 203, part C, pp 343-350.

8. Abe K; Imai M; Kometani E. The performance of Ball-Piston Multi – Stroke Type Low Speed High Torque Motor. (Report Nº 1, Experimental Study on Performance of Spherical Surface of Piston). *Bulletin of the JSME* Vol. 22, 167; 1979 pp 700-706.

9. Abe K; Ono K. The performance of Ball-Piston Multi – Stroke Type Low Speed High Torque Motor. (2nd report, practical analysis on multi-stroque type cam profile). Trans. Japan Soc. Mech. Engrs. (B). (395, Jul. 1979) pp 974-981.

10. Kobayashi S.; Ikeya M. Elastohydrostatic Lubrication of Piston Balls and Hydrostatic Slipper Bearings in Swashplate Type Axial Piston Motors. *10th International Conference on Fluid Power – the future for Hydraulics,* 5 – 7 April 1993. Brugge, Belgium, pp 311-322.
11. Meyer D. Reynolds Equation for Spherical bearings. *Journal of Tribology ASME*. January 2003. Vol 125 pp 203-206.
12. Josep M Bergada, Mecanica de fluidos problemas resueltos, ISBN 978-84-8301-776-0, UPC 2008.

7

Experimental Test Rigs

In this chapter, we present a little description of the three test rigs, which have been used to undertake the different experiments employed to validate the computational models developed in the project. ***It has to be stated that development of these test rigs is not the part of this thesis and has not been done by the author.***

7.1 Introduction.

In order to verify the validity of all the simulations performed during this project, three test rigs, located in the fluid Power laboratory of Cardiff University, United Kingdom, were used for experimentation. The first test rig is used to measure the dynamic behavior of the slipper, including the effect of the grooves. The second test rig will be used to measure the dynamic behavior of barrel and its fluctuations with respect to the port plate and the third to measure fluctuating pressure at the outlet of the pump and inside the pistons chamber. It has to be mentioned that Dr. JM Bergadà, has been working over the past ten years with this university, and has intervened in the design and creation of two of these three test rigs, **the professor in charge of all the design and development was Professor John Watton.** Along these years, several experiments have been undertaken using these test rigs.

A short description of these test rigs is given in next sections. ***It has to be bared in mind that the development of these test rigs is not part of this thesis and is not done by the author, only the experimental results, which have been performed by Dr JM Bergada over the years, are used to validate the CFD models and are therefore included in the PhD thesis.***

7.2 Test rig one (To measure slipper performance).

In order to experimentally validate the slipper CFD models, the test rig represented in figure 7.1 was used.

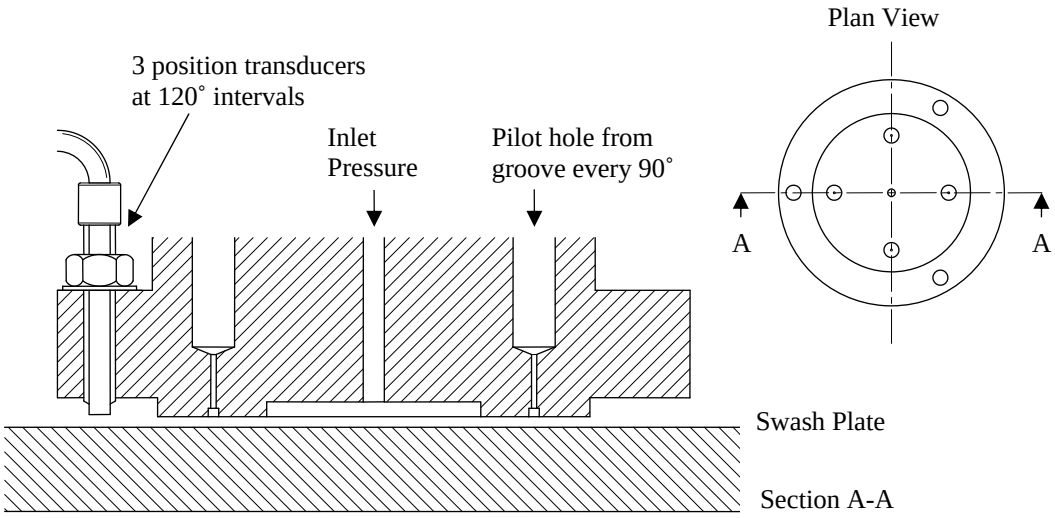

a) Cross section of the slipper area

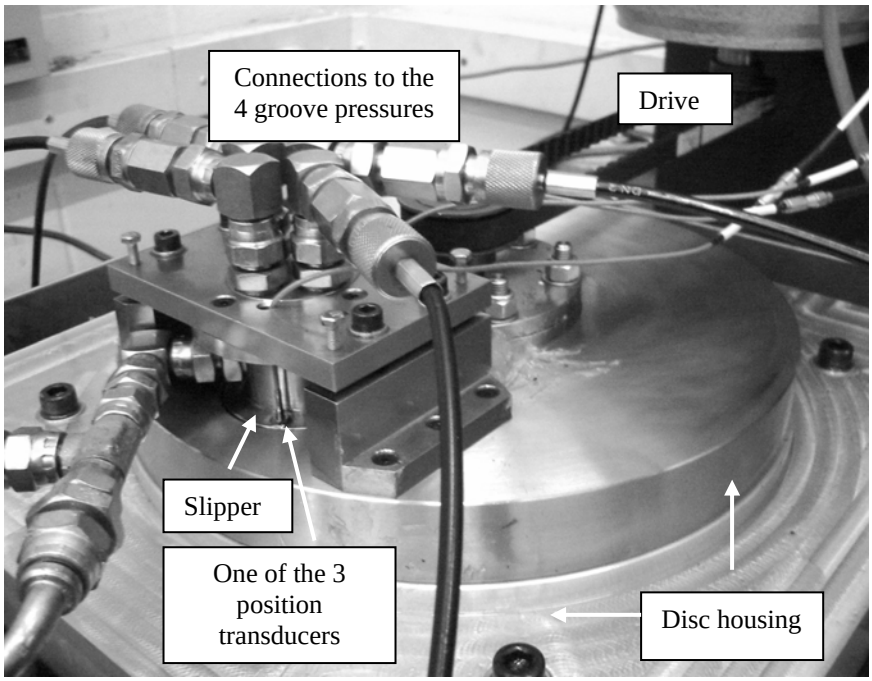

b) Slipper, disc housing and drive system

Figure 7.1 - Experimental apparatus regarding slipper performance.

Three position transducers, having a measurement accuracy of 0.5 microns, were attached to the slipper at 120^{o} intervals. These sensors require non-ferrous measuring face for optimum performance and therefore the housing assembly was manufactured from aluminium while the slipper assembly was manufactured from stainless steel. The slipper is held in position using four screws and the required slipper orientation was achieved by turning four additional positioning screws. Using this method the slipper could be positioned completely parallel to the swash plate or to any desired tilt. Four holes, 0.5

mm diameter and at every 90^o, were drilled at the centre of slipper groove allowing measurement of the pressure inside the groove at its four radial positions. Static tests were performed with a slipper central clearance 5, 10, 15 and 20 microns. In all positions, 6 different pressures were applied to the slipper, these being 3, 5, 8, 10, 13 and 15 MPa. The slipper was built with a scale 2:1 when compared with the slipper that initiated this project, shown in figure 1.2. This was done to be able to physically locate both the position sensors and the pressure measuring points. However, the size of the test rig slipper is not unlike those that exist in larger pumps such as the set of pistons and slippers supplied by Oilgear Towler UK to the authors for reference. The test rig slipper dimensions are:

- Orifice radius 1mm
- Inner land inside radius 10,15mm
- Inner land outside radius 14,7mm
- Groove width 1mm
- Outside radius 20,5mm
- Groove depth 0.8 mm.
- d_{sw} (distance between slipper centre and plate centre) = 92 mm.

Since the test rig allows rotation of the swash plate, a second set of tests were performed to study the effect of tangential velocity on slipper plate leakage and slipper groove pressure distribution. The variable-speed tests were performed for two central clearances of 10 and 15 microns and with no tilt. A set of swash plate turning speeds were studied in the range 0 to 1000 rpm, the maximum turning speed corresponding to a tangential velocity on the slipper main axis of 9,6 m/s. The range of inlet pressures used were 3, 5, 7, 9, 11, 13 MPa.

7.3 Test rig two (To measure barrel performance).

To measure the barrel dynamic displacement the tests rig presented in figure 7.2 was created. Two Micro-Epsilon inductive position transducers, capable of measuring to an accuracy of 0.1μm, were used and located at one end of the “Y” axis and at 45 degrees. The transducer calibration showed an excellent linearity and produced calibration factors of 47.75μm/volt. The barrel dynamic displacements were measured and figure 7.3 presents the dynamic displacement measured at 18 MPa. Notice that at least two waves are superposed; the main wave has a frequency of around 24 Hz which is the pump rotational frequency, the frequency of the second wave being nine times the pump frequency. The low frequency wave is due to the barrel face run out, while the highest frequency is due to each piston torque effect when entering and leaving the pressure kidney port. Therefore, the superimposed sinusoidal wave is easily extracted from the measurement.

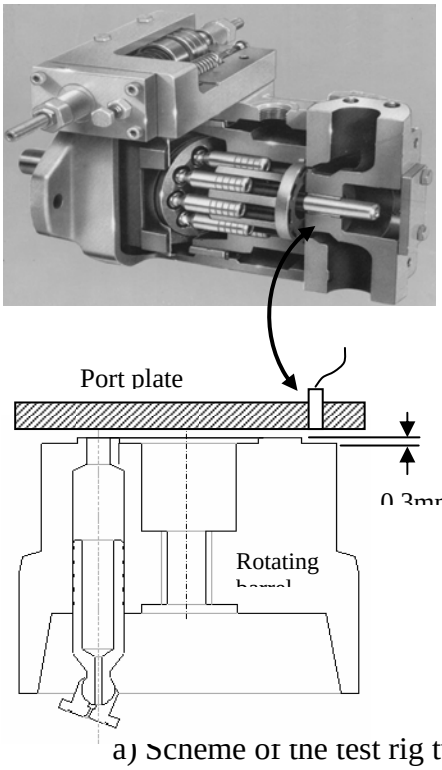

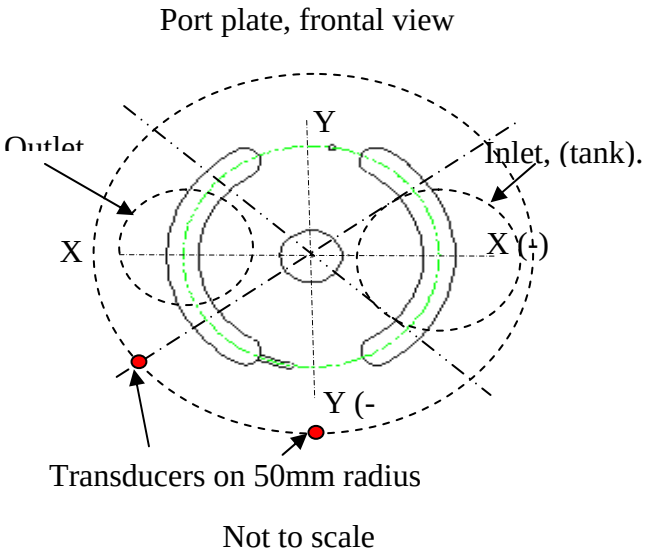

a) Scheme of the test rig two, showing the transducer's position.

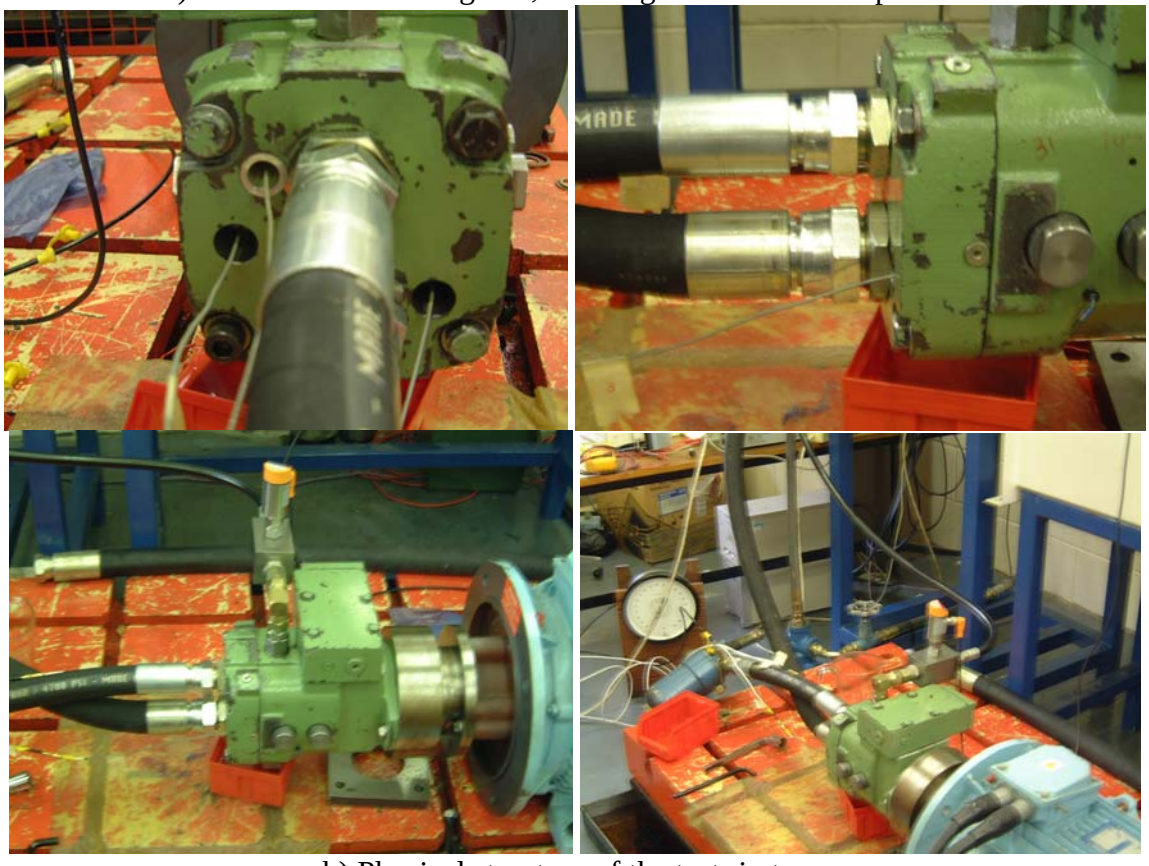

b) Physical structure of the test rig two.

Figure 7.2 - Test rig used to measure the barrel dynamics.

It is expected that the future measurements extracted from the second version of this test rig, shown in figure 7.2b, which used three position transducers, would clarify the average gap between the barrel and the valve plate as a function of the pump operating conditions. Such average gap distance will be introduced as an input in the CFD barrel/plate model and this will allow us to evaluate the barrel / plate leakage.

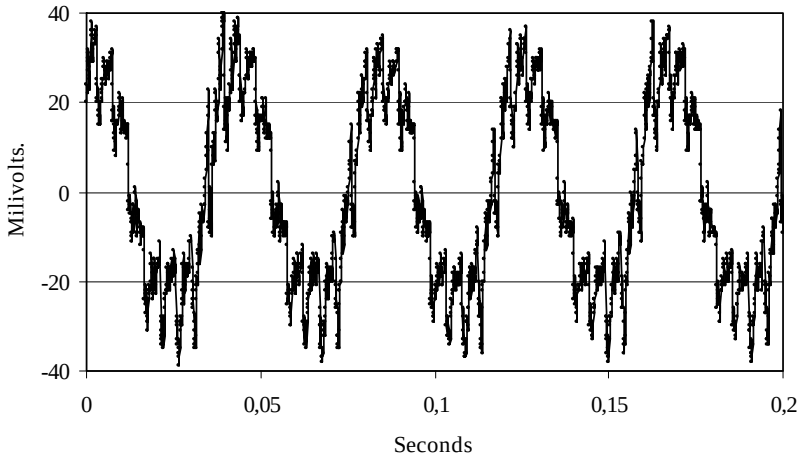

Figure 7.3 - Barrel dynamic gap measurements obtained from the position transducer located over the “YY” axis. Outlet pressure 18 MPa.

7.4 Tes rig three (To measure the pressure ripple).

Figure 7.4 shows two of the three pressure transducers which turn with the barrel and measure the dynamic pressure inside the piston/cylinder chamber. Via using this test rig, it has been found out, the pressure dynamics inside the piston chamber as a function of the pump operating conditions. Another pressure transducer located at the pump pressure port, has been used to measure the dynamic pressure ripple at the pump exit. These measurements have been used to compare the full pump dynamic simulation model with the experimental results, and therefore will allow validating the overall pump model.

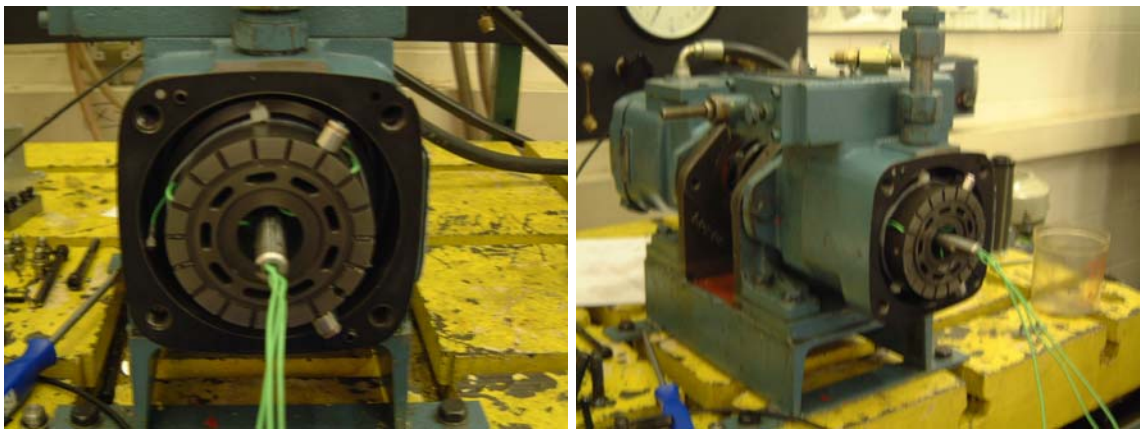

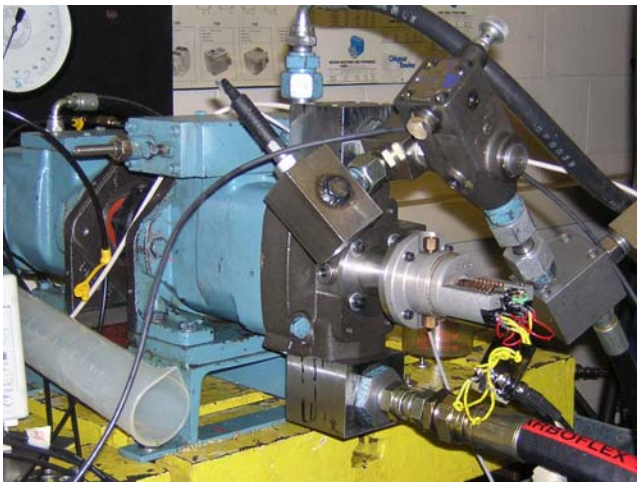

Figure 7.4 - Photographs of the test rig number 3.

8

Full Pump Model

The present chapter is focused on understanding the flow losses and the resulting flow dynamics for a piston pump. First, equations to evaluate leakages in all piston pump gaps are collected from the literature and presented, later the equations will be linked to determine the general dynamic flow characteristics. A numerical integration approach is then used to give the temporal pressure in each pump cylinder and the temporal leakage in all the pump clearances.

8.1 Introduction.

In theory the study of the piston-cylinder pressure ripple should be straightforward, since the differential equations involved are well understood. Such equations need as input, the different leakages through the pump clearances, but the problem increases when trying applying the equations to axial piston pump clearances. To overcome this difficulty several researchers have used different approaches, Foster and Hannan [1], integrate the dynamic pressure differential equation of the cylinder and evaluate the leakage experimentally, an interesting point in this paper is that they took into account the effect of the oil volume at the inlet and delivery lines, the paper introduces a link between pressure transients into the cylinder and the noise generated by the pump. Manring [2-4] assumes all leakage flows as laminar and uses a linear relation between pressure drop and flow, being necessary to find the leakage constant for every pump clearance. Ivantysynova [5-9] integrates the Reynolds equation of lubrication, linked with the energy equation to evaluate dynamically every leakage, pressure distribution and temperature in all piston pump clearances. The implicit solution is performed via a numerical computer program, with all computer sub-routines linked to create a macro program called CASPAR which evaluates the entire pump behaviour.

Very recently Ji-en Ma et al, [10] presented a single and multi-cylinder piston pump dynamics, in where they considered some equations to evaluate the leakage across the different piston/barrel gaps. They studied very carefully the leakage across the triangular timing grooves; they also considered the fluid inertia of the timing grooves, the paper

simulated pressure ripple is compared with the experimental one and clarifies the effect of the timing grooves regarding the piston dynamics, they also optimize the timing groove length for a particular application.

The numerical model developed for the slipper in chapters 2&3 is based on Navier Stokes equations (in order to understand the vorticity inside the groove) which produce very good results and allows to fully understand the effect of the groove on slipper surface, but being a full three dimensional NVS model, it is much slower than Reynolds equation model therefore the use of such model in order to formulate a full numerical model for the pump dynamic ripple becomes impractical. On the other hand, the numerical models developed for Barrel and piston are based on Reynolds equation and can be used for the full pump model.

It has to be noticed that in order to formulate a numerical model for pump dynamic ripple, only leakages through the different clearances of the pump are required and there exist analytical equations for such leakages developed by Bergada in literature. Although it has to be pointed out that these equations have their limitation on operating conditions and are developed under certain assumption as explained later for each case but produce good results under their limiting operating conditions. Therefore in this project, analytical equations developed by Bergada [11-14] in literature are collected for each component from the corresponding publications and after testing them against the numerical results, the equations will then be combined to study dynamic pressure ripple and leakages. The effect of a pump design change will then be presented.

8.2 Leakage on barrel plate.

An analytical model for the leakage and pressure distribution between the barrel and the top plate is developed by Bergada at al [11] from the integration of Reynolds equation of lubrication in polar coordinates. The same method was used by Jacazio and Vatta [15], although, a more precise integration is undertaken by Bergada. While taken tilt and rotation into account and assuming the flow moves in radial direction, the leakage barrel-plate can be given by equations (8.1-8.2) as describe in Bergada el al [11].

$$Q_{exter} = \frac{\left(p_{exter} - p_{inter}\right)}{12\,\mu \ln\left(\frac{r_{exter}}{r_{exter2}}\right)}\left[\begin{array}{l} h_0^3\left[\theta\right]_{-\theta_1}^{\theta_1} + 3h_0^2\,\alpha\, r_{mexter}\left[\sin\theta\right]_{-\theta_1}^{\theta_1} + \\ 3h_0\,\alpha^2\, r_{mexter}^2\left[\frac{1}{4}\sin(2\theta)+\frac{\theta}{2}\right]_{-\theta_1}^{\theta_1} + \alpha^3\, r_{mexter}^3\left[\frac{1}{12}\sin(3\theta)+\frac{3}{4}\sin\theta\right]_{-\theta_1}^{\theta_1} \end{array}\right] \tag{8.1}$$

$$Q_{inter} = -\frac{\left(p_{exter} - p_{inter}\right)}{12\,\mu \ln\left(\frac{r_{inter}}{r_{inter2}}\right)}\left[\begin{array}{l} h_0^3\left[\theta\right]_{-\theta_1}^{\theta_1} + 3h_0^2\,\alpha\, r_{minter}\left[\sin\theta\right]_{-\theta_1}^{\theta_1} + \\ 3h_0\,\alpha^2\, r_{minter}^2\left[\frac{1}{4}\sin(2\theta)+\frac{\theta}{2}\right]_{-\theta_1}^{\theta_1} + \alpha^3\, r_{minter}^3\left[\frac{1}{12}\sin(3\theta)+\frac{3}{4}\sin\theta\right]_{-\theta_1}^{\theta_1} \end{array}\right] \tag{8.2}$$

The total leakage barrel-plate will be the addition of the two leakage flows, which corresponds to the internal and external land of the barrel, see figure 4.1. According to equations (8.1 & 8.2) leakage barrel plate will depend on the geometry, internal and external pressures, tilt, and the central clearance. Leakage due to the small groove should also be included, but it has been pointed out by Bergada [11] that such leakage is insignificant when compared to the main groove and therefore will be neglected.

8.2.1 Comparison between analytical and numerical results for barrel-plate leakage.

Figure 8.1 represent the comparison between the leakage calculated from equations (8.1 & 8.2) and from the numerical model developed in chapter 4 at different clearances and 25 Mpa inlet pressure. A perfect agreement between equations and numerical results are found under the case studies.

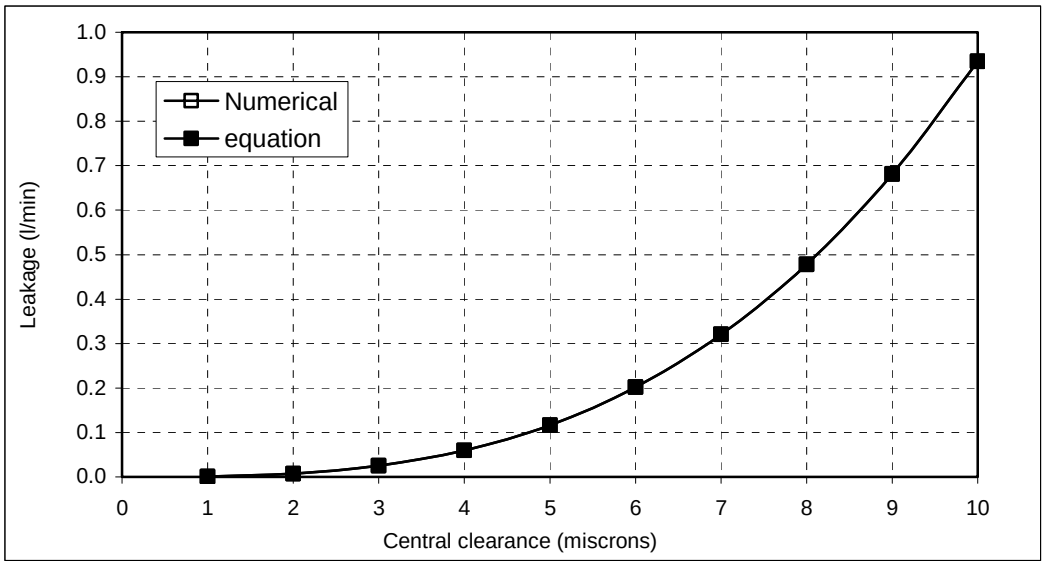

Figure 8.1 - Leakage barrel-plate versus different central clearances and maximum alpha at each clearance, Inlet pressure 25MPa.

8.3 Leakage slipper - swash plate.

The basis of the theory for the development of leakage between slipper-swash plate was outlined in Bergada and Watton [12, 13]. The following assumptions are made in order to determine the set of equations for the slipper-plate leakage.

1. Flow will be considered laminar in all cases.
2. The slipper plate clearance is not uniform; the slipper is tilted.
3. Steady conditions are considered.
4. Slipper rotation effects are taken into account.
5. Flow will be radial at the slipper face.

When taking in to account the above described assumption, the leakage slipper-plate can be given by equation (8.3) as described in Bergada [12, 13]. Due to the complexity of the integral, equation (8.3) has been integrated numerically.

$$Q_{leakage} = -\int_0^{2\pi} \frac{k_1}{12\,\mu}\, d\theta \tag{8.3}$$

Where,

$$k_1 = \frac{p_{tank} - p_{inlet} - \dfrac{3\mu\omega_S\,\alpha\sin\theta}{2}\left[\displaystyle\sum_{i=1}^{i=n} \frac{r_{mi}\left(r_{i-1}^2 - r_i^2\right)}{\left(h_{0i} + \alpha r_{mi}\cos\theta\right)^3}\right] - 3\mu\omega_S\,\alpha\sin\theta\left[\displaystyle\sum_{i=1}^{i=(n-1)} \frac{\ln\left(\dfrac{r_{i+1}}{r_i}\right)\left[\displaystyle\sum_{j=1}^{j=i} r_j^2\left(r_{m(j+1)} - r_{mj}\right)\right]}{\left(h_{0(i+1)} + \alpha r_{m(i+1)}\cos\theta\right)^3}\right]}{\displaystyle\sum_{i=1}^{i=n} \frac{\ln\left(\dfrac{r_i}{r_{(i-1)}}\right)}{\left(h_{0i} + \alpha r_{mi}\cos\theta\right)^3}} \tag{8.4}$$

Notice that the parameter k_1, equation (8.4), is given in generic form, being "n" the number of slipper lands, including the grooves and the slipper central pocket. For the present slipper, the number of lands is four, since the slipper under study has the central pocked, a first land, the groove and a second land. Therefore equation (8.4) will need to be defined for the slipper under study and then substituted in equation (8.3).

8.3.1 Comparison between analytical and numerical results for slipper-plate leakage

On figure 8.2 is presented the leakage in a tilt slipper with groove, again results from CFD and equations are being compared. Notice that the leakage found by the equations is about 5% bigger than the one found via using CFD developed in chapter 3. such differences can be explained when understanding that the Navier stokes equation takes into account the pressure distribution along the tangential direction, and such distribution is specially relevant inside the groove, then an smaller pressure differential between the central land and groove, will bring an smaller flow. It is important to notice that, the equations produce very good results for leakage between slipper and plate at low tilts, smaller than (0.01^o) and in literature has been found that slipper tends to run at very small tilts, therefore using the analytical equations rather than the numerical model does not introduce much error in slipper leakage and produce much faster results.

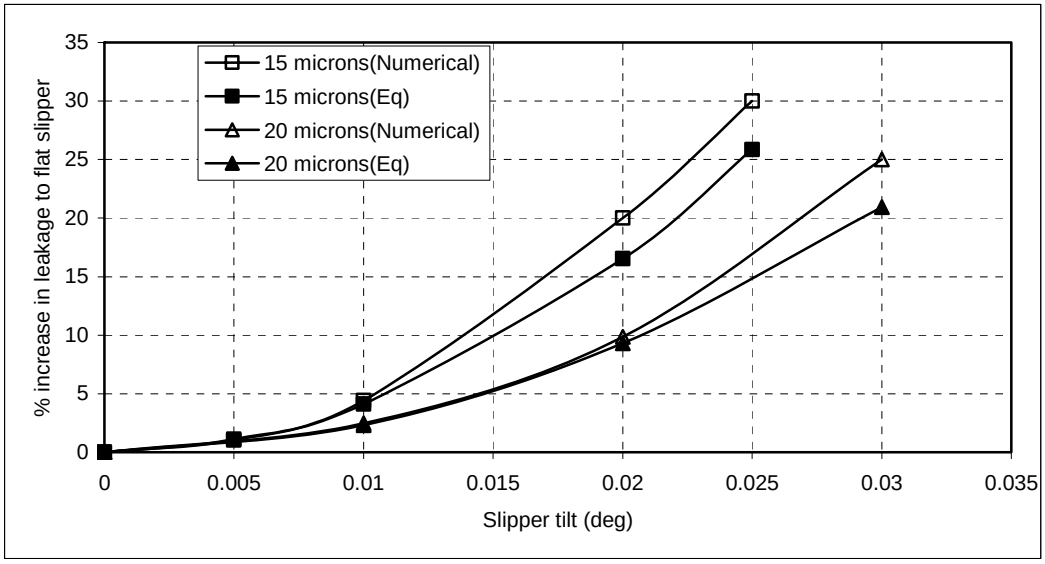

Figure 8.2 - Leakage between the slipper-swash plate clearance, comparison CFD and equations.

8.4. Leakages between Piston and Barrel.

For pison barrel gap, the equations developed by Bergada [14] are based on the one-dimensional Reynolds equation of lubrication, the Couette Poiseulle equation, and the continuity equation. The following assumptions have been made while developing the analytical model for the leakages between piston-barrel clearance:

1. Laminar flow is being considered in all cases.
2. The flow is two-dimensional.
3. Relative movement between piston and barrel exists.
4. The gap piston cylinder is simulated as the gap between two flat plates.
5. No eccentricity is considered.
6. Each land and groove is modelled as a flat plate.

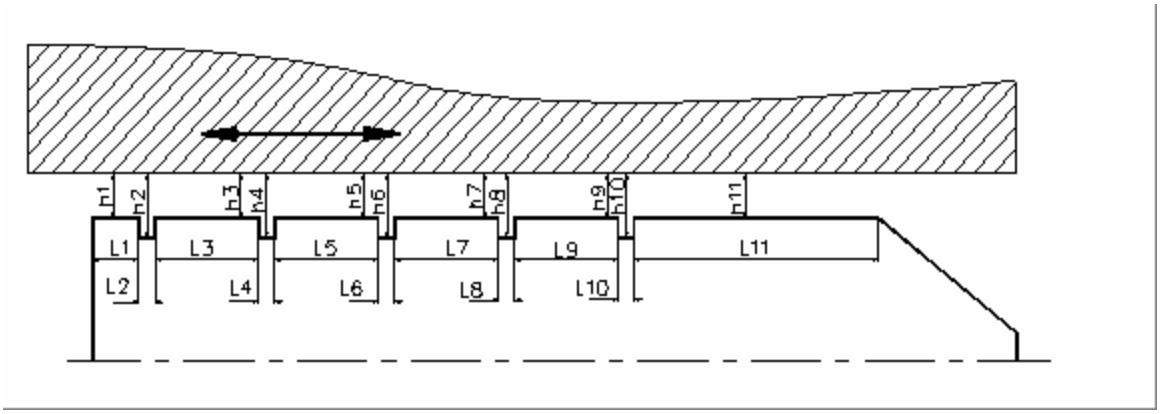

Figure 8.3 – Piston Geometry.

The piston main dimensions are: see figure 8.3:

$h_1 = h_3 = h_5 = h_7 = h_9 = h_{11}$.
$h_2 = h_4 = h_6 = h_8 = h_{10} = h_1 + 0.4$ mm.
$L_1 = 1.42$ mm
$L_{11} = 19.5$ mm
$L_2 = L_4 = L_6 = L_8 = L_{10} = 0.88$ mm
$L_3 = L_5 = L_7 = L_9 = 4$ mm

The leakage through piston-barrel gap can be given by equation (8.5) which has been developed by the integration of one dimensional Reynolds equations by taking in to account above specified assumptions.

$$q_p = \pi d\left[\frac{h_1 R_p \tan\alpha \left(-\sin(\omega t)\right)\omega}{2}\right] - \frac{\pi d}{12}\left[\frac{P_{Tank} - P_{interior} - 6R_p \tan\alpha\left(-\sin(\omega t)\right)\omega\mu\left[\frac{h_{10}-h_1}{h_{10}^3}\right](l_2+l_4+l_6+l_8+l_{10})}{\frac{\mu}{h_{11}^3}\left(\sum_{i=1}^{11} l_i - \frac{l_{11}}{2} - R_p\tan\alpha\cos(\omega t)\right) + \mu\left[\left(\frac{1}{h_2^3}-\frac{1}{h_1^3}\right)(l_2+l_4+l_6+l_8+l_{10})\right]}\right] \quad (8.5)$$

Equation (8.5) gives the dynamic leakage piston-cylinder for any given swash plate angle and considering the dimensions of the five grooves cut on the piston and the real length of the piston inside the barrel. Equation 8.5 assume piston to be positioned at lower death centre at time t=0.

8.4.1Comparison between analytical and numerical results for piston-barrel leakage

Figure 8.4 presents a comparison between analytical and numerical leakage for piston-cylinder clearance at 1000 rpm pump turning speed, 10 microns central clearance, 30 Mpa inlet pressure. Figure represents a good agreement between numerical and analytical results.

It is important to point out that piston eccentricity can not considered when calculating leakage using analytical equation 8.4, but it has already been proven by numerical analysis in chapter 5 that in presence of grooves, piston eccentric displacement does not effect the leakage as long as a fix central clearance is maintained between piston and cylinder. Therefore equation 8.4 produces very good results for leakage between the piston cylinder clearance under all working conditions.

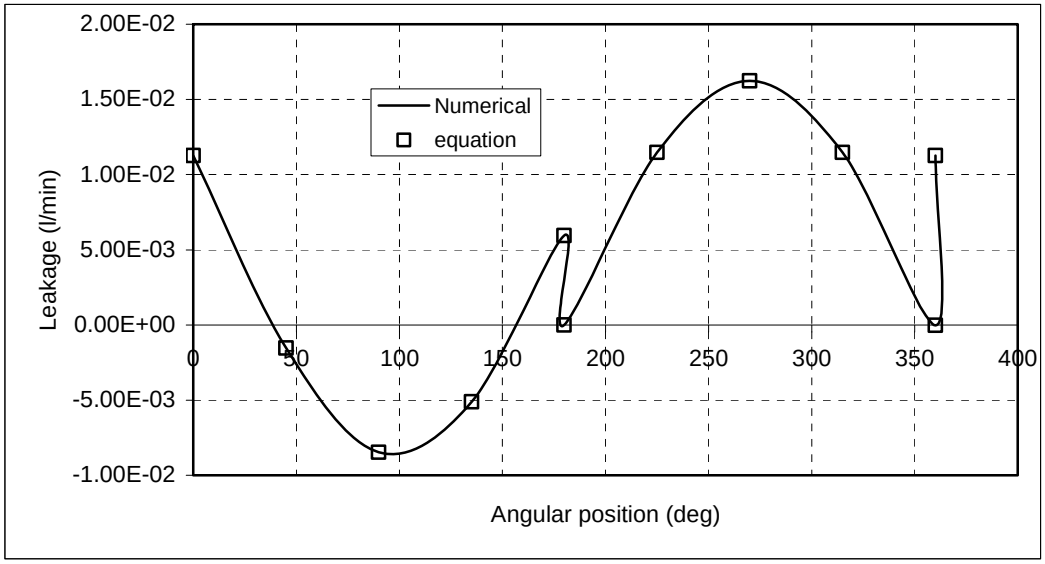

Figure 8.4 – Leakage between piston cylinder clearance versus angular position at 30Mpa inlet pressure, 1000 rpm pump turning speed, 10 microns central clearance comparison between numerical and equation.

8.5 Flow leaving each piston chamber.

Since the area through which the flow is leaving each piston chamber is much bigger than the rest, the flow is traditionally assumed as turbulent, for such cases the conventional equation used is:

$$Q_{out-piston} = \text{sign}(p_{piston} - p_d)\, C_d\, A_c \sqrt{\frac{2}{\rho}\left|p_{piston} - p_d\right|} \qquad (8.5)$$

The discharge coefficient is generally assumed as constant and equal to 0.6 although in reality depends on the cross sectional area and pressure differential. The temporal cross sectional area (A_c) can be calculated from table 8.1.

Table 8.1 – Definition of A_c (Contact area with port plate)

Angular Position	A_c	Connecting side
$\theta \geq 0$ & $\theta \leq 8$	$A_{Sg/1^o}(\theta + 8)$	Pressure
$\theta \geq 8$ & $\theta \leq 24$	$A_{Sg/1^o} + A_{Mg/1^o}(\theta - 8)$	Pressure
$\theta \geq 24$ & $\theta \leq 40$	$A_{Sg/1^o} + A_{Mg/1^o}(\theta - 8) - A_{Sg/1^o}(\theta - 24)$	Pressure
$\theta \geq 40$ & $\theta \leq 140$	$32\, A_{Mg/1^o}$	Pressure
$\theta \geq 140$ & $\theta \leq 172$	$32\, A_{Mg/1^o} - A_{Mg/1^o}(\theta - 140)$	Pressure
$\theta \geq 172$ & $\theta \leq 180$	A_{hole}	Pressure

$\theta \geq 180$ & $\theta \leq 188$	A_{hole}	Tank
$\theta \geq 188$ & $\theta \leq 220$	$A_{Mg/1^o}(\theta - 188)$	Tank
$\theta \geq 220$ & $\theta \leq 320$	$32\, A_{Mg/1^o}$	Tank
$\theta \geq 320$ & $\theta \leq 352$	$32\, A_{Mg/1^o} - A_{Mg/1^o}(\theta - 320)$	Tank
$\theta \geq 352$ & $\theta \leq 360$	$A_{Sg/1^o}(\theta - 352)$	Pressure

Where,

$$A_{Mg/1^o} = \frac{\pi}{360}\left(r_{ext}^2 - r_{int}^2\right) \quad A_{Sg/1^o} = \frac{\pi}{360}\left(R_{ext}^2 - R_{int}^2\right) \quad A_{cm} = \left(r_{ext}^2 - r_{int}^2\right)\tan^{-1}\left(\frac{r_{ext} - r_{int}}{2\,R_{swash}}\right) \tag{8.6}$$

Therefore, the actual area, across which output flow will exist, flow leaving the piston chamber towards the pump outlet, can be given by equation (8.6) and it is represented in figure 8.5. Notice that due to the entrance small groove the area increase has two different slopes.

$$A = \begin{cases} A_c & \text{if } A_c \leq A_{cm} \\ A_{cm} & \text{else} \end{cases} \tag{8.7}$$

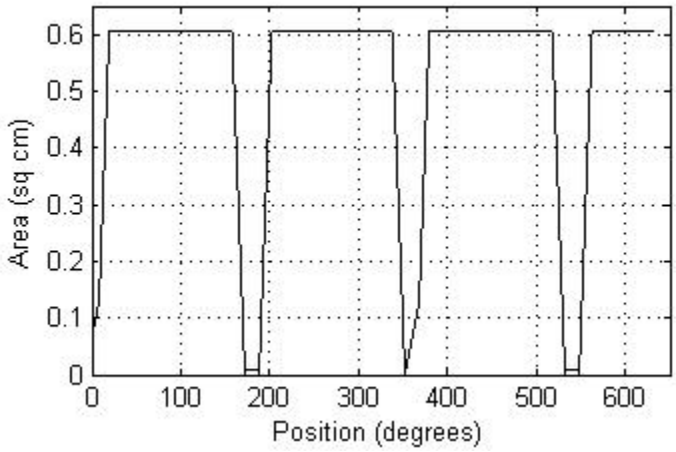

Figure 8.5 – Temporal cross section area (A)

It is noticed that the output area across which the flow towards the pump output will leave, goes from zero to a maximum every 165 degrees. When a piston enters in contact with the timing groove, the output area increase rather sharply, and once the piston enters in contact with the main groove, the area increase in a lower rate, wile the piston is fully in contact with the main groove, the output area remains constant. When calculating the temporal timing groove area, it should also be considered the timing groove depth, since the input area is in reality the cross sectional area perpendicular to the fluid flow. From figure 8.5 it is also noticed that when a piston groove leaves the main groove, during 10

degrees, the area of contact between the cylinder and the main groove is null, there will exist no flow between that particular piston chamber and the pump pressure groove.

8.6 Temporal piston cylinder differential equation.

As the swash plate is moving, the volume of each piston/cylinder chamber and its connecting side changes with time. The connecting side of the piston as a function of swash plate position is given in table 1 and the temporal volume of each piston can be given by equation (8.8) as function of swash plate angular position.

$$\forall = \forall_0 + \frac{\pi d^2}{4} R_p \tan\alpha \left(\cos\theta - 1\right) \tag{8.8}$$

Where, $\forall_0$ = is the cylinder volume when the piston is located at the bottom dead centre.

The temporal pressure inside each piston can be found by applying continuity equation in integral form in the piston cylinder chamber, as given in equation (8.9).

$$\frac{dp_{piston}}{dt} = \frac{\beta}{\forall}\left(-Q_{slip-plate} - Q_{barrel-plate} - Q_{sphere} - Q_{piston-barrel} - Q_{out-piston} - \frac{d\forall}{dt}\right) \tag{8.9}$$

Equation (8.9) gives the temporal pressure inside the piston/cylinder chamber as a function of the flow leaving the chamber, the fluid bulk modulus and the temporal volume of the chamber.

Once all leakage equations are being substituted in equation (8.9) and after integration is performed, the time dependent pressure distribution inside one piston/cylinder chamber and the time dependant leakages through all pump gaps can be evaluated.

8.7 Temporal out flow ripple (Combination of nine pistons with out flow valve)

In order to study the effect of the nine pistons regarding the entire pump dynamics, it was decided to apply the continuity equation in integral form, when combining the output flow from all the pistons connected to higher pressure side at any time instant, which resulted in equation (8.10).

$$\frac{dp_d}{d\theta} = \frac{\beta}{\omega \forall_{valve+pipe}}\left(\sum_{i=1}^{n_p} Q_{out\text{-}piston} - Q_{outlet}\right) \qquad n_p = \text{no of pistons connected to outlet} \tag{8.10}$$

The output flow ripple through the relieve valve can be given as:

$$Q_{outlet} = \text{sign}(p_d - p_{out})\, C_d\, A_{valve} \sqrt{\frac{2}{\rho}\left|p_d - p_{out}\right|} \tag{8.11}$$

The relief valve dimensions and its dynamics do affect the overall pump behaviour and therefore it would be necessary to simulate the relief valve dynamics in order to include its behaviour when studding the overall pump behaviour. Nevertheless the relief valve changing area has been implemented in the model

8.8 Computational technique.

Figure 8.6 shows a combined flow assembly of all the pistons under pressure, area and leakage nomenclature. A computer program has been written while combining all the equations (8.1-8.11) according to the flow chart shown in figure 8.6 in MATLAB. The numerical integrations have been performed by using fifth order Runge-Kutta method. The output flow ripple simulations have been performed for a valve pressure (outlet pressure) of 10MPa.

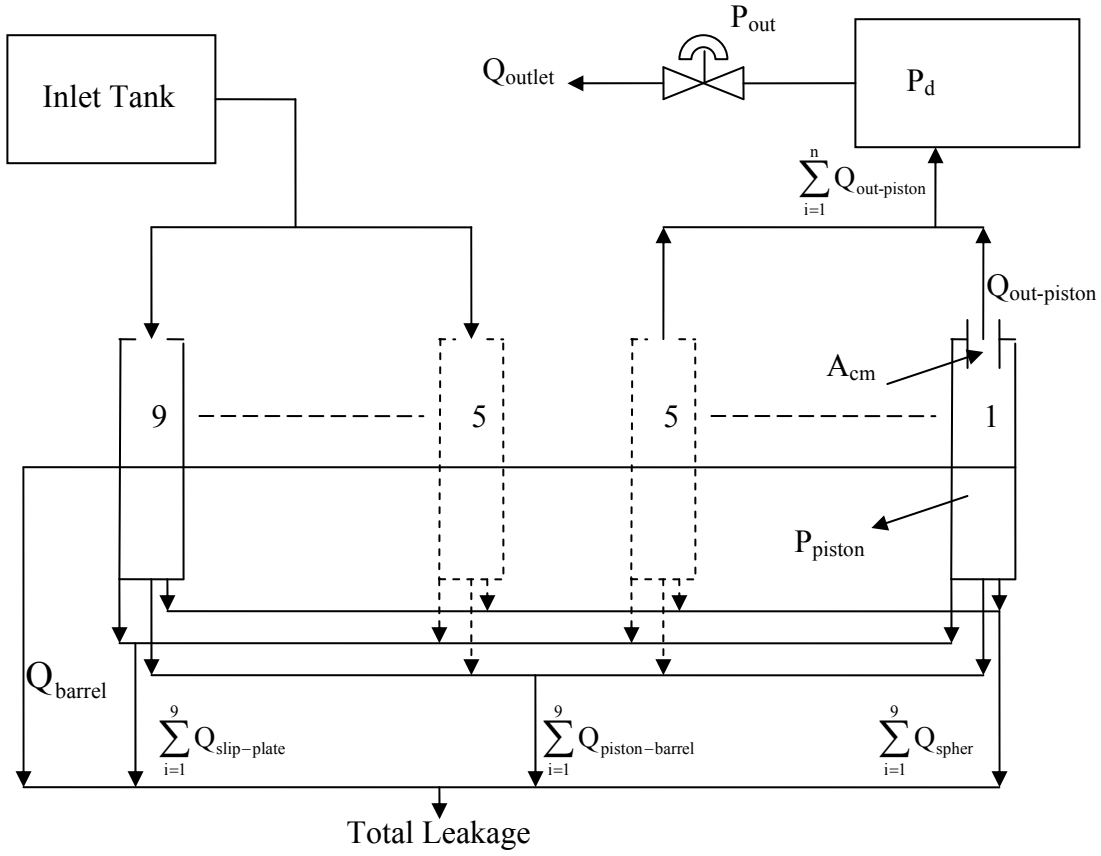

Figure 8.6 – A combine assembly of all pistons with nomenclature in Axial Piston pump.

8.9 Results

Figure 8.7 presents the comparison between experimental and simulated piston/cylinder pressure ripple for 20 degrees swash plate angle, 1000 rpm pump turning speed and 10 MPa output pressure. This figure shows a reasonably good agreement between simulation and experimental results, although the difference between the shapes of the flow ripple

has to be noticed. Such difference in shape of the pressure ripple can be due the difference between the real timing groove temporal changing area and the real relief valve area and the areas which has been used in the simulation. Although in the simulation the real measurements of such areas were intended to be used, we fear that the dimensions available to us might have differ a bit versus the real dimensions of the pump tested. It is expected that such modification in area will further improve the match between experiments and simulation results.

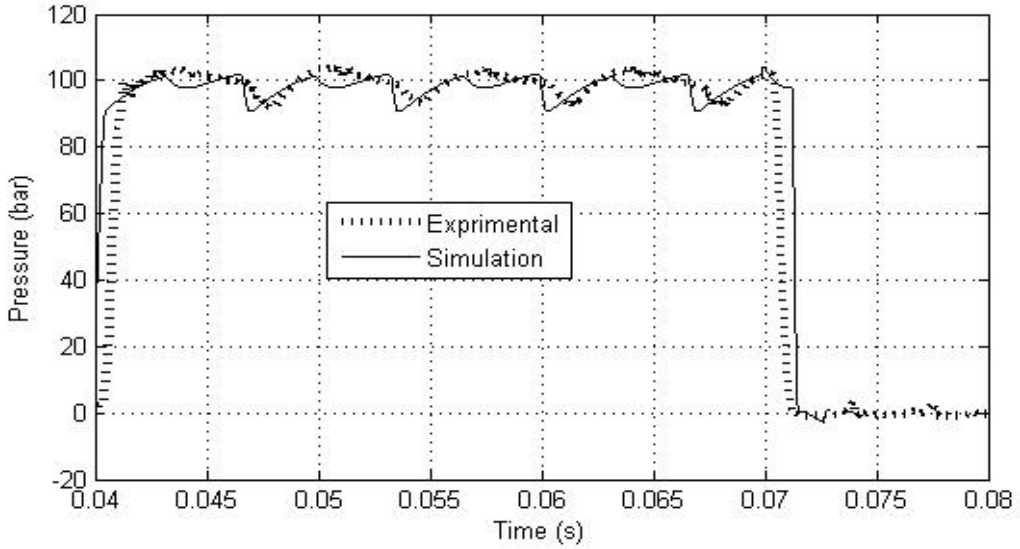

Figure 8.7 – Temporal pressure ripple inside the piston chamber at 100 bar output pressure, 1000 rpm pump turning speed, 20^{o} swash plate angle, comparison experimental and simulation.

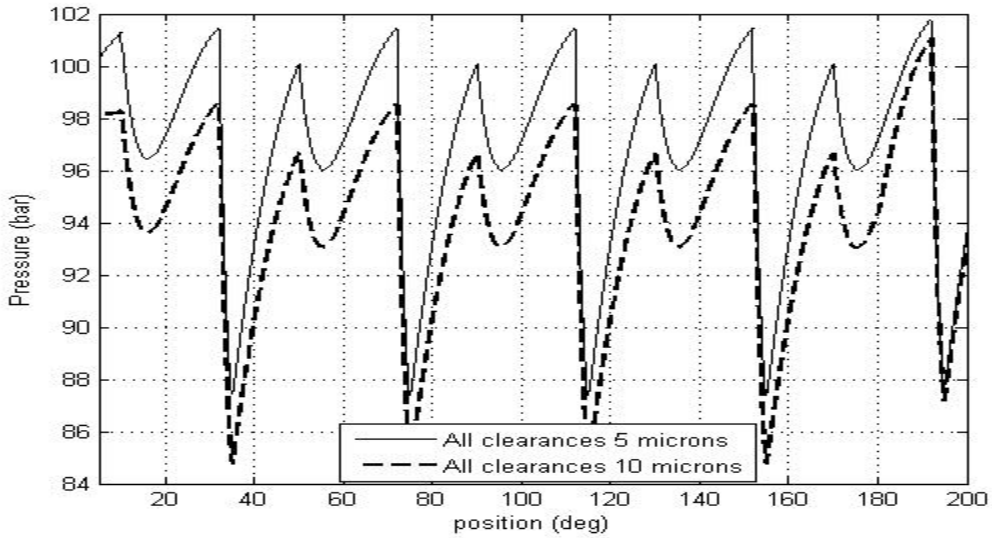

Figure 8.8 – Output pressure ripple of the pump for 100 bar out let pressure, 1000 rpm pump turning speed, 20^{o} swash plate angle, 5 and 10 microns of clearances through all the sliding surfaces.

By using the simulation code, it is possible to modify the clearances through all the gaps to understand the behaviour of pump when it becomes old. For such purpose, figure 8.8 presents the output pressure ripple given by the pump at 10 MPa outlet pressure, 1000 rpm pump turning speed, 20° swash plate angle, when two different clearances of 5 and 10 microns have been considered through all the sliding surfaces. It can be noticed from the figure that an increase of 5 microns in all the clearances, decreases the pressure by 0.3 MPa for this particular case.

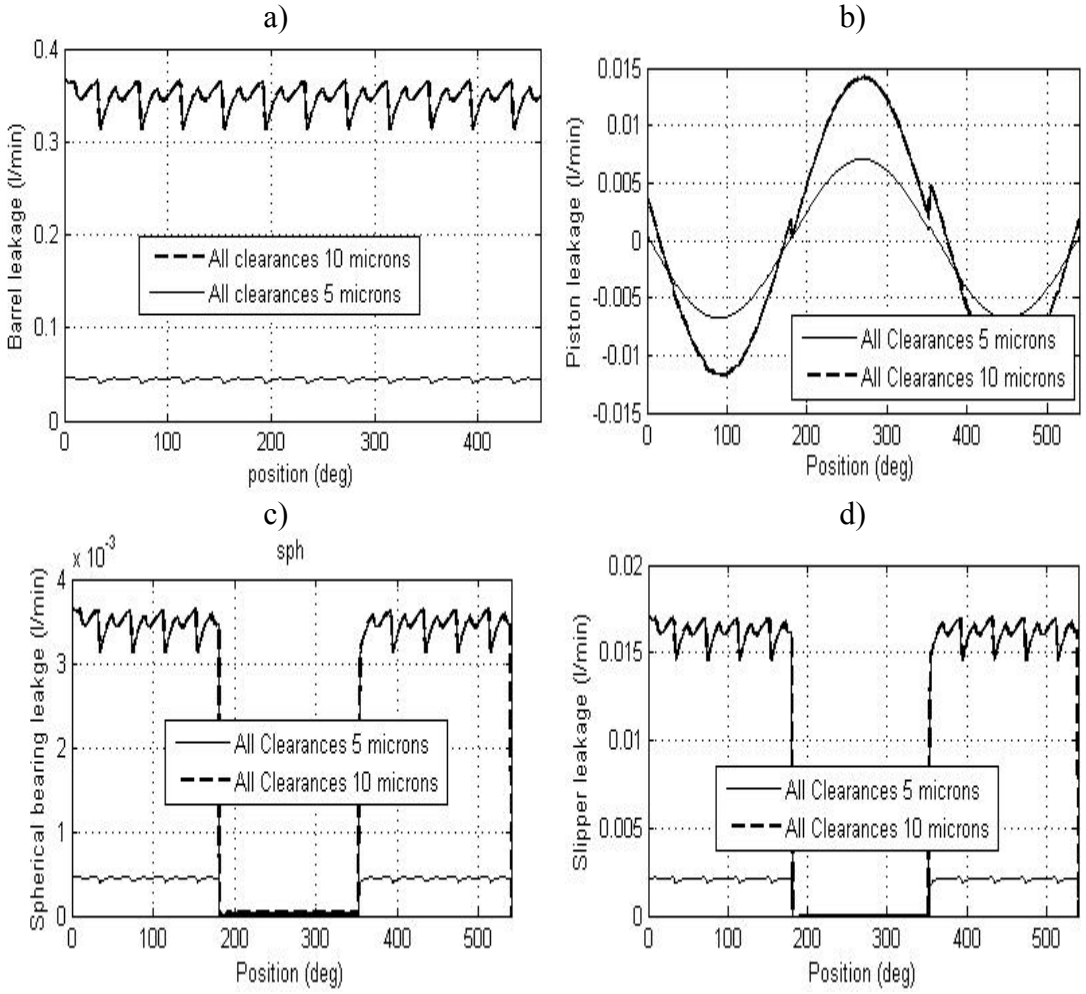

Figure 8.9 – Leakages through different gaps of one piston at 10 MPa out let pressure, 1000 rpm pump turning speed, 20° swash plate angle, 5 and 10 microns of clearances through all the sliding surfaces. [a] Barrel plate leakage. [b] Piston cylinder leakage. [c] Spherical bearing leakage. [d] Slipper leakage.

Figure 8.9 presents temporal leakages from all four sliding surfaces of the pump at 10 MPa output pressure, 1000 rpm pump turning speed and at two different clearances of 5 and 10 microns through all sliding surface. It can be noticed from the figure that the barrel has the highest temporal leakage among slipper-plate, piston-cylinder and spherical bearing clearances. The barrel leakage always remains high as it is always connected to high pressure side. On the other hand, slipper and spherical bearing produce their high

leakage when connected to high pressure side. The leakages from slipper and spherical bearing are negligible when connected to tank side. In opposite to that piston produce high out ward leakage when connected to tank side. As explained in chapter 5, the reason behind such behavior is that, piston is moving towards outward direction when connected to tank side; producing higher outward Poiseuille flow and resulting into higher leakage.

To understand the contribution to the total leakage from the each component more precisely, table 8.1 presents the total leakage over one rotation of the pump from different component of the pump. It can be noticed from the table that contribution of the barrel to the total is highest being over 77%. Slippers produce the second highest leakage contributing 16% of the total leakage. The leakage contribution from piston and spherical bearing clearances are much lower.

Table 8.1 - Total leakage from each component over one cycle, combining all 9 pistons

Clearance	5 microns		10 microns	
Slipper – plate clearance	9.3893e-006L	16.26%	7.2843e-005L	16.27%
Piston – cylinder clearance	1.5931e-006L	2.76%	1.2371e-005L	2.76%
Spherical bearing clearance	2.0103e-006L	3.48%	1.5601e-005L	3.48%
Barrel plate clearance	4.4741e-005L	77.5%	3.4702e-004L	77.49%
Total	5.7734e-005L		4.4784e-004L	

8.10 Conclusions.

The analytical equations for leakages through different piston pump clearances are collected from the literature and tested against the numerical models, finding a good agreement with the numerical results. A full numerical model for the pump has been formulated by connecting all these leakage equations through continuity. The model developed in this chapter gives freedom to modify the clearances through each gap, in order to understand the pump behavior as the pump becomes old. Two clearances of 5 and 10 microns have been analyzed, finding a 0.3 MPa pressure drop in output pressure ripple. Total leakages from each component have been evaluated for a same value of the clearance in each gap, finding the contribution from barrel plate being the highest and slipper being second highest. In more realistic cases, the clearances in different gaps have different values, being the barrel plate clearance much lower than slipper plate. Therefore under such conditions, the contribution of the slipper leakages becomes more important.

Nomenclature.

A_c	-	Piston chamber outlet area. (m^2).
C_d	-	Discharge coefficient.
d	-	Piston diameter (m).
h_o	-	Barrel, slipper, central height (m).
k_1	-	Slipper constants (Nm).

l_i	-	Length of a single land (m).
n	-	Number of lands, including the grooves.
n_p	-	Instantaneous number of pistons over the discharge.
$p_{inlet.}$	-	Pressure inside the piston chamber (N/m^2)
$p_{interior.}$	-	Pump outlet pressure (N/m^2)
$p_{exterior}$	-	Pump inlet pressure (tank pressure) (N/m^2)
Q	-	Generalised flow (m^3/s).
Q_{exter}		Leakage barrel plate towards the external radius (m^3/s).
Q_{inter}		Leakage barrel plate towards the internal radius (m^3/s).
r	-	Barrel, slipper generic radius (m)
r_m	-	Average radius between land borders (m).
R_P	-	Piston pith radius (m).
α	-	Barrel, slipper tilt angle. (rad)
γ	-	Small groove angle (rad)
θ	-	Barrel angle (rad).
μ	-	Fluid dynamic viscosity. (Kg/m s).
ω	-	Bbarrel angular velocity (rad/s).
ω_S	-	Slipper spin (rad/s).
$A_{Mg/1^o}$		Area of main groove per unit angle (m^2/deg).
$A_{Sg/1^o}$		Area of small groove per unit angle (m^2/deg).
A_{cm}		Area of the hole at the top of the piston (m^2).
$\forall$		Volume corresponding to subscript (m^3).

Reference:

1. Foster K, Hannan D.M; Fundamental Fluidborne and Airborne Noise Generation of Axial Piston Pumps. *Seminar on Quiet Oil Hydraulic Systems*. Paper C257 / 77. *Institution of Mechanical Engineers*. London, England. 1977.

2. Manring N.D. The Discharge Flow Ripple of an Axial-Piston Swash-Plate Type Hydrostatic Pump. *Journal of Dynamic Systems, Measurement, and Control. ASME.* June 2000, Vol 122 pp 263-268.

3. Manring N.D; Damtew F.A. The Control Torque on the Swash plate of an Axial Piston Pump utilizing Piston -Bore Springs. *Journal of Dynamic Systems, Measurement, and Control. ASME.* September 2001, Vol 123 pp 471-478.

4. Manring N.D; Zhang Y. The Improved Volumetric Efficiency of an Axial - Piston Pump Utilizing a Trapped - Volume Design. *Journal of Dynamic Systems, Measurement, and Control. ASME.* September 2001, Vol 123 pp 479-487.

5. Ivantysynova M; Huang C. Investigation of the Flow in Displacement Machines Considering Elastohydrodynamic Effect. *Proceedings of the 5th JFPS International Symposium on Fluid Power*, November 13, Nara 2002 Japan Vol. 1 pp 219-229.

6. Ivantysynova M; Grabbel J; Ossyra JC. Prediction of a Swash Plate Moment Using The Simulation Tool CASPAR. *ASME International Mechanical Engineering Congress & Exposition*. November 17-22, 2002, New Orleans, Louisiana USA. IMECE2002-39322 pp 1-9.

7. Wieczorek U; Ivantysynova M. Computer Aided Optimization of Bearing and Sealing Gaps in Hydrostatic Machines – the Simulation Tool CASPAR. *International Journal of Fluid Power* 3 (2002) No. 1 pp 7-20.

8. Ivantysynova M. A New Approach to the Design of Sealing and Bearing Gaps of Displacement Machines. *Fluid Power forth JHPS International Symposium* 1999. pp 45-50.

9. Ivantysynova M; Lasaar R. An Investigation into Micro – and Macrogeometric Design of Piston / Cylinder Assembly of Swash plate machines. *International Journal of Fluid Power* 5 2004 No 1 pp 23-36.

10. Helgestad BO; Foster K; Bannister F K. Pressure Transients in an Axial Piston Hydraulic Pump. *Proceedings of the Institution of Mechanical Engineers,* Vol 188 No 17 / 74. 1974, 189 – 199.

11. Bergada JM, Watton J, Kumar S. Pressure, flow, force and torque between the barrel and port plate in an axial piston pump. Journal of dynamic systems, measurement and control, Jan 2008, Vol 130. N 1. pp 011011-1/16

12. Bergada JM and Watton J. A direct leakage flow rate calculation method for axial pump grooved pistons and slippers, and its evaluation for a 5/95 fluid application. *5th JFPS international Symposium on fluid power,* Nara Japan. November 13, 2002.

13. Bergada JM and Watton J. Axial piston pump slipper balance with multiple lands. *ASME International Mechanical Engineering Congress and exposition. IMECE 2002.* New Orleans Louisiana November 17-22 2002. Vol 2 paper 39338.

14. Bergada JM; Watton J. A New Approach Towards the Understanding of the flow in Small clearances applicable to Hydraulic Pump Pistons With Pressure Balancing Grooves. *7th International Symposium on Fluid Control, Measurement and Visualization. Flucome 2003*. Sorrento Italy. August 25-28 pp 1-8.

15. Jacazio G; Vatta F. The Block-lift in Axial piston Hydraulic Motors. *The ASME/ASCE Bioengineering, Fluids Engineering and Applied Mechanics Conference.* Boulder, Colorado USA June 22-24, 1981 pp. 1-7.

9

Conclusions

In this thesis, it is being analyzed each part of an axial piston pump regarding pressure, force, torque, leakage and under some cases Vorticity and when considering the presence of the grooves. The conclusions subjected to each component are as follow:

9.1 Slipper.

A Navier Stokes based model is formulated to evaluate the performance of the slipper under the presence of the groove on its surface. As the model is based on three dimensional Navier Stokes equation, it is possible to analyze the Vorticity in the slipper plate clearance along with the pressure, force, torque and leakages. Four different working conditions have been considered.

1) Flat static - When slipper is positioned parallel to swash plate (flat slipper) and no relative movements exist between slipper and swash plate surfaces, is called as flat static conditions.

2) Flat Dynamics - When slipper is positioned parallel to swash plate (flat slipper) and there exist a relative movements between slipper and swash plate surfaces, is called as flat dynamics conditions.

3) Tilt Static - When slipper is positioned at an angle to swash plate surface, such condition is called as tilted slipper and if the slipper is static with respect to swash plate, it is called as tilt static conditions.

4) Tilt Dynamics - When slipper is positioned at an angle to swash plate surface, and there exist a relative movement between slipper and swash plate surfaces, it is called as tilt dynamics conditions.

Under flat static conditions, it is found that the normalized pressure inside the groove is independent of inlet pressure; force acting on the slipper and leakage are a linear function of pressure. Leakage has a third order dependency on clearance slipper/plate, while slipper pressure distribution is for the cases studied, independent of clearance. When modifying groove position, the displacement of the groove towards the slipper inner pocket (inner boundary) leads to increase in leakage and force acting over the slipper. If the groove central axis is maintained at the centre of the slipper land, an increase of groove width will bring an increase in force acting over slipper and leakage. When the groove is positioned near the outer boundary of the slipper, the narrower the groove width the higher the force on the slipper and the lower the leakage. Independently on the groove position and width, an increase in groove depth leads to an increase in leakage until reaching a certain depth, up to which leakage remains constant.

Under flat and dynamic conditions, the tangential speed has negligible effect on the force acting over the slipper. It creates nevertheless a small torque respect to the two slipper main axis. At higher speed, there exists a noticeable pressure differential inside the groove. Leakage is independent on turning speed. Vorticity inside the slipper groove has been studied to analyze the momentum transfer inside the groove. In general two forced vortexes appear inside the groove. The primary one located at the groove bottom is the most responsible for maintaining the pressure along the groove in angular direction. This vortex exist under all working conditions, it is created by mutual adjustment between slipper/plate flow and no slipping condition on slipper groove wall. A secondary vortex is also near the groove face. Its existence is due to interaction between slipper-plate flow and primary vortex. This secondary vortex exists only in the region of higher velocity gradient.

Under tilted static conditions, pressure is found to be very stable along the angular direction in presence of the groove. The maximum pressure differential across the slipper radius, for inlet pressure 10 MPa, 0.042^{o} tilt and 15μm central clearance, decreases from 0.3 MPa to 0.03 MPa due to the presence of a groove. Groove pressure differential increases when central clearance decreases. Average pressure inside the groove decreases with the increase of tilt. Percentage decrease in force acting on the slipper is found to be independent of inlet pressure although highly dependent on slipper/plate central clearance. At lower clearances, the force decrease with tilt increase is more severe. As the slipper tilt is considered along the X-axis, the torque with respect to X-axis is found to be zero. On the other hand there exists Y directional torque. The magnitude of the Y torque is found to be increasing with the increase of tilt. Slipper leakage is found to be a strong function of clearance as it was found for flat slipper. Slipper leakage increases with the increase of tilt. When modifying the groove position, the displacement of the groove towards the slipper inner pocket (inner boundary) leads to an increase in leakage and force acting over the slipper, as it was found for flat slipper, but the effect under tilted

conditions is more severe than for the flat slipper case. Under tilt conditions, it is found, there exist three vortexes inside the groove, two at groove top edges and one at the bottom of the groove. The existence of the bottom vortex depends on tilt and inlet pressure. At higher tilt and higher pressure, the angular length of the bottom vortex increases. The bottom vortex appears in the locations where a huge momentum interchange between particles is needed. The two small vortexes appearing at the groove top edges remain rather constant in shape along the slipper groove, tilt and inlet pressure have a second order effect on the top vortexes.

Under tilted dynamics conditions, when doing simulation under such conditions, it was not possible to achieve a full convergence. It is found that after a certain number of iterations, residue starts fluctuating. When analyzing the Vorticity inside the groove at different iterations level, it has been concluded that flow inside the groove is time dependent. Under such conclusion, it is not possible to analyze the Vorticity inside the groove by the simulation code develop during this project, as the simulation code is design to handle steady state problems.

The attempt of converting the steady state code into transient one has not been made due to the fact that it takes 10 to 15 days to achieve the full convergence under tilt static conditions from the simulation code on a normal Personal Computer. Converting the code into transient will increase this time further and will make the simulation impractical. Therefore it might be a better choice to develop a transient code using unstructured grid and finite element method rather than boundary fitted grid and finite volume method. It has to be said that no security can be given that such code will produce a faster result than the code based on boundary fitted grid.

It has been found, when analysing pressure distribution, torque, force and leakage out side the groove at different iteration levels that these quantities are much weaker function of time compared to the flow inside the groove. Therefore it can be understood that the flow inside the grooves is highly depend on time but the flow out side the groove is a much weaker function of time. As a result, even though the simulation code is designed to handle steady states problems, it is still possible to get a very good idea about the behaviour of slipper characteristics (pressure, force, torque and leakages) under tilt dynamic conditions.

It has been found that an increase in turning speed tends to destabilize the pressure distribution below slipper but the effect of this destabilization is more severe in absence of the groove. The effect of disk turning speed is more severe at lower clearances. Force and torque are found to be increasing with increase in turning speed but leakages tends to decrease with increase in turning speeds.

9.2 Barrel – plate.

Reynolds equation of lubrication has also been applied to the gap between the barrel and port plate by using finite difference method. Leakage was found to be greater across the

external land than the internal land, for the same operating pressure, and typically by a factor of 2 whether it be related to pressure or central clearance. As expected, the small timing groove produced a significantly lower leakage than the main groove and could probably be neglected from a total flow loss point of view. It was found that cavitation in pumps is more likely to appear for smaller clearances, smaller output pressures and bigger turning speeds.

The effect of precisely defining piston position was shown to be crucial when calculating the total force on the barrel, the total force reducing as the number of active pistons changes from 4 to 5 during one cycle. This was shown to be due to the balance between piston pressure effects and groove effects, the former becoming more dominant as the number of pistons active changes from 4 to 5.

The total static torque is dominated by the contribution about the YY axis as anticipated from other work and simple considerations of the pumping mechanism. Individual torque contributions were shown to increase with pressure in almost a linear manner, the torque effect of the combined grooves being larger than the opposing torque due to piston pressure.

Both dynamic torques acting over the barrel XX and YY axes were taken from Bergada et al [27] and were introduced into a Simulink model to evaluate the barrel temporal position. In particular, the importance of precise modelling of the flow continuity mechanism was shown to be crucial in predicting the correct waveform shapes.

The results clearly show the torque increase as each piston groove is connected to the timing groove, as established by the theory presented. This was in spite of the requirement to extract the required data from a noisy signal due to barrel run-out. A good correlation between simulated and experimental results was found.

The fluctuation wave will present two main peaks, a small one related to the torque created when each piston enters in contact with the timing groove, and a main one created when each piston leaves the pressure kidney port, its frequency is 216 Hz. Along with the main fluctuation wave, appear another wave of a frequency around 1000-1100 Hz, this second fluctuation wave is more clearly seen when the system stiffness is high, system stiffness depends on the pump spring constant, pump central axis constant, and elastic/plastic metal to metal reaction forces, therefore as pressure increases, film thickness decreases, metal to metal contact increases, and these small perturbation peaks more clearly appear. The damping coefficient also plays an important role regarding the barrel dynamics, since as temperature increases, the damping coefficient decreases, allowing the barrel to move more freely, this is why at high temperatures and high pressures, the fluctuation wave is more clearly seen. The elastic/plastic metal to metal forces enhances the perturbation peaks increasing their amplitude.

9.3 Piston cylinder.

A finite volume based Reynolds equation model has been formulated for the piston-cylinder clearance which considers the piston eccentricity and the relative tangential movement between piston and cylinder. Different configurations of the grooves have been evaluated in search of finding minimum leakage, minimum appearance of cavitation and maximum restoring torque. Based on the observations, the following conclusions have been made:

1. The use of grooves cut on the piston surface brings stability to the piston, since it increases piston stiffness.

2. The grooves located on the central part of the piston, appear not to be useful regarding the pressure stabilization, torque, force or even cavitation point of view.

3. To avoid cavitation, it is important to consider the inclusion of grooves at the piston stroke length and near to the piston pressure side. In fact, wherever it is expected cavitation to appear, the use of a groove will tent to prevent cavitation from appearing.

4. Regarding the restoring torque point of view, configurations G2 and G1o are undesirable, configuration $G1_{2i}$ (one groove at the inner edge at second groove position) seams to be the best location from restoring torque point of view, since the magnitude of the restoring torque produced by the pressure distribution is quite high and rather independent of turning speed.

5. For a piston without grooves, leakage piston-cylinder decreases as the piston tilt increases, the decrease is more relevant at higher clearances.

6. As the number of grooves being cut on piston surface increases, the effect of piston tilt becomes less relevant regarding the piston cylinder overall leakage. As already established in literature, the increase in number of grooves will bring an increase in leakage.

7. Among the configurations studied, $G1_{2i}$ is the one bringing the best performance because it produces higher restoring torque at all pump turning speeds, leakage is fairly independent of piston tilt and although overall leakage is slightly higher that the non groove configuration, it is much lower than the configuration G5.

9.4 Spherical Bearing.

The literature found for spherical bearing is quite vast and well established. No further effort has been made to analyze the characteristic of the spherical bearing. Reynolds equation of lubrication in spherical coordinates has been integrated analytically in order to calculate leakage in spherical bearing clearance; such leakage has been used when

simulating the outflow ripple of the pump. It has to bear in mind that, integration of Reynolds equation has already been done by several researchers in literature.

9.5 Full pump model.

The numerical model developed for slipper in chapter 2&3 is based on Nervier Stokes equations (in order to understand the vorticity inside the groove) which produce very good results to fully understand the effect of the groove on slipper surface but being a full three dimensional NVS model, it is much slower than Reynolds equation model therefore the use of such model in order to formulate a full numerical model for the pump dynamic ripple become impractical.

In order to formulate the full pump model, the analytical equation for leakages through different piston pump clearances are collected from the literature and tested against the numerical models, finding a good agreement with the numerical results. A full numerical model for the pump has been formulated by connecting all these leakage equations through continuity. The model developed in this thesis gives freedom to modify the clearances through each gap, in order to understand the pump behavior as the pump becomes old. Two clearances of 5 and 10 microns have been analyzed, finding a 0.3 MPa pressure drop in output pressure ripple. The comparison between the experimental and the computational results regarding dynamic pressure ripple show a good agreement.

The dynamic and total leakages from each component have been evaluated for a same value of the clearance in each gap, finding the contribution from barrel plate being the highest and slipper being second highest. In more realistic cases, the clearances in different gaps have different values, being the barrel plate clearance much lower than slipper plate. Therefore under such conditions, the contribution of the slipper leakages becomes more important.

9.6 Possibility of future work.

In this thesis project, author tried to formulate all the models which can analyze the problem as close as possible to the real conditions while maintaining the maximum possible accuracy but there are still some areas where a further work is required to be done.

1. In order to fully analyze tilt slipper under dynamic conditions, a transient model needs to be formulated.

2. As we are dealing with very low clearances, it might be interesting to consider the surface roughness in the models.

3. When formulating the full pump model, the discharge are of each piston (A_c see chapter 8), needs further improvements.

4. As explained in chapter 7, the new version of test rigs two, which used three position transducers, would clarify the average gap between the barrel and the valve plate as a function of the pump operating conditions. Such average gap distance can be introduced as an input in the CFD barrel/plate model and this will allow us to evaluate the barrel / plate leakage for more practical cases.

References.

1. Bergada JM, Watton J, Kumar S. Pressure, flow, force and torque between the barrel and port plate in an axial piston pump. Journal of dynamic systems, measurement and control, Jan 2008, Vol 130. N 1. pp 011011-1/16